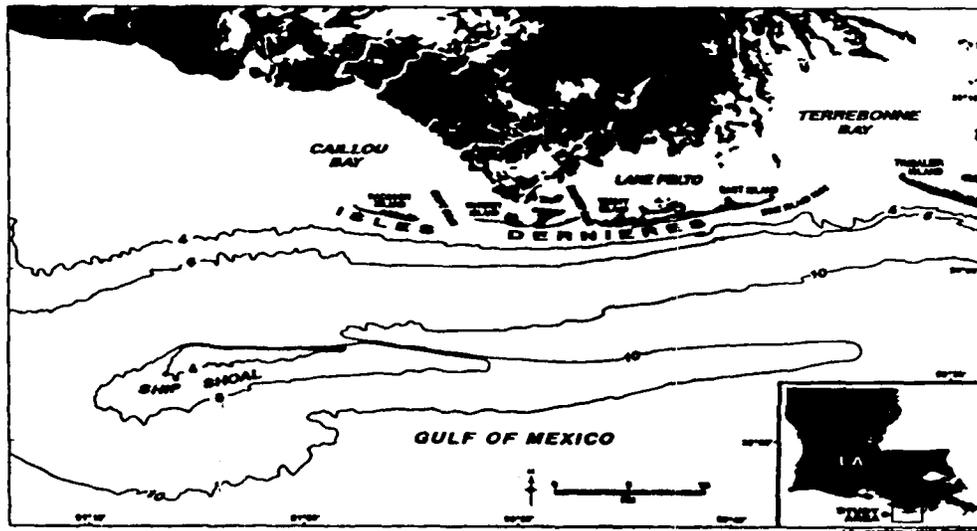# Wave Climate Modeling and Evaluation Relative to Sand Mining on Ship Shoal, Offshore Louisiana, for Coastal and Barrier Island Restoration

Final Report

October 1996

Wave Climate Modeling and Evaluation Relative to Sand Mining on Ship Shoal, Offshore Louisiana, for Coastal and Barrier Island Restoration

Final Report

October 1996

Authors:

Gregory W. Stone
and
Jingping Xu

COASTAL
MORPHODYNAMICS
LABORATORY

MMS U.S. Department of the Interior
Minerals Management Service

Louisiana State University
Department of Geography and Anthropology

DISCLAIMER

This report has been reviewed by the Minerals Management Service and approved for publication. Approval does not signify that the contents necessarily reflect the views and policies of the Service, nor does mention of trade names or commercial products constitute endorsement or recommendation for use.

Contents

List of Figures

List of Tables

1 Introduction

Program Overview

It is now well established in the literature that the barrier islands comprising the Isles Dernieres (Figure 1) have been experiencing among the highest rates of shoreline retreat in the United States (McBride *et al.*, 1992; Williams *et al.*, 1992; Stone and Penland, 1992). As summarized in Figure 2, the primary factors responsible for deterioration of these islands includes (1) eustatic sea-level rise; (2) compactional and geological subsidence; (3) wave erosion; (4) wind deflation; (5) reduction in sediment supply and (6) anthropogenic activity. Historical erosion rates along the Isles Dernieres ranged from 4.8 m/yr. (East Island) to 22.9 m/yr. (Wine Island) over the last century or so (McBride *et al.*, 1992). Recent evidence indicates an apparent acceleration in erosion, approximating 213% over the last decade (Williams *et al.*, 1992). Based on these data, it is estimated that several of the islands will disappear within the next decade or two (McBride *et al.*, 1992). Given the recent impact of Hurricane Andrew along this coast (Stone *et al.*, 1993; Stone *et al.*, 1995; Grymes and Stone, 1995), it is highly probable that this time period is less.

With the degradation of barrier systems, it is likely that mainland shoreline erosion and wetland loss will occur in response to a more energetic, local wave field (Penland and Suter, 1988; McBride *et al.*, 1992)--although, the critical links have not yet been fully investigated (List and Hansen, 1992). Recent data indicate that land loss in the Terrebonne Bay area averaged 0.86 km²/yr. between 1932 and 1990 (Britsch and Dunbar, 1993). Although preliminary, work carried out by van Heerden *et al.* (1993) indicates a large-scale relationship between degradation of the Isles Dernieres, increasing tidal prism, and, subsequently, enhancement of wetland loss.

The work of van Heerden *et al.* (1993) indicates that approximately 11.6 million cubic meters of sand would be required to restore the Isles Dernieres to a configuration indicative of the late 1800's. Their work indicates that with such a configuration, there will be an increase in wetlands of 30,000 acres, in addition to reductions in salinity, tidal current velocity and shoreline erosion. Several studies, funded largely by the U.S. Minerals Management Service, have indicated the potential use of Ship Shoal (Figure 1) as a source of clean quartz sand (approximately 1.2 billion cubic meters) for beach nourishment along Isles Dernieres (Mossa, 1988; Suter et al., 1989). Although dredging of the material appears both technically and economically feasible (Byrnes and Groat, 1991), a detailed evaluation of the potential impacts associated with such an undertaking has not yet been undertaken. The data presented here build on the findings of Mossa (1988), and Byrnes and Groat (1991) which pertained to the impact of dredging portions of Ship Shoal on wave refraction patterns, and qualitative assessments of the resultant wave energy distribution along the Isles Dernieres.
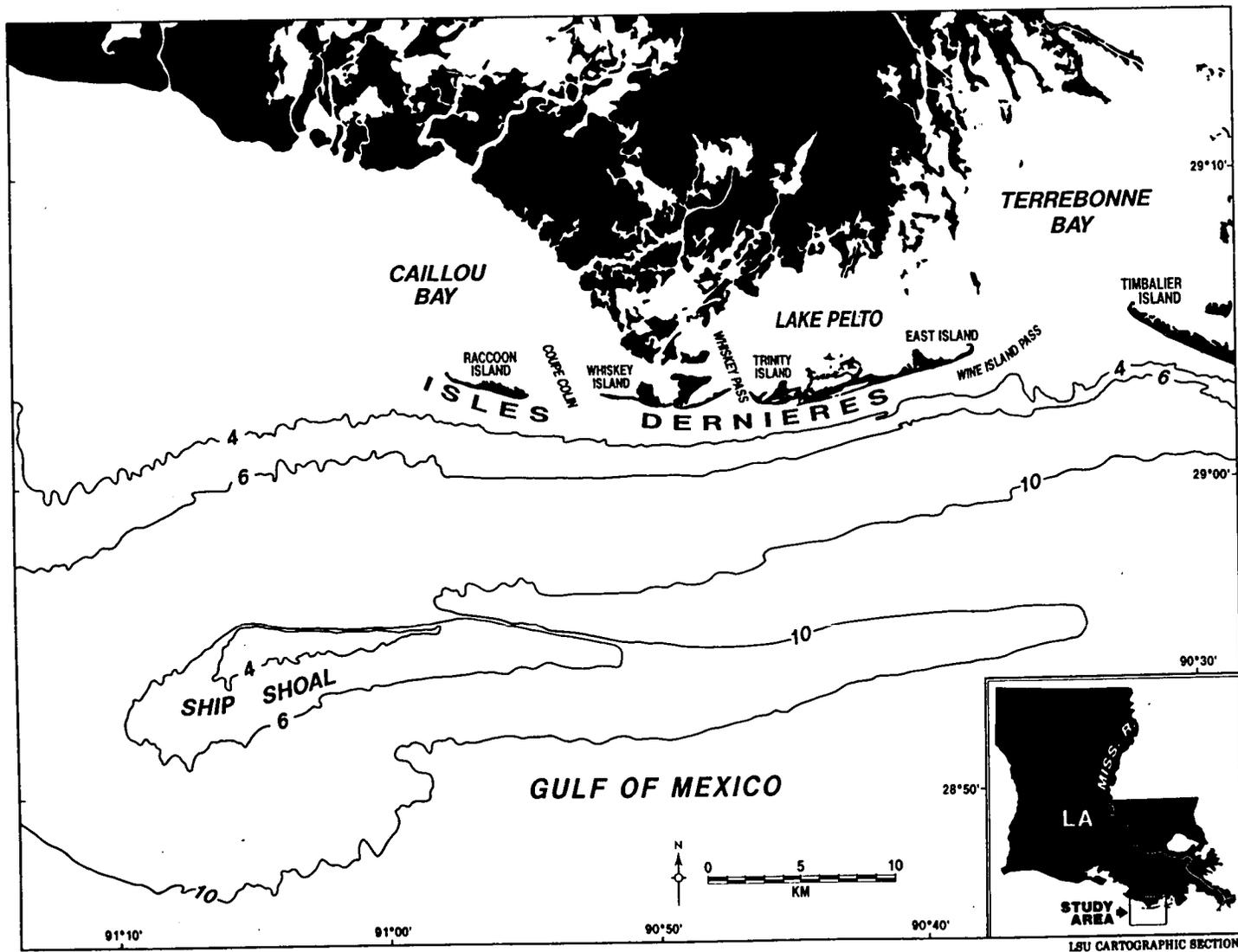
Figure 1   Map of the study area. Bathymetric contours in meters.

BEACH NOURISHMENT
AND RENOURISHMENT

ANTHROPROGENIC
INFLUENCES

OVERWASH/
OFFSHORE
TRANSPORT

RATE
OF
DETERIORATION

APERIODIC
ATMOSPHERIC
FORCINGS

BREACHING/
INLET
FORMATION

RELATIVE
SEA-LEVEL
RISE

REDUCTION IN
SEDIMENT SUPPLY
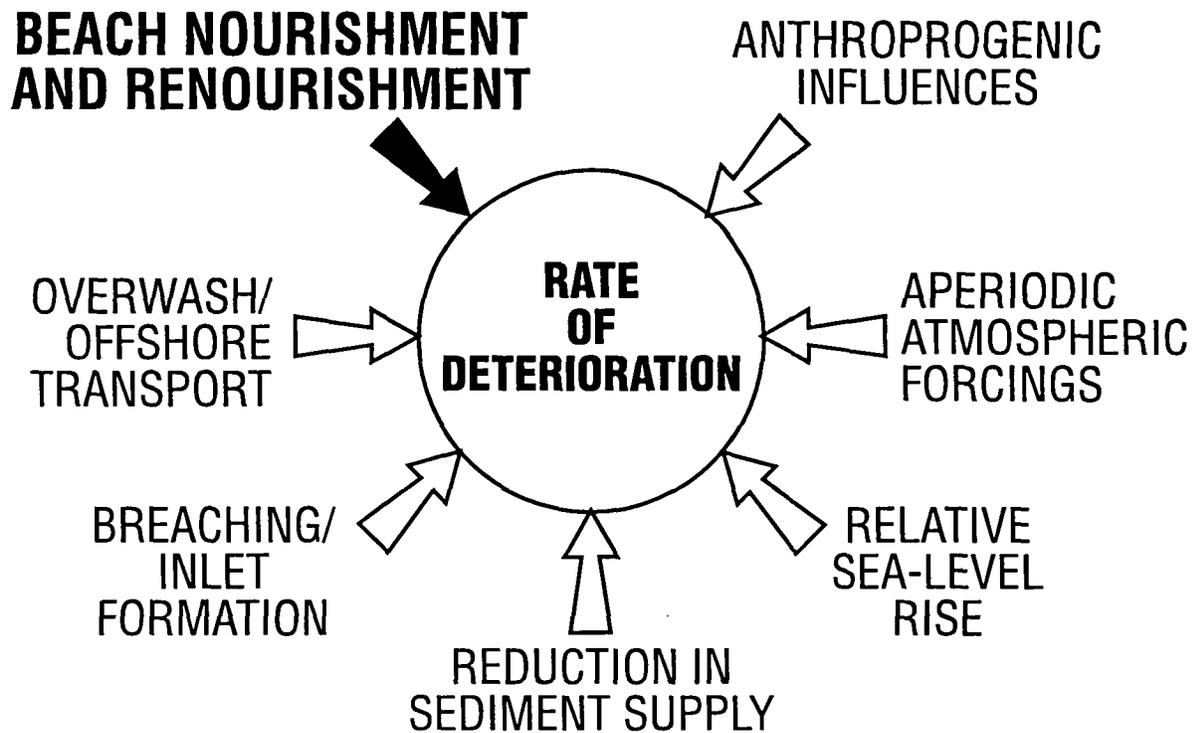
Figure 2   Primary factors responsible for barrier island deterioration in Louisiana.

The degree to which Ship Shoal mitigates the wave climate along the Isles Dernieres has not yet been established. Consequently the potential impacts associated with large-scale extraction of sediment from Ship Shoal should not be attempted prior to a <u>detailed</u> evaluation of the wave and current field in this area. Specifically, a combination of wave and current data obtained from *in situ* measurement and numerical modeling is necessary to understand more completely the effects of Ship Shoal on the wave and current field. The objective of this project is to numerically model the wave field and quantify the effects of shoal removal on wave conditions in the study area. Although total removal of the shoal is an unlikely scenario, this approach will permit an evaluation of the importance of Ship Shoal on the wave field during a variety of fairweather, storm and hurricane-generated wave scenarios.

Program Principal Investigators and Supporting Personnel

All aspects of this program (including this report) have been carried out by the principal investigators:
Dr. Gregory W. Stone (Louisiana State University)
Dr. Jingping Xu (Louisiana State University)

Mr. Xiongping Zhang was responsible for digitizing, some computer programming, and other technical support.

Report Organization

In this report we present background to the problem, methodological techniques and results in a structured and detailed form so that readers may have direct access to the relevant information. There are 6 chapters in total:

Chapter 1---project introduction and overview.

Chapter 2---regional setting and study site description.

Chapter 3---wave models.

Chapter 4---data acquisition.

Chapter 5---technical discussion.

Chapter 6---conclusions.

2 Regional Setting and Study Site Description

Introduction

This chapter provides a general description of the geological, climatological and oceanographic setting of the study area and background information pertaining to the wave climate in the study area. It also reviews and summarizes previous work and available data for the area.

Site Description and Regional Setting

The study site is located off the coast of Terrebonne Parish, south central Louisiana (Figure 1). The morphology of the study area is the product of a process combining relative sea-level rise with regressive (delta building) sequences, and transgressive (delta abandoning) sequences of the Mississippi River (Penland, 1990). Over the last 7000 years the Mississippi River has built six major delta lobes (Frazier, 1967). Except for the Modern delta and Atchafalaya delta complexes, all other abandoned deltas have responded to the Holocene transgression by undergoing erosion, subsidence, sediment redistribution, and landward migration. Isle Dernieres, Timbalier islands, and Ship Shoal are all products of these processes. Ship Shoal is a marine sand deposit located 15 km offshore of Isles Dernieres near the 10 m bathymetric contour and was formed by the erosion of a submerged barrier shoreline. The shoal is approximately 50 km long, comprised of well-sorted, clean quartz sand and is the easternmost member of a group of Holocene inner shelf shoals located southwest of the Mississippi River delta plain (Penland et al., 1986). Bathymetric comparisons covering a time span of over a century since 1853 indicate that Ship Shoal has migrated landward by approximately 1.5 km (Penland et al., 1986; List et al., 1994).

Penland et al. (1986) identified seven major sedimentary facies in the study area and its vicinity based on lithology, texture, sedimentary structures, faunal assemblages and stratigraphic position. Of the seven facies, the first three are the most significant with regards to characterization of the surficial sediment and the environments of deposition. The first facies, representing the crest of Ship Shoal, is located within the upper 5 m of the shoal and is characterized as a very well-sorted, well-rounded 99% quartz sand that coarsens upward within the unit from 0.13 mm at the base to about 0.16 mm at the top. The second facies, which represents the central body (or shoal front) of Ship Shoal, is a 1.2 to 3.4 m thick, moderately sorted and very fine to fine (0.12 to 0.15 mm), sand that underlies facies 1. Facies 3 is characterized by poorly sorted, very fine sand (0.1 to 0.13 mm), with interbedded layers of silty clay. It represents the lower extent, or shoal base, of Ship Shoal. The shoal crest contains 112 million m^3 of sand and resides within the zone of active normal and storm wave processes. Water depths over the shoal crest range from 2.7 m in the west to 7.0 m in the east. The shoal front and shoal base environments contain approximately 430 and 640 million m^3 of sand respectively. Because these two facies are in deeper water, they are subjected to a lower energy environment.

A block diagram illustrating shoal facies and depositional environment (Penland *et al.*, 1986) is shown in Figure 3.

Climatology

Coastal Louisiana has a climate classified as humid subtropical (Muller and Fielding, 1987) with a significant amount of well distributed rainfall (Faiers *et al.*, 1994). The governing controls on the climate are the subtropical location of Louisiana and proximity to the Gulf of Mexico resulting in long hot summers, and short, mild winters (Muller and Fielding, 1987). The airflow for the area is dominated by the semi-permanent, North Atlantic, high pressure cell. Airflow into the Louisiana coastal region, emanating from the tropical Gulf of Mexico, Caribbean and south Atlantic, follows the occurrence of this high pressure system during spring, summer and early autumn. The high moisture content of the dominant maritime air tends to reduce the temperature range from day to night by approximately 20°F, with highs and lows approximating 90 and 70° (Muller and Fielding, 1987). Average annual temperatures range between 67 and 70°F, although freezing temperatures have been experienced in the winter.

High pressure systems over the North American continent play an important role along the Louisiana coast. During the winter season, three distinct end-member type cold fronts impact the northern Gulf of Mexico: (1) the Arctic surge; (2) the Gulf cyclone; and (3) the mid-latitude cyclone. These extratropical weather systems produce local variations in wind direction, intensity and duration and thereby significantly affect wave and sediment transport processes along the Louisiana coast. Intense winter surface anticyclones are associated with outbreaks of Arctic and polar air which surge southward out of northern Canada to the Gulf of Mexico coast when a highly amplified PNA ridge-trough pattern occurs (Rohli and Rogers, 1993). This distinct polar jet stream configuration guides polar anticyclones into the Gulf region. There are two distinctive anticyclone paths: one track guides polar anticyclones into Texas while the other track guides polar anticyclones into Florida (Rogers and Rohli, 1991). In the south-eastern USA, relationships are strongest between circulation and the number of storms, probably caused by the ability of large-scale flow to steer frontal storms into an area (Henderson and Robinson, 1994). Locally, arctic surge type cold fronts produce short-lived pre-frontal southerly winds and strong post-frontal northerly winds which last for several days.

Gulf cyclones periodically develop in the northwest Gulf of Mexico and impact much of the northern Gulf including Louisiana. Cyclogenesis in this region has been studied by several investigators (Heckman and Thompson 1978; Atlas et al., 1983; Murty *et al.*, 1983; Lewis and Hsu 1992). Atlas *et al.* (1983) suggested that cold air outbreaks in the northwest Gulf can produce cyclonic vorticity in the lower levels of the atmosphere which can lead to the formation of a Gulf cyclone. Perturbations in the jet stream enhance development of extratropical storms and if only one mechanism is in place, cyclogenesis may be weak or may not even occur. The authors further contended that during El Nino years the southward displaced polar jet results in an abnormally large number of Gulf cyclones.

SHIP SHOAL DEPOSITIONAL MODEL
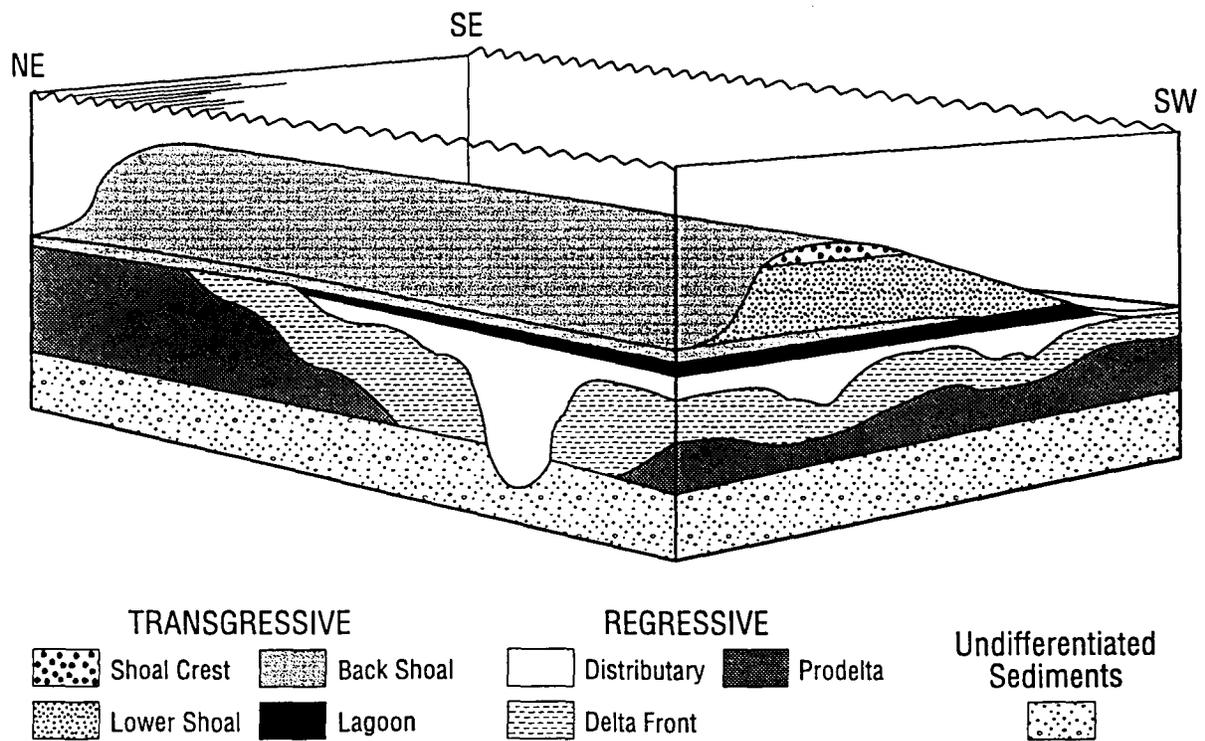
Figure 3   Sedimentary facies of Ship Shoal (modified from Penland *et al.*, 1986).

The migrating mid-latitude type cold front is the most common of the three and perhaps produces the most significant changes at the coast. Periodically a teleconnection between the eastern Pacific and North American continent exist producing stormier conditions in the Gulf of Mexico. This teleconnection can be linked to large-scale circulation changes associated with warming events in the eastern tropical Pacific. A vigorous low-latitude mean flow across the Gulf of Mexico and increased frontal activity result in stormier weather in this region as mid-latitude cyclones are steered to lower latitudes. Migrating mid-latitude cyclones can produce strong pre-frontal winds which raise water levels in Louisiana bays. With the passage of a front, strong post-frontal northerly winds increase wave energy conditions. Storm waves propagate landward on a super-elevated water surface thereby concentrating wave energy higher on the foreshore profile causing erosion.

Summer temperatures of 100^0 F or more are not uncommon in the northern portions of the state. This is particularly apparent during prolonged dry periods when a reduction in cloud cover allows significant increases in solar radiation reaching the earth's surface. Daytime highs have occasionally reach 110^0 F with an all-time high reaching 114 F in Bossier Parish. Along the coast, higher humidity and more consistent cloud-cover reduces insolation thereby moderating daytime temperatures in the 90's. The combination of high humidity and temperatures produces heat index values of 110^0 F on a regular basis. Such high values frequently occur in conjunction with reduced air quality.

Freezing temperatures are a relatively common component of winters in Louisiana, although occur seldom along the coast. In the northern parishes, several running days of freezing temperatures are not uncommon. A minimum temperature of -16 ^{0} F was recorded in Webster Parish. By contrast, along the coastal parishes, temperatures rarely fall below zero and when they do, the freeze does not exceed 48 hours. During cold front events, particularly "Arctic Outbreaks", strong northerly winds may reduce temperatures to 0 ^{0} F.

Although a number of large rainfall events have been associated with frontal passages, tropical storms and hurricanes induce, by far, the highest rates of precipitation, particularly in the coastal parishes (State Climatologist, personal communication, 1995). Unpublished data from the Southern Regional Climate Center at Louisiana State University show that single totals of approximately 1050 mm are common across the state annually. Historical reviews (Faiers et al., 1994) suggest that several sites have experienced one-day totals over 380 mm and the state's maximum of 559 mm recorded in Cameron Parish in 1962. Monthly accumulations of 760 mm have been recorded at several sites around the state. In the north this can be attributed to frontal activity and to tropical cyclone activity in the coastal parishes. Annual rainfall in excess of 203 cm has been reported on numerous occasion around the state with an all time record of near 2850 mm set in New Orleans in 1991 (State Climatologist, personal communication, 1995).

Cyclones

One of the most important causes of shoreline erosion on Louisiana's barrier islands is the frequent occurrence of hurricanes and major storms. Striking the Louisiana coast approximately once every three years (Neumann et al., 1992), hurricanes account for as much as 90% of shoreline retreat. Based on the analysis of historic maps and storm records, Kahn (1980) showed that the hurricanes accounted for 50-90% of total shoreline retreat in the Chandeleurs. Hurricane Camille (1969) and Frederic (1979) each caused between 40 and 80 m of shoreline erosion. Hurricane Audrey (1957) accounted for dune crest retreat of between 15 and 91 m along the Chenier Plain coastline (Morgan et al., 1957). Muller and Fielding (1987) noted that the peak frequency (13%) for hurricanes and tropical storms occurs in September. While the Atlantic Basin hurricane season officially extends from June 1 to November 30, a review of past tropical events indicates that Louisiana has experienced storms as early as late May, with the state's season essentially ending in October. No storm has made landfall in the state during the month of November in over one hundred years with only three systems extending west of 90^0 longitude in the Gulf of Mexico during that month. During the 20th century, approximately seventy tropical storms have made landfall in or near the state (Neumann, 1992), including more than two dozen hurricanes. The earliest recorded hurricane to impact the area was in 1711 when a three-day storm was reported in September in the general area of modern-day New Orleans (Dr. Donald Davis, Louisiana State University, personal communication, 1995).

Neumann et al. (1992) presented tropical cyclone tracks and statistical summaries for storm systems traversing the North Atlantic during the period 1871 through 1992. The report showed that Louisiana experienced among the fewest hurricane landfalls over a period of one hundred years when compared with the remainder of the northern Gulf from Texas to Florida. Grymes (1995) provides a map of Louisiana showing frequency of hurricane and tropical storm landfall between 1886 and 1993. The western half of the Isle Dernieres was the worst affected coastal segment which experienced five hurricanes and four tropical storms. Chandeleur Islands, because of their shoreline orientation, has the lowest incidence of storm landfalls. Of all hurricanes to impact Louisiana, only two have been classed as "major", i.e., category 4 or 5. These were Audrey (1957) and Camille (1969).

The most recent hurricane to have impacted the coast was Andrew in 1992. Stone et al. (1993) provide a comprehensive chronological overview of the climatological and hydrological aspects associated with Hurricane Andrew and its morphological impacts along the Louisiana coast. The initial storm surge effects in Louisiana's coastal marshes were experienced when the system was over 150 miles offshore. Storm surges were found to exceed 1.2 m in the marshes that coincided with the front right quadrant of the system. In addition, the vast majority of storm wave inundation and morphological change occurred east of the storm track along the barriers east of Point Au Fer Island to Grand Isle. A more detailed account of the climatology and meteorology of Hurricane Andrew has been provided by Grymes and Stone (1995). Stone and Finkl (1995) provide a collection of research papers dealing with the meteorology, sea state and biophysical impacts of Hurricane Andrew on the Florida and Louisiana coastal zones. Impacts

of Hurricane Andrew on tree mortality and nutrient flux as well as the structural impact on the forested wetlands of the Atchafalaya Basin have also been identified in this report.

In the Atchafalaya, Terrebonne, and Timbalier bay systems, evidence indicating two contrasting effects of the storm surge was presented by Halford (1995): first a period of rapid water level increase (or decrease depending on location relative to the storm tracks) within a short period of time (3 to 6 hours) during which most marsh destruction took place, and most of the coarse-grained sediments were deposited on the marsh surface; second, relaxation of the water surface occurred after the storm moved inland over an approximate 24 hour period, during which the fine-grained sediment was distributed across the marsh surface.

On synthesizing the data obtained from various authors on the impacts of Andrew on Louisiana, Stone and Finkl (1995) made some important conclusions that have direct significance to this study. Firstly, while the barrier systems underwent a phase of destruction during the hurricane, particularly those along the Isle Dernieres, some post-storm recovery was apparent during over flights three years later. Secondly, the pre-storm condition of the marshes pre-determined the severity of response to Andrew. Stable marshes showed evidence of vertical accretion after the storm in many areas, whereas unstable marshes underwent severe destruction. A model elucidating the linkage between atmospheric forcing and coastal morphosedimentary response has not yet been developed for regions of the Louisiana coast. In addition, while the historical record of shoreline change has been established a detailed evaluation of the role of hurricanes in long-term shoreline migration has not yet been established.

Waves, Tides and Sea-Level

The study area and its vicinity can be categorized as a low energy environment. In a 20 years (1956-1975) hindcast Wave Information Study (WIS) conducted by the U.S. Army Corps of Engineers (Hubertz and Brooks, 1989), statistics from the hindcast stations adjacent to the study area indicated an annual-mean significant wave height of 1.0 ± 0.2 meters and mean peak period of 4.5 - 6.0 seconds. The maximum hindcast wave heights at the same stations exceeded 5 m, and the wave peak period associated with the largest wave exceeded 11 seconds. The monthly mean significant wave heights in winter months (Dec. - Mar.) were 0.2 - 0.6 m higher than that of the rest of the year. The data also show that the predominant wave directions were from the southeastern quadrant.

Despite the dominant low wave energy environment in the study area, tropical storms and hurricanes influence sea state significantly. The 20-year hindcast of hurricane waves shows that the significant wave height for a 50-year return period is greater than 15 m. The 5-year return period significant wave height approximates 6-7 m. Fair weather wave conditions can be estimated using data from the Wave Information Study for the period 1956-1975 (Hubertz and Brooks, 1989). At hindcast stations 18 (28.5N, 91.5W), 19 (28.5N, 91.0W), 19 (28.5N, 90.5W), located

south of the Isle Dernieres and Timbalier Islands, the data show an average wave height of 1.0±0.2 meters and period of 4.5-6.0 seconds. The dominant wave directions are from the southeast quadrant (90°-180°), the percentages of occurrence of hindcast waves in this quadrant are 42% (station 18), 67% (station 19) and 68% (station 20). Additional discussion of these data is presented in Chapter 4 of this report.

Tidal patterns in the Gulf of Mexico differ markedly from other ocean basins in that tidal range extremes are determined by the astronomical declination of the moon rather than the cumulative gravitational effects of the moon and sun on the earth. When the moon reaches maximum declination, the diurnal (daily) tidal producing forces reach a maximum and the resulting Tropic tides achieve a relatively large range (typically 60 cm in the Louisiana area). Conversely, at minimum declination when the moon lies on the equatorial plane, tide producing forces are reduced resulting in lower Equatorial tides (typically less than 15 cm) having a semidiurnal or mixed pattern around the Louisiana coast. Over a lunar month, two periods of Tropic and Equatorial tides are evident around the Louisiana coast, although this may be significantly influenced by local conditions including freshwater discharge to the coast. The dominantly diurnal tidal pattern in the Gulf may be attributed to the system having a period of oscillation which closely approaches the diurnal harmonic of 24 hours (Marmer, 1954). This hypothesis has been questioned because of independent findings showing significantly smaller resonant periods in the Gulf, and the necessary inclusion of a non-existent amphidromic point in the middle of the Gulf to satisfy Marmer's argument (Royer and Reid, 1966; Zetler and Hansen, 1970).

3   Wave Models

Introduction

Several numerical models exist with the general capabilities of wave height prediction from deep water to the break point. These models define the wave field as monochromatic or single period waves, one-dimensional spectral waves, two-dimensional spectral waves or shallow water waves. As presented earlier, the objectives of wave modeling in this project are two-fold: (1) large-scale (or global scale) modeling that provides the wave characteristics across the south-central Louisiana shelf, including the study area; and (2) local wave modeling that outputs higher resolution information (e.g. wave breaking) to evaluate the potential impacts of shoal removal on nearshore wave conditions. Several of the more commonly used models are presented below and evaluated for the use in this study. Additional model reviews may be found in Holthuijusen *et al.*, 1989; O'Reilly and Guza, 1991, 1993).

RCPWAVE

RCPWAVE is a short-wave numerical model used to predict linear, plane wave propagation over an open coast region of arbitrary bathymetry (Cialone *et al.*, 1992). The model solves finite difference approximations of an elliptical equation (Berkhoff, 1972, 1976) in a significantly simplified form to estimate the complete linear wave transformation process with the restriction of a mild bottom slope. This is accomplished using the following three equations

$$\frac{1}{a}\left(\frac{\partial^2 a}{\partial x^2} + \frac{\partial^2 a}{\partial y^2} + \frac{1}{CC_g}(\nabla a \cdot \nabla(CC_g)) \right) + k^2 - |\nabla s|^2 = 0 \tag{1}$$

$$\frac{\partial}{\partial x}(|\nabla s|\sin\theta) + \frac{\partial}{\partial y}(|\nabla s|\sin\theta) = 0 \tag{2}$$

$$\frac{\partial}{\partial x}(a^2 CC_g|\nabla s|\cos\theta) + \frac{\partial}{\partial y}(a^2 CC_g|\nabla s|\sin\theta) = 0 \tag{3}$$

In the above equations,

x,y	=two orthogonal horizontal coordinate directions
a(x,y)	=wave amplitude function
C(x,y)	=wave celerity
C_g(x,y)	=group velocity
k(x,y)	=wave number
s(x,y)	=wave phase function
θ	=local wave direction

RCPWAVE uses linear wave theory because it has been shown to yield fairly accurate first-order solutions to wave propagation problems and at a relatively low cost. Refractive and bottom-induced diffractive effects are included in the model; however, the model can not treat diffraction caused by structures extending above the water surface. Application of this model does not include nonlinear effects nor a spectral representation of irregular waves.

REF/DIF 1

This combined refraction-diffraction wave model (Kirby and Dalrymple, 1993) is a weakly nonlinear numerical model that is based on a parabolic equation governing the complex amplitude A of the fundamental frequency component of a Stokes wave. The governing parabolic equation is given by:

$$2ikCC_gA_x + 2k(k\,k_0)CC_gA + i(kCC_g)_xA + (CC_gA_y)_y - k(CC_g)K'|A|^2A = 0 \tag{4}$$

where (x,y) are horizontal coordinates, k_0 is a reference wavenumber related to the initial conditions of the incident wave, C is phase speed, C_g is group velocity, and

$$K' = k^3\left(\frac{C}{C_g}\right)\frac{\cosh 4kh + 8 - 2\tanh^2 kh}{8\sinh^4 kh} \tag{5}$$

This model applies a nonlinear approach to compute wave propagation, dissipation and breaking. It includes both refraction and diffraction effects explicitly, thus permitting the modeling of waves in regions where the bathymetry is irregular and where diffraction is important. Unlike the wave tracing technique, it computes wave heights and directions on a model grid rather than on irregularly spaced rays. Therefore, regions where wave rays cross due to local focussing or where caustics are caused by other means are treated correctly, and no infinite wave heights are predicted (Kirby and Dalrymple, 1993). REF/DIF 1 assumes a mild bottom slope (<1:3) and weak

nonlinearity. In dealing with nonlinearity, REF/DIF 1 applies a hybrid model which provides a smooth patch between the Stokes dispersion relationship, valid in deep water, and Hedges'(1976) dispersion relationship that is used in shallow water where the Stokes relationship becomes invalid when the Ursell parameter exceeds 40. It is capable of simulating the energy dissipation in the following forms: (1) Laminar surface and bottom boundary layer; (2) Turbulent bottom boundary layer; (3) Porous sand; and (4) Wave breaking.

Although REF/DIF 1 can compute numerous frequencies per computer run, it can only calculate waves at a single frequency per calculation because the wave-wave interactions between different frequencies are not included. Therefore, REF/DIF 1 is an efficient model to be used for monochromatic waves.

REF/DIF S

REF/DIF S (Kirby and Ozkan, 1994) is a weakly nonlinear combined refraction and diffraction model that simulates the behavior of a random sea over an irregular bottom bathymetry, incorporating the effects of shoaling, refraction, energy dissipation and diffraction. It includes most features present in the model REF/DIF 1 so it can also be used to model the behavior of monochromatic waves.

REF/DIF S is used with two-dimensional wave spectra. The input frequency spectrum in conjunction with a directional spreading function are divided into discrete wave components characterized by a certain frequency and direction. REF/DIF S stacks parabolic models for the individual wave components, propagating them simultaneously through the domain. After each step, the complex amplitudes for all wave components are known and the significant wave height $H_{1/3}$ can then be computed in the following manner

$$H_{1/3}(x,y) = \sqrt{8 \sum_{n=1}^{N} |A(x,y)_n|^2} \tag{6}$$

where N is the total number of wave components and $A(x,y)_n$ is the amplitude of the wave component n. The authors of REF/DIF S are continuing to develop the spectral capabilities of the model. A new version that will include the wave generation (wind forcing) was being developed at the time of writing.

STWAVE

STWAVE is a finite-difference model for near-coast time-independent spectral wave energy

propagation simulations (Cialone *et al.*, 1992). It is based on a simplified spectral balance equation

$$\frac{\partial}{\partial x}\left(CC_gE(f,\theta)\right) + \frac{\partial}{\partial y}\left(CC_gE(f,\theta)\right) + \sum_{i=1}^{N}S_i = 0 \tag{7}$$

where
$E(f,\theta)$ = spectral energy density
f = frequency of spectral component
θ = propagation direction of spectral component
S_i = source terms (shoaling, refraction, wind forcing, wave-wave nonlinear interactions, bottom interaction, etc.)

STWAVE simulation requires a wave energy spectrum specified for the input boundary of the computational grid. It transforms the spectrum across the grid, including refraction and shoaling effects. The spectrum is modified to include the effects of bottom diffraction and the convergence/divergence of energy influenced by the local bathymetry. Wind-wave generation, nonlinear energy transfer, wave field and wave-bottom dissipation and wave breaking are considered. The model is computationally efficient because of its assumption that only wave energy directed into the computational grid is significant, i.e., wave energy not directed into the grid is neglected. STWAVE has been successfully used in several projects (Kraus *et al.*, 1994; Dr. Don Resio, personal communication).

Comparison of the Models and Selection

The models described previously are compared against the following criteria: representation (scale), efficiency, accuracy, spectral capability, computational grid size requirement, breaking criteria, and wind-wave generating. The performance of each model against the criteria is shown in the matrix overleaf.

It is apparent from the matrix that STWAVE has the highest composite score because of its spectral capability, inclusion of a wind-forcing function, high accuracy, and high efficiency. Thus, considering the objectives of the study, STWAVE was selected for use in this study.

	RCPWAVE	STWAVE	REF/DIF 1	REF/DIF S
Representation	**Global**	**Global**	**Local**	**Local**
Efficiency	**High**	**High**	**High**	**Moderate**
Accuracy	**N/A**	**Documented Yes[1]**	**Documented Yes[2]**	**Documented Yes[2]**
Spectral Capability	**No**	**Yes**	**No**	**Yes**
Grid Size Requirement	**Restricted by $\Delta x/\Delta y$, not Δx or Δy**	**$\Delta x < 0.5$ L Recommended[3]**	**$\Delta x < 0.2$ L Required[4]**	**$\Delta x < 0.2$ L Required[4]**
Breaking Criteria	**Weggel(1972)**	**Resio(1987)**	**Dally *et al.* (1985)**	**Thornton and Guza(1983)**
Wind-Wave Generating	**No**	**Yes**	**No**	**Yes[5]**

1 - Kraus *et al.*, 1994
2 - Vincent and Briggs, 1989; Berkhoff *et al.*, 1982
3 - Dr. Resio, personal communication, 1995
4 - Kirby and Ozkan, 1994
5 - In a new version being worked on at the time of writing

Wave Transformation During Hurricane Andrew

Deep water wave boundary conditions obtained from a calibrated hindcast model were used to simulate the rate of energy dissipation of long waves across the Louisiana continental shelf during Hurricane Andrew. The simulation represented deep water wave conditions off the Louisiana coast when Hurricane Andrew reintensified prior to landfall, and transformation of these waves during shoreward propagation and breaking along the coast using a standard depth-limiting instability ratio (McCowan criterion).

A wave-energy dissipation model (*WAVENRG*) was used in this study to simulate wave propagation and decay across the Louisiana shelf during Hurricane Andrew. The model, written by May (1973) and modified by Stone (1991), applies linear wave theory to simulate the first order wave field across a bottom slope by computing wave refraction, shoaling and bottom friction. The model was adopted for use in this study because it readily provided output by which near bottom maximum orbital velocities could be calculated in addition to two dimensional changes in wave-energy dissipation and attenuation. By assuming that there is no significant energy loss due to internal friction, friction at the free surface, adverse currents, or percolation

into the bottom (May, 1973), the wave height at a specific location (i.e. water depth) can be described given a known deep water wave height, by

$$H_i = K_r K_s H_0 \tag{8}$$

In (8), K_r is the refraction factor, K_s is the shoaling factor and H_0 is the wave height.

In addition to K_r and K_s, the bottom friction also causes decay of the wave height. The time rate of energy dissipation due to bottom friction is

$$\frac{dE}{dt} = c_f \rho\, u^3 \tag{9}$$

where c_f (=0.03, see May, 1973) is a dimensionless friction coefficient, ρ is water density and u is the near-bottom horizontal wave orbital velocity whose linear expression is

$$u = \frac{\pi H}{T \sinh(kD)} \cos(kx - \omega t) \tag{10}$$

where T is wave period, ω is the radian frequency, and x denotes the direction of wave travel direction. Since u in (10) is periodic, the mean rate can be computed by

$$\overline{\frac{dH}{dt}} = \frac{1}{T} \int_0^T \left(\frac{4 c_f u^3}{gH} \right) dt \tag{11}$$

The change of wave height in space (along a ray) will be:

$$\overline{\frac{dH}{dx}} = \frac{2 T c_f \omega^3 H^2}{3 L \pi g \sinh^3(kD)} \tag{12}$$

Therefore, the wave height loss due to bottom friction is:

$$\delta H = -0.67 \int_{x_0}^{x_i} \left(\frac{T c_f \omega^3 H^2}{L \pi g \sinh^3(kD)} \right) dx \tag{13}$$

Combining (8) and (13) gives the estimated wave height, i.e.

$$H_i = K_r K_s H_0 + \delta H \tag{14}$$

4 Data Acquisition

Introduction

Computational bathymetric grids and deep water wave conditions (directional amplitude and period weighted by frequency of occurrence) are necessary inputs for numerical modeling of surface wave behavior across the study site. Three different types of bathymetric grid were generated for application in this study. The grids differed in resolution, and underwent embedding of "local" (high resolution) in "global" (coarser resolution) grids. A quantitative inventory and assessment of the wave climate in the vicinity of the study area is presented in addition to quantification of wave parameters at the offshore boundary of the computational grids.

Bathymetric Grid Development

Multiple bathymetric data sources were acquired to establish the computational grids. These data sources included National Ocean Service (NOS) bathymetric charts and U.S. Geologic Survey (USGS) field surveys conducted in 1984 and 1986 (List *et al.*, 1994). Two types of NOS charts (Scale 1:80,000, Mean Lower Low Water North American Datum of 1983; and Scale 1:458,596, Gulf Coast Low Water Datum of 1927) were digitized to produce respective grids. The USGS survey data were then embedded in the lower resolution digitized data set to reflect the most recent bathymetry. Modular GIS Environment (MGE) software was used to digitize, manipulate, analyze, and display data on creating the bathymetric grid file. The software includes MGE Nucleus, MGE Coordinate System Operations, MGE Projection Management, MGE Grid Generation, and MGE Terrain Analyst2. All work was carried out on the Microstation environment which is a CAD product from Bently Systems Incorporated. Hardware support was Intergraph's Clix and TD workstation systems. Two three-dimensional seed files with two different projections for the study site were generated using the MGE Coordinate System. One seed file was a UTM (Universal Transverse Mercator) projection with the North American Datum in zone 15. The second seed file was a Mercator projection with the North American 1983 datum.

There are two main methods that can be used to convert a base map to a design file. One is to create a design file from scanned base-map features and the other is to digitize base-map features. In this project, the digitizing method was selected, because water depths were more easily digitized directly from the map than scanned and converted to text in the design file. A blank design file called **lafourch.dgn**, based on the Mercator projection seed file was created. The central Meridians and parallels were set. The map was affixed to the digitizing table and a design file setup based on at least four selected control points on the map. When the error was less than a given value (0.02%), the setup was accepted and digitizing to a graphic design file commenced. On completion of the digitizing procedure, the MGE Terrain Analyst module was used to manipulate the file.

The MGE Terrain Analyst is a specialized software package developed by Intergraph Corporation for the analysis, manipulation, modification, and graphical display of computerized terrain-modeling data. Graphic design files are used for loading features (elements), placing terrain displays, and performing analysis. The 3-D design file features, which include coastline position and water depth, were loaded into a TIN (Triangular Irregular Network) model using Import Design File Features. The TIN model was created from the terrain features using Convert Feature. A TIN model consists of a set of triangular facets formed from the coordinates of point, linear, and area features. Because each feature coordinate defines a triangle vertex, it maintains triangular-neighborhood and feature-type relationships and all input data points are preserved. This method provides an efficient, yet precise, method of representing the terrain surface. The model is stored in a file with .TIN extension. Because the regular ASCII grid file requires the Grid model, the TIN model is converted to the grid model.

A grid model is defined as a regular matrix of elevation/depth values referenced to a common datum. Data in the grid model were formatted in a binary data storage format that conformed to Intergraph corporation's standard grid format. The Grid model was converted from the TIN model using the function TIN to GRID and the appropriate grid spacing defined.

A lower resolution grid was developed for purposes of simulating wave propagation and energy dissipation during Hurricane Andrew. The bathymetric grid (Figure 4) used in this phase was generated from digitizing NOS Chart 1116A (Scale 1:458,596) which covers the area from 26.85 °N to 29.82 N and from 89.22 W to 93.52 W. Grid dimensions of 180 x 240 were established with a square grid size of 2.293 km.

The core component of this project necessitated a substantially higher resolution grid representing bathymetric configurations in intermediate and shallow water. The grid developed has dimensions of 432 x 910 with a square grid size of 100 m. The data were digitized from NOS Charts 11356 and 11357 (Scale 1:80,000; North American Datum of 1983) covering the area from 28° 35'N to 29 20'N and 90 11'W to 91 30'W (Figure 5). The digitized database was updated by embedding the data from a USGS field survey conducted in 1984 and 1986 (List *et al.*, 1994) (Figure 6). The vertical datum for the soundings is Mean Lower Low Water (MLLW), determined from the Grand Isle tide gauge from 1960 to 1978. A high resolution gridding interval was established for more detailed work on the shoreface with spacing on the Y axis (onshore-offshore) of 22.5 m and 135 m in the X (alongshore) direction.

Deep Water Database for Winter Storms and Fairweather

The deep water wave inputs representing winter storms and fairweather conditions were obtained from three sources (Table 1): (1) 20 years (1956-1975) of hindcast data obtained from the Wave Information Study (WIS) (Abel *et al.*, 1989; Hubertz and Brooks, 1989); (2) National Oceanic and Atmospheric Administration (NOAA)'s National Data Buoy Center (NDBC) buoy 42017 (25.9°N, 89.7°W); and (3) Louisiana-Texas Shelf Physical Oceanography Progra (LATEX)
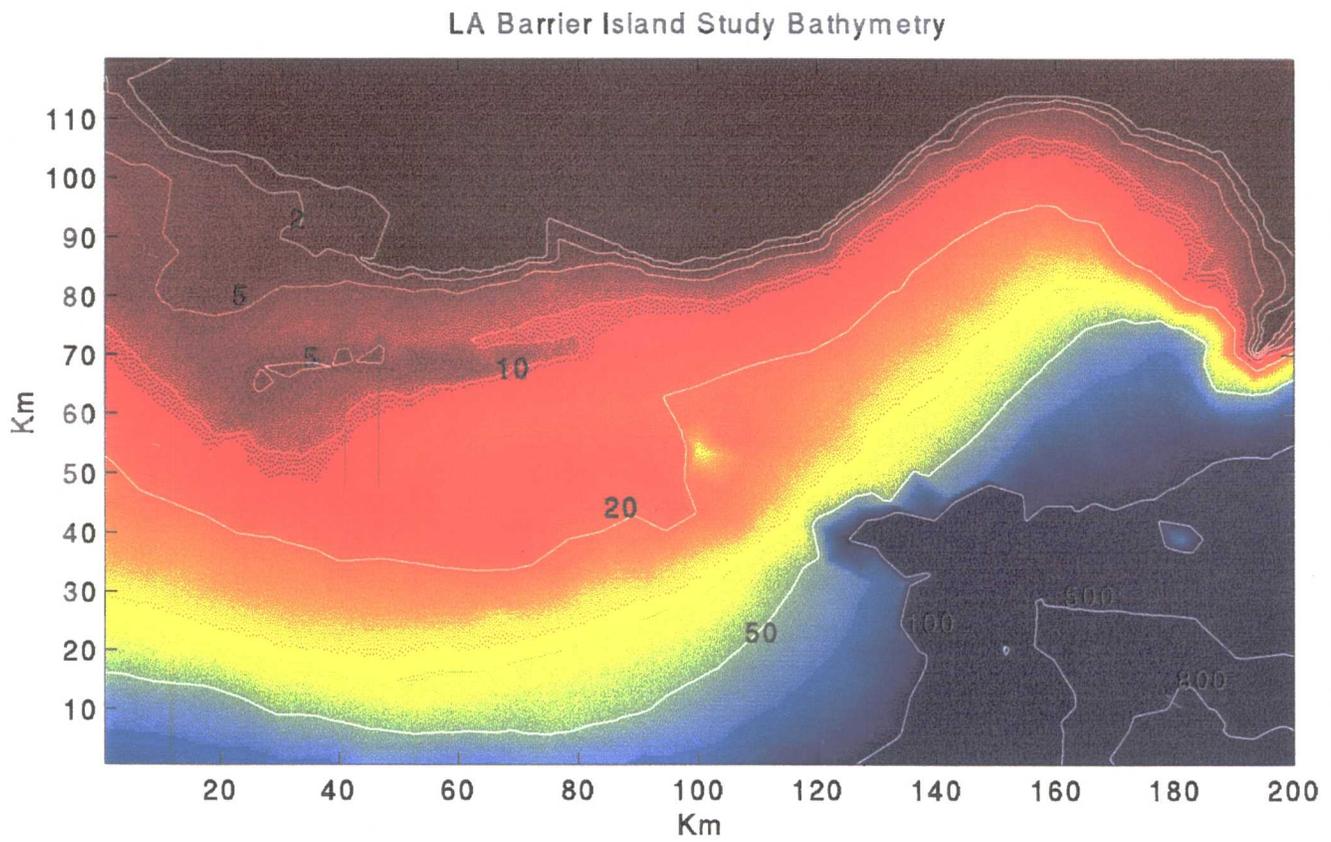
Figure 4   Low resolution bathymetric grid used in Hurricane Andrew simulations.
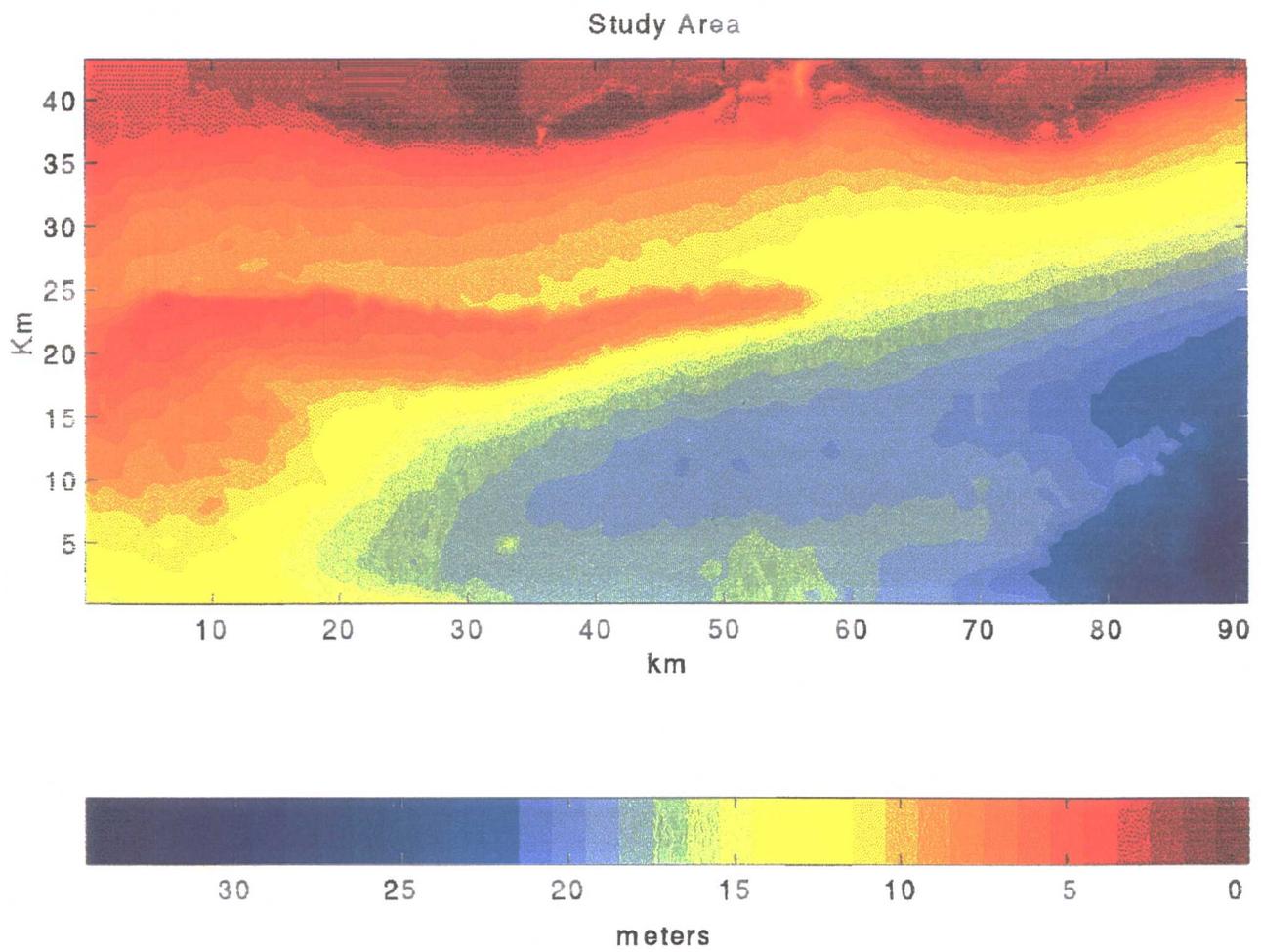
Figure 5   High resolution bathymetric grid across the inner shelf incorporating Ship Shoal.
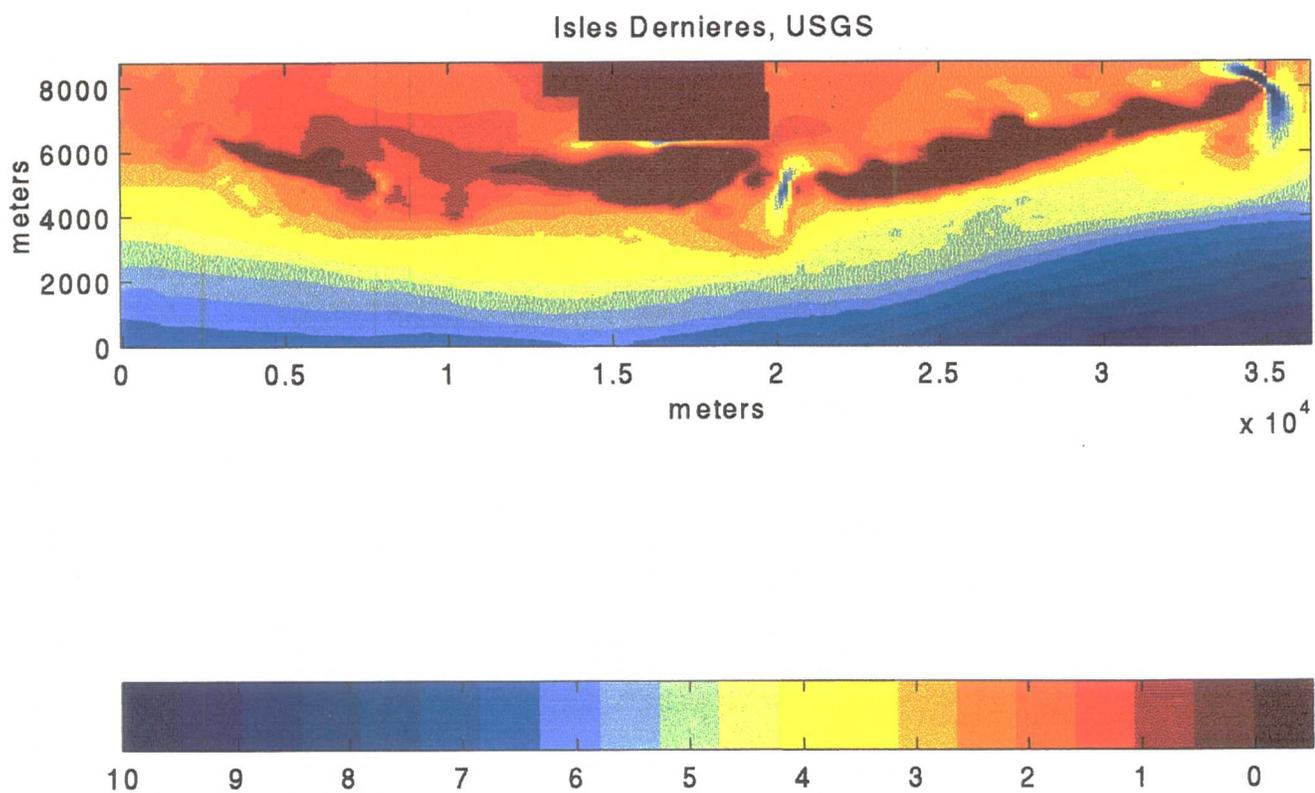
Figure 6   High resolution bathymetry of Ship Shoal and its vicinity, surveyed by USGS in 1986.

station 16 (28.9°N, 90.5°W) (unpublished data supplied by Dr. Steven F. DiMarco, Texas A&M University).

Table 1. Sources of wave climate data

Sources	Lat. (N)	Long. (W)	Water Depth (m)
WIS 19	28.5°	91.0°	33
WIS 20	28.5°	90.5°	38
WIS 21	28.5°	90.0°	91
NDBC 42017	27.5°	90.5°	407
LATEX 16	28.9°	90.5°	21

Among the three sources, the WIS data set provides the most complete information. Statistics from three hindcast stations 19, 20, and 21 (Figure 7 for locations) had shown an annual-mean significant wave height of 1.0±0.2 meters and mean peak period of 4.5 - 6.0 seconds. The maximum wave heights from these stations exceeded 5 m, and the wave peak period associated with the largest wave exceeded 11 seconds. The monthly mean significant wave heights in winter months (Dec. - Mar.) were 0.2 - 0.6 m higher than that of the rest of the year. The predominant wave directions were from the Southeastern quadrant (135.0°, 112.5°, and 90.0° for Stations 19, 20 and 21 respectively). The average directions associated with the largest waves were also mostly from this quadrant (125°, 117°, and 112° for the three stations). If the percentages of occurrence of wave directions being in the range of 90° - 180° are summed, the percentages for the four stations are 76%, 85%, and 85% respectively.

Among the buoys that NDBC has administered within the Gulf of Mexico, 42017 (27.5°N, 90.5°W) is more significant for the purpose of the current project because of its close location to the study area (Figure 8). However, only 6 months (Apr. - Sep. 1989) of data are available from NDBC 42017. Although limited, the time series shows that the monthly mean significant wave heights ranged from 0.6 to 1.4 m (Figure 9) and peak periods from 4.5 to 5.3 seconds (Figure 10). A storm at the end of July, 1989 generated the maximum significant wave height of 5.1 meters for the 6-month period. The peak period corresponding to the largest wave was almost 8 seconds. The 12-month (Aug. 1991 - Jul. 1992) time series from buoy 42001 (25.9°N, 89.7°W) showed that the monthly mean significant wave heights ranged from 0.6 to 1.8 m and monthly mean peak periods from 4.3 to 5.5 seconds (Figures 11 and 12). The monthly mean significant wave heights, which also show a decreasing trend from winter to summer months, compared reasonably well with the WIS hindcast data. No wave directions were recorded during both periods.
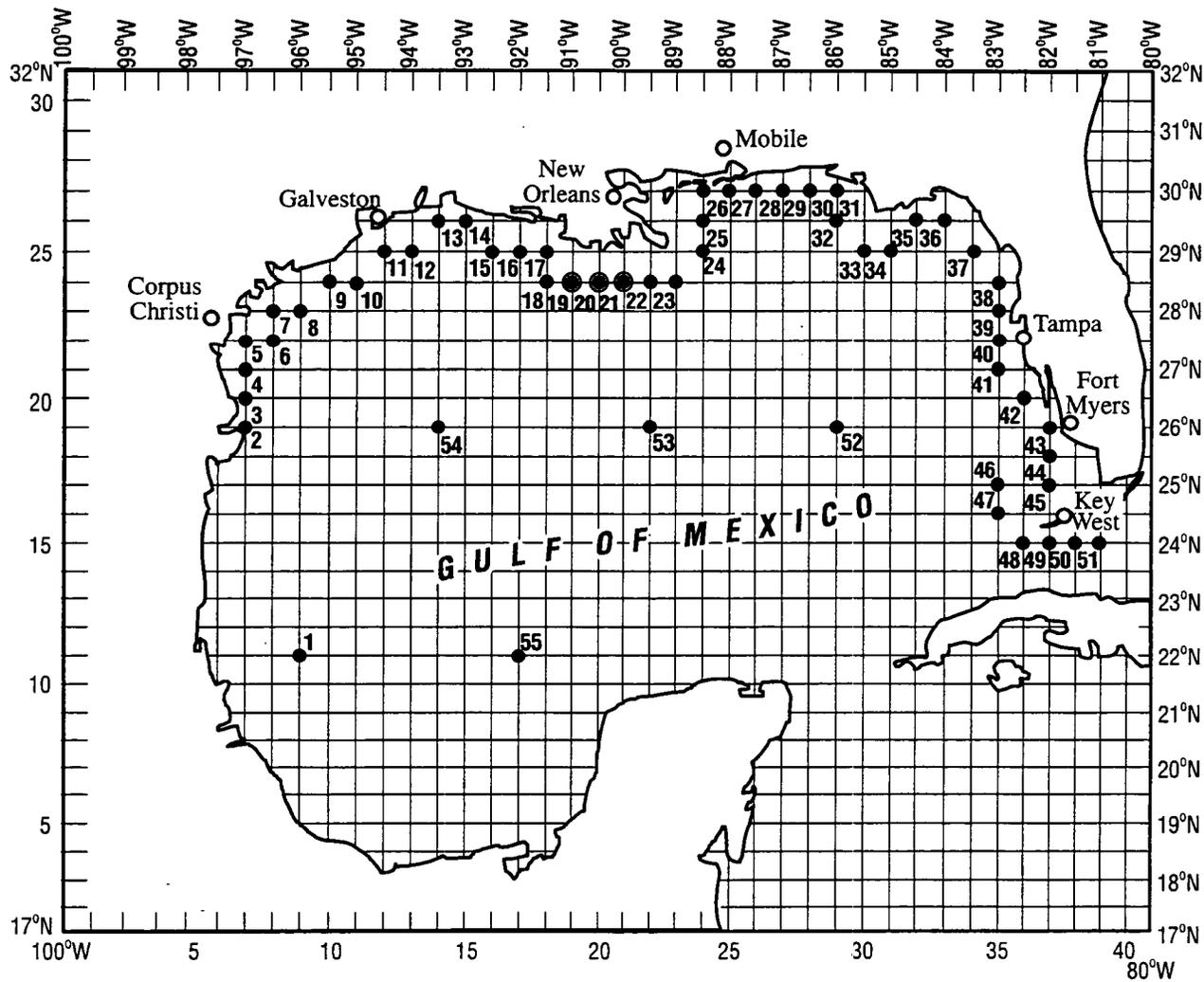
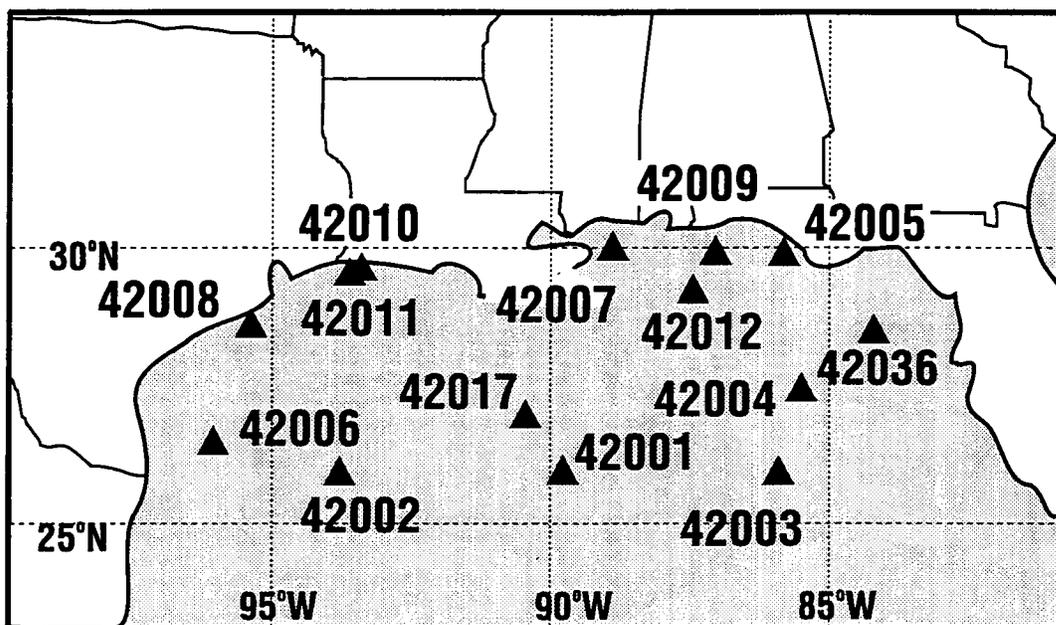Figure 7   Map of Wave Information Study stations in the Gulf of Mexico.

Figure 8   Map of National Data Buoy Center stations in Gulf of Mexico.
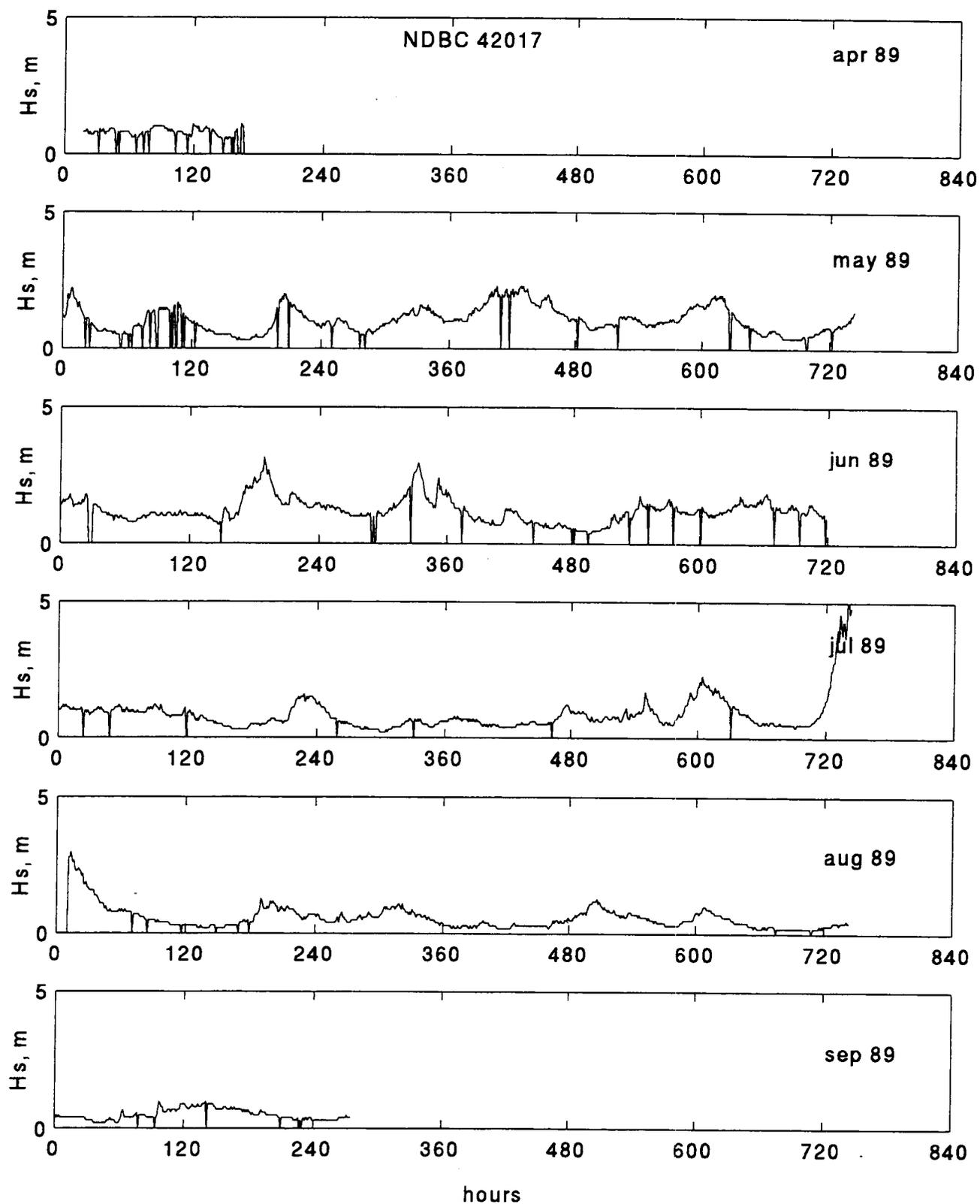
Figure 9   Time series of Hs from NDBC 42017, April - September 1989.
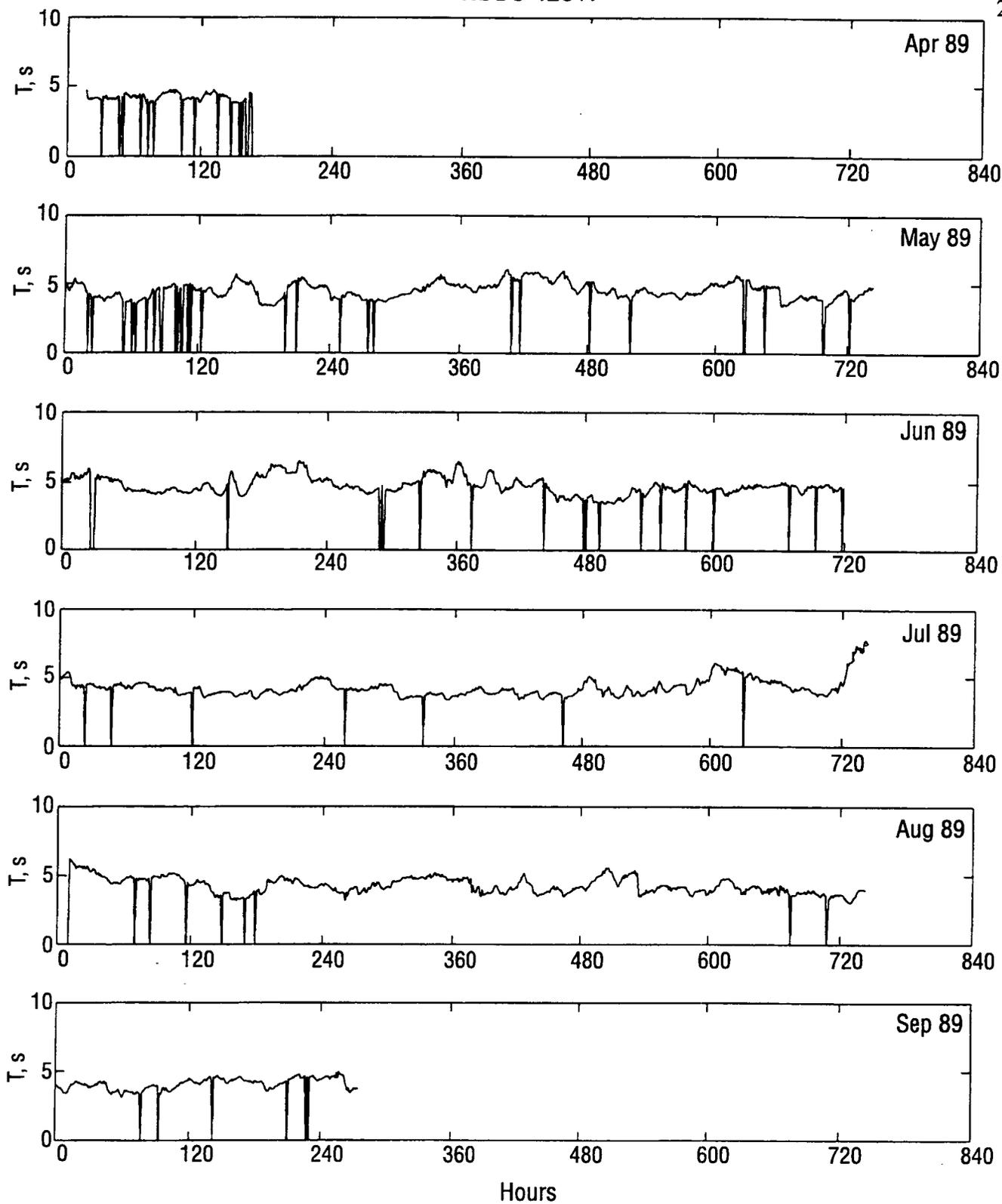
NDBC 42017

Figure 10 Time series of Tp from NDBC 42017, April - September 1989.
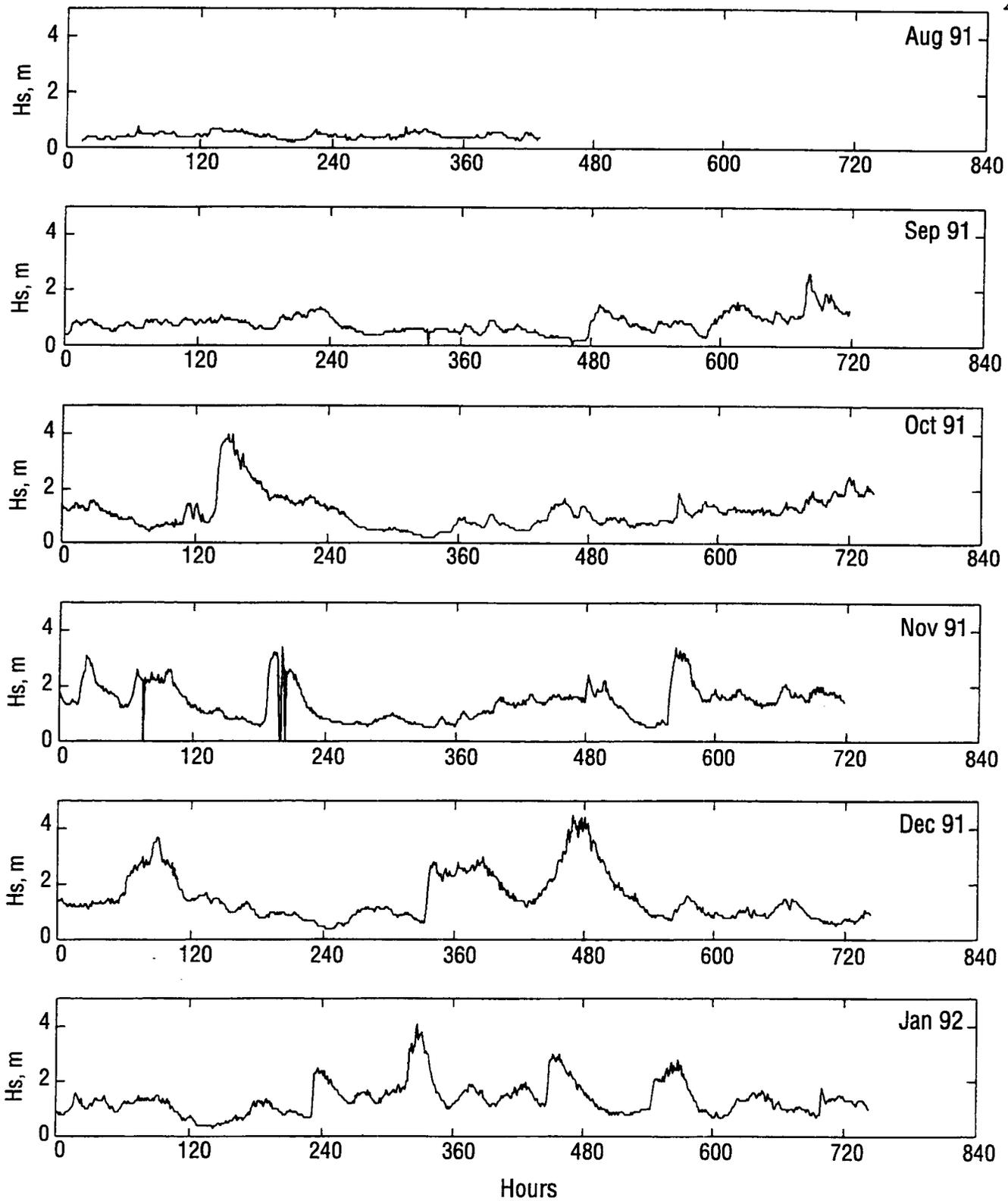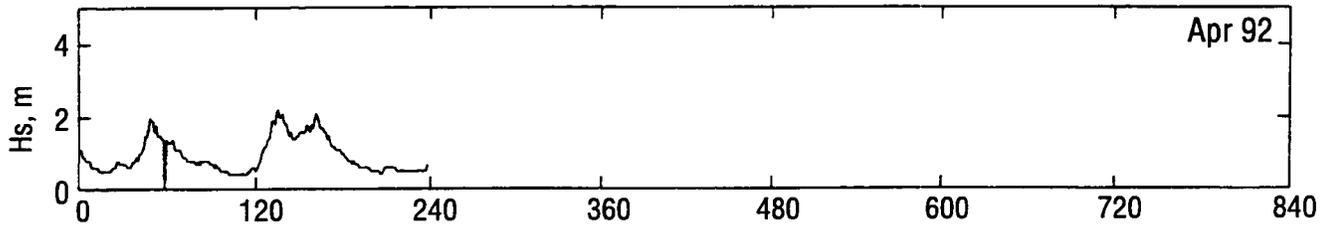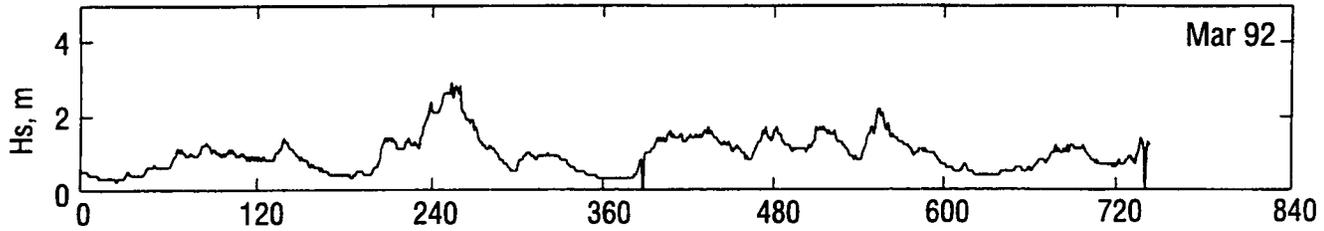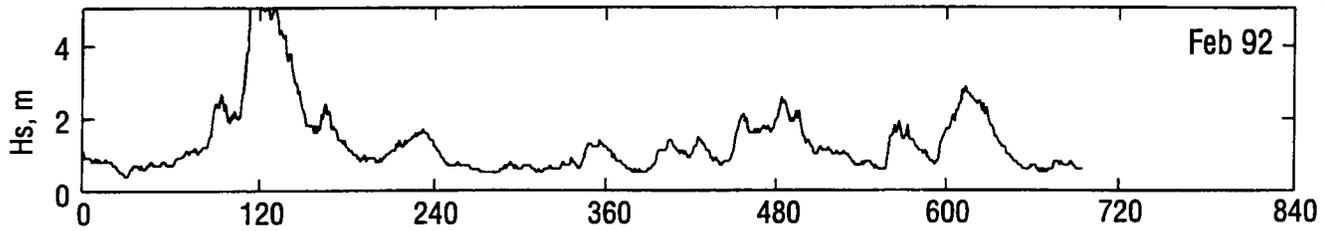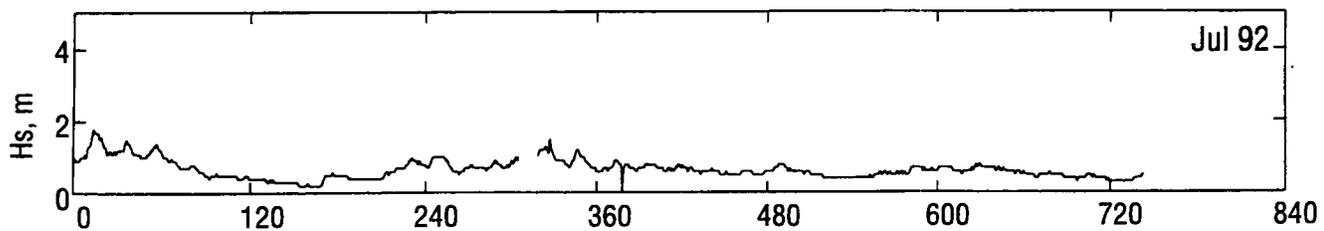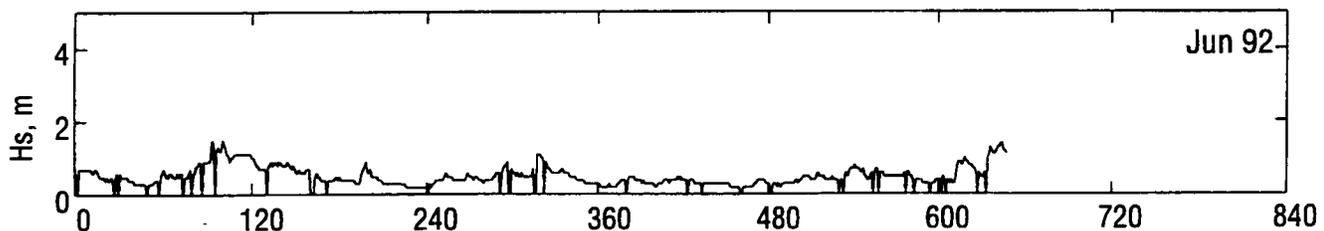
NDBC 42001

Figure 11a Time series of Hs from NDBC 42001 August 1991 - January 1992.

NDBC 42001

No data for May 92

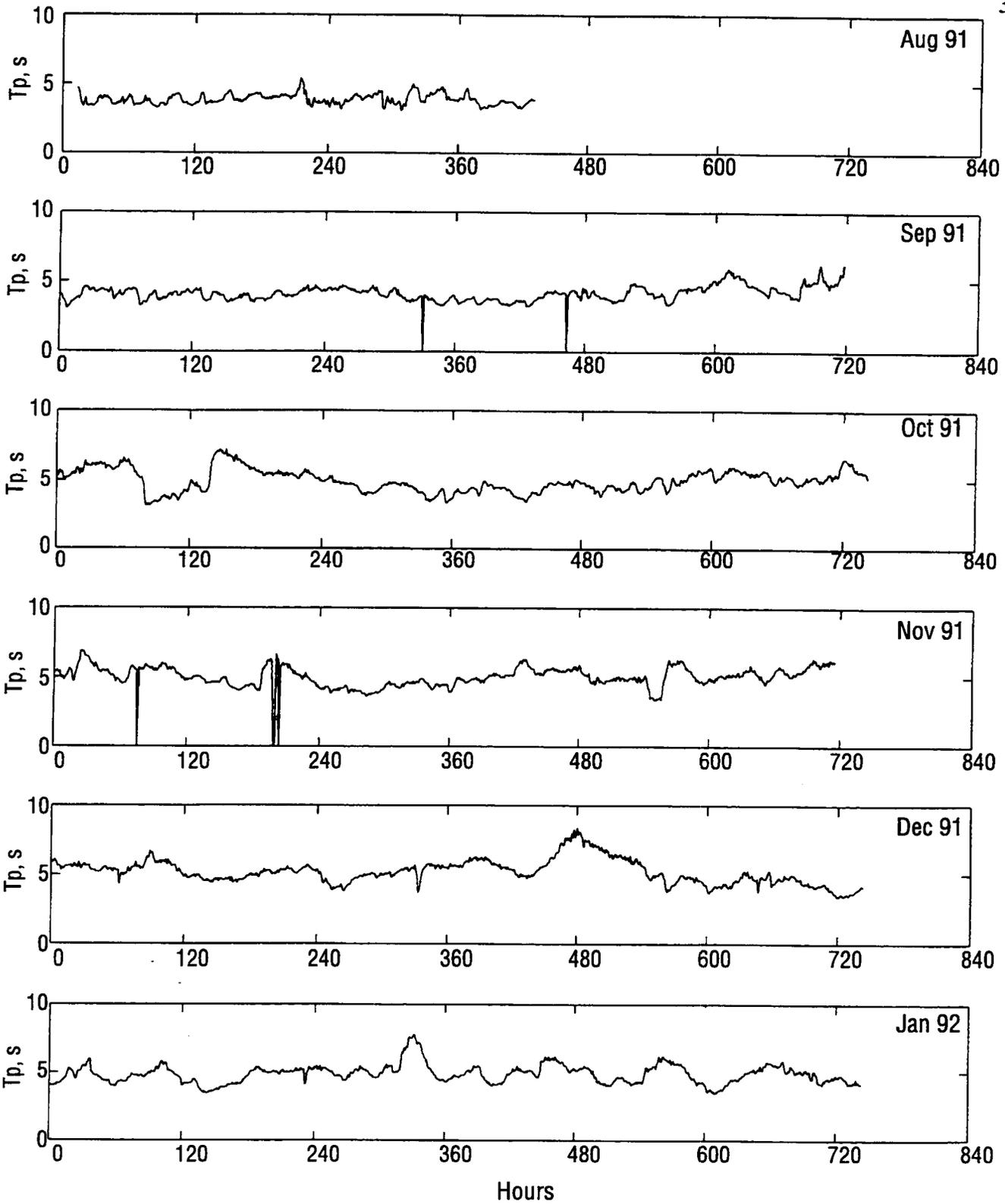Figure 11b Time series of Hs from NDBC 42001 February 1992 - July 1992.

NDBC 42001

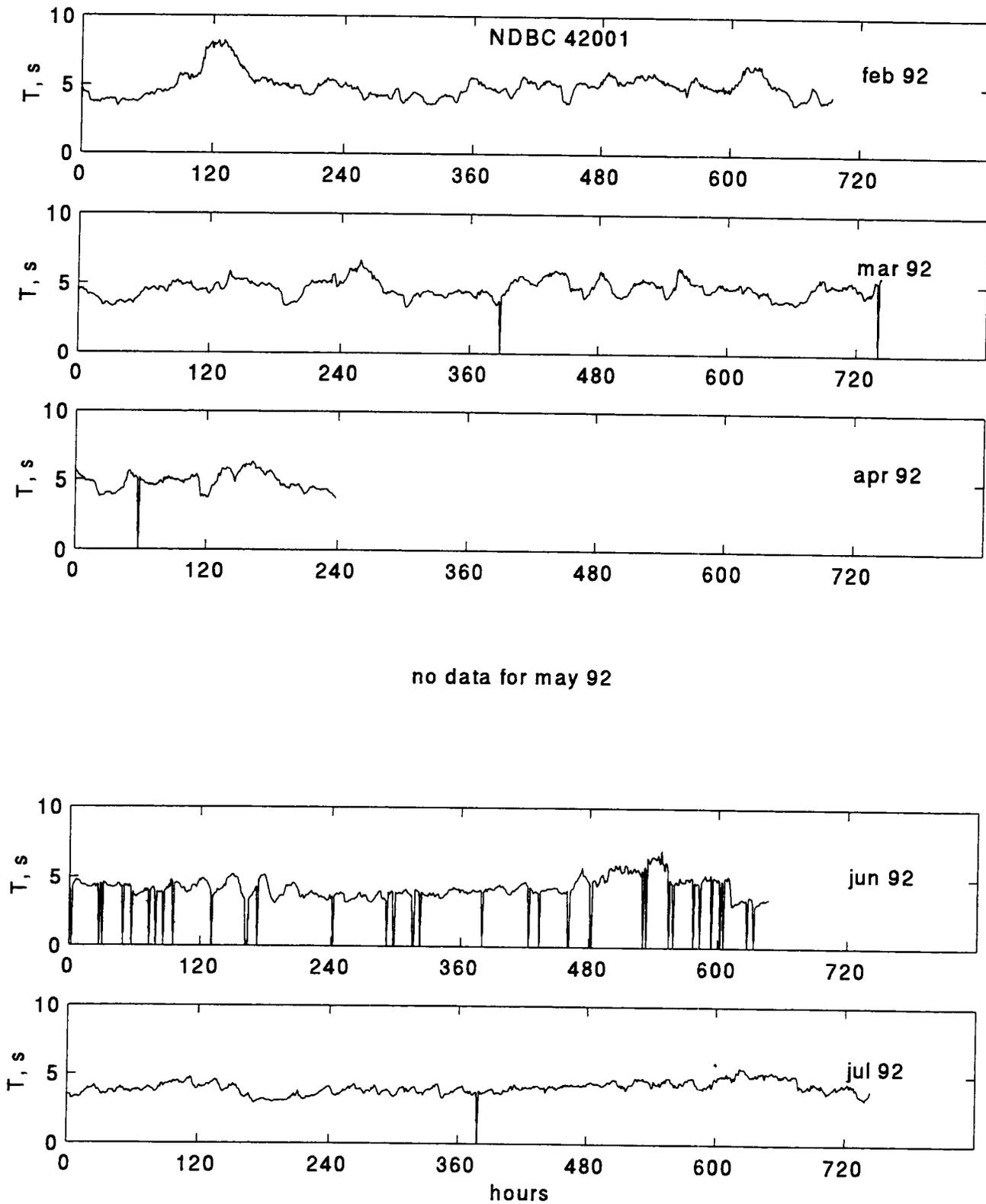Figure 12a Time series of Tp from NDBC 42001 August 1991 - January 1992.

Figure 12b Time series of Tp from NDBC 42001 February 1992 - July 1992.

LATEX station 16 (28.9°N, 90.5°W) is located within the general study area. The wave data recorded by MiniSpec (Coastal Leasing, Inc.) directional wave gauges during a 6-month period (Dec. 1993 and Feb. - Jun. 1994) show that the monthly-mean wave heights varied from 0.3 to 1.3 m and period from 5.5 to 6 seconds (Figures 13 and 14). The dominant wave directions agree with the previous data sets showing the importance of southeasterly approaching waves (Figure 15). On synthesizing these data, four scenarios are presented which represent the respective deep water wave conditions for fairweather through severe storms--excluding hurricanes (Table 2).

Table 2. Incident wave parameters used for deep water wave boundary conditions

Case	H_s(m)	T_p(s)	APPROACH DIR. θ(deg.)[1]	DESCRIPTION
1	6	11	-45,00, +45	Severe Storm
2	4	9	-45,00, +45	Strong Storm
3	2	6	-45,00, +45	Weak Storm
4	1	5	-45,00, +45	Fairweather

[1] -45 = SOUTHWEST APPROACH
   45 = SOUTHEAST APPROACH
   00 = SOUTH APPROACH

Deep Water Database for Hurricane Andrew

Measured deep water wave conditions do not exist for Hurricane Andrew with the exception of NDBC data obtained from two buoys located in the left quadrants of the cyclone (see Stone *et al*, 1993, 1995; Grymes and Stone, 1995). Maximum significant wave heights approached 6 m at one of the buoys located closest to the storm center, however, this is an underestimation of wave conditions in the front right quadrant. Several approaches have been used to estimate the significant wave height during hurricanes (Long, 1979; Abel *et al*, 1989; Hsu, 1991; 1994). The Hsu (1991) method relates maximum significant wave height in deep water to sea-level pressure (P_0) at the storm center by,

$$H_s = 0.2(1013 - P_0) \tag{15}$$

The equation appears reliable on comparison with measured wave heights during Hurricanes Gloria and Kate (Hsu, 1991) and when compared with data sets obtained by Abel *et al* (1989) (see

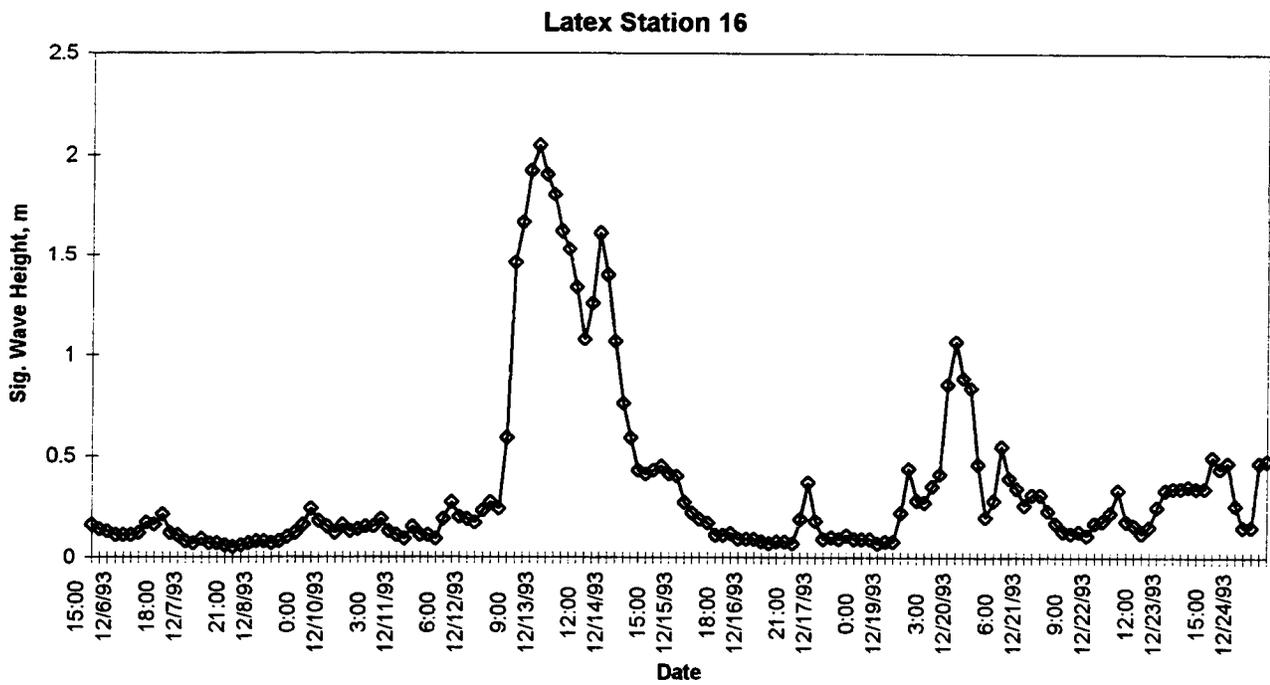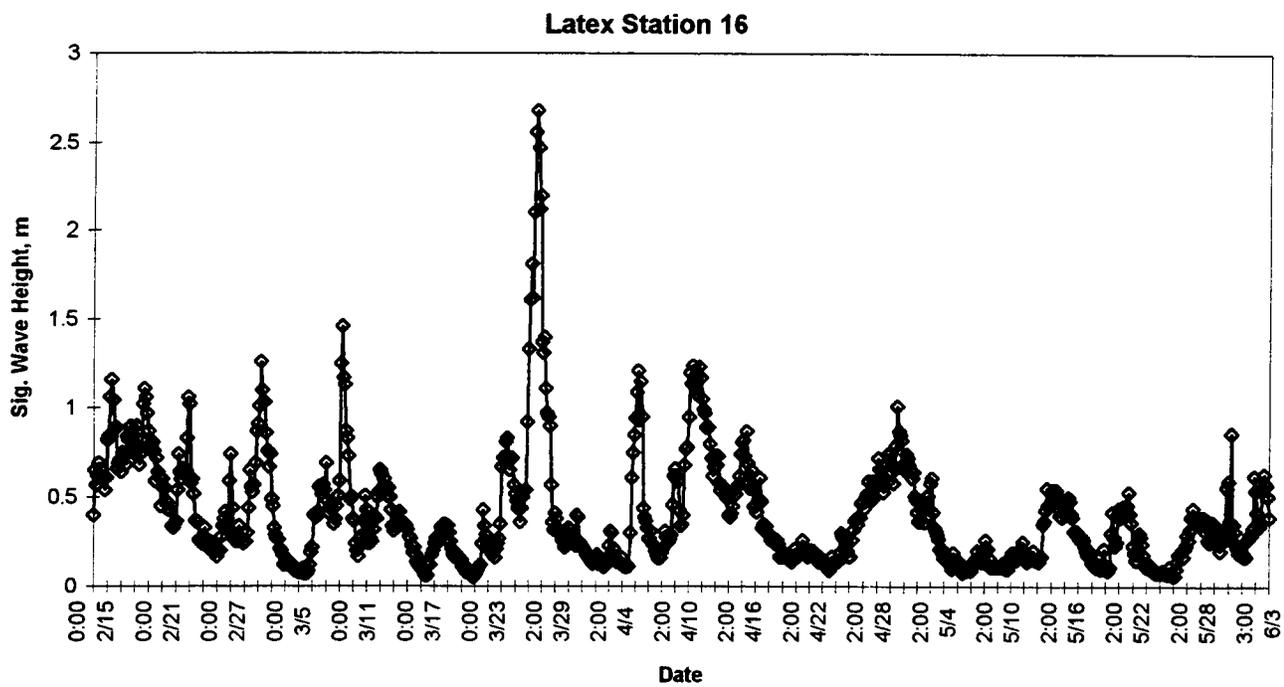Figure 13a Time series of Hs from Latex 16, 6 - 24 December 1993.

Latex Station 16

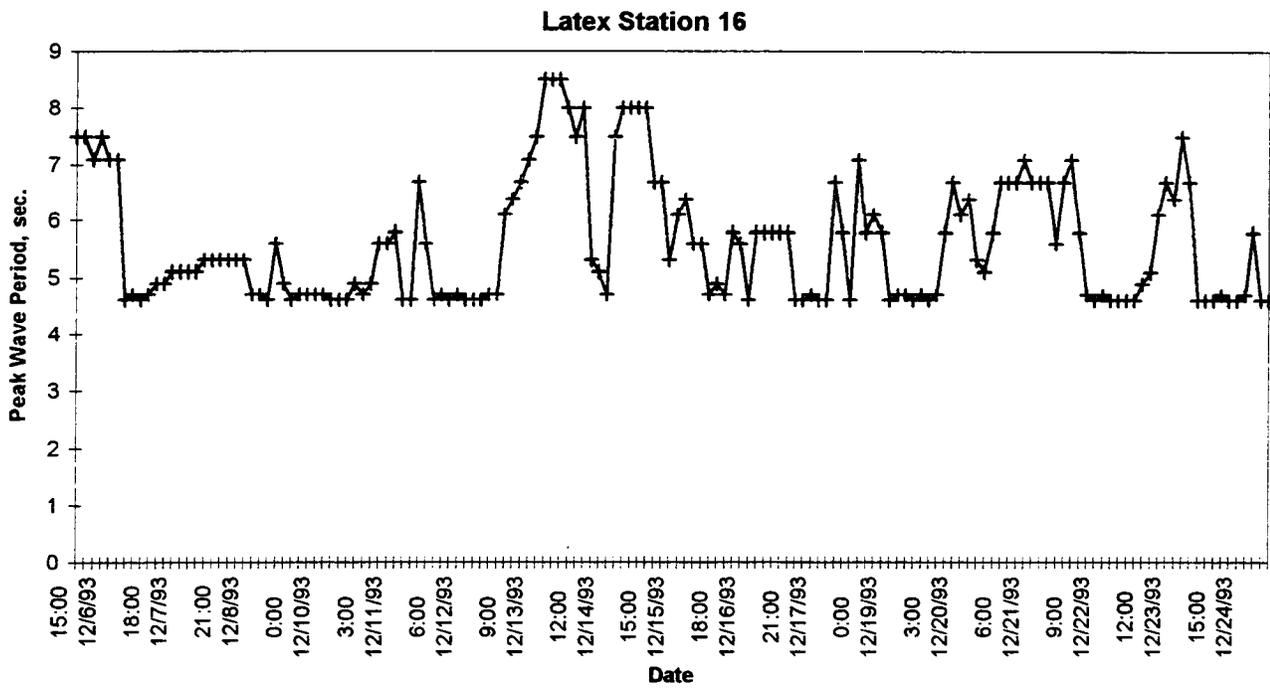Figure 13b Time series of Hs from Latex 16, 15 February - 3 June 1994.

Figure 14a Time series of Tp from Latex 16, 6 - 24 December 1993.

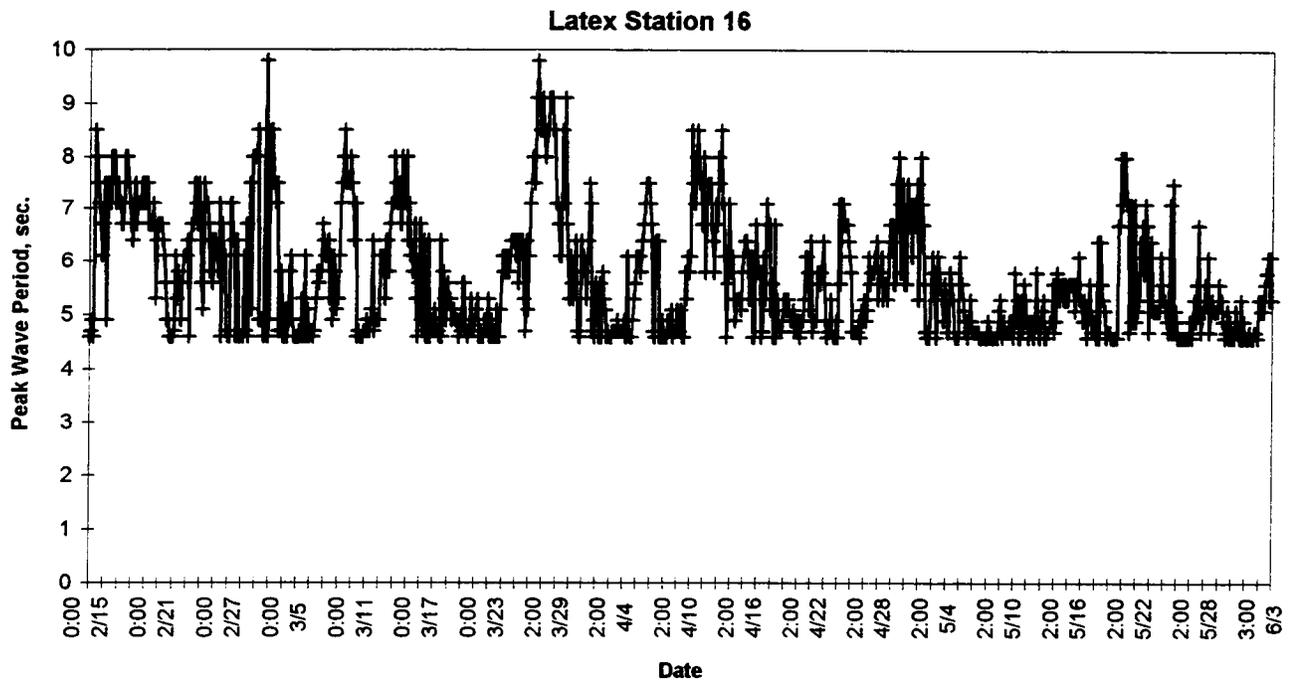Figure 14b Time series of Tp from Latex 16, 15 February - 3 June 1994.

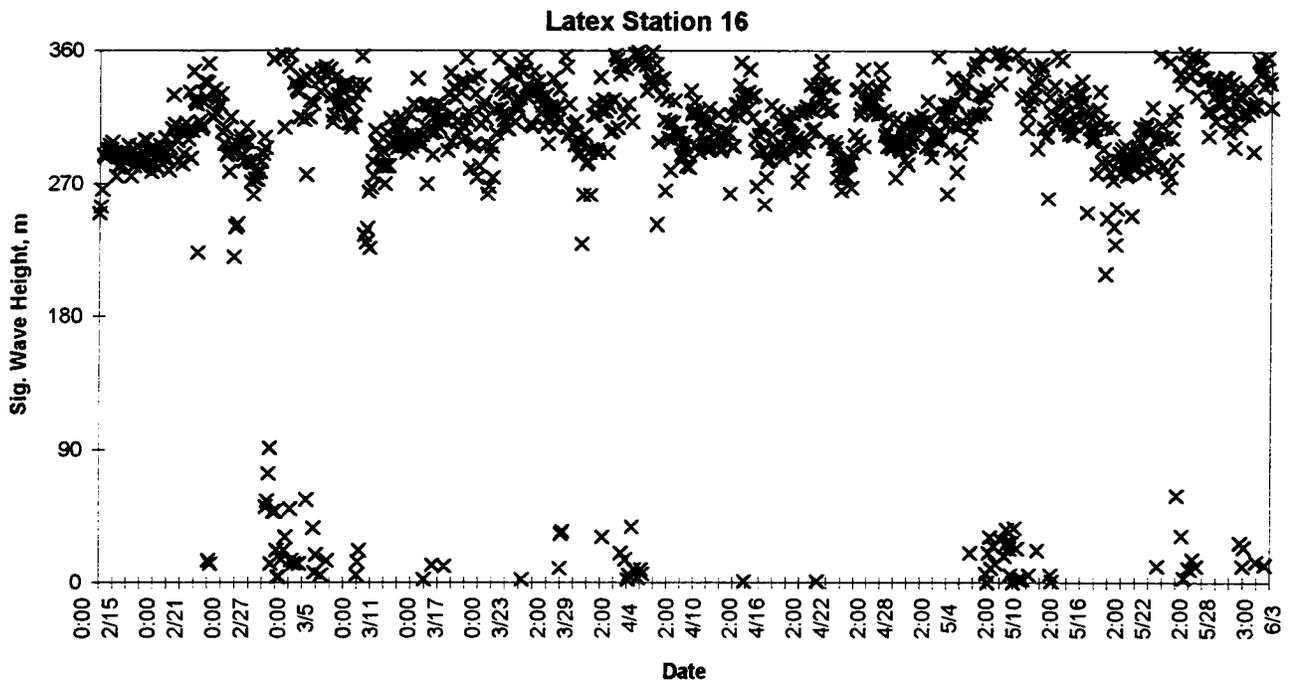Figure 15a Time series of Direction from Latex 16, 6 - 24 December 1993.

Figure 15b   Time series of Direction from Latex 16,   15 February - 3 June 1994.

Hsu, 1994). Applying equation (15) off the Louisiana coast implies that H_s in deep water, approximated 14 m. This is in agreement with observations of inferred wave heights made on several platforms off the Louisiana coast (Bothelo *et al*, 1994) and hindcast data obtained by Cardone and Cox (1992). In the latter, a wave hindcast model was used to generate a two-dimensional wave spectrum at hourly intervals for the Gulf. The hindcast data show significant wave heights increasing from 8 m off the Florida coast, to 13.3 m south of the Mississippi River delta where the cyclone strengthened before landfall (Stone *et al*, 1993, 1995; Grymes and Stone, 1995). The hincast data show good agreement when compared with the NDBC buoy time series, although a small phase lag does exist (Cardone and Cox, 1992).

To simulate peak intensity wave conditions off the Louisiana coast, the hindcast data generated by Cardone and Cox (1992) were used as input to the *WAVENRG* model providing the opportunity to incorporate decreases in wave height outward from the storm center, as a function of a decaying wind field. The input data are presented in Table 3, and consist of seven sectors in which the significant deep water wave height ranges from 11 to 13.3 m, and the significant wave period approximates 14 secs. Water depths in which wave propagation began varied from 300 m to 1200 m, a location 30 km to 230 km south of Main Pass. A deep water wave approach angle of 135 degrees was selected to simulate the storm track of Hurricane Andrew as it moved across the Louisiana continental shelf (Stone *et al*, 1993). A hindcast storm surge of 0.5 m was used for deep water conditions as calculated by Cardone and Cox (1992).

Table 3. Input to *Wavenrg* obtained from the hindcasts of Cardone and Cox (1992).

Section	Rays	Latitude (°N)	Sig. Wave Height (m)	Wave Period (s)
1	2 - 14	26.91 - 27.18	11.0	14
2	15 - 21	27.18 - 27.33	12.0	14
3	22 - 35	27.33 - 27.62	13.0	14
4	36 - 52	27.62 - 27.97	13.3	14
5	53 - 66	27.97 - 28.26	13.0	14
6	67 - 73	28.26 - 28.40	12.0	14
7	74 - 83	28.40 - 28.50	11.0	14

Longitude = 89.25 °W

5   Technical Discussion

Introduction

To quantify numerically, the impacts of Ship Shoal on wave climate, the approach taken centered on removal of the entire shoal complex from the bathymetric grid. By comparing the wave fields obtained from running the wave model over these two grids, the significance of Ship Shoal in affecting the wave climates under different conditions was examined. Figures 16 and 17 show the three-dimensional images of the two bathymetric configurations. As much as 6 m thick of sand was removed at the west portion of the shoal, and the total volume of sand extracted from Ship Shoal was 1.1×10^9 m^3. It is important to note that this approach was necessary to determine the role Ship Shoal plays in mitigating the wave climate. Total removal of Ship Shoal is highly unlikely in the foreseeable future given recent estimates of the volume of sand required to restore the Isles Dernieres, i.e., 11.6×10^6 m^3 (van Heerden *et al*, 1993). Considering this statistic, Ship Shoal could provide enough source material for approximately 95 nourishment/renourishments.

Wave Transformation Analysis

Configuration of Model Input and Bathymetric Grid

As discussed previously, three deep water wave approaches are considered for this project: 0^0 (approach direction from the south)^0, 45 (southeast), añd -45 (southwest) with the corresponding deep water wave statistics (Table 2). Given a set of input significant wave heights H_s, peak wave periods T_p, and wave directions θ, STWAVE generates a JONSWAP spectrum, an input wave energy matrix of 15 frequencies and 35 directions.

Case 1 (H_s=6 m, T_p=11 sec.)

Case 1 represents a severe storm in the Gulf of Mexico. Three wave directions are simulated (southeast, south and southwest) although directional spectra indicate that the main approach during storms of this nature in the study area is from the southeast. Figures 18 through 20 represent the image contour plots of the significant wave height generated by STWAVE for the three directions. A sequence of figures is presented for each wave approach where "a" represents the wave height distribution with the Ship Shoal in place, "b" represents shoal removal, and "c" the percentage difference in significant wave heights attributable to the effects of the shoal on wave climate. Interpretation of these figures leads to the following conclusions:

(1). Significant wave height increases from west to east across Ship Shoal as a function of a commensurate increase in water depth.

(2). The removal of Ship Shoal results in a significant increase in wave height during this storm simulation, although restricted to the leeward flank of the western segment of the shoal.
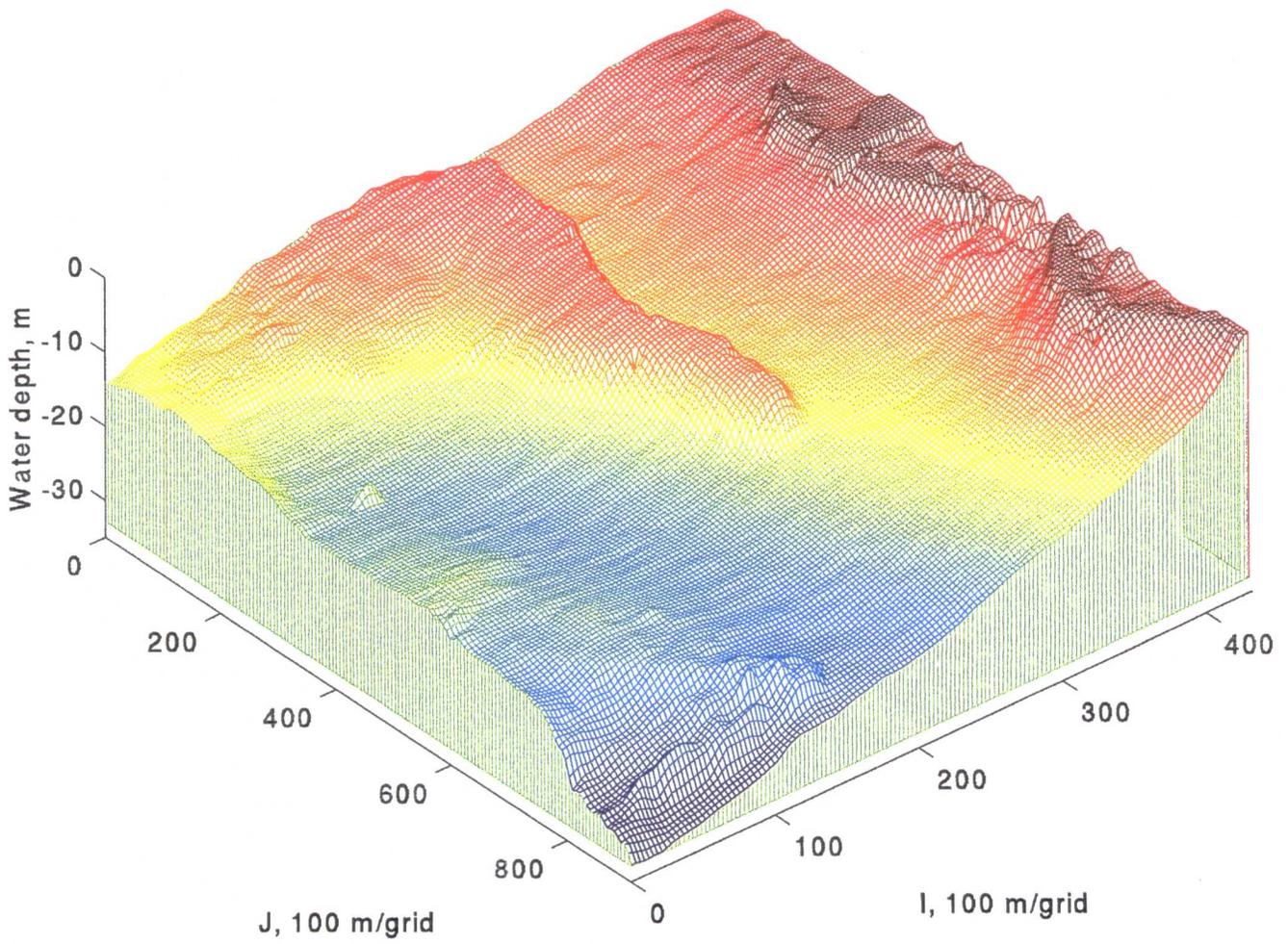
SOUTH-CENTRAL LOUISIANA SHELF

Figure 16 3D view of the bathymetric grid, with Ship Shoal.
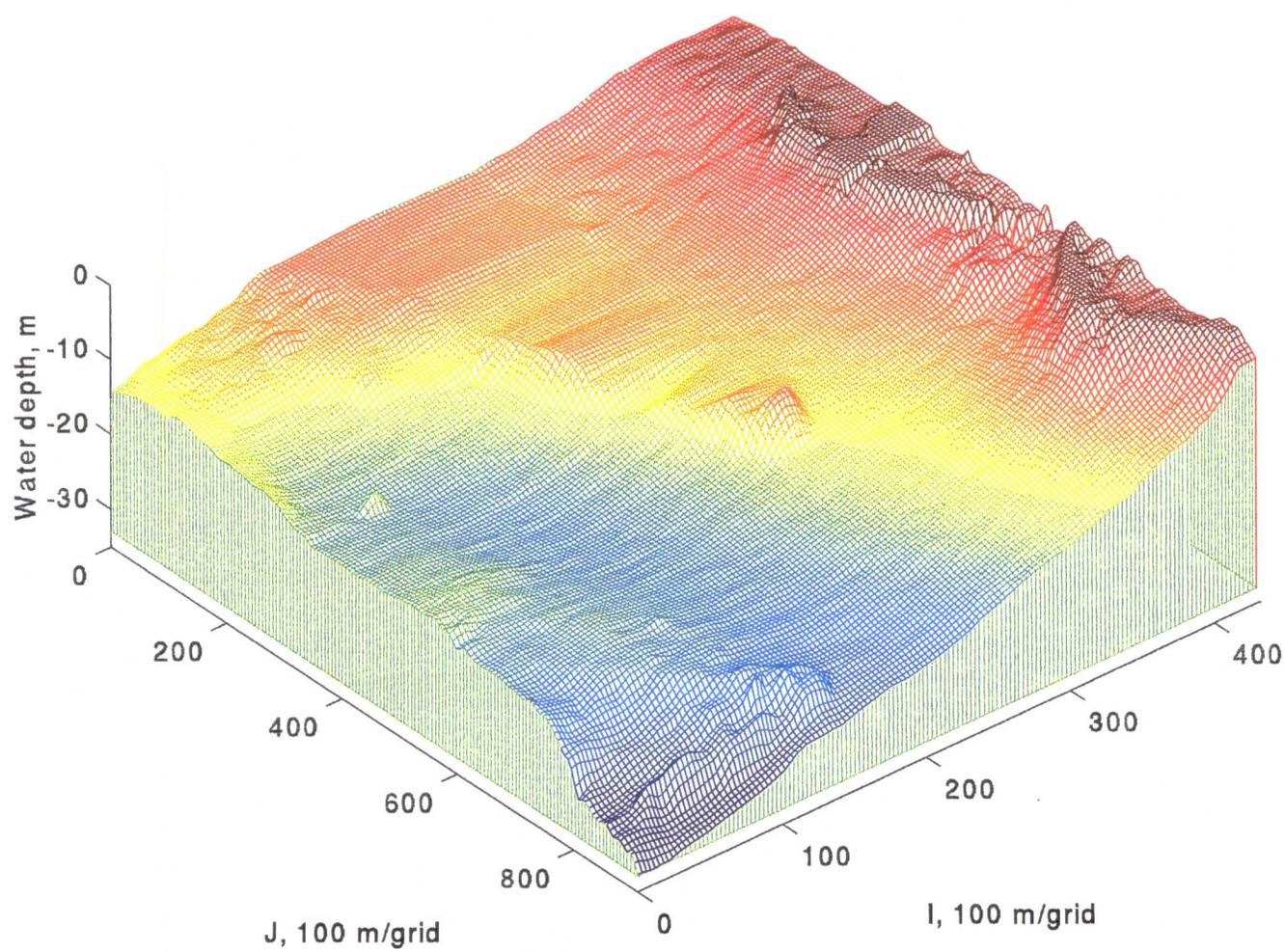
HYPOTHETICAL SOUTH-CENTRAL LOUISIANA SHELF

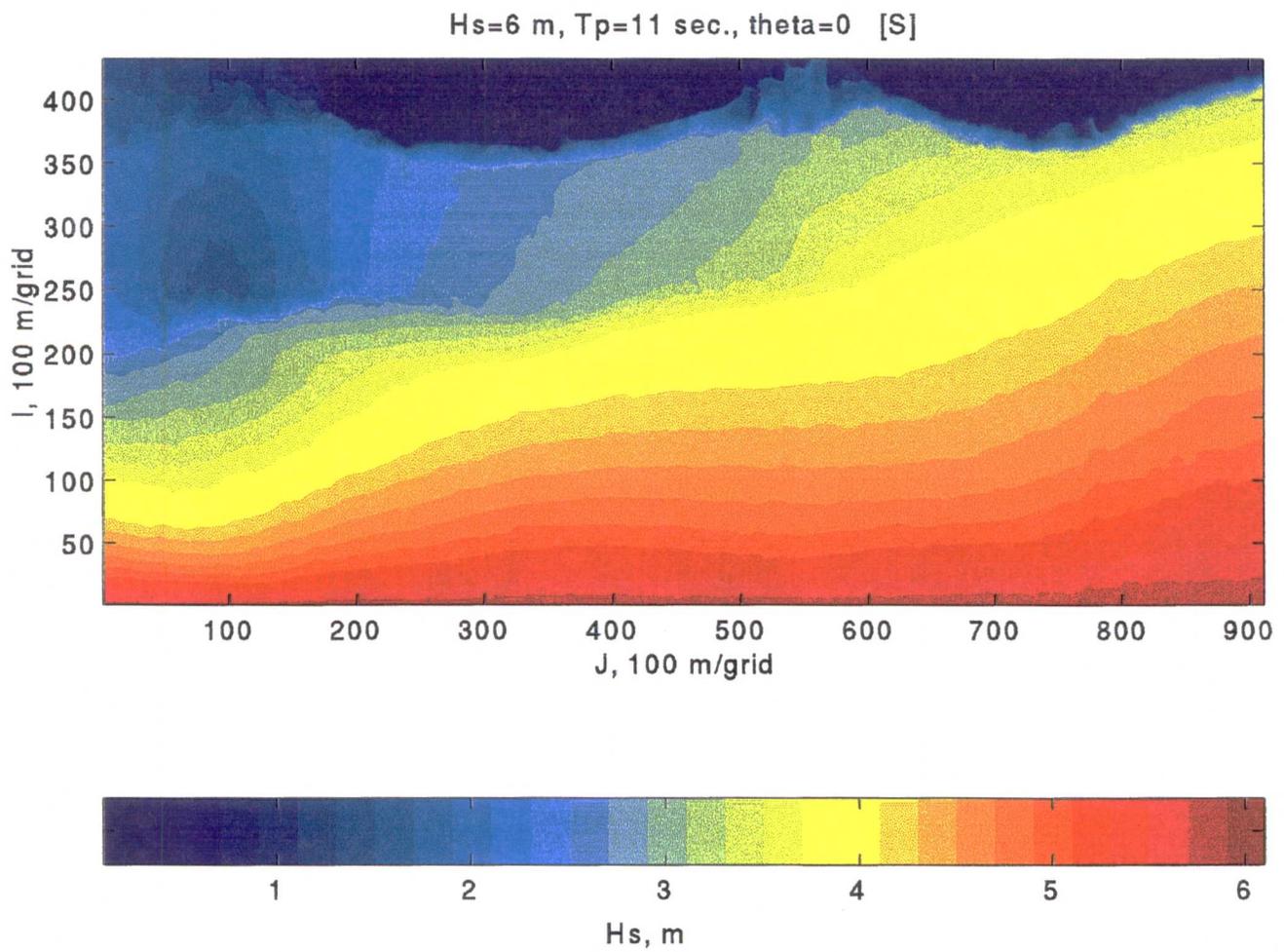Figure 17 3D view of the bathymetric grid, without Ship Shoal.

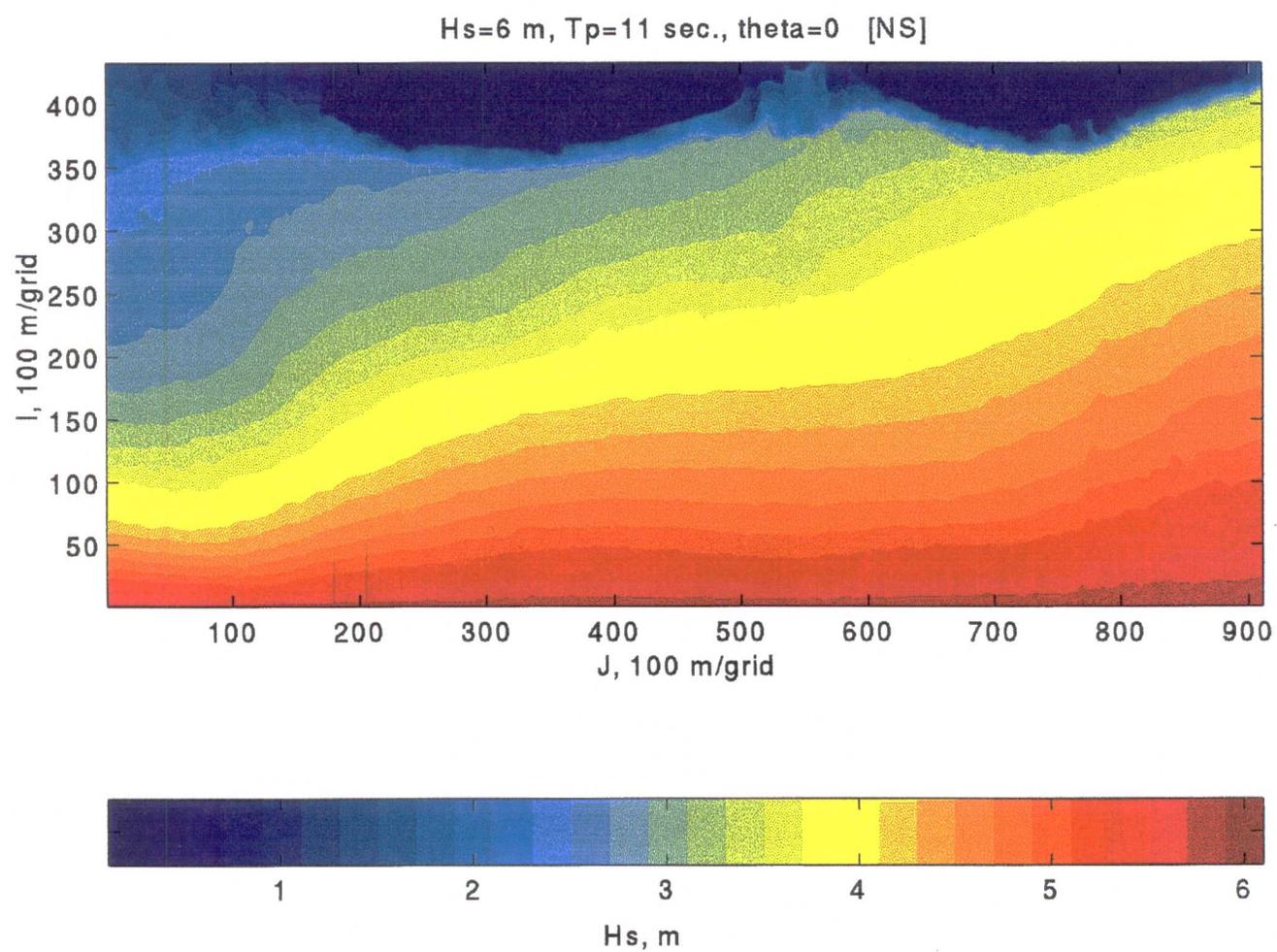Figure 18a Image of modeled significant wave height, H_s. Case 1, $\theta = 0°$, with Ship Shoal.

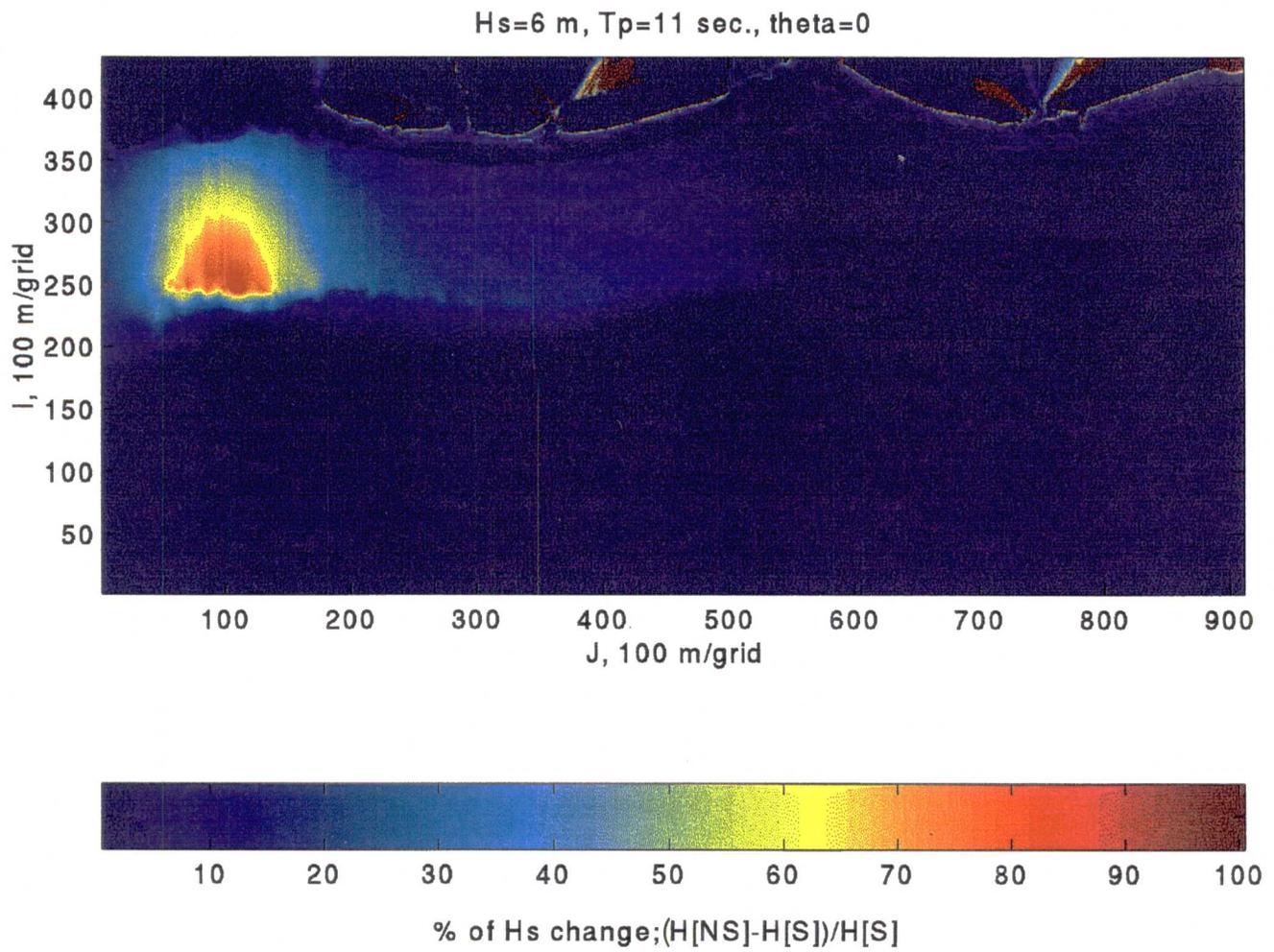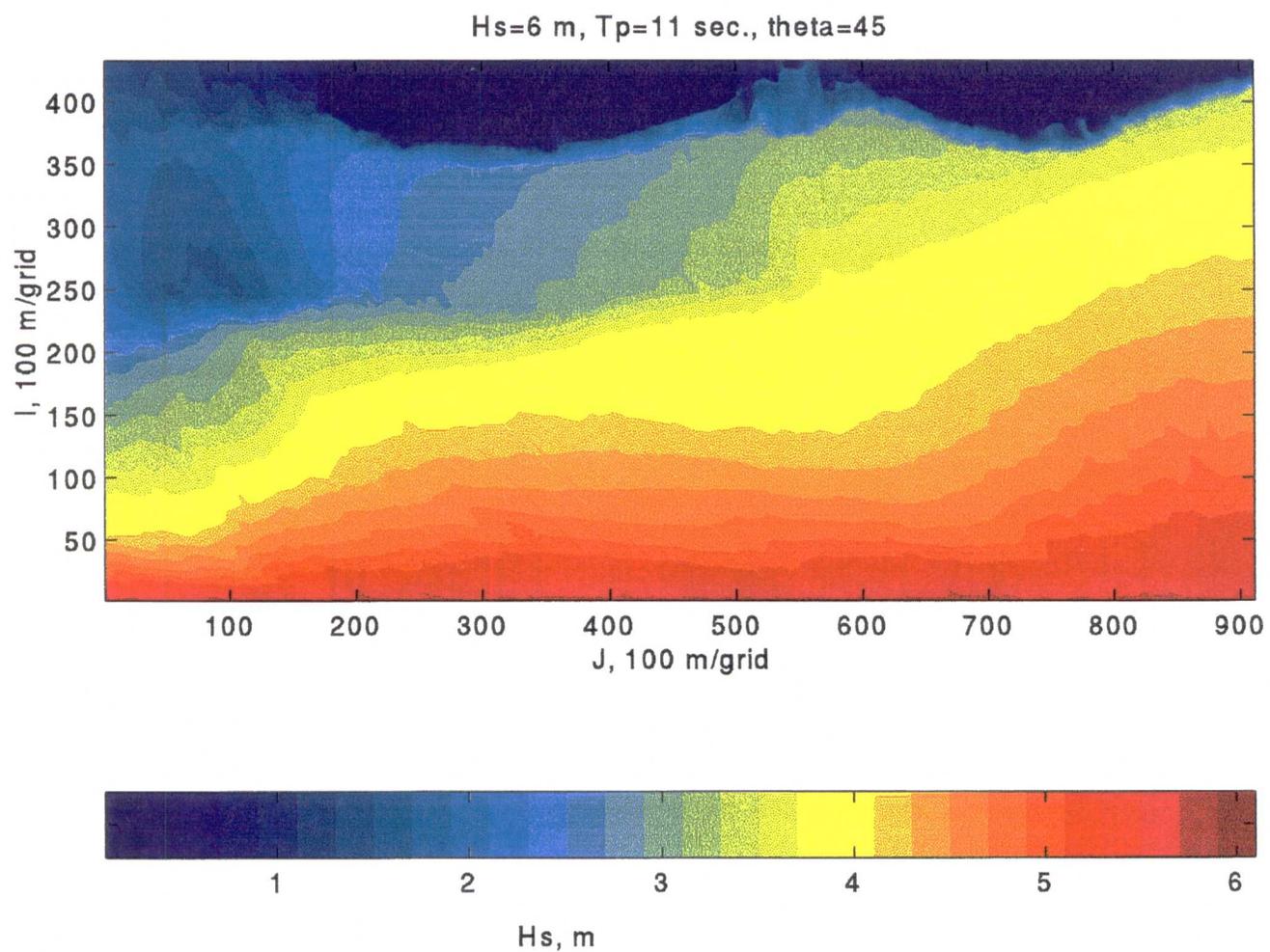Figure 18b Image of modeled significant wave height, H_s. Case 1, $\theta=0°$, without Ship Shoal.

Hs=6 m, Tp=11 sec., theta=0

% of Hs change;(H[NS]-H[S])/H[S]

Figure 18c Image of percentage of H_s increase due to shoal removal. Case 1, $\theta = 0°$.

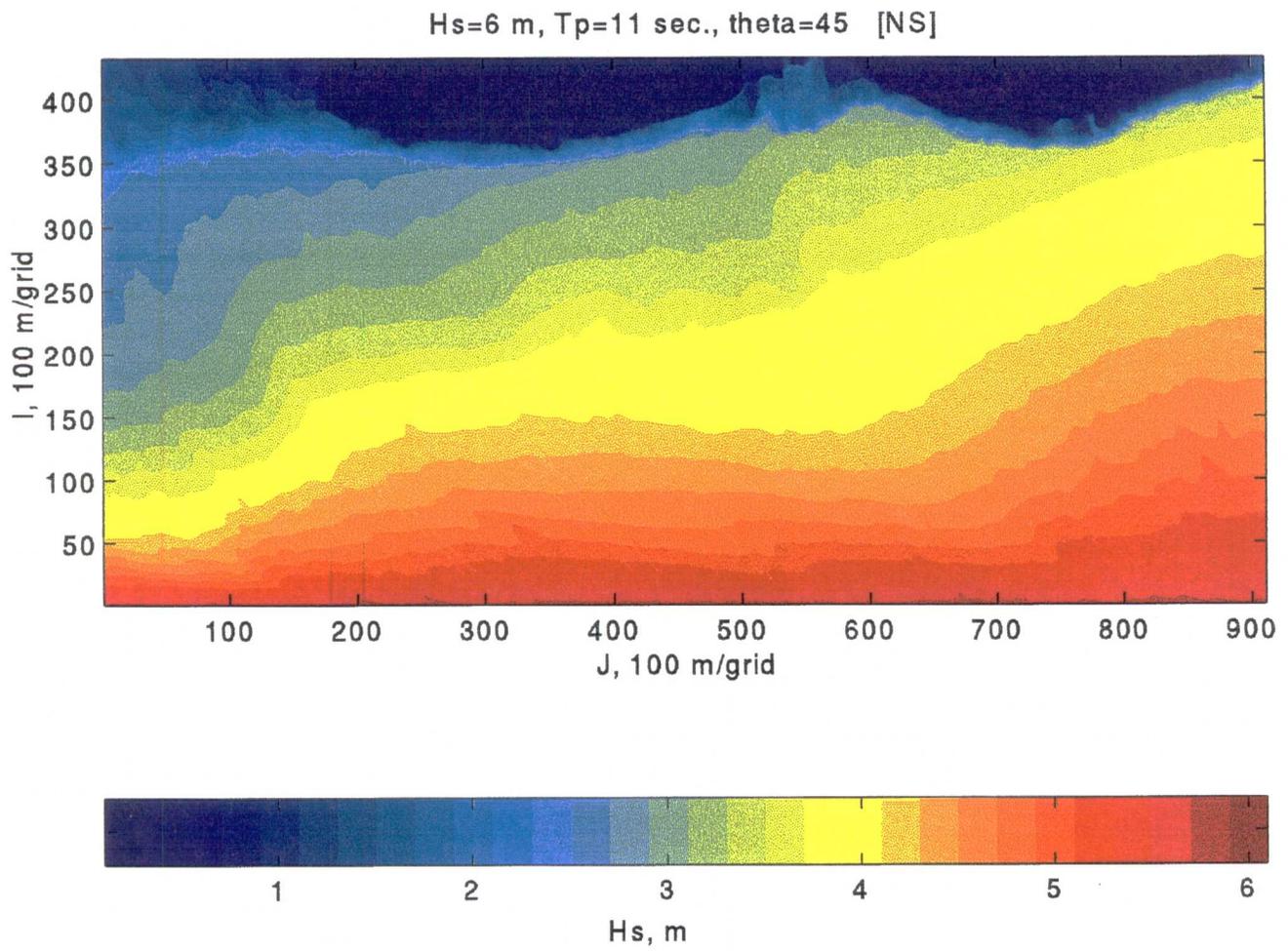Figure 19a Image of modeled significant wave height, H_s. Case 1, $\theta = 45°$, with Ship Shoal.

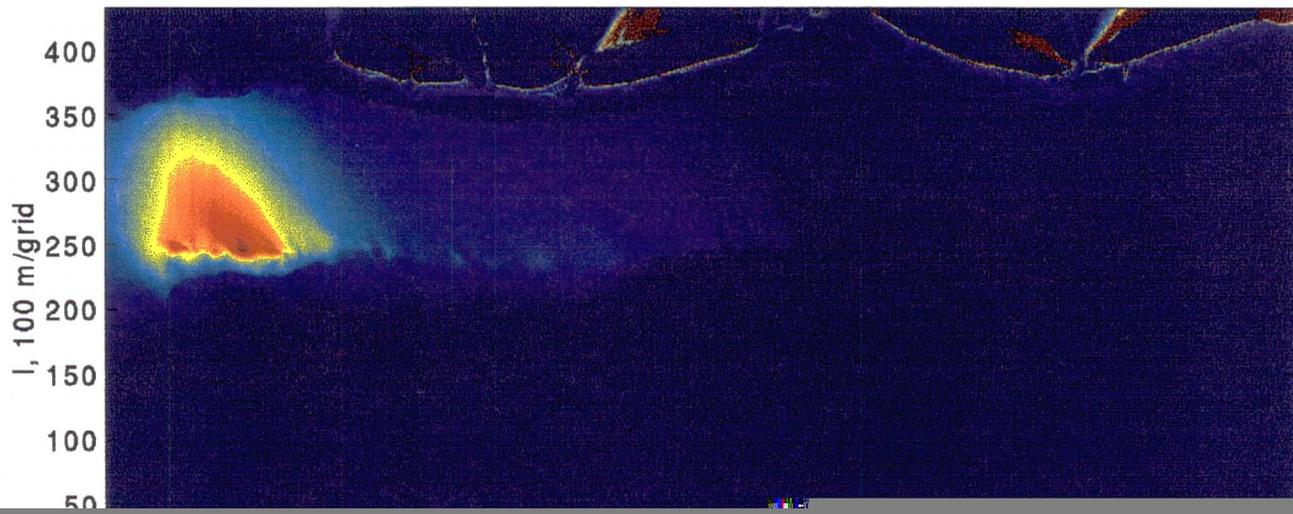Figure 19b Image of modeled significant wave height, H_s. Case 1, $\theta = 45°$, without Ship Shoal.
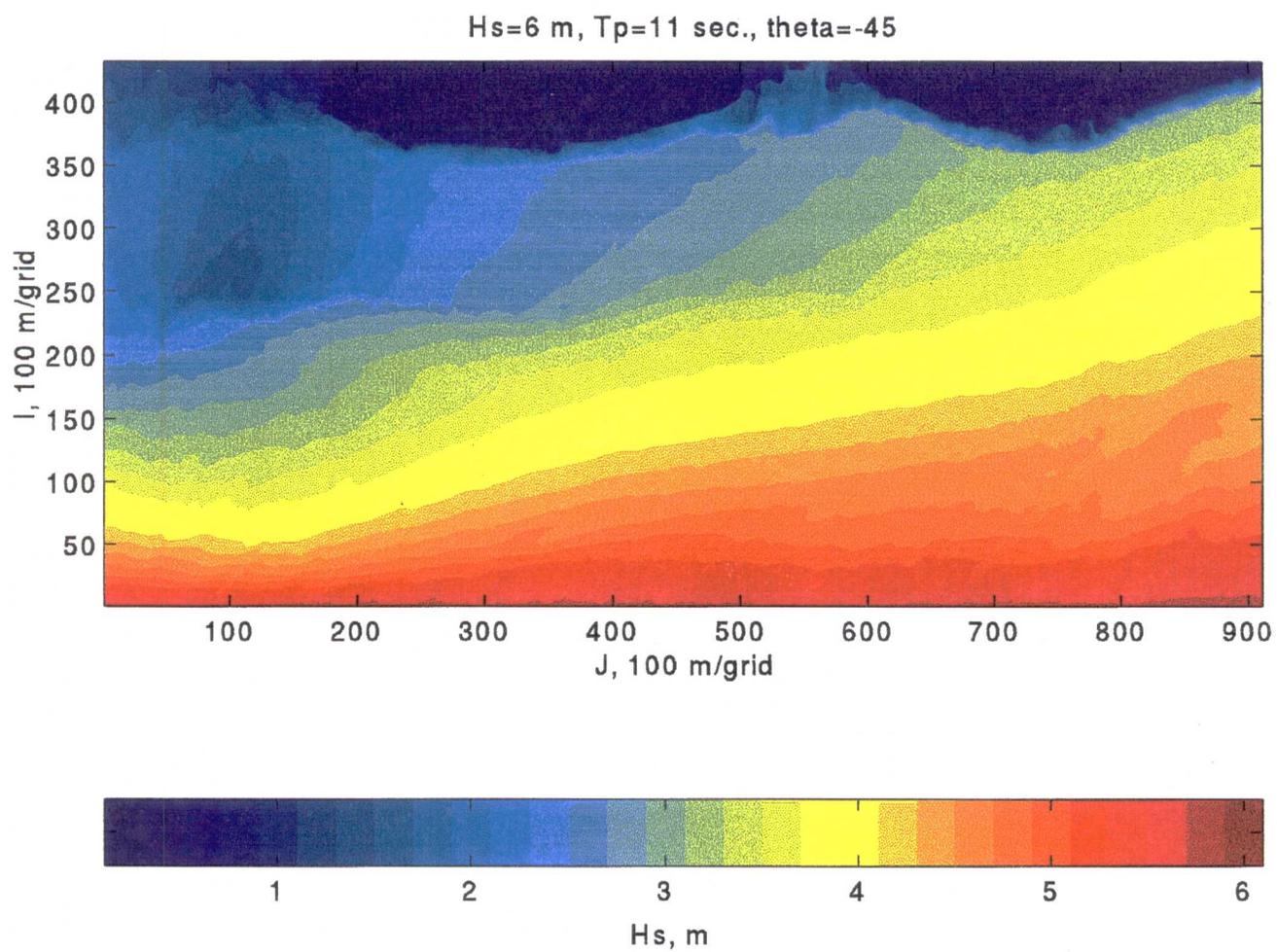
Hs=6 m, Tp=11 sec., theta=45

Hs=6 m, Tp=11 sec., theta=-45

Figure 20a Image of modeled significant wave height, H_s. Case 1, $\theta = -45°$, with Ship Shoal.
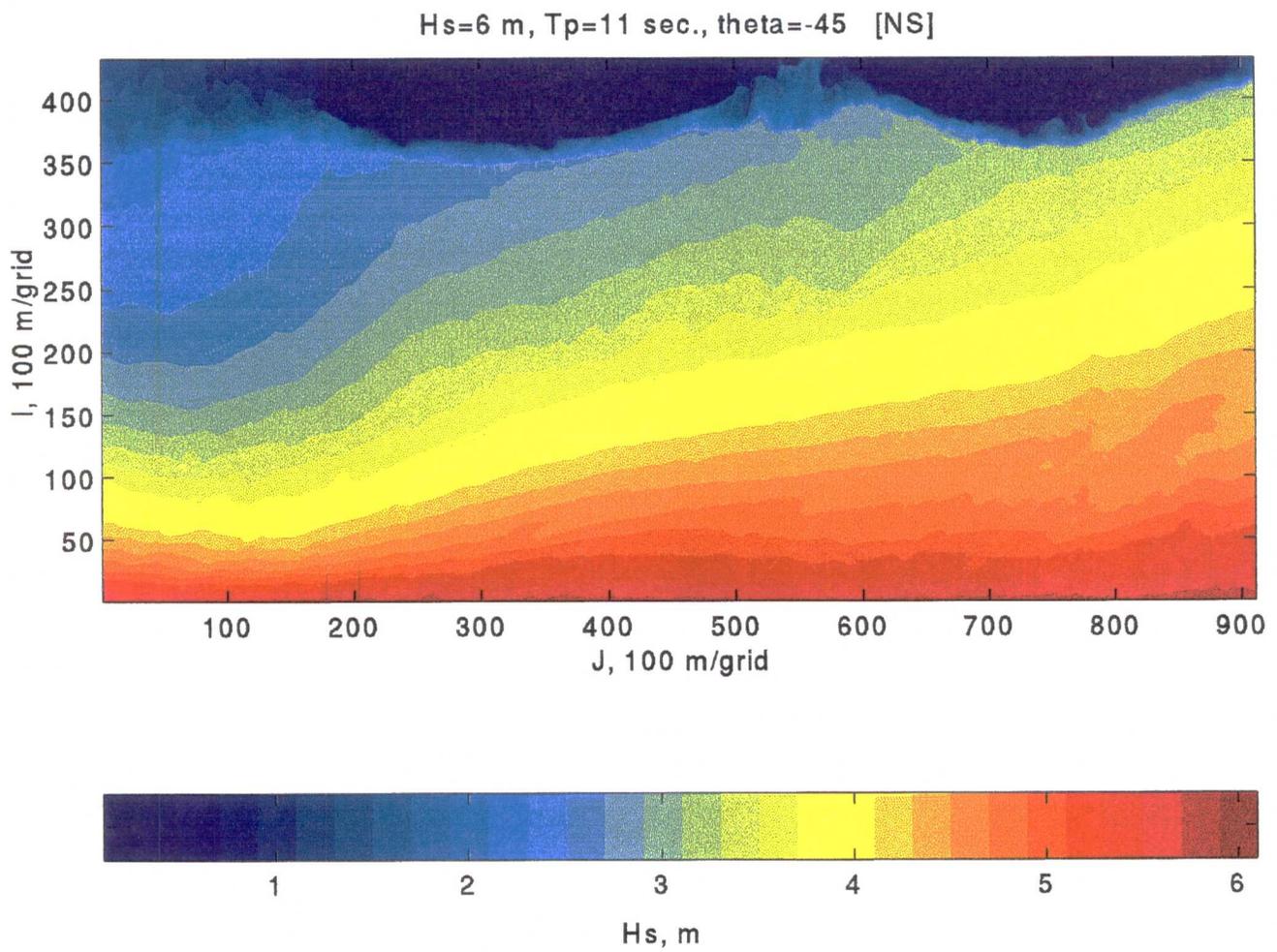
Hs=6 m, Tp=11 sec., theta=-45 [NS]

Figure 20b Image of modeled significant wave height, H$_s$. Case 1, θ=-45°, without Ship Shoal.
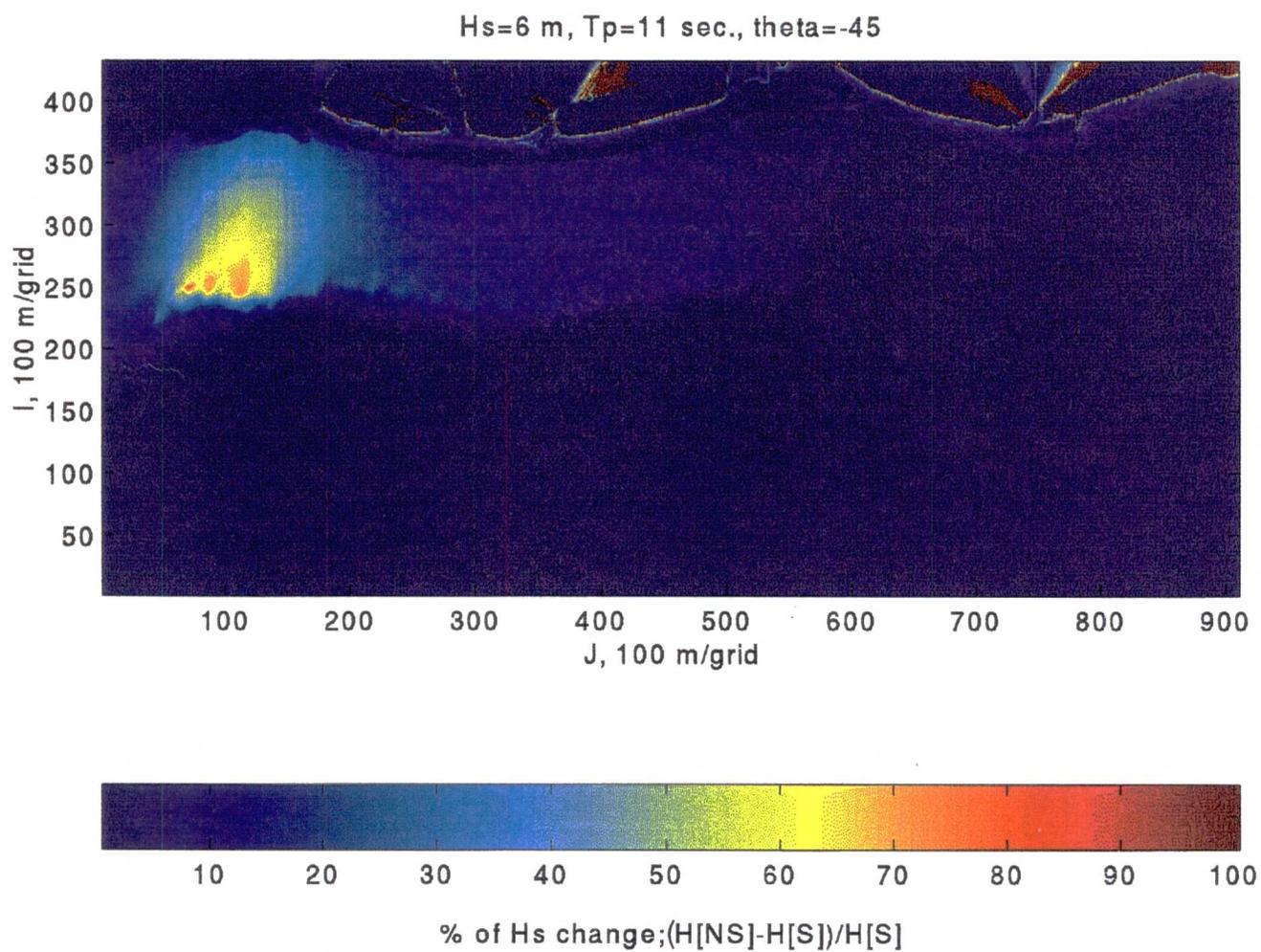
Figure 20c Image of percentage of H_s increase due to shoal removal. Case 1, $\theta = -45°$.

(3). Although the patterns of wave transformation (the west-east increasing wave height gradient) and wave height increase (the locality of the most significant increase) due to shoal removal are very similar for each wave approach direction simulated, directionality does have important implications (Figures 18c, 19c, and 20c). The magnitude of wave height increase and the area within which wave height increases more than 60% are greatest when the wave approach is southeast ($\theta = 45°$). For example, the greatest value of wave height increase in Figure 19c is 100%. Waves propagating from the south ($\theta = 0°$) result in a smaller wave height increase-- approximately an order of magnitude less than that associated with southeast waves. Southwest ($\theta = -45°$) waves undergo the lowest wave height change in both magnitude and geographical extent. This is a direct function of higher rates of energy dissipation and wave attenuation seaward of the western flank of the shoal where the inner shelf slope decreases markedly in comparison to the east flank.

Two longitudinal sections (J=150 and J=400) corresponding to a geographic position west of Racoon Point and Whiskey Island respectively, are plotted in Figures 21 and 22. The top-most panel in each figure is the sectional bathymetric profile pertaining to the inclusion and exclusion of Ship Shoal. The three panels below are the plots of the sectional profiles representing the outputs for the three incident wave directions in which "a" is a plot of the significant wave height generated by STWAVE over the two bathymetric configurations; "b" shows the change in significant wave height due to the removal of Ship Shoal; and "c" represents the depth-limited wave breaking index. The data demonstrate that the magnitude of the wave height increase (40-60%) due to the removal of the shoal on the west flank of the shoal area (Figure 21a) is much larger than that at the east flank (10-20%) (Figure 22a). The directionality of the changes can also be recognized, especially in Figure 21. Since the unit-width volumes of sand removed from the shoal at these two sections are approximately the same, the magnitude of wave height increase is more dependent on among other things the local water depth, rather than the removed volume of sand. This is because the water depth dictates where wave breaking occurs. The depth-limited breaking criteria used in STWAVE is 0.65. In Figure 21c, waves from all three directions break over the west portion of Ship Shoal. As shown in Figure 22c, wave breaking does not occur over the eastern flank of the shoal due to much deeper water depths, although the breaking wave index increases substantially.

It is apparent in both sectional profiles that waves break further inshore (the second breaking phase for section J=150) for both simulations with and without the shoal complex. The data suggest that removal of Ship Shoal does not impact the nearshore wave field along the Isles Dernieres during this particular storm simulation.

The distribution of wave energy was evaluated qualitatively through wave refraction diagrams. Wave orthogonals or rays, were generated for scenarios including and excluding Ship Shoal for the three deep water wave approaches (Figures 23, 24 and 25). In each of the figures, "a" represents wave ray patterns for the bathymetry containing Ship Shoal and "b" excludes the shoal. Refraction is clearly evident over the western portion of the shoal and is not evident on removal of the entire complex. It is worthy of note that laboratory work (Vincent and Briggs,
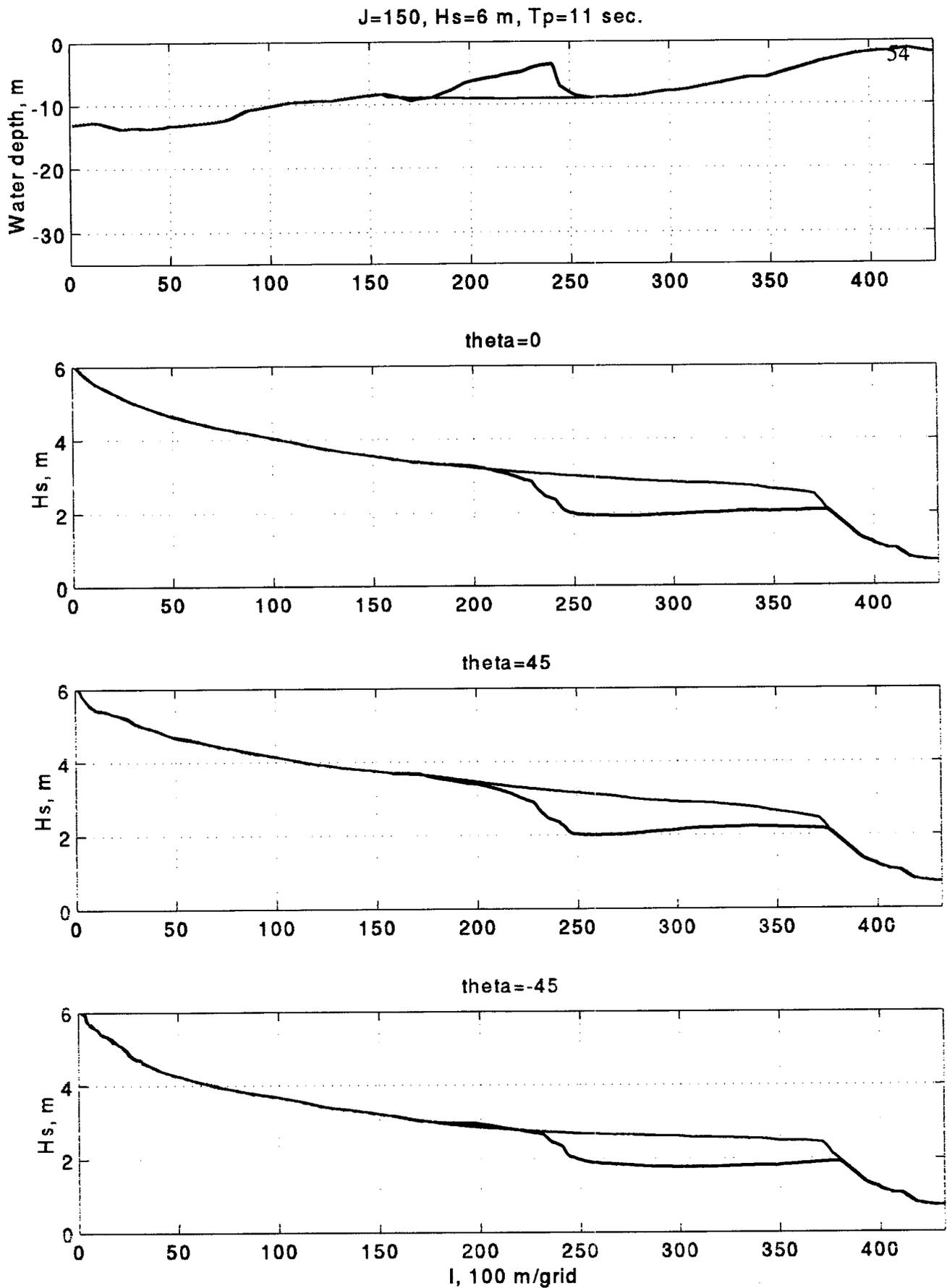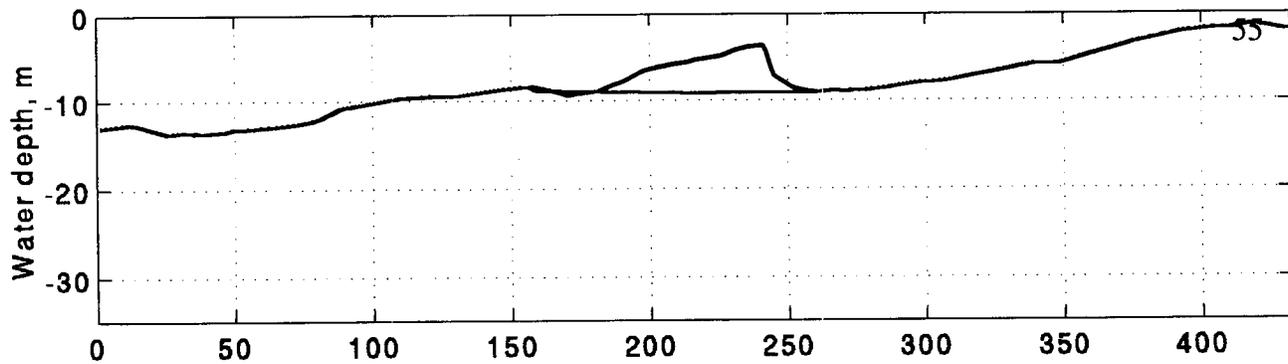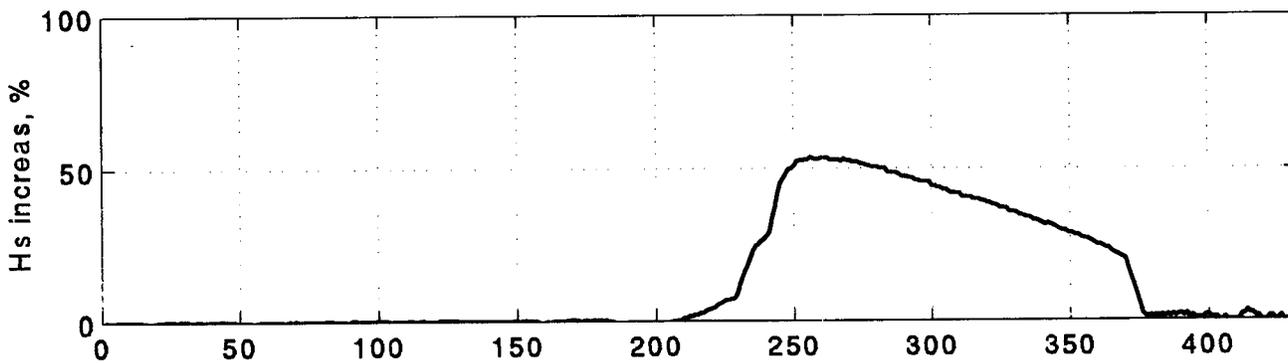
Figure 21a Cross-sectional profiles of significant wave height, H_s along J=150 in Case 1.
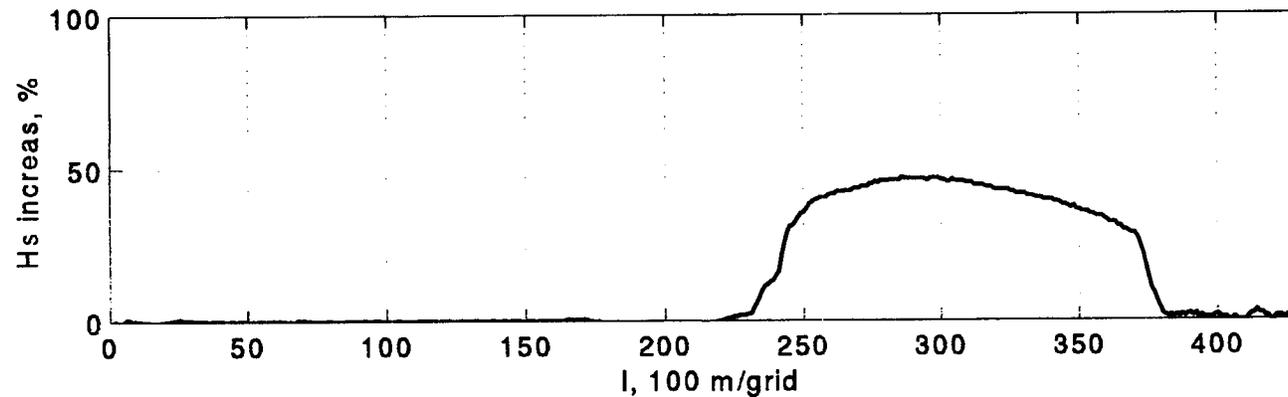
Figure 21b Cross-sectional profiles of percentage of H_s increase due to shoal removal along
J=150 in Case 1.

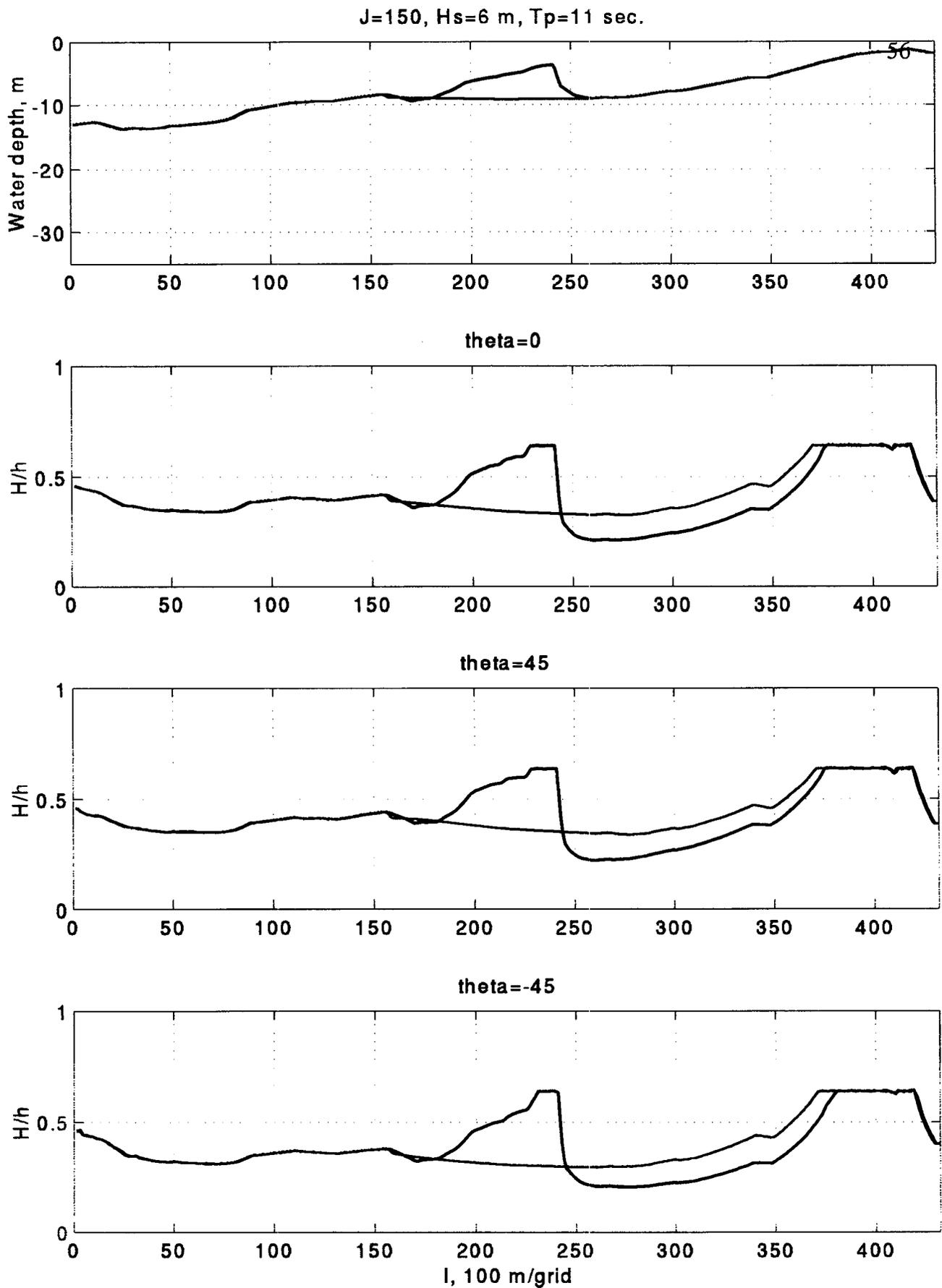J=150, Hs=6 m, Tp=11 sec.

theta=0

theta=45

theta=-45

I, 100 m/grid

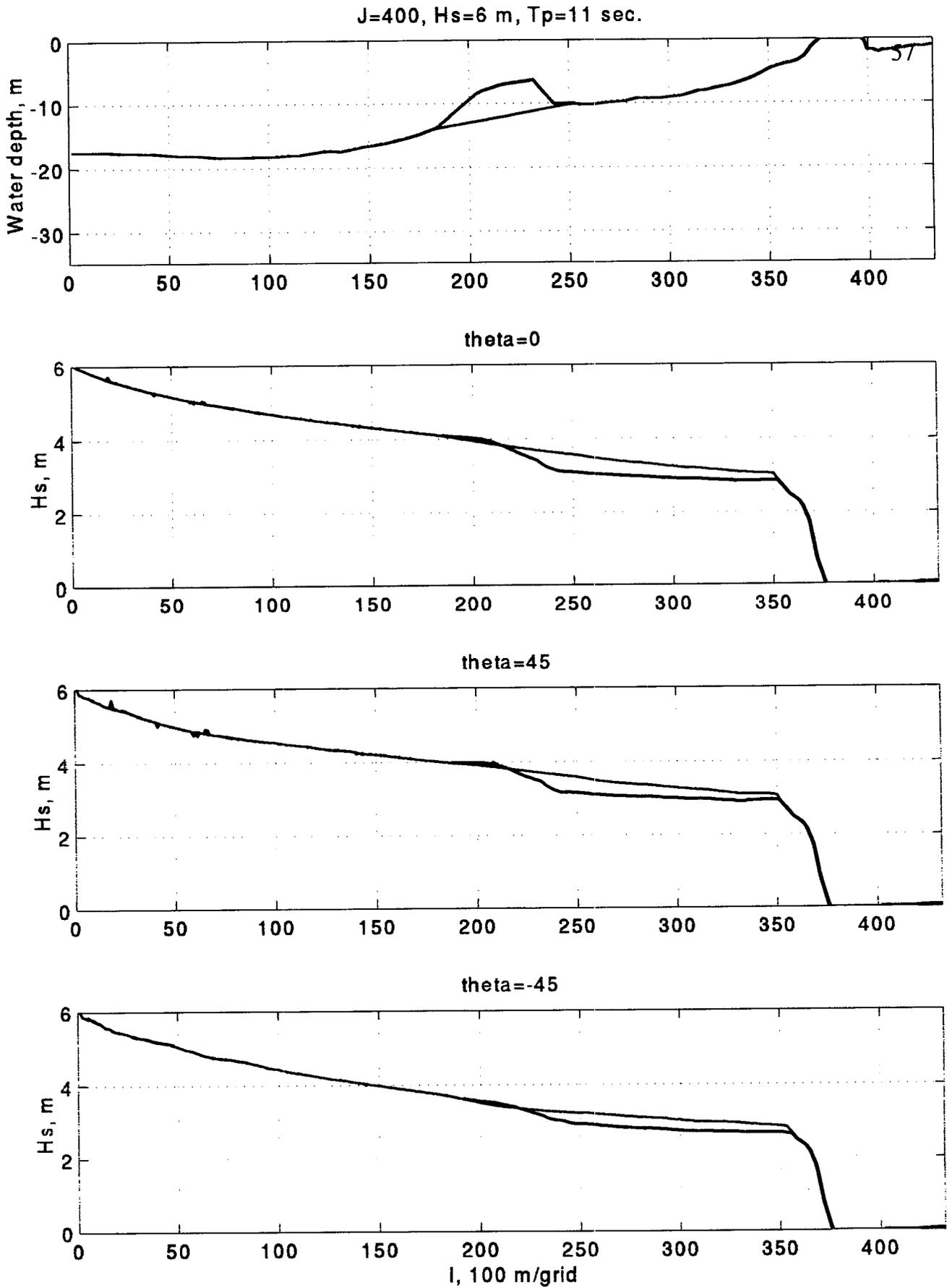Figure 21c Cross-sectional profiles of significant depth-limited wave breaking index, H/h, along J=150 in Case 1.

Figure 22a Cross-sectional profiles of significant wave height, H_s along J=400 in Case 1.
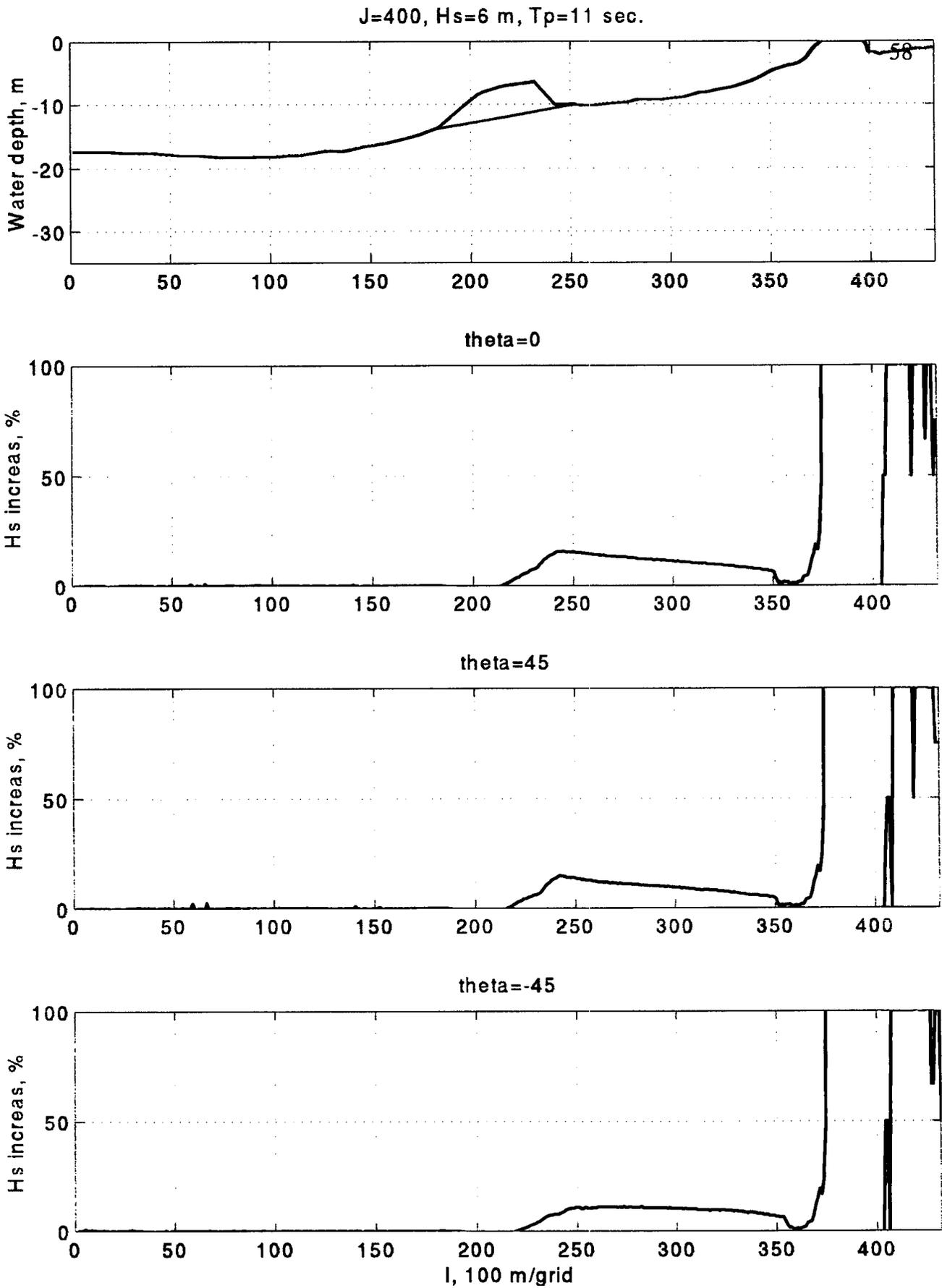
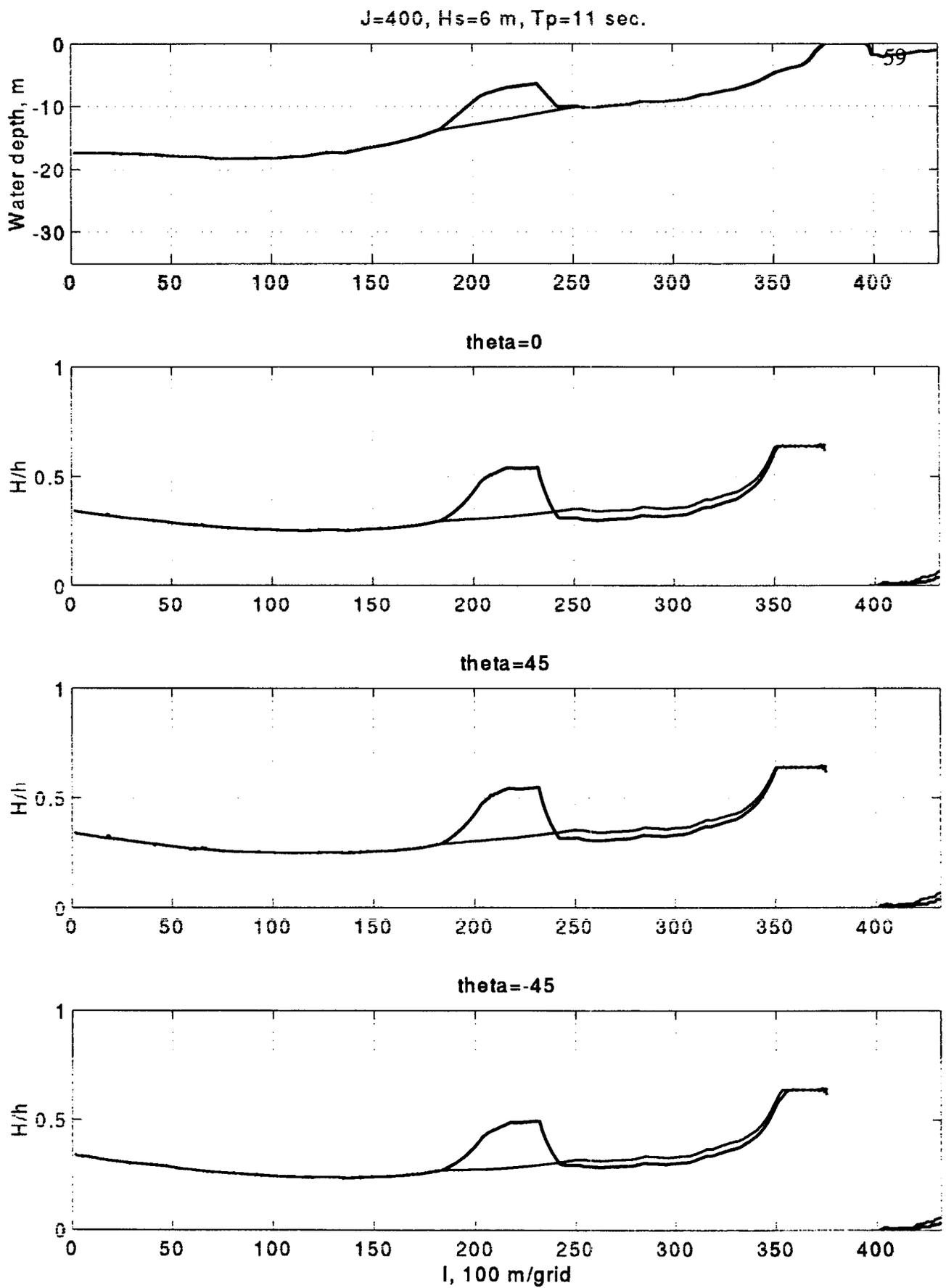Figure 22b Cross-sectional profiles of percentage of H_s increase due to shoal removal along J=400 in Case 1.

Figure 22c Cross-sectional profiles of depth-limited wave breaking index, H/h, along J=400 in Case 1.
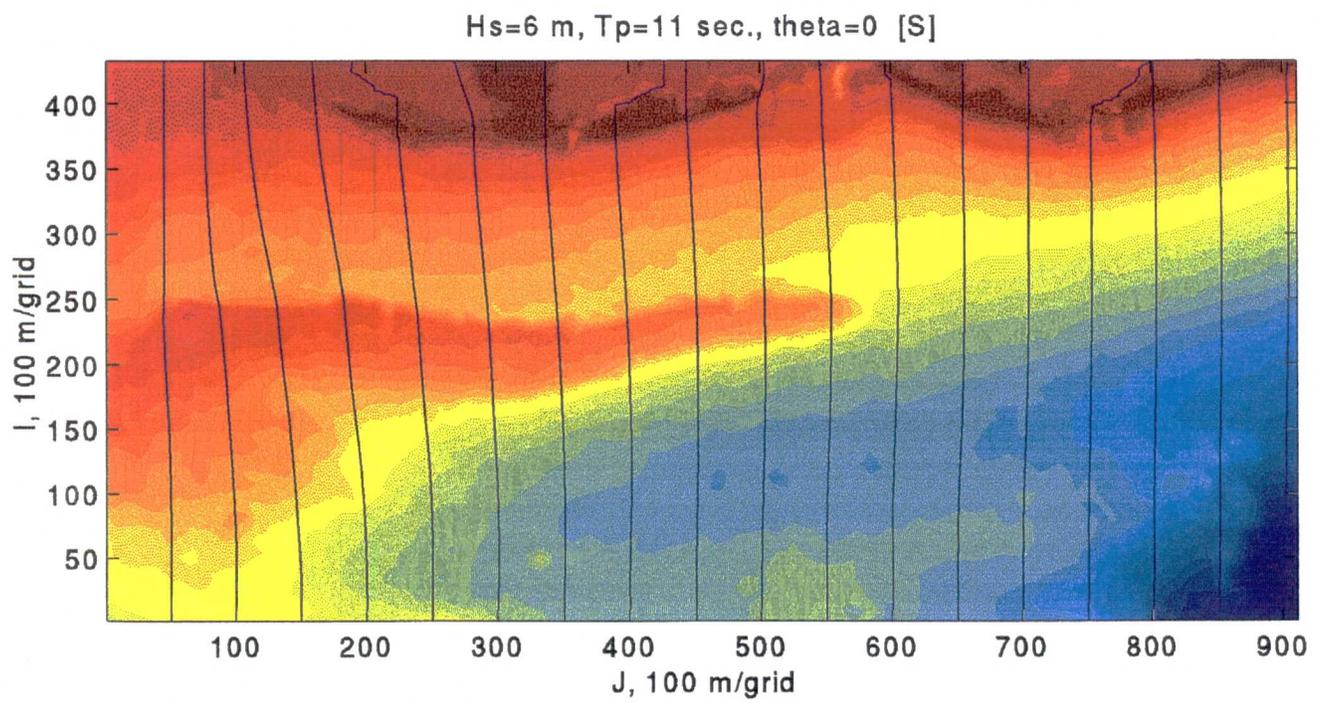
Figure 23a Modeled wave rays when θ=0° in Case 1 with Ship Shoal.

Figure 23b Modeled wave rays when θ=0° in Case 1 without Ship Shoal.

Figure 24a Modeled wave rays when θ=45° in Case 1 with Ship Shoal.
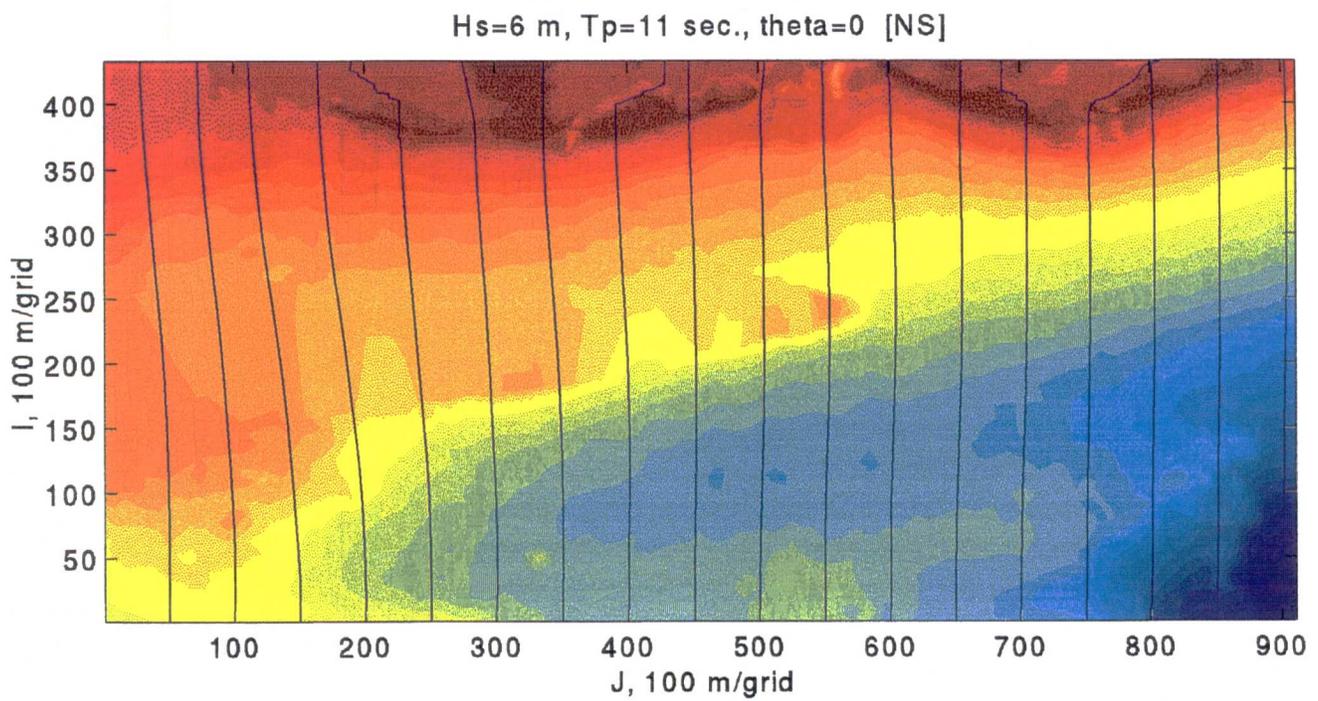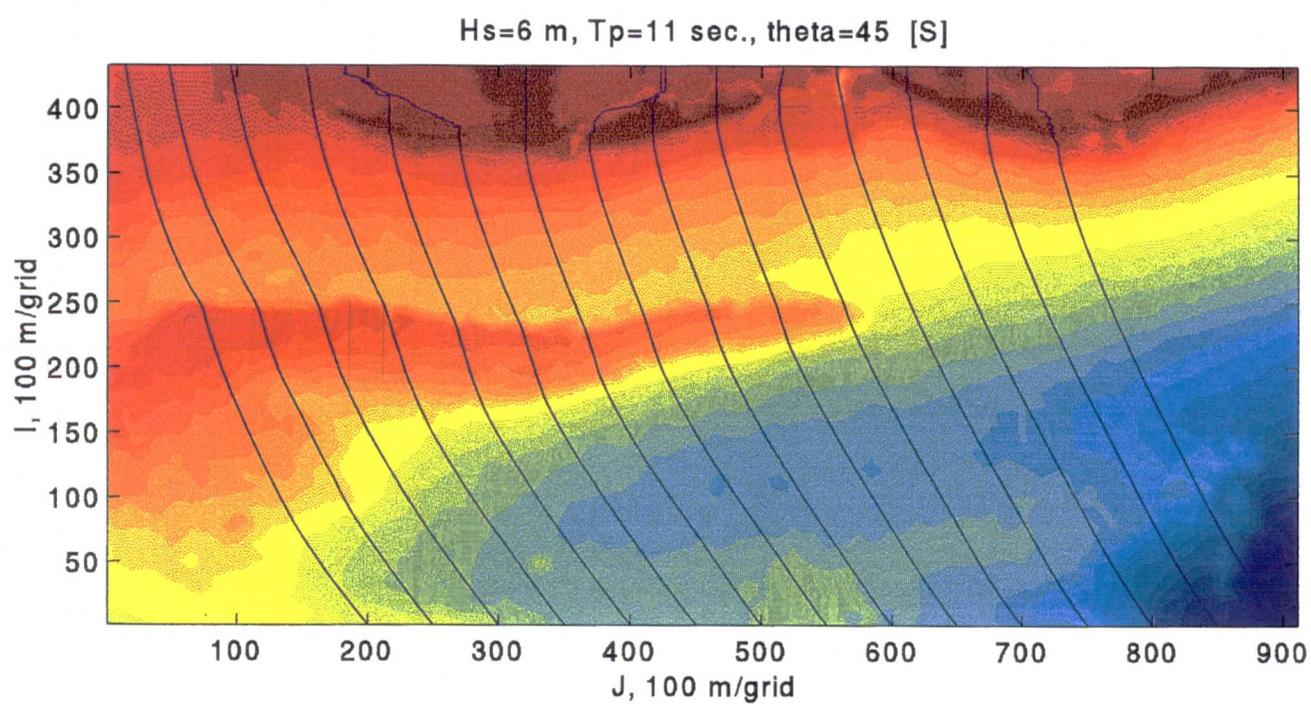
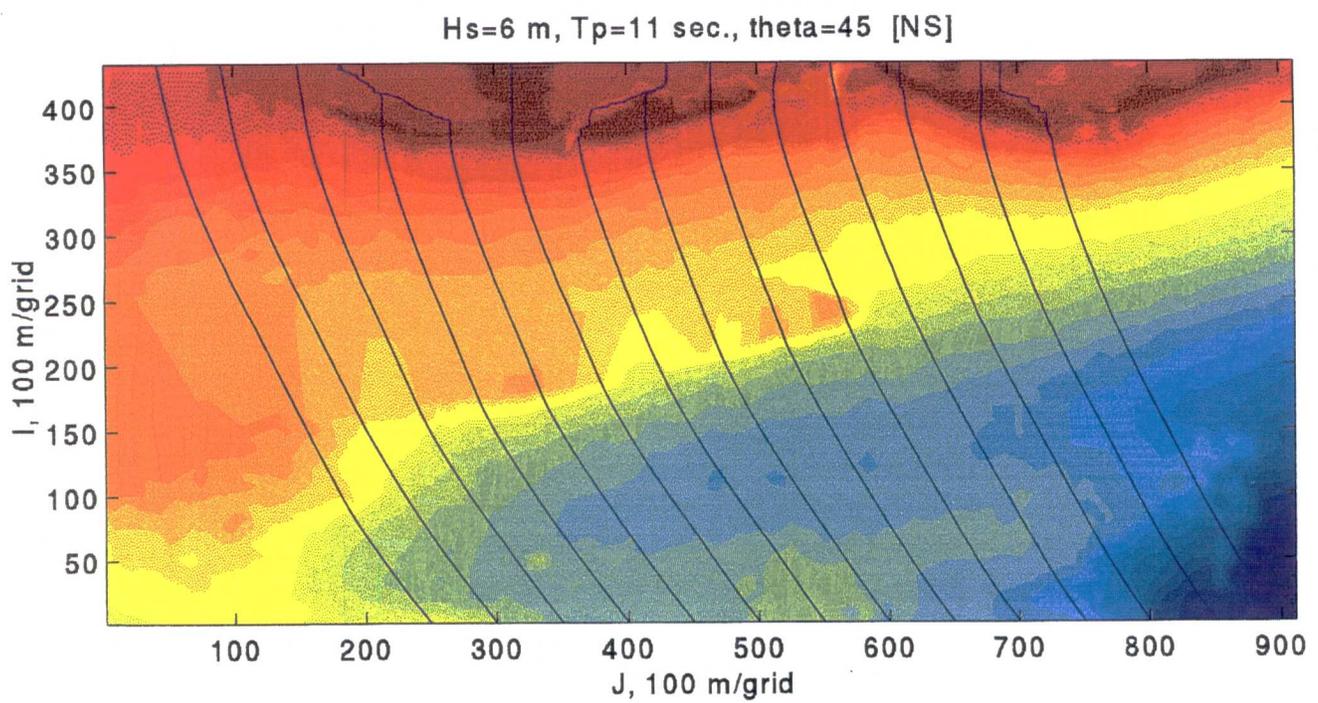Figure 24b Modeled wave rays when θ=45° in Case 1 without Ship Shoal.

Figure 25a Modeled wave rays when θ=-45° in Case 1 with Ship Shoal.

Figure 25b Modeled wave rays when θ=-45° in Case 1 without Ship Shoal.

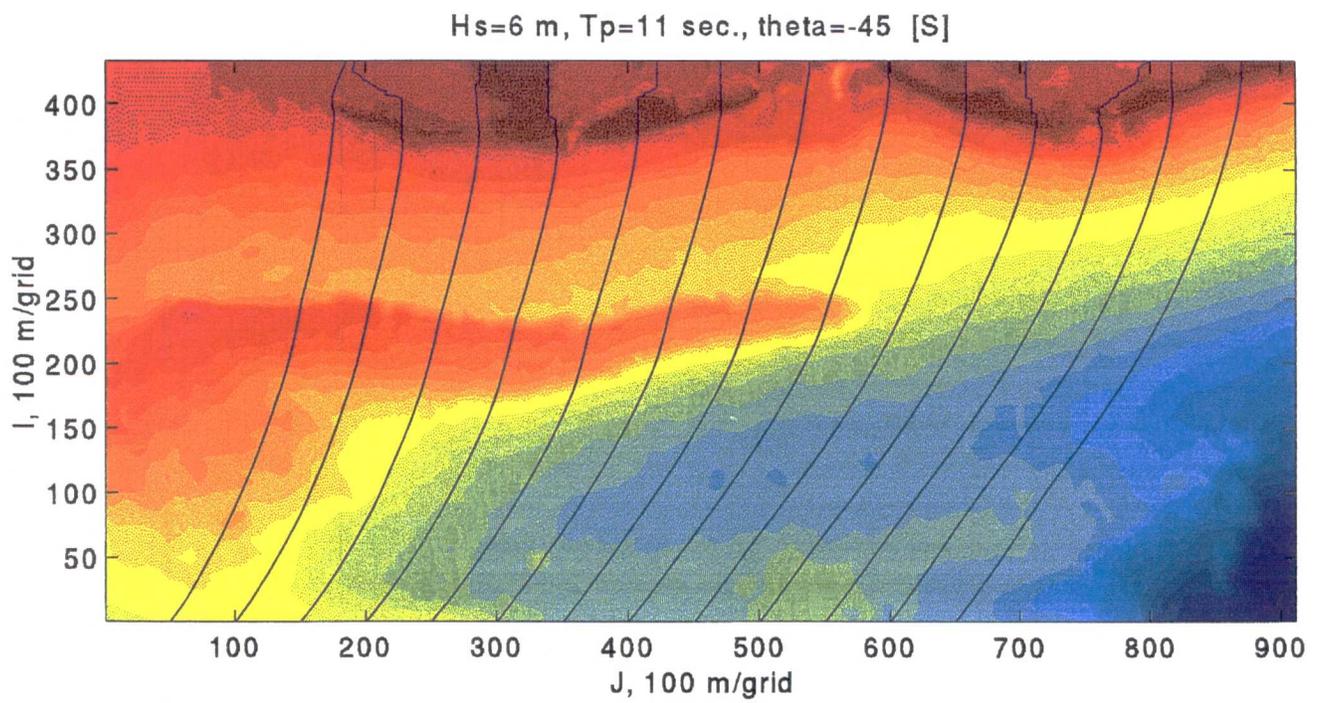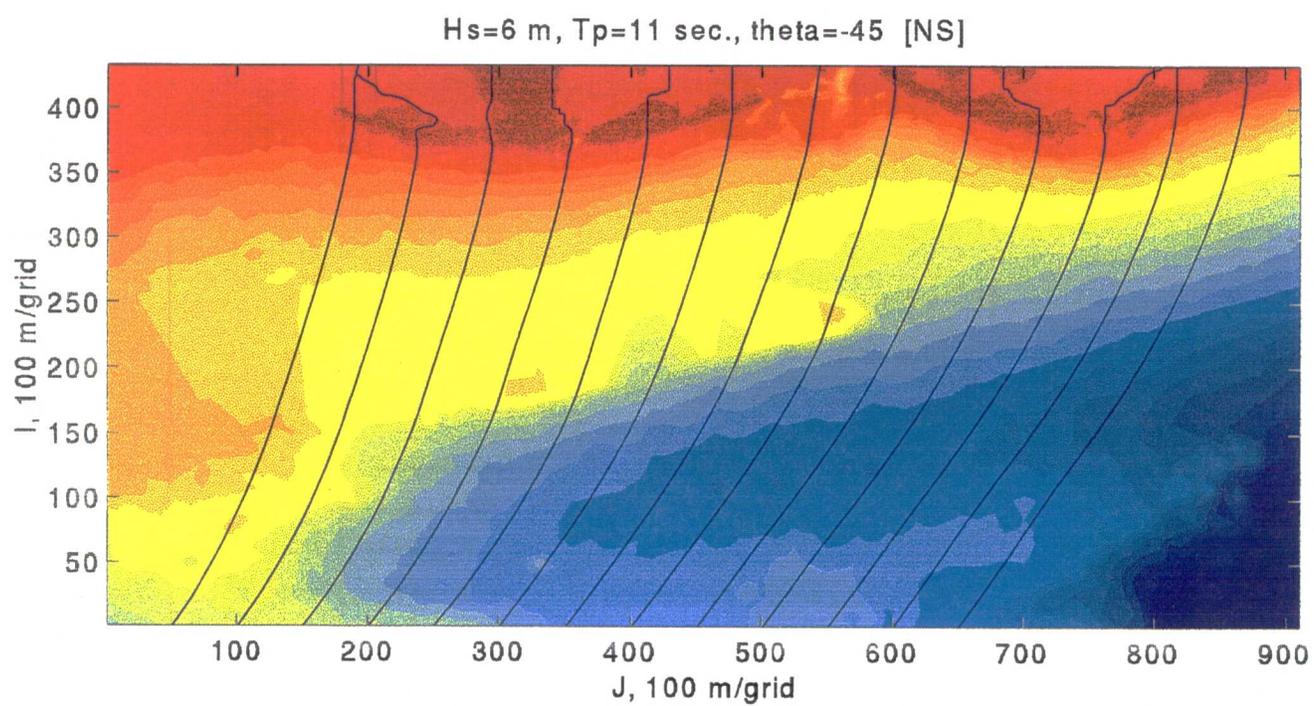1989) and numerical studies (Kirby and Ozkan, 1994) suggest that the transformation of spectral waves displays much less of a refraction effect than when using a monochromatic one. Thus, the refraction patterns derived by STWAVE over the shoal are less pronounced than would be evident from models using monochromatic waves and first order wave theory (cf RCPWAVE used by Byrnes and Groat, 1991).

Case 2 (H_s=4 m, T_p=9 sec.)

Case 2 represents a storm condition weaker in magnitude than Case 1. To make reading this report easier, the image contour plots of significant wave heights for each deep water direction are presented in Appendix A along with refraction diagrams. The plots showing percentage change in significant wave height due to shoal removal are presented in the main body of the text in Figures 26, 27 and 28. Interpretation of the data leads to the following conclusions:

(1). Similar gradients in nearshore significant wave height (H_s increasing from west to east) are observed in all plots for the three incident wave directions. The gradients are caused by the water depth difference between the east and west portion of the study area (water depth increasing from west to east). However, the gradients in this case are smaller than those in Case 1. This implies a reduction in the influence of water depth as exerted on wave height and period, and, more specifically, wave transformation and dissipation owing to the increase in relative water depth, h/L, where h is water depth and L is the local wave length (cf., Kundu, 1990).

(2). The removal of Ship Shoal also results in a significant increase of the wave height, however, as expected, the magnitudes of wave height increase are smaller than those determined for Case 1. For example, while the highest value in Figure 18c is more than 80%, the maximum in Figure 26 is only 40%. The wave height increase is restricted to the shoal area, especially along the western portion of Ship Shoal where the water depths are less.

(3). The directionality within the wave transformation as well as the wave height variation due to the removal of Ship Shoal can also be clearly seen in Figures 26, 27 and 28. Both the magnitude of wave height increase and the lobe area within which wave height increases more than 30% are the largest when the wave approach is southeast (θ=45°). For example, the greatest value of wave height increase in Figure 27 is 50%. When waves propagate from the south (θ=0°), the magnitude of wave height increase is smaller, and propagation from the southwest (θ=-45°) results in the lowest value of both the magnitude and the lobe area.

Similar to case 1, longitudinal profiles are presented (J=150 J=400) (Appendix A-7 through A-12) and display the following: bathymetric configurations with and without Ship Shoal; significant wave height distribution generated by STWAVE for respective bathymetries; increase of the significant wave height due to the removal of Ship Shoal and the depth-limited wave breaking index. Comparisons with the corresponding plots in Case 1, indicate that the magnitude of the wave height increase is much smaller, although the spatial variation in the increase is similar to that found in the previous case. As discussed previously, the relative water depth is the controlling factor in wave propagation, dissipation and breaking. As shown in Appendix A-9,
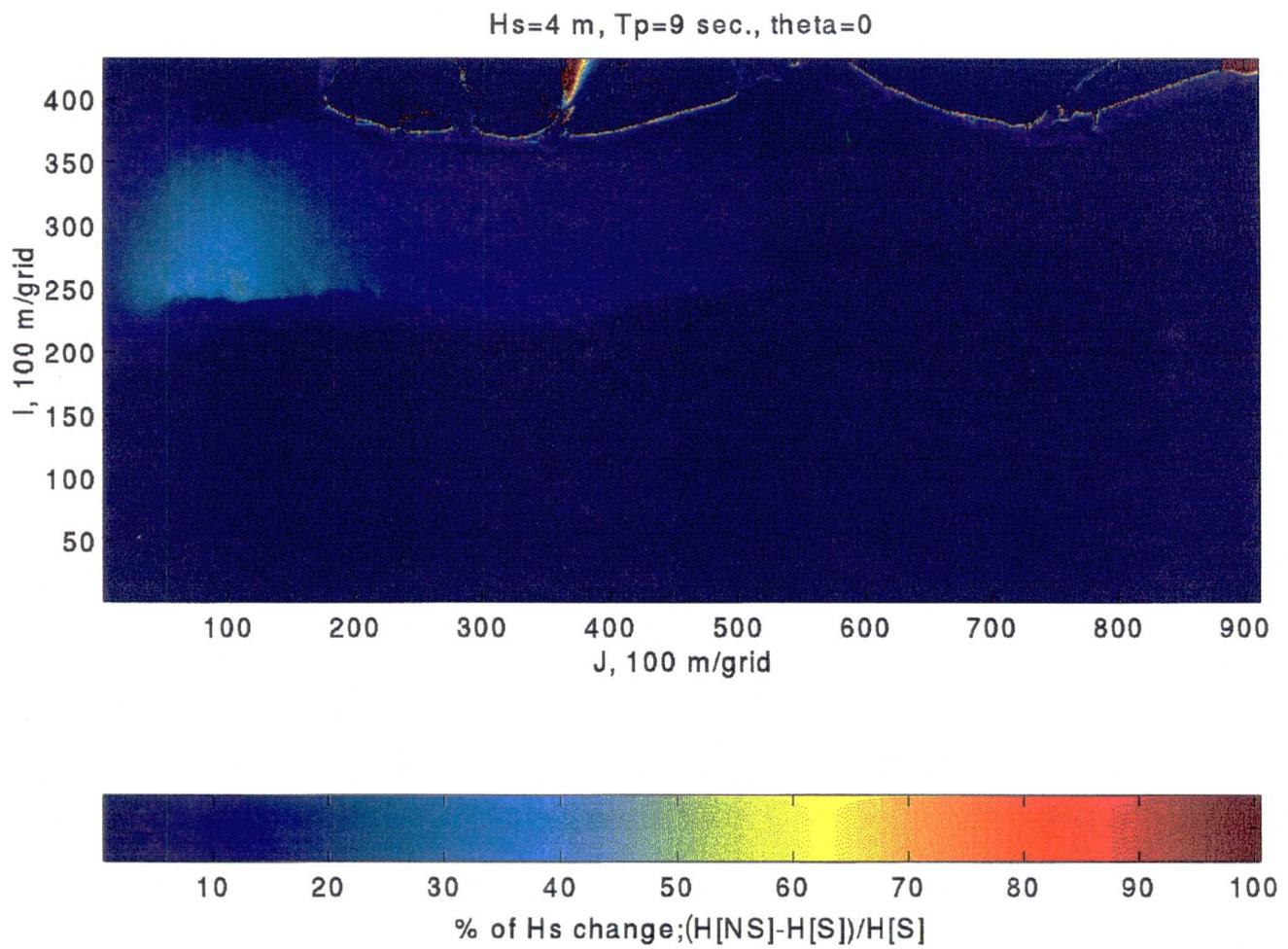
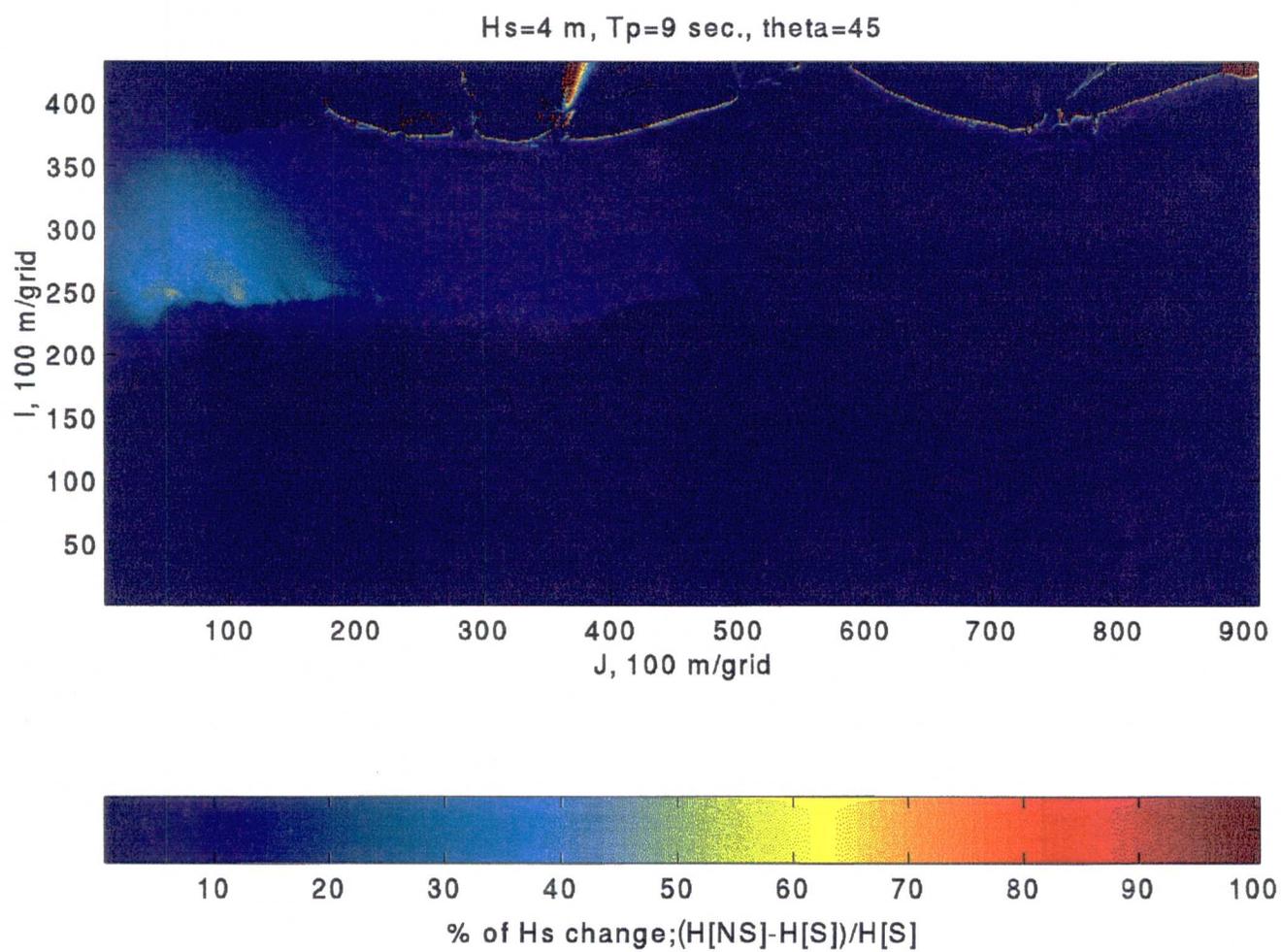Figure 26 Modeled percentage of H_s increase due to shoal removal. Case 2, $\theta = 0°$.

Hs=4 m, Tp=9 sec., theta=45

% of Hs change;(H[NS]-H[S])/H[S]

Figure 27 Modeled percentage of H_s increase due to shoal removal. Case 2, $\theta = 45°$
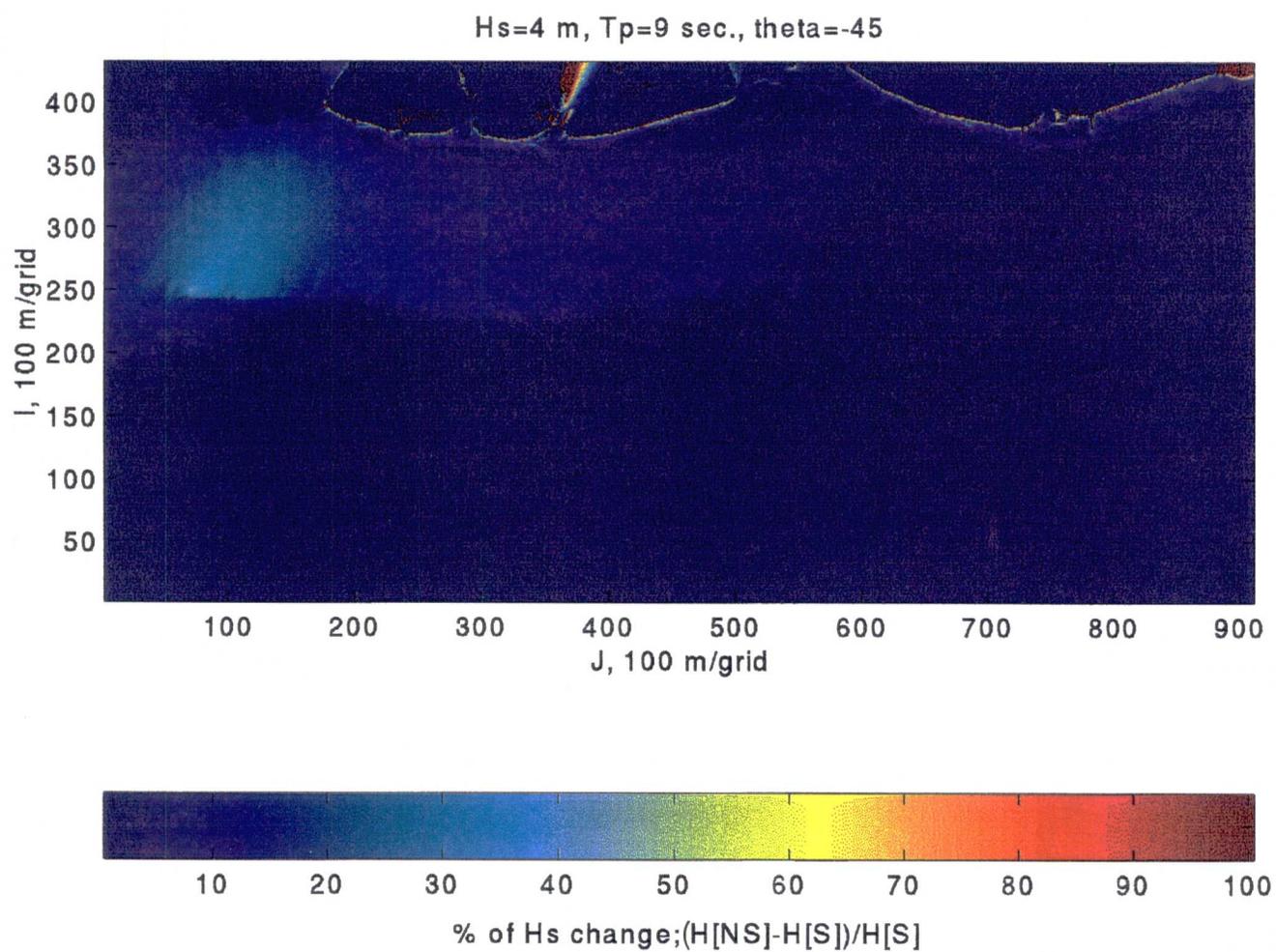
Hs=4 m, Tp=9 sec., theta=-45

Figure 28 Modeled percentage of H_s increase due to shoal removal. Case 2, $\theta = -45°$

though waves from all three directions did not break over the west portion of Ship Shoal, the breaking index is still much greater than that in Appendix A-12. Both sectional profiles show waves breaking further inshore for both present and hypothetical bathymetric scenarios. Consequently the significant wave height collapses to the same value in the nearshore (Appendix A-7) or the land boundary (Appendix A-10) for both scenarios. Thus, the removal of Ship Shoal does not alter the nearshore significant wave height under storm conditions in Case 2. The nearshore breaker zone in Case 2 is approximately 1 - 2 km further inshore when compared to that generated in Case 1.

Wave refraction patterns are shown in Appendix A-13 through A-18 for the three incident wave approach directions. Refraction is particularly pronounced over the western portion of Ship Shoal during oblique approaches.

Case 3 (H_s=2 m, T_p=6 sec.)

Case 3 was selected to represent a weak storm condition. The format adopted for Case 2 is used here and the relevant data presented in Appendix B. The plots showing percentage change in significant wave height due to shoal removal are presented in the main body of the text in Figures 29, 30 and 31. Similar to the previous cases, the same three incident wave directions were used in the simulations. Interpretation of the data leads to the following conclusions:

(1). An increasing nearshore wave height gradient from west to east is apparent but is much less than that observed in Case 1 and Case 2. This is because, for a shorter and smaller wave, the relative water depth, h/L, is very high, when compared to those values in Case 1 and Case 2, throughout the study area except the surfzone. Thus, the significant wave heights become insensitive to the differential water depth across the shoal (i.e., west-east orientation).

(2). In the area where the significant wave height increases substantially on removing Ship Shoal for stronger storms, the magnitudes of wave height increase becomes minimal in all three directions simulated in Case 3 (Figures 29, 30 and 31). For example, the maximum value of percent increase in significant wave height is approximately 20% (Figure 29), significantly less than for storms previously discussed (40% and 80%). The wave height increase is restricted to the western margin of the shoal complex where water depths are significantly less.

(3). The data suggest that varying wave direction plays a minor role on wave-shoal interaction and, therefore, resultant wave climate.

Section profiles are plotted in Appendix B for bathymetric configurations including and excluding Ship Shoal showing the increase of the significant wave height due to shoal removal and the depth-limited wave breaking index. On comparison with previous cases, as expected, the magnitude of the wave height increase becomes much smaller, although the spatial variation is similar to those in the previous cases. Differential water depths from the west and east flanks of the shoal continues to exercise control on the magnitudes of significant wave height increase and wave breaking index, although the degree of control is considerably less than found in cases 1 and
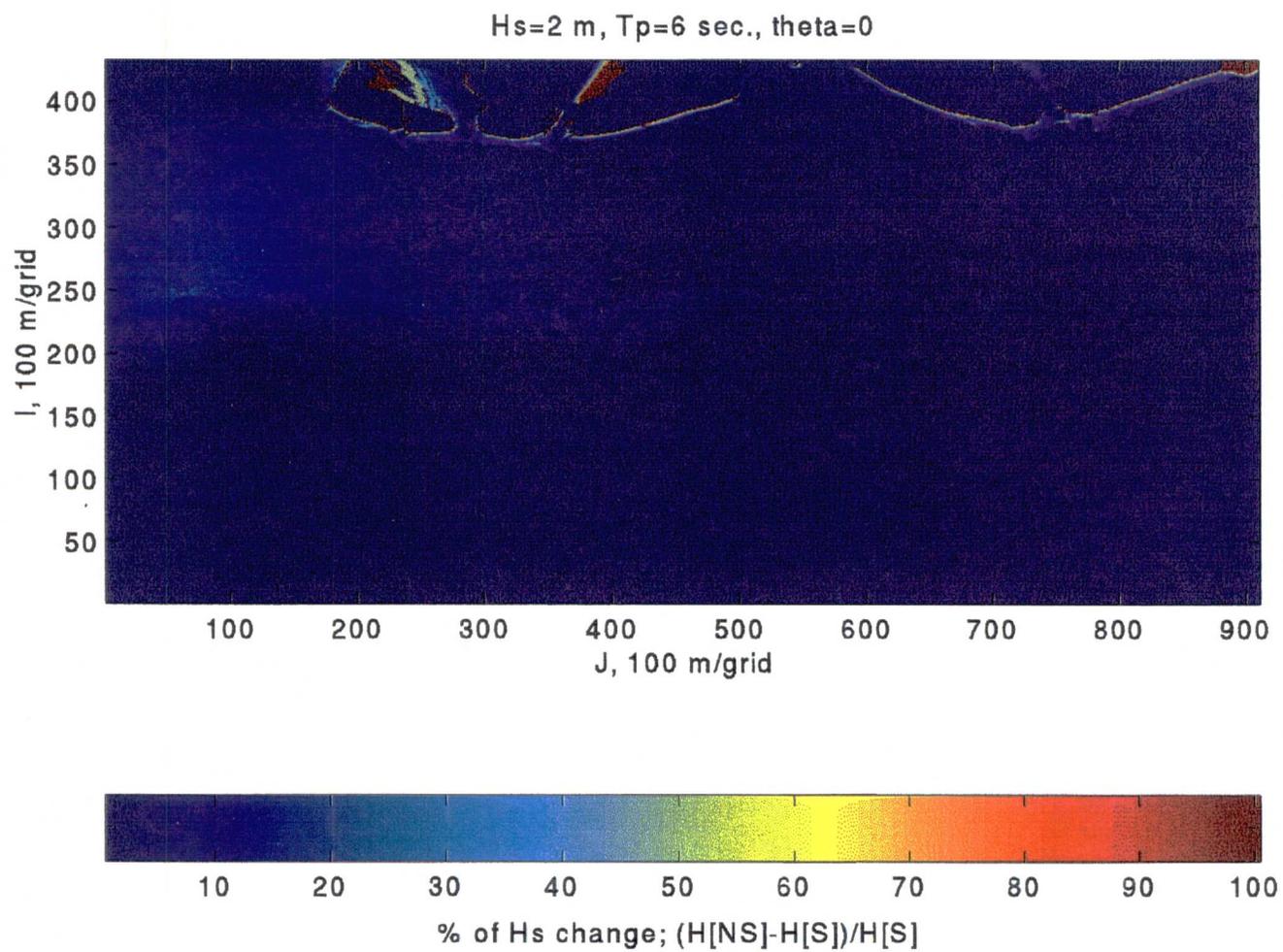
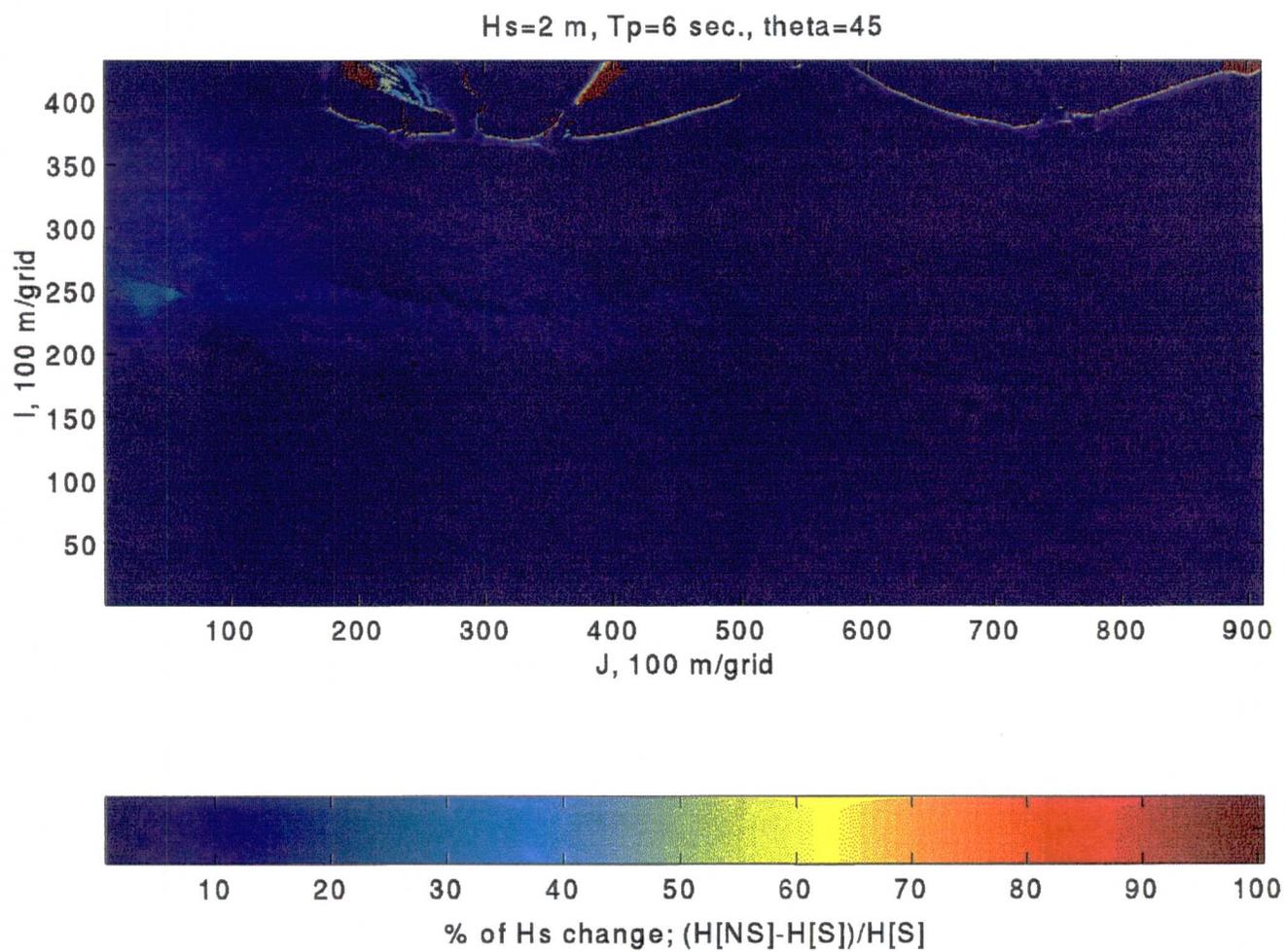Figure 29 Modeled percentage of H_s increase due to shoal removal. Case 3, $\theta = 0°$

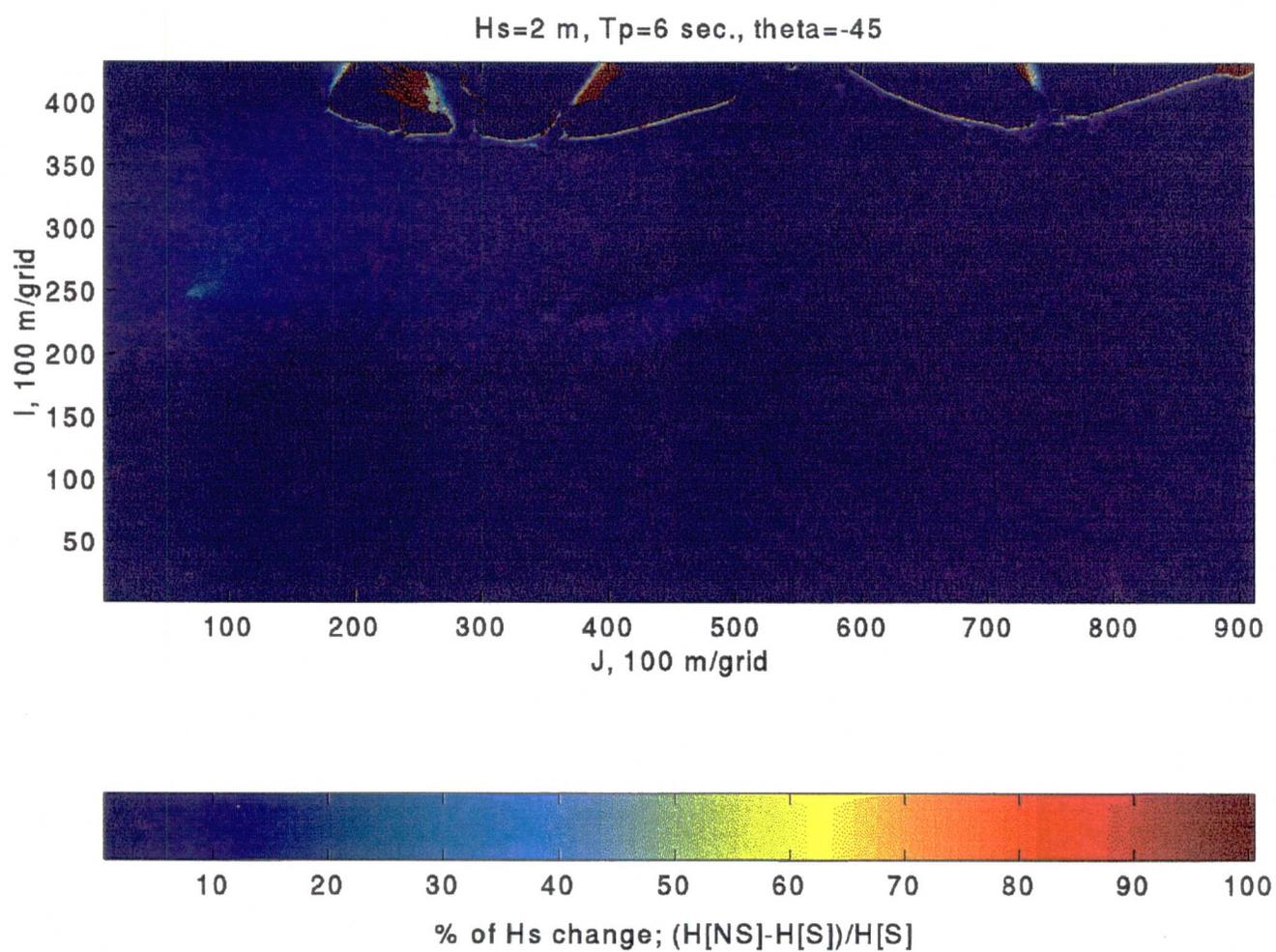Figure 30 Modeled percentage of H_s increase due to shoal removal. Case 3, $\theta = 45°$

Figure 31 Modeled percentage of H$_s$ increase due to shoal removal. Case 3, $\theta = -45°$

2. Waves propagating landward in Case 3 do not break over the western portion of the shoal, a condition not met in either Cases 1 or 2. Because of this, the significant wave height from the model run over the hypothetical bathymetry (shoal removed) is always slightly greater than the wave height derived from the model run over the present bathymetry. On the east flank of the shoal, wave breaking occurs in the nearshore (Whiskey Island, in this section), and the breaker zone is further inshore relative to the position of the breaker zone in Case 1 and Case 2. Consequently, the significant wave height from both runs (with and without Ship Shoal) attains the same value at the landward boundary. Thus, the data suggest that the removal of Ship Shoal does not affect the nearshore significant wave height. Notable impacts on the entire significant wave height distribution across the inner shelf landward of the shoal are negligible (Appendix B-11).

Wave refraction diagrams for bathymetric configuration including and excluding Ship Shoal are shown in Appendix B-13 through B-18 for three incident directions. Refraction effects are noticeable over the western flank of the shoal during oblique wave approaches. However, as expected, the signal is significantly weaker than observed in previous cases.

Case 4 (H_s=1 m, T_p=5 sec.)

Case 4 represents fair weather wave conditions. As in the previous cases, incident waves from three directions are propagated over the same bathymetry in the numerical simulations and the data are presented in Appendix C. The percentage change in significant wave heights due to shoal removal are presented in the main body of the text in Figures 32, 33 and 34. The following conclusions are presented:

(1) The longshore gradients of nearshore significant wave height (H_s increasing from west to east) are negligible on comparison with previous scenarios. This can be explained as follows; for the shortest and smallest wave, the relative water depth, h/L, is also the highest (among the 4 cases discussed in this report) everywhere in the study area except the surfzone. Thus, the significant wave heights become insensitive to the differential water depth in the west-east orientation.

(2) In the area where the significant wave height increased dramatically due to the removal of Ship Shoal in both Case 1 and Case 2, the magnitudes of wave height increase due to shoal removal also becomes negligible for all three wave approaches in Case 4 (Figures 32, 33 and 34), representing incident wave directions of 0°, 45°, -45° respectively). For example, the maximum values in Figures 32, 33 and 34) are all smaller than 10%, comparing the highest values of 80% in Figure 18c and 40% in Figure 26. The wave height increase is also restricted to the shoal area, especially at the west-most part of Ship Shoal where the water depth is the shallowest.

(3) As noted in previous Case 3, directionality has a minimal effect on the wave climate.

The cross-shore sections at the same two locations are plotted in Appendix C-7 through C-12) to display the sectional profiles of the present (with Ship Shoal) and hypothetical (without Ship
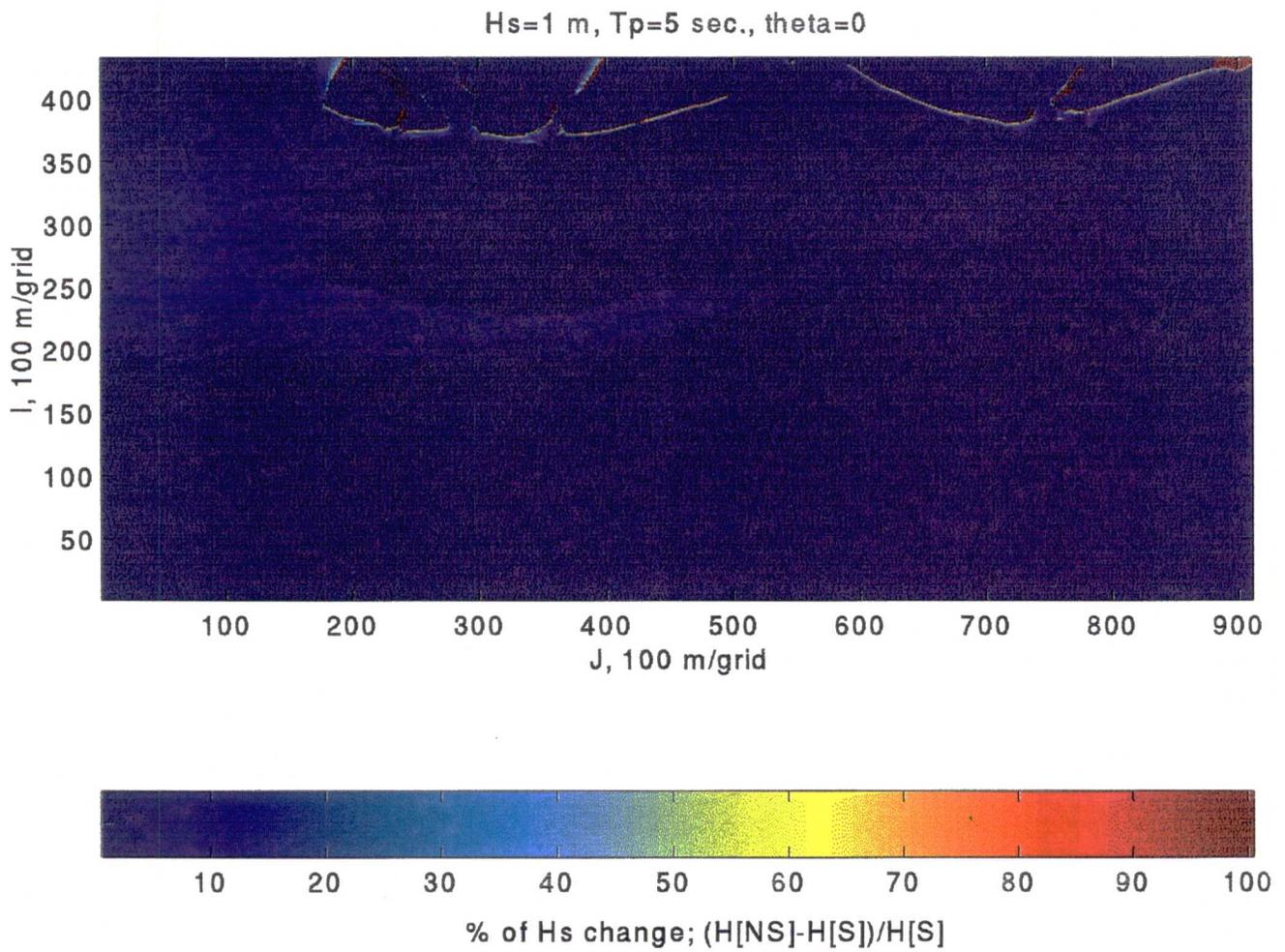
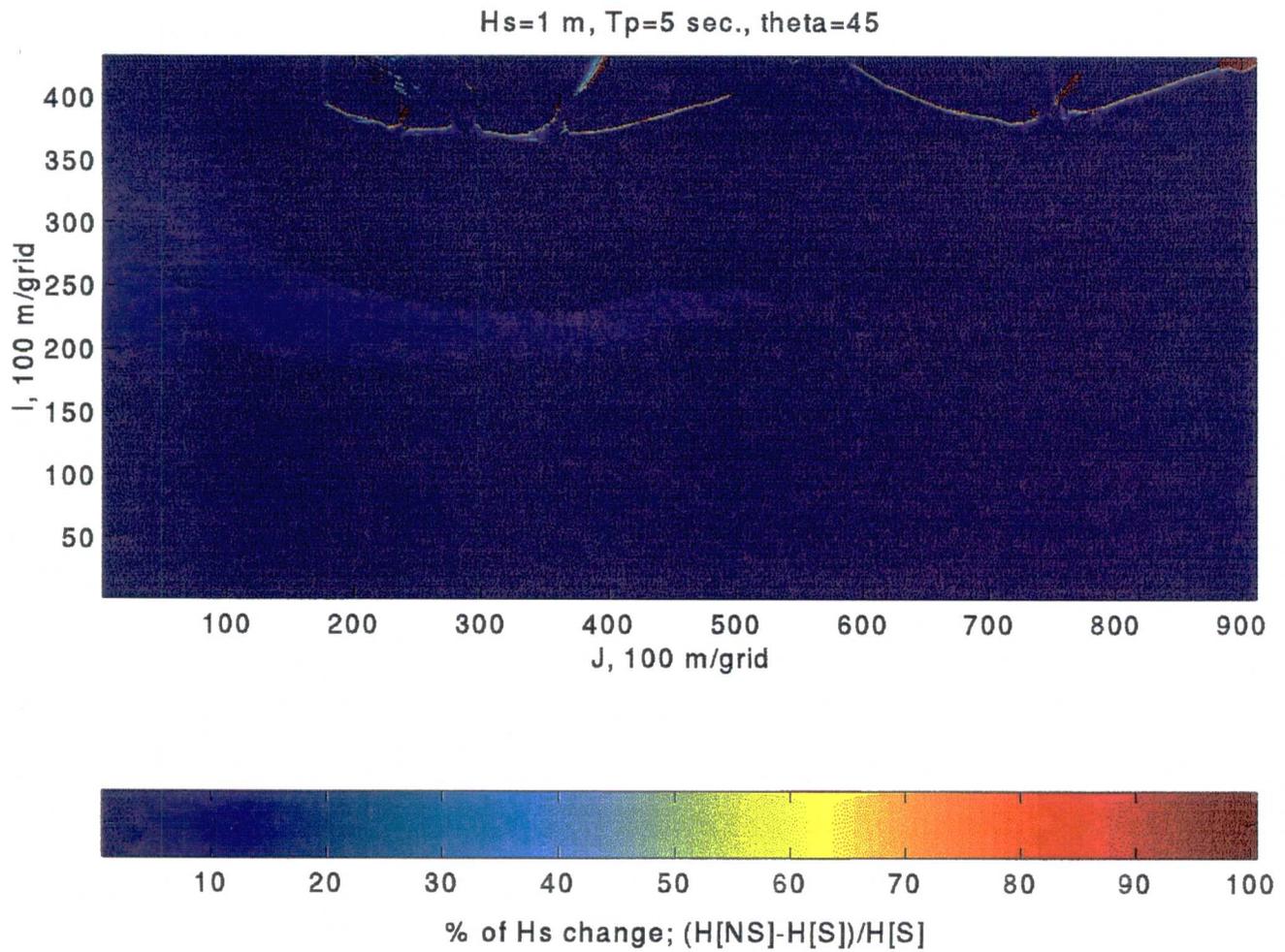Figure 32 Modeled percentage of H_s increase due to shoal removal. Case 4, $\theta = 0°$

Hs=1 m, Tp=5 sec., theta=45

% of Hs change; (H[NS]-H[S])/H[S]

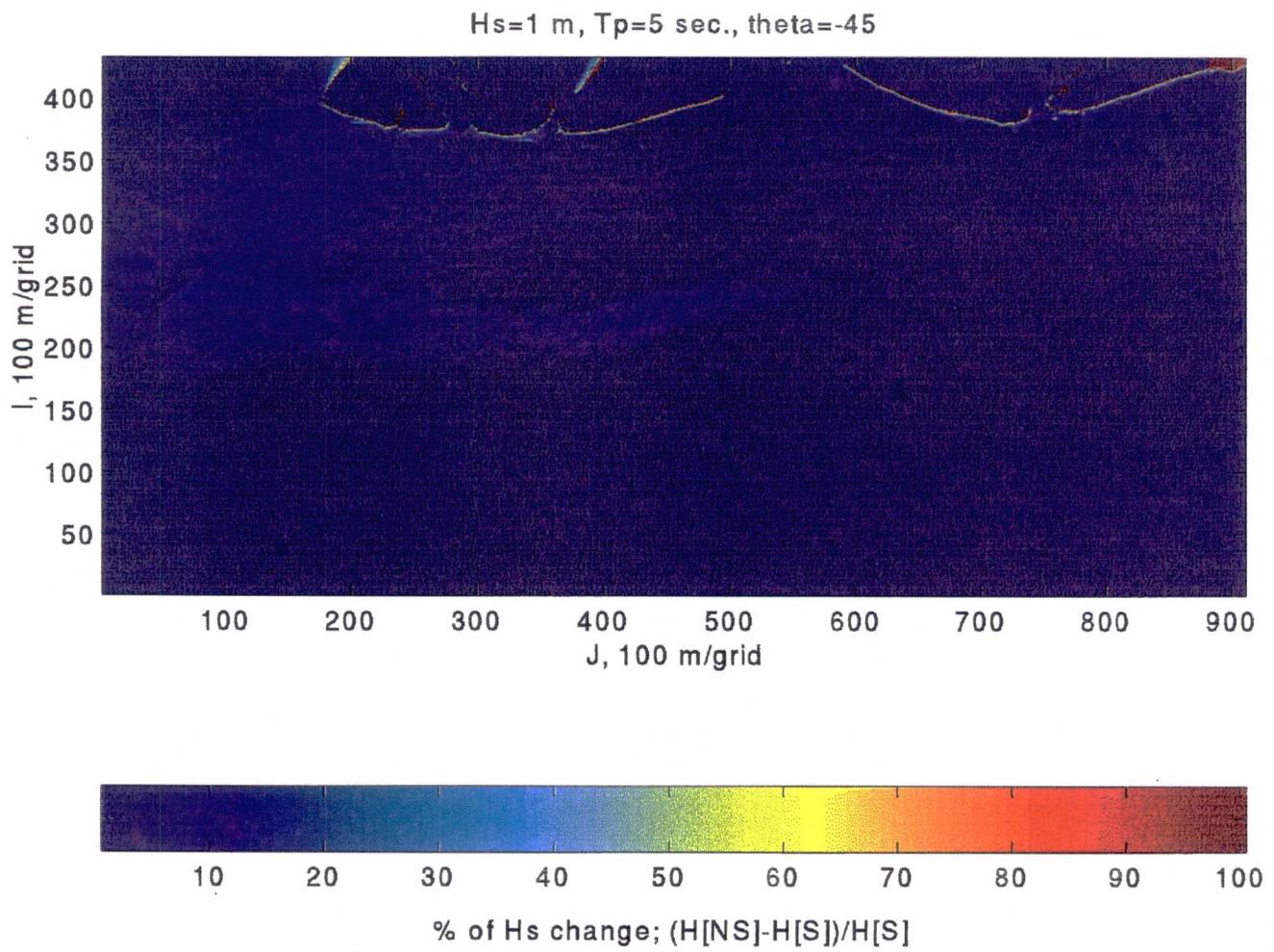Figure 33 Modeled percentage of H$_s$ increase due to shoal removal. Case 4, $\theta = 45°$

Figure 34 Modeled percentage of H_s increase due to shoal removal. Case 4, $\theta = -45°$

Shoal) bathymetric configurations; the significant wave heights generated from running the model over the two bathymetric configurations; the increase of the significant wave height due to the removal of Ship Shoal and the depth-limited wave breaking index. Comparing with the corresponding plots in the three previous cases, it is apparent that the magnitude of the wave height increase becomes much smaller, although the spatial variation and directionality of this wave height increase are similar to those in the previous cases. The difference in water depths between the section J=150 and section J=400 causes the differential magnitudes of significant wave height increase and wave breaking index, although these differences are almost negligible. In cross-shore section J=150, waves do not reach the breaking stage. Consequently, the significant wave height from the model run over the hypothetical bathymetry remains slightly greater than the wave height derived from the model run over the present bathymetry. However, in section J=400 (Appendix C-7 through C-9) wave breaking occurs at the landward boundary (Whiskey Island, in this section), and the breaker zone is further inshore relative to its position in previous cases. The removal of the shoal does not have an impact on the nearshore significant wave height.

Wave refraction diagrams are presented in Appendix C-13 through C-18 for both bathymetries and respective wave approaches. Refraction over the shoal complex is minimal.

Effects of Wind Forcing

Towards the end of this project, the National Data Buoy Center released wind data for station 42001 that could for the first time, be used in conjunction with the deep water wave climate to test the importance of including the wind forcing function on wave climate. In this section we present the model output for the same four cases discussed above with the wind forcing term included.

In Appendix D-1 through D-8 the effect of including the wind function on wave height is demonstrated along sectional profiles J=150 and 400 for the deep water wave boundary conditions used in the previous discussion. As discussed earlier, it is more appropriate to use the event-specific rather than the average parameters in modelling the cases presented in this study. The time series of wind speed was examined with respect to the events that were selected from the time series of wave height to represent the 4 cases. The selected values of wind speed are listed in Table 4.

The two cross-shore sectional profiles of the modeled significant wave height for each of the listed 4 cases are plotted in Appendix D for a southeast wave approach. The topmost panel in each figure shows the present and hypothetical bathymetric profiles. The second panel shows the comparison of the wave height profiles over the present bathymetry with and without the wind forcing term. The third panel shows the comparison of the wave height profiles over the hypothetical bathymetry (Ship Shoal removed) with and without the wind forcing term. In the bottom panel, the two wave height profiles generated with and without the wind forcing term are plotted for both bathymetries.

Table 4. Wind speeds and directions used to test the wind forcing term

Case	H_s(m)	T_p(s)	Wind Speed (ms^{-1})	Wind Direction θ(deg.)[1]
1	6	11	20	-45,00,45
2	4	9	15	-45,00,45
3	2	6	10	-45,00,45
4	1	5	5	-45,00,45

[1] -45 = SOUTHWEST APPROACH
   45 = SOUTHEAST APPROACH
   00 = SOUTH APPROACH

In Case 1, the 20 m/s wind blowing in the direction of wave propagation maintains a 0.5 m higher significant wave height seaward of the west portion of Ship Shoal (section J=150). Waves are reduced to slightly higher than 2 m over the shoal, a value which is equal on comparing it with and without the wind forcing function. Over the hypothetical bathymetry inclusion of the wind forcing function results in a gradual increase in wave height difference due to increasing fetch. The maximum value of the increase is < 1 m. Thus the wind-present wave height at this location increases by as much as 2 m, a 90% increase, after Ship Shoal is removed compared to the 40% shown in the wind-free simulation. The nearshore breaking wave height is more than 0.5 m higher, and the nearshore breaker zone is 0.5 - 1.0 Km further offshore when the wind function is included. Over the eastern part of the shoal where the water depth is greater, the magnitude of wave height increase due to the wind forcing is relatively higher. The significant wave height is increased by as much as 1 m seaward of Ship Shoal. The locations of nearshore wave breaking either before or after Ship Shoal removal are less than 0.5 Km further offshore because of the increase of the breaking wave height. As in the wind-free simulations, the effect of Ship Shoal removal on the wave height is limited to the leeward periphery of the shoal itself. In the nearshore, shoal removal does not increase the wave height with or without the wind forcing function. Additionally, the differential water depths over the shoal show similar impacts on the wave height distribution with the wave height increase due to Ship Shoal removal being significantly smaller along the eastern part of the shoal than along the west.

In all three of the remaining cases, the properties and patterns of the wave height increase due to the addition of the wind forcing term in the numerical model are similar to what have been described above, although the magnitudes of these changes are different from case to case. In Case 2, the magnitude of the significant wave height increase due to the addition of a 15 m/s wind is also approximately 0.5 m seaward of the west part of Ship Shoal prior to breaking. Unlike in Case 1, however, the significant wave height after breaking does not collapse to the same value as in the wind-free simulation. Over the hypothetical bathymetry this magnitude continually

increases shoreward until the waves reach the breaking condition. Removal of Ship Shoal will result in a 50% increase of the significant wave height. This is much larger than the magnitude (between 25% to 30%) where wind forcing was neglected. The magnitude of wave height increase due to the wind forcing over the east part of the shoal is as much as 0.8 m. Cases 3 and 4 represent a weak storm and a fair weather condition respectively. Although wave breaking does not occur when the waves approach Ship Shoal, higher energy dissipation in this area results in a larger degree of significant wave height change due to the removal of Ship Shoal. The 10 m/s wind in Case 3 causes more than 0.5 m of significant wave height increase, and the 5 m/s wind in Case 4 causes a 0.2 m increase.

The distribution of the percent change in significant wave heights due to shoal removal for each deep water wave boundary condition, and associated wind speed, is plotted for the three wave approach directions in Appendix D-9 through D-20. As expected, while the inclusion of the wind forcing function allows for an increase in the wave height, the effects attributable to the removal of Ship Shoal are limited to the periphery of the leeward flank of the system, particularly along its western boundary. Changes in the wave approach direction redistributes the increase in wave height in the lee of the shoal complex. This does not, however, impact breaker wave heights in the nearshore along the Isles Dernieres.

Hurricane Andrew Simulation

Wave Height and Attenuation
Wave heights decreased from approximately 11 m in 150-200 m of water, to 2 m in 15-20 m of water off the Isles Dernieres (Figure 35). The rate of attenuation decreased significantly across Ship Shoal, where the majority of long waves underwent total energy dissipation rather than breaking. Shoreward propagation of waves across Ship Shoal was limited. West of Main Pass, 12 and 13 m waves began attenuating in depths of around 200 m, and experienced a generally higher attenuation rate than those simulated off the Isles Dernieres. The higher energy portion of the attenuated wave spectrum was shifted closer to the coast around the eastern terminus of Timbalier Island and further east (Figure 35). The variability in this distance is a direct function of continental shelf slope and not deep water wave boundary conditions. As discussed below, differential attenuation across the shelf had a significant impact on wave energy conditions along the adjacent coast.

Maximum Near-Bottom Orbital Velocity
Calculated maximum near-bottom orbital velocities became weakly-developed in water depths of around 200 m, and approached 20 cm sec^{-1} in approximately 150 m of water (Figure 36). Since sediment comprising this portion of the shelf is generally fine-grained clay transported from the Mississippi Delta proper (*cf* Treadwell, 1955; Shepard, 1956; Coleman, 1982), it is unlikely that sediment resuspension due to surface gravity waves occurred at this depth. However, based on the relationship between threshold velocities, quartz grains and longer period waves
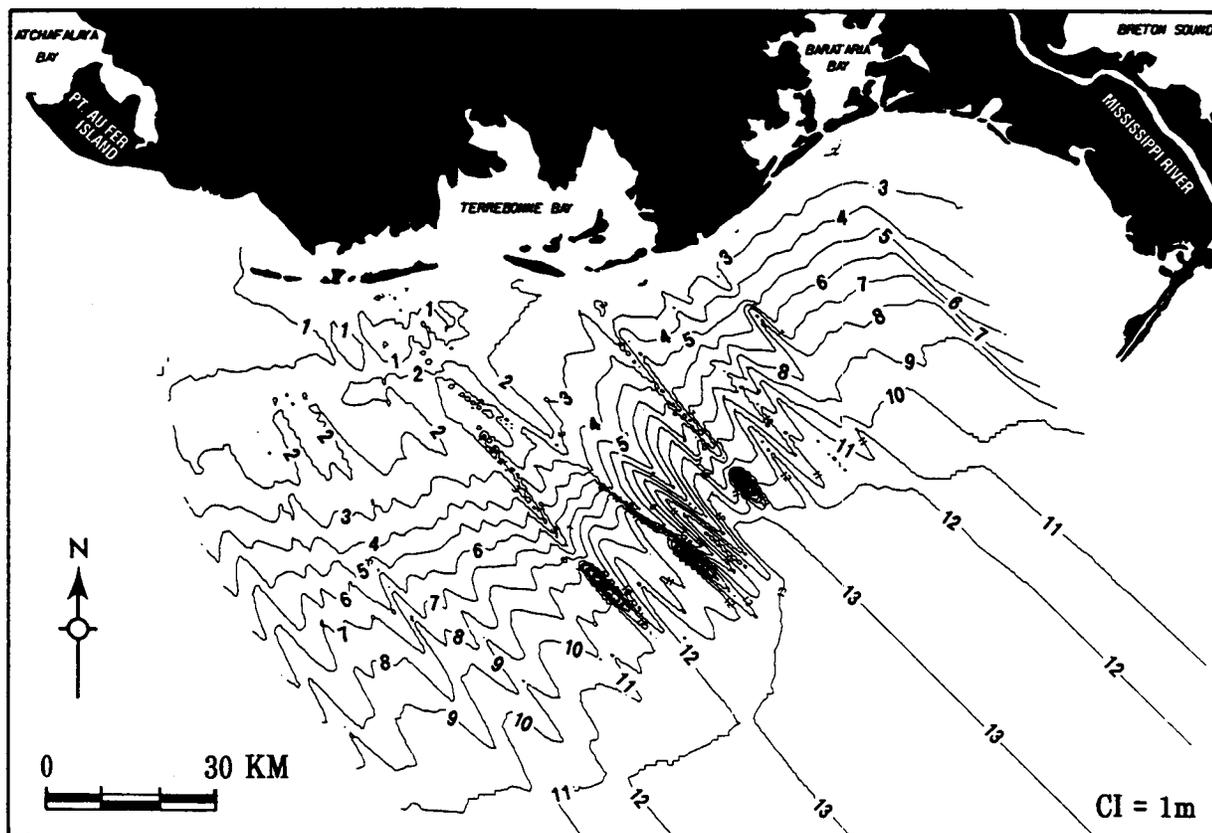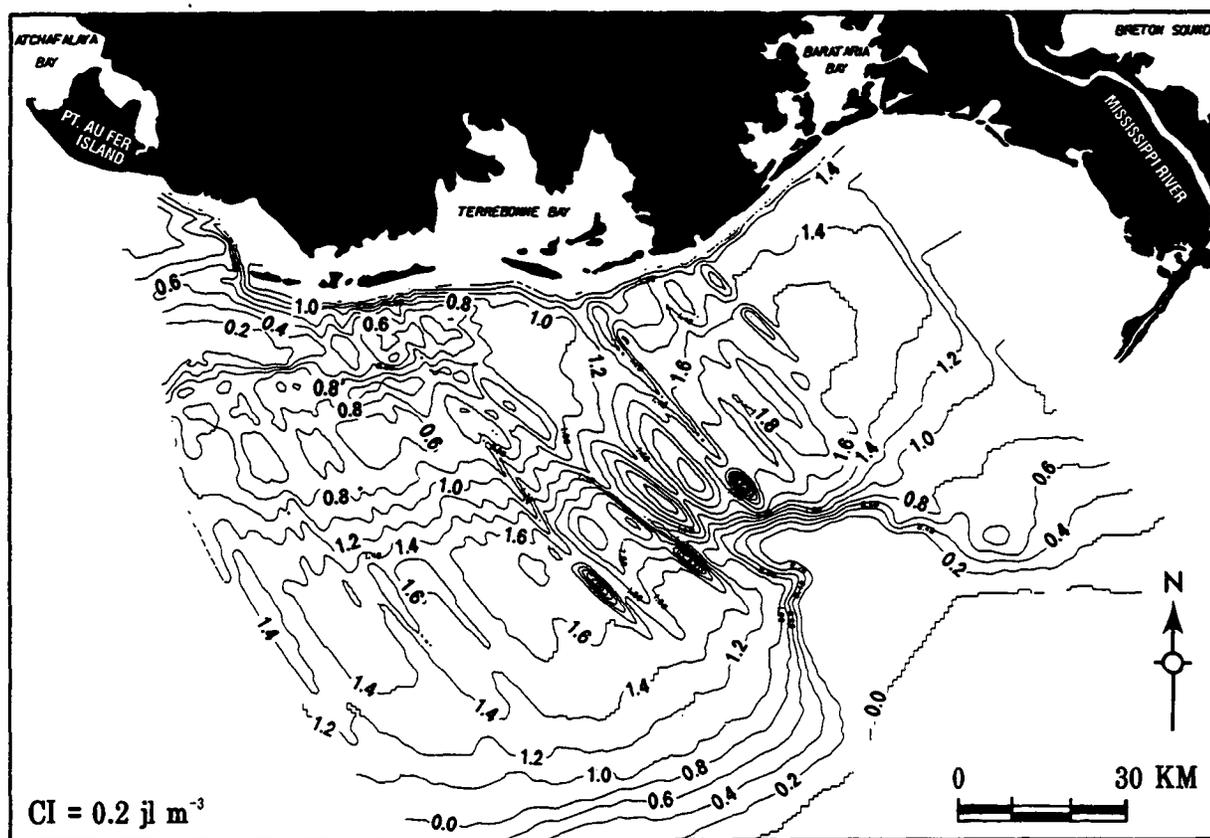
Figure 35 Contour plot of the simulated wave height across the Louisiana shelf during Hurricane Andrew. Contour intervals are 1 meter.
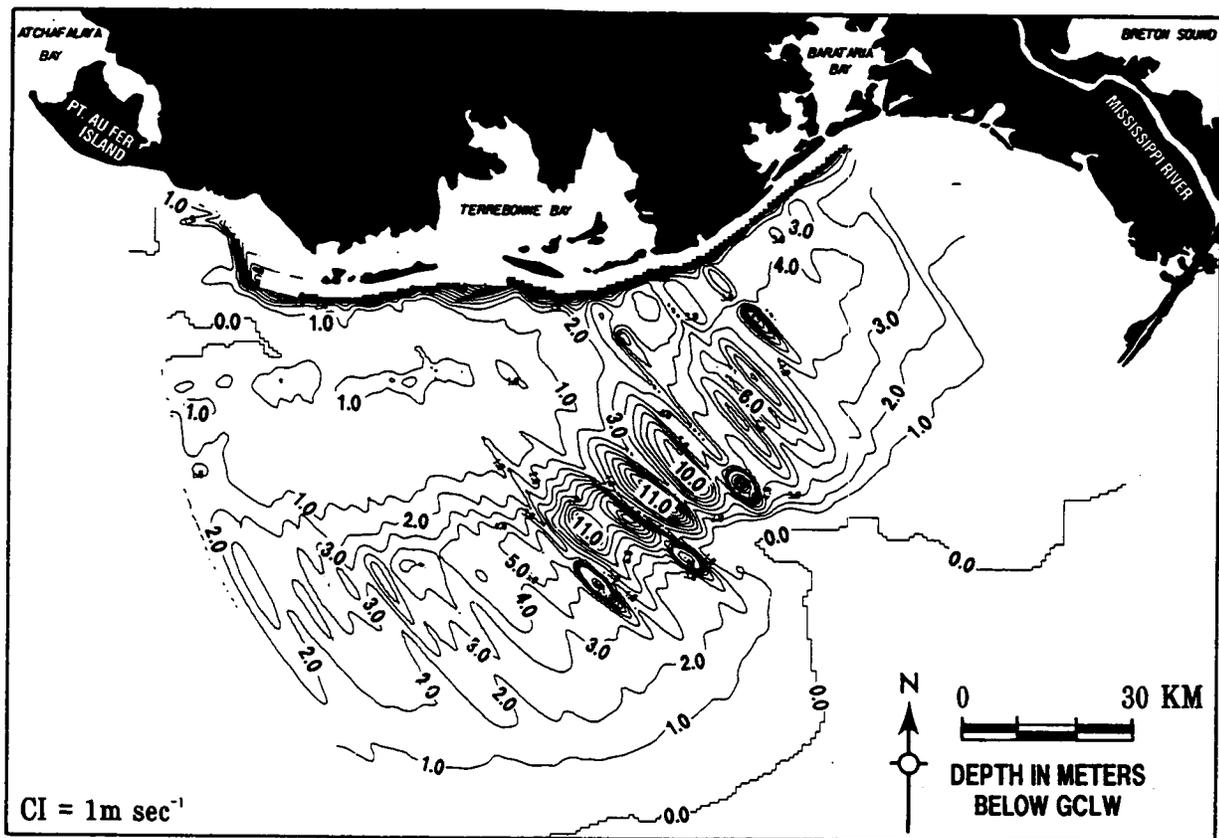
Figure 36 Contour plot of the simulated maximum near-bottom orbital velocities across the Louisiana shelf during Hurricane Andrew. Contour intervals are 1 m/s.

proposed by Komar and Miller (1975), it is apparent that velocities had achieved the critical threshold for entrainment of medium sand (20 cm sec^{-1}) at 150 m depths. Near-bottom orbital velocities increased significantly across the shelf due to a rapid decrease in water depth, and were typically 150-200 cm sec^{-1} in approximately 30 m of water. Two current meters deployed in 20.5 and 37 m depths south of Terrebonne Bay at LATEX moorings 14 and 16 (see DiMarco *et al*, 1995), recorded near bottom velocities in excess of 100 and 80 cm sec^{-1} respectively, prior to instrument failure or movement, during the peak of Hurricane Andrew. (It is perhaps worthy of note that the calculated orbital velocity in 30 m water depths would have exceeded the entrainment velocity for particles well within the gravel range.) Bottom velocities decreased gradually across the lower gradient inner shelf incorporating the Ship Shoal complex, due to a gradual decrease in depth and incident wave height. East of the Mississippi Canyon, bottom orbital velocities increased at a greater rate than on the west flank, due to a steeper shelf slope. On attaining a maximum of approximately 200 cm sec^{-1} in 40 m of water, bottom velocities decreased only slightly to approximately 140 cm sec^{-1} in shallow water.

Energy Dissipation Across the Continental Shelf

A two-dimensional distribution of wave energy dissipation across the shelf is shown in Figure 37. Since the energy dissipation gradient is a direct function of the effects of shoaling, refraction and friction on wave height, it is expected that the variable shelf slope would differentially impact the rate of wave energy dissipation across the Louisiana shelf during Hurricane Andrew.

Wave energy dissipation became apparent in water depths of approximately 150-200 m. The rate of wave energy decay (dE/dR) varied considerably across the shelf due to differential bottom slope-wave height effects. Given the significance of wave height in computing dE/dR, the distribution of both are plotted in Figure 38 for two locations across the shelf; west and east of the Mississippi Canyon, with the former extending across Ship Shoal. West of the Canyon, a larger proportion of the wave energy dissipation occurred approximately 100 km offshore reaching a peak near 5 jl m^{-3} in water depths between 25-30 m. Waves decreased in height to approximately 7 m and with additional shoreward propagation, continued to loose energy at a significantly slower rate. On moving across the Ship Shoal complex, the rate of energy decay increased from <0.5 jl m^{-3} to 2 jl m^{-3} before final peaking during breaking. East of the Canyon, the shorter, steeper nature of the shelf reduced it's ability to absorb wave energy during shoreward propagation. Consequently, although the decay gradient is similar to that west of the Canyon, the peak decay value of 3 jl m^{-3} was significantly less and located considerably closer to shore—approximately 20 km offshore in 25-30 m of water. Prior to breaking, the energy dissipation rate decreased only slightly, resulting in considerably higher wave energy conditions along this portion of the coast than further to the west.

A more detailed account of the wave field during Hurricane Andrew and morphological changes along the south-central Louisiana coast are presented in Stone *et al*. (1995).

Figure 37 Contour plot of the simulated wave energy dissipation rates across the Louisiana shelf during Hurricane Andrew. Contour intervals are 0.2 jl/m³.
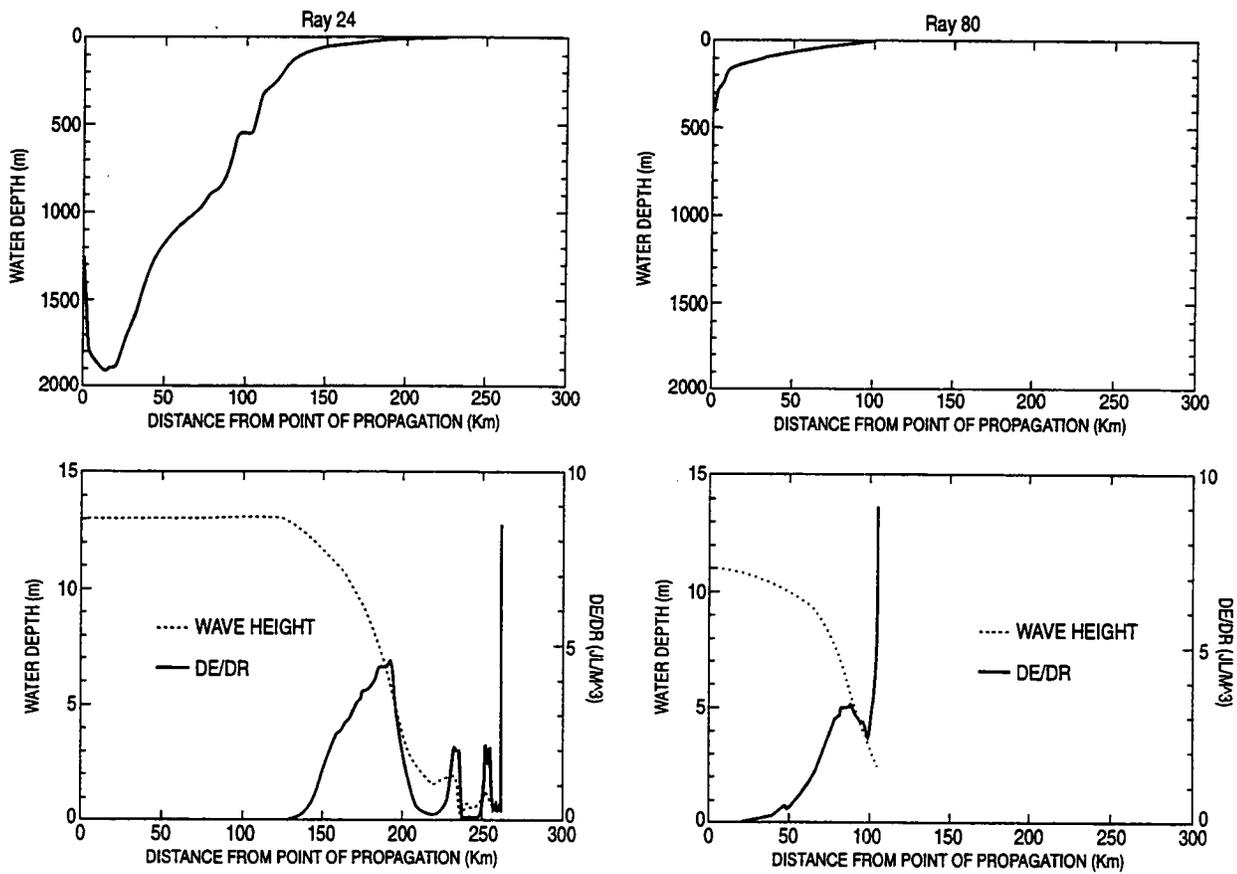
Figure 38 Wave height - energy relationships from two wave rays west (Ray 24) and east (Ray 80) of the Mississippi Canyon. The respective bathymetric profiles are also shown for comparison.

6 Conclusions

The following main conclusions can be made from the research conducted on the significance of Ship Shoal regarding wave climate off the Isles Dernieres.

(1) The removal of Ship Shoal will alter the wave propagation, dissipation and the wave energy distribution. The magnitude and the spatial distribution of the alteration depend on the initial wave conditions.

(2). During severe storms (Case 1) and strong storms (Case 2), the propagating waves reach breaking conditions seaward of the western flank of Ship Shoal. Therefore, removal of Ship Shoal causes a maximum increase of the significant wave height by 90% - 100% (*i.e.*, almost double the present value) in Case 1, and 40% -50% in Case 2, over the shoal and immediately adjacent to the lee of the complex. Wave breaking does not occur on the east flank of the shoal because of much deep water, and the magnitude of the wave height increase due to shoal removal is significantly less on comparison with that on the west flank.

(3) During the weak storms (Case 3) and fair weather conditions (Case 4), waves do not reach breaking conditions over any part of Ship Shoal. The magnitudes of the significant wave height increase due to the removal of the shoal is considerably smaller, only 10% - 20% on the west part of the shoal. The values of wave height change on the east part of the shoal are minimal.

(4) The nearshore wave fields are largely dependent on the offshore wave conditions. Under the high energy conditions in Case 1 and Case 2, removal of Ship Shoal results in higher nearshore breaking wave heights, however, the breaker zone is displaced between 0.5 - 1.0 Km offshore. Ultimately, waves in the surfzone eventually collapse to the same energy level on comparing with and without shoal scenarios, suggesting that shoal removal will not have a significant impact on wave energy conditions along the Isles Dernieres. The nearshore impact is even less noticeable under the weaker energy conditions in Case 3 and Case 4, particularly along the east of the study area.

(5) Wave approach direction exerts significant control on the wave climate leeward of Ship Shoal for stronger storm conditions (Cases 1 and 2) but not weak storms or fairweather waves.

(6) Inclusion of the wind function increases wave height in all simulations. The magnitude of the increase is dependent on the deep water wave height and the slope of the shoreface profile. In Case 1, the surfzone is widened by almost 1.0 Km whereas in Case 4, the change is minimal. Removal of Ship Shoal results in a 50% increase of the significant wave height. This is much larger than the magnitude (between 25% to 30%) when wind forcing is neglected. The magnitude

of wave height increase due to the wind forcing over the east part of the shoal is as much as 0.8 m.

(7) While the inclusion of the wind forcing function allows for an increase in the wave height, the effects attributable to the removal of Ship Shoal are limited to the periphery of the leeward flank of the system, particularly along its western boundary.

(8) Changes in the wave approach direction redistributes the increase in wave height in the lee of the shoal complex. This does not, however, impact breaker wave heights in the nearshore along the Isles Dernieres.

(9) Simulation of long wave propagation landward during Hurricane Andrew indicates near total wave energy dissipation, as opposed to breaking, over Ship Shoal. A much smaller percentage of low amplitude waves crossed the shoal complex. Peak wave energy dissipation rates occurred, however, seaward of Ship Shoal in approximately 25 - 30 m water depths.

(10) The data presented in this report suggest that the entire removal of Ship Shoal will not significantly influence the wave climate beyond the leeward periphery of the complex, such as the nearshore zone along the Isles Dernieres. The data suggest that this conclusion is valid for winter storm conditions and hurricanes similar to that of Hurricane Andrew.

(11) Conclusion (10) implies that given the unlikely situation that the entire volume mass of sediment be removed from Ship Shoal during a single dredging event, wave climate changes peripheral to the shoal will be substantially reduced given the removal of significantly lower volumes of sediment than that simulated here.

REFERENCES

Abel, C.E., Tracy, B.A., Vincent, C.L. and Jensen, R.E., 1989. Hurricane Hindcast Methodology and Wave Statistics for Atlantic and Gulf Hurricanes from 1956-1975. USAE Waterways Experiment Station, Vicksburg, MS, WIS Report 19, 33 p.

Atlas, D., Chou, S.H., and Byerly, W.P., 1983. The Influence of Coastal Shape on Winter mesoscale Air-Sea Interactions. Monthly Weather Review, 111, 245-252.

Berkhoff, J. C. W., 1972. Computation of combined refraction-diffraction. Proceedings of the 13th International Conference on Coastal Engineering, American Society of Civil Engineers, 1, 471-490.

Berkhoff, J. C. W., 1976. Mathematical models for simple harmonic linear water waves, wave diffraction and refraction. Publication No. 1963, Delft Hydraulics Laboratory, Delft, The Netherlands.

Berkhoff, J. C. W., N. Booij and A. C. Radder, 1982. Verification of numerical wave propagation models for simple harmonic linear waves. Coastal Engineering, 6, 255-279.

Botelho, D.L.R., Ullmann, R.R., Chancellor, D.P., and Versowsky, P.E., 1994. A Survey of the Structural Damage Caused by Hurricane Andrew on Some of the Platforms Located in the South Timbalier Area. Proc. 26 th. Annual Offshore Technology Conference, Houston, TX., p. 9-18.

Britsch, L. D. and J. B. Dunbar, 1993. Land loss rates: Louisiana coastal plain. Journal of Coastal Research, 9, 324-338.

Byrnes, M.R. and Groat, C., (eds.), 1991. Characterization of the Development Potential of Ship Shoal Sand for beach Replenishment of the Isles Dernieres. Final Report to the U.S. Minerals Management Service, 164 p.

Cardone, V.J. and Cox, A.T., 1992. Hindcast Study of Hurricane Andrew (1992) Offshore Gulf of Mexico. Ocean Weather Inc., Cos Cob, CT., 40 pp.

Cialone, M. A., D. J. Mark, L. W. Chou, D. A. Leenknecht, J. E. Davis, L. S. Lillycrop and R. E. Jensen, 1992. Coastal Modeling System (CMS) user's manual. Instruction Report CERC-91-1, WES, Corps of Engineers, Vicksburg, MS.

Coleman, J.M., 1982. Deltas: Processes of deposition and Models for Exploration. IHRDC Publishers, Boston, MA., 124 pp.

DiMarco, S.F., Kelly, F.J., Jun Zhang, and N.L. Guinasso, 1995. Directional Wave Spectra on the Louisiana-Texas Shelf During Hurricane Andrew. Journal of Coastal Research, Special Issure 21, 217-233.

Faiers, G.E., Grymess, III, J.M., Keim, B.D. and Muller, R.A., 1994. A re-examination of Extreme 24-hour Rainfall in Louisiana, USA. Climate Research, vol. 4, pp. 25-31.

Frazier, D.E., 1967. Recent Deposits of the Mississippi River, their Development and Chronology. *Gulf Coast Assoc. Geol. Socs. trans.,* 17, p. 287-311.

Grymes, J. W. and G. W. Stone, 1995. A review of key meteorological and hydrological aspects of Hurricane Andrew. Journal of Coastal Research, Special Issure 21, 6-23.

Halford, K.J., 1995. Estimating the Dynamic Water-Level Surfaces Associated with Hurricane Andrew Crossing the Louisiana Coast. Journal of Coastal Research, Special Issue 21, p. 265-279.

Hedges, J. R., 1976. An empirical modification to linear wave theory. Proc. Inst. Civil Eng., 61, 575-579.

Henderson, K.G. and Robinson, P.J., 1994. Relationships Between the Pacific North teleconnection Patterns and Precipitation Events in the South-Eastern USA. International Journal of Climatology, 14, p. 307-323.

Hsu, S.A., 1991. Forecasting Hurricane Waves. *Mariners Weather Log,* 35, 2, p. 57-58.

Hsu, S.A., 1994. Estimating Hurricane Waves. *Mariners Weather Log,* 38, 1, p. 68.

Holthuijsen, L.H., Booij, N. and Hebers, T.H.C., 1989. A Prediction Model for Stationary, Short-Crested waves in Shallow Waterwith Ambient Currents. Coastal Engineering, 13, p. 23-54.

Hubertz, J. M. and R. M. Brooks, 1989. Gulf of Mexico hindcast wave information. WIS report 18. US Army Corps of Engineer, Waterways Experiment Station, Vicksburg, MS.

Kahn, J.H., 1980. The Role of Hurricanes in the Long term degradation of a Barrier Island Chain: Chandeleur Islands, Louisiana. MS Thesis, Louisiana State University, Dept. of Marine Science.

Kirby, J. T. and R. A. Dalrymple, 1993. Combined refraction/diffraction model REF/DIF 1, User's manual, Report No. CACR-92-04, University of Delaware, 68 pp.

Kirby, J. T. and H. T. Ozkan, 1994. Combined refraction/diffraction model for spectral wave conditions, REF/DIF S version 1.1, University of Delaware, 128 pp.

Komar, P.D. and Miller, M.C., 1975. On the Comparison Between Threshold of Sediment Movement Under Waves and Unidirectional Currents with a Discussion of the Practical Evaluation of Threshold. *J. Sed. Pet.*, 45, 1, 362-368.

Kraus, N. C., L. T. Gorman and J. Pope, 1994. Kings Bay coastal and estuarine physical monitoring and evaluation program: coastal studies. US Army Corps of Engineer, Waterways Experiment Station, Vicksburg, MS.

Lewis, J.K. and Hsu, S.A., 1992. Mesoscale Air-Sea Interactions Related to Tropical and Extratropical Storms in the Gulf of Mexico. Journal of geophysical research (Oceans), 97, C2, p. 2215-2228.

List, J.H. and Hansen, M.E, 1992. The Value of Barrier Islands: 1. Mitigation of Locally-generated Wind-Wave Attack on the Mainland. USGS Open File Report 92-7222, 18 pp.

List, J., B. E. Jaffe, A. J. Sallenger, Jr., S. J. Williams, R. A. McBride and S. Penland, 1994. Louisiana barrier island erosion study: Atlas of seafloor changes from 1878 to 1989. USGS Miscellaneous Investigations Series I-2150-B, 82pp.

Long, R.B., 1979. Forecasting Hurricane Waves. *Mariners Weather Log*, 23, 1.

Marmer, H.A., 1954. Tides and Sea-Level in the Gulf of Mexico. Fishery Bulletin of the Fish and Wildlife Service, 89, p. 101-118.

May, J.P., 1973. Sedimentary and geomorphic response to Systematic variations of wave Energy in the Nearshore Zone. Ph.D. dissertation (unpub.), Department of Geology, Florida State University, Tallahassee, FL 32503, 209 pp.

Mossa, J., 1988. Analysis of the Environmental Effects of Sand resource Utilization on the Louisiana Continental Shelf. Open-File Series No. 88-01. Louisiana Geological Survey, Baton Rouge, LA.

Muller, R.A. and Fielding, B.V., 1987. Coastal Climate of Louisiana. *In*: Turner, R.E. and D.R. Cahoon, eds. Causes of Wetland Loss in the Central Gulf of Mexico. US Mineral Management Service, OCS, MMS 87-0119, pp. 13-29.

Murty, T.W., McBean, G.A. and McKee, B., 1983. Explosive Cyclogenesis over the Northeast Pacific Ocean. Monthly Weather Review, 111, p. 1121-1135.

McBride, R. A., S. Penland, M. Hiland, S. J. Williams, K. A. Westphal, B. Jaffe and A. H. Sallenger Jr., 1992. Analysis of barrier shoreline change in Louisiana from 1853 to 1989. In: Williams, S. J. et al. (eds.), Atlas of Barrier Island Changes in Louisiana from 1853 to 1989. USGS Miscellaneous Investigations Series I-2150-A, 36-97.

Morgan, J.P., Nichols, L.G. and Wright, M., 1958. Morphological Effects of Hurricane Audrey on the Louisiana Coast. Coastal Studies Institute, Louisiana State University, baton Rouge, LA 70803, 58-3, 53 pp.

Neumann, C.J., Cry, G.W., Caso, E.L. and Jarvinen, B.R., 1992. Tropical Cyclones of the North Atlantic Ocean, 1871-1986. US Department of commerce, NOAA, Asheville, NC p. 186.

Nummedal, D., 1982. Hurricane landfalls along the N.W. Gulf coast, in Nummedal, D., ed. Sedimentary processes and environments along the Louisiana-Texas coast. Field trip guidebook for the 1982 Ann. Meeting of the Geological Soc. America, New Orleans, LA, October, 1982, p. 63-78.

O'Reilly, W.C. and Guza, R.T., 1993. A Comparison of Spectral Models in the Southern California Bight. Coastal Engineering, 17.
O'Reilly, W.C., 1993. The Southern California Wave Climate: Effects of Islands and bathymetry. Shore and Beach, 61, 3, p. 14-19.

Penland, S.P., Suter, J.R., and Boyd, R., 1985. Barrier Island Areas Along Abandoned Mississippi River Deltas. Marine Geol., 63, 197-233.

Penland, S., Suter, J.R. and Moslow, T.F., 1996. Inner-Shelf Shoal Sedimentary Facies and Sequences: Ship Shoal, Northern Gulf of Mexico. In: T.F. Moslow and E.G. Rhodes (eds.), Modern and Ancient Shelf Clastics: A Core Workshop. SEPM Core Workshop No. 9, p. 73-123.

Penland, S. and J. R. Suter, 1988. Barrier island erosion and protection in Louisiana: A coastal geomorphological perspective. Transactions of the Gulf Coast Association of Geological Societies, 38, 331-342.

Rogers, J.C. and Rohli, R.V., 1991. Florida Citrus Freezes and Polar Anticyclones in the Great Plains, Journal of Climate, 4, 11, p. 1103-1113.

Rohli, R.V. and Rogers, J.C., 1993. Atmospheric Teleconnections and Citrus Freezes in the Southern United States, Physical geography, 14, 1, p. 1-15.

Royer, T.C. and Reid, R.O., 1966. Gravity Waves in a Rotating Basin-Normak Mides. Department of Oceanography, Texas A&M University, Project 471, ref. 66-27T, 85 pp.

Shepard, F.P., 1956. Marginal sediments of Mississippi delta. Bull. Amer. Assoc. Petroleum Geol., 40, 11, p. 2537-2623.

Stone, G.W., 1991. Differential Sediment Supply and the cellular nature of Longshore Sediment transport along Coastal Northwest Florida and Southeast Alabama since the Late Holocene. Ph.D.

dissertation (unpub.), Department of Geography, University of Maryland, College Park, MD. 20742, 376 pp.

Stone, G.W. and Penland, S., 1992. Historic Shoreline Change along the Northern Gulf of Mexico. *In*: S.K. Majumdar, G.S. Forbes, E.W. Miller and R.F. Schmalz (eds.), Natural and Technological Disasters: Causes, Effects and preventive Measures, The Pennsylvania Acadamey of Science.

Stone, G.W., Grymes, J.M., Robbins, K., Underwood, S.G., Steyer, G. and Muller, R.A., 1993. A Chronological Overview of Climatological and Hydrological Aspects Associated with Hurricane Andrew and its Morphological effects along the Louisiana Coast, U.S.A. *J Shore and Beach*, 61, 2, 2-13.

Stone, G. W., J. P. Xu and X. Zhang, 1995. Estimation of the wave field during Hurricane Andrew and morphological change along the Louisiana coast, Journal of Coastal Research, 18, 234-253.

Stone, G.W. and Finkl, C.W., (eds.), 1995. Impacts of Hurricane Andrew on the Coastal Zones of Florida and Louisiana: 22-26 August 1992. Journal of Coastal research, Special Issue 21, 364 pp.

Treadwell, R.C. 1955. Trafficability and Navigability of Delta-Type Coasts, Trafficability and Navigability of Louisiana Coastal marshes: Sedimentology and Ecology of Southeast Louisiana. Louisiana State University, Tech. Rept. 6, 78 pp.

van Heerden, I. Ll., Suhayda, J.N. and Kemp, G.P., 1993. The Importance and Role of Barrier Islands to Coastal Wetlands in Terrebonne Parish. Report Submitted to the Terrebonne Parish Consolidated Governmnet, Houma, LA.

Vincent, C. L. and M. J. Briggs, 1989. Refraction-diffraction of irregular waves over a mound. Journal of Waterway, Port, Coastal, and Ocean Engineering, 115, 269-284.

Williams, S. J., S. Penland and A. H. Sallenger Jr., 1992. Louisiana barrier island erosion study: Atlas of shoreline changes in Louisiana from 1853 to 1989. USGS Miscellaneous Investigations Series I-2150-A, 103 p.

Zetler, B.D. and Hansen, D.V., 1970. Tides in the Gulf of Mexico - A Review and Proposed Problem, Bulletin of Marine Science, 20, 1, p. 57-69.

APPENDIX A. Case 2: $H_s = 4$ m, $T_p = 9$ seconds
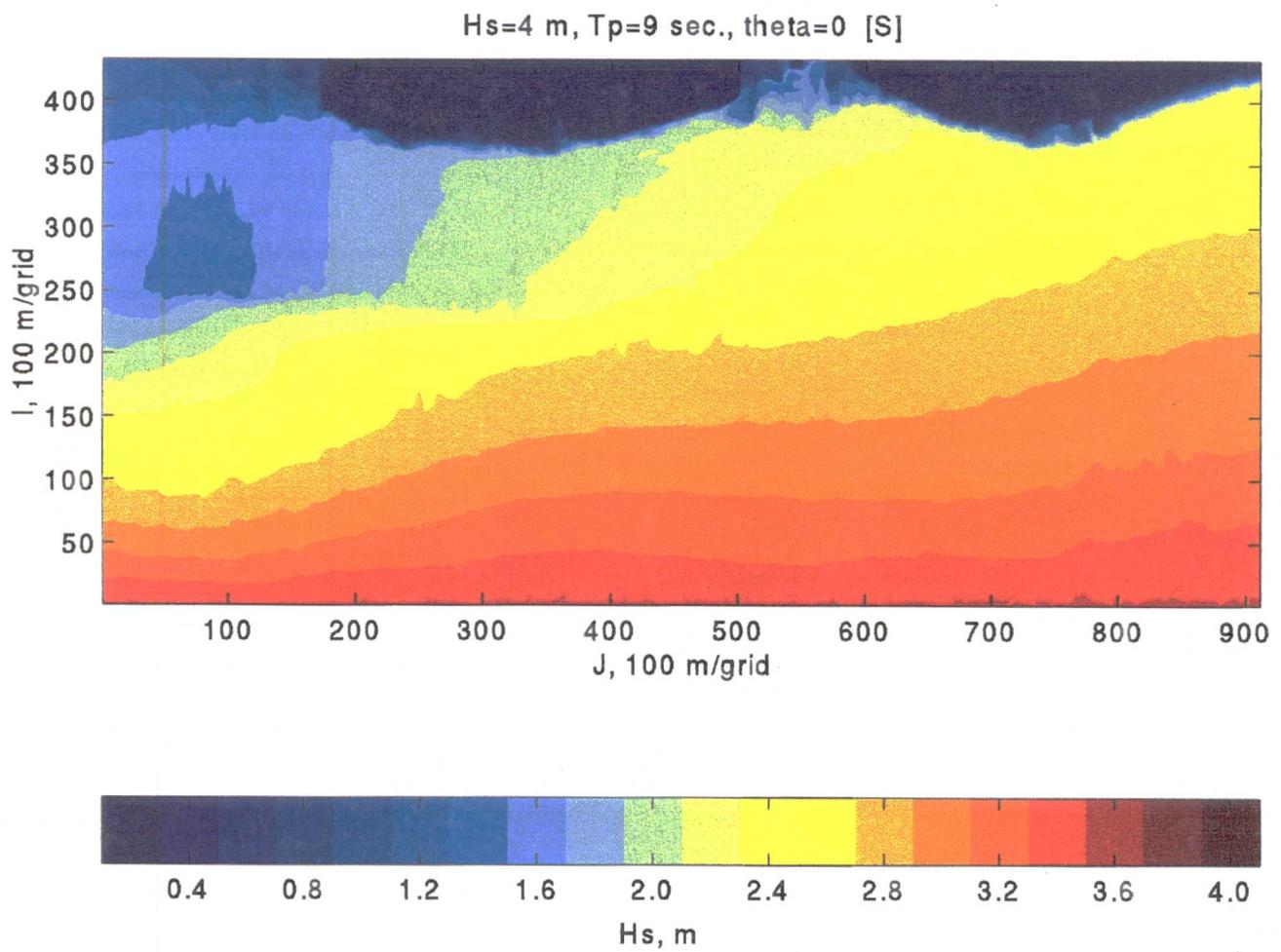
Figure A-1 Image of modeled significant wave height, Case 2, $\theta = 0°$, with Ship Shoal.
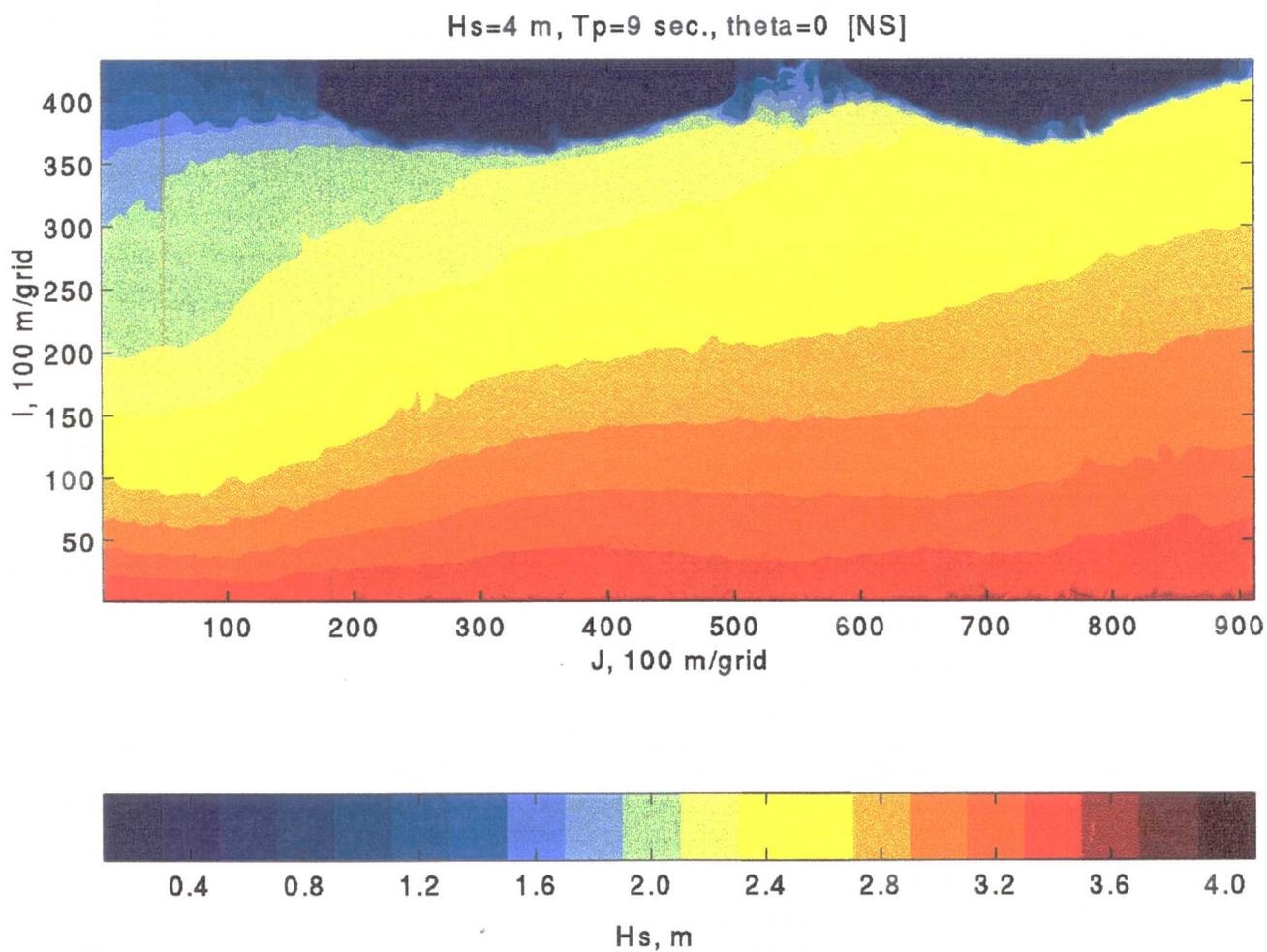
Figure A-2 Image of modeled significant wave height, Case 2, $\theta=0°$, without Ship Shoal.
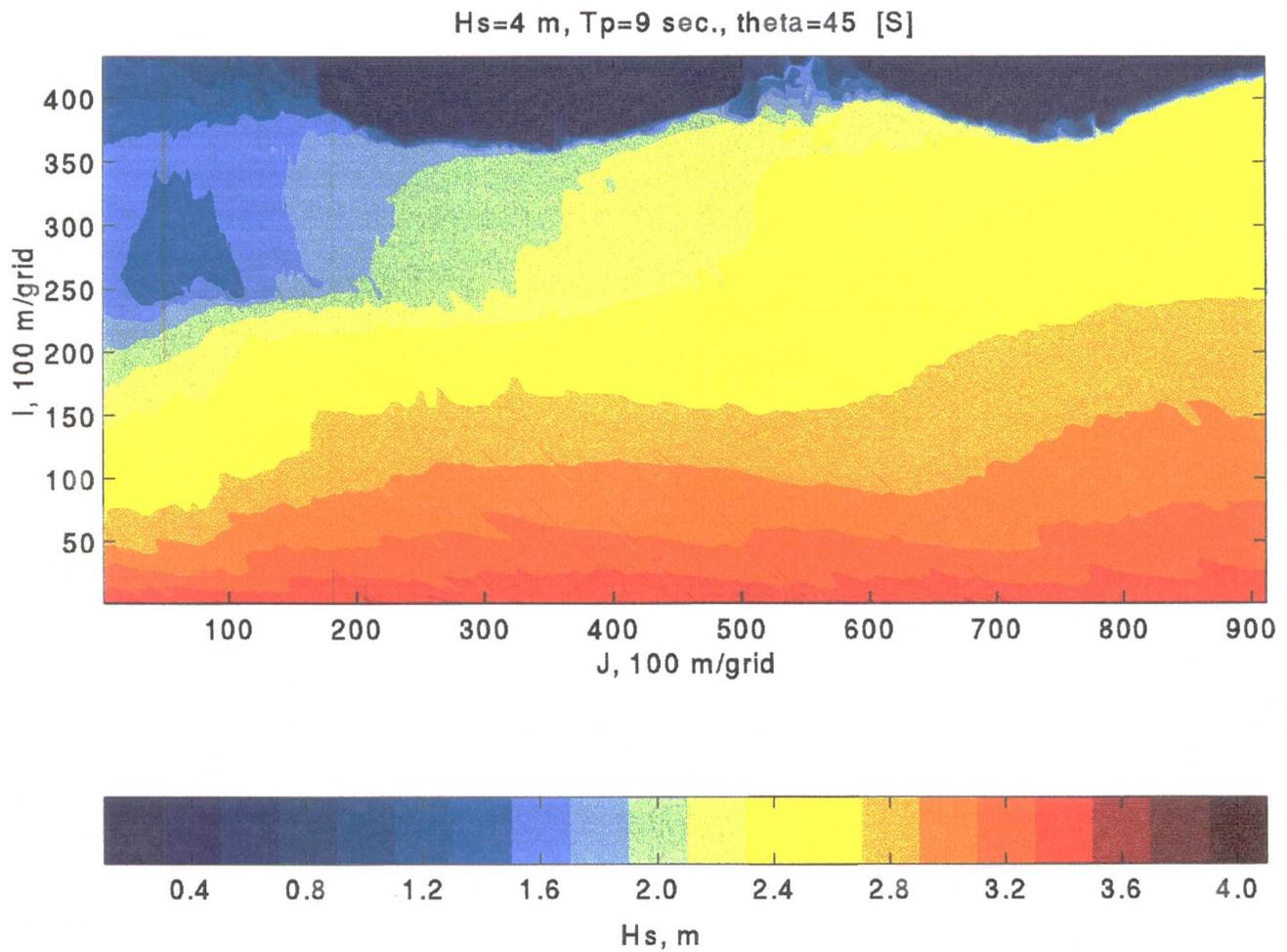
Figure A-3 Image of modeled significant wave height, Case 2, $\theta = 45°$, with Ship Shoal.

Hs=4 m, Tp=9 sec., theta=45 [NS]
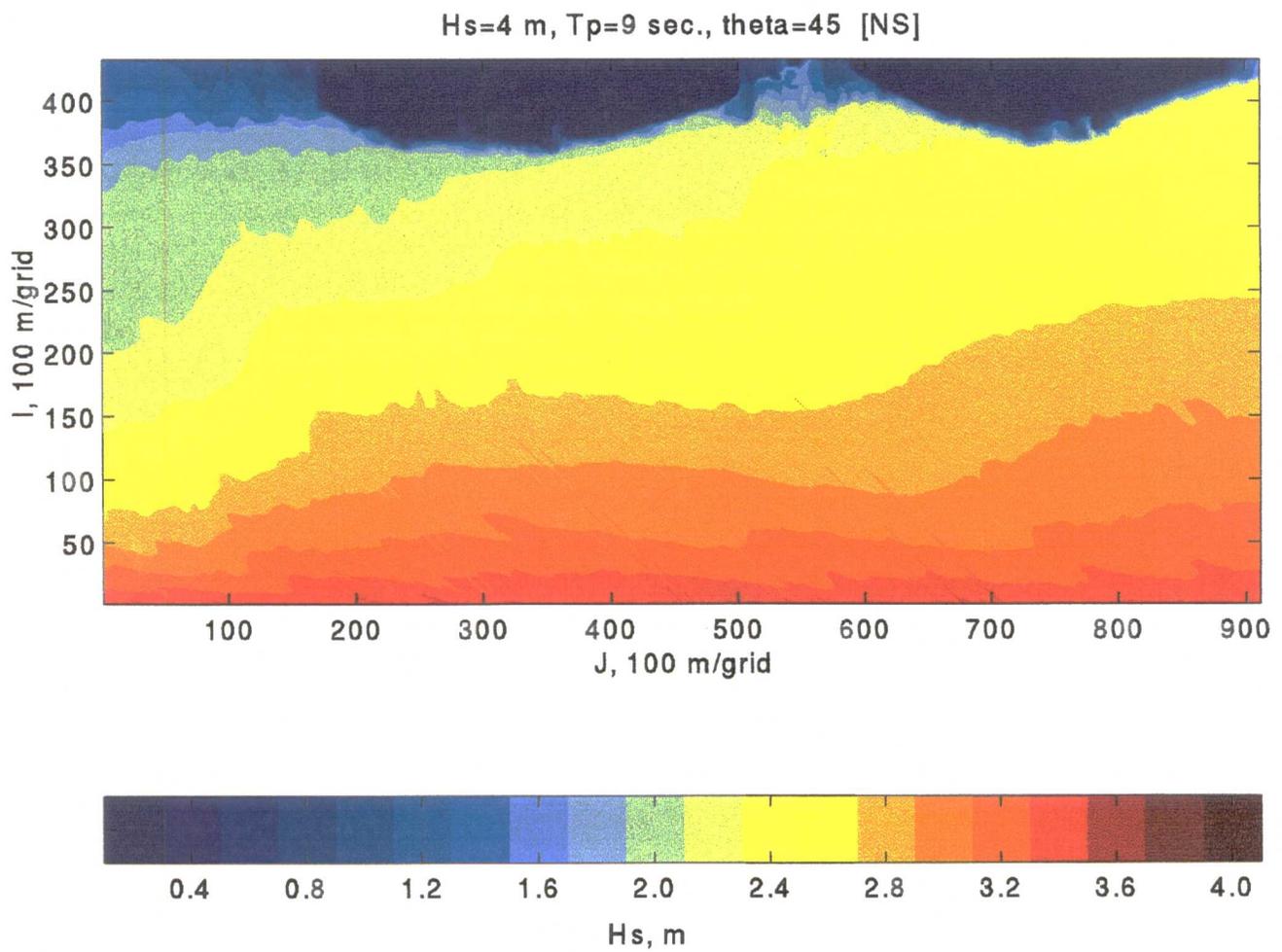
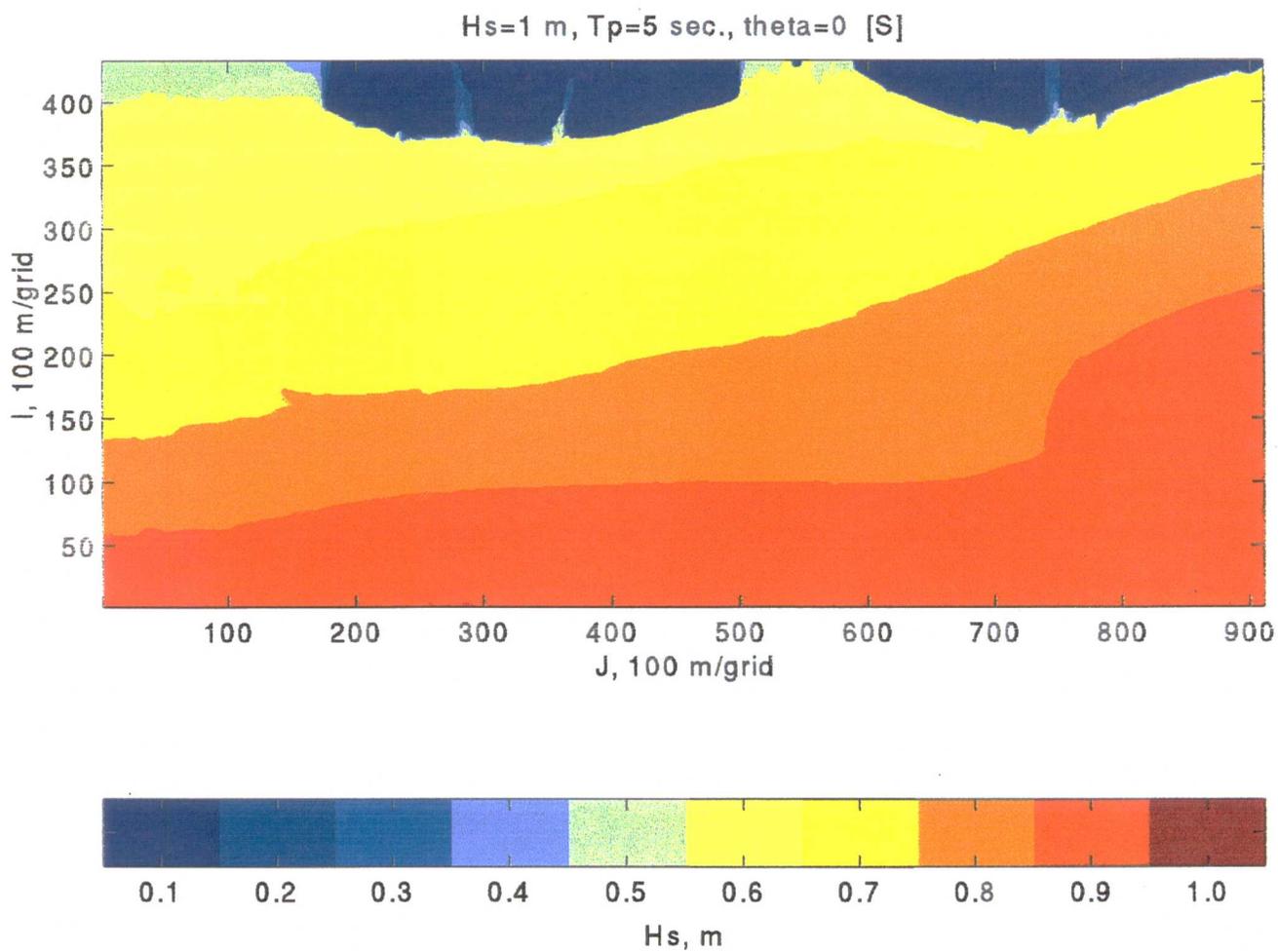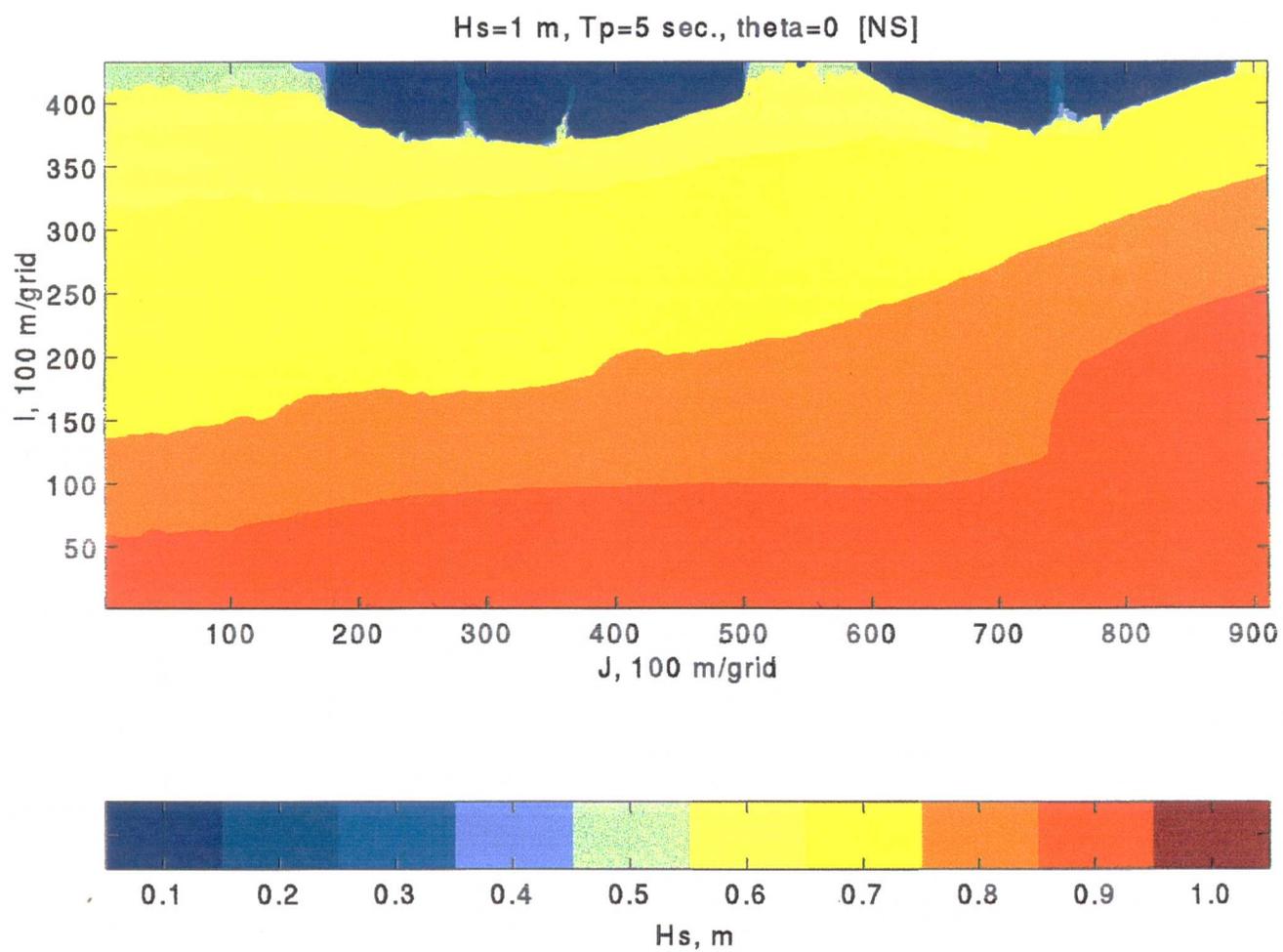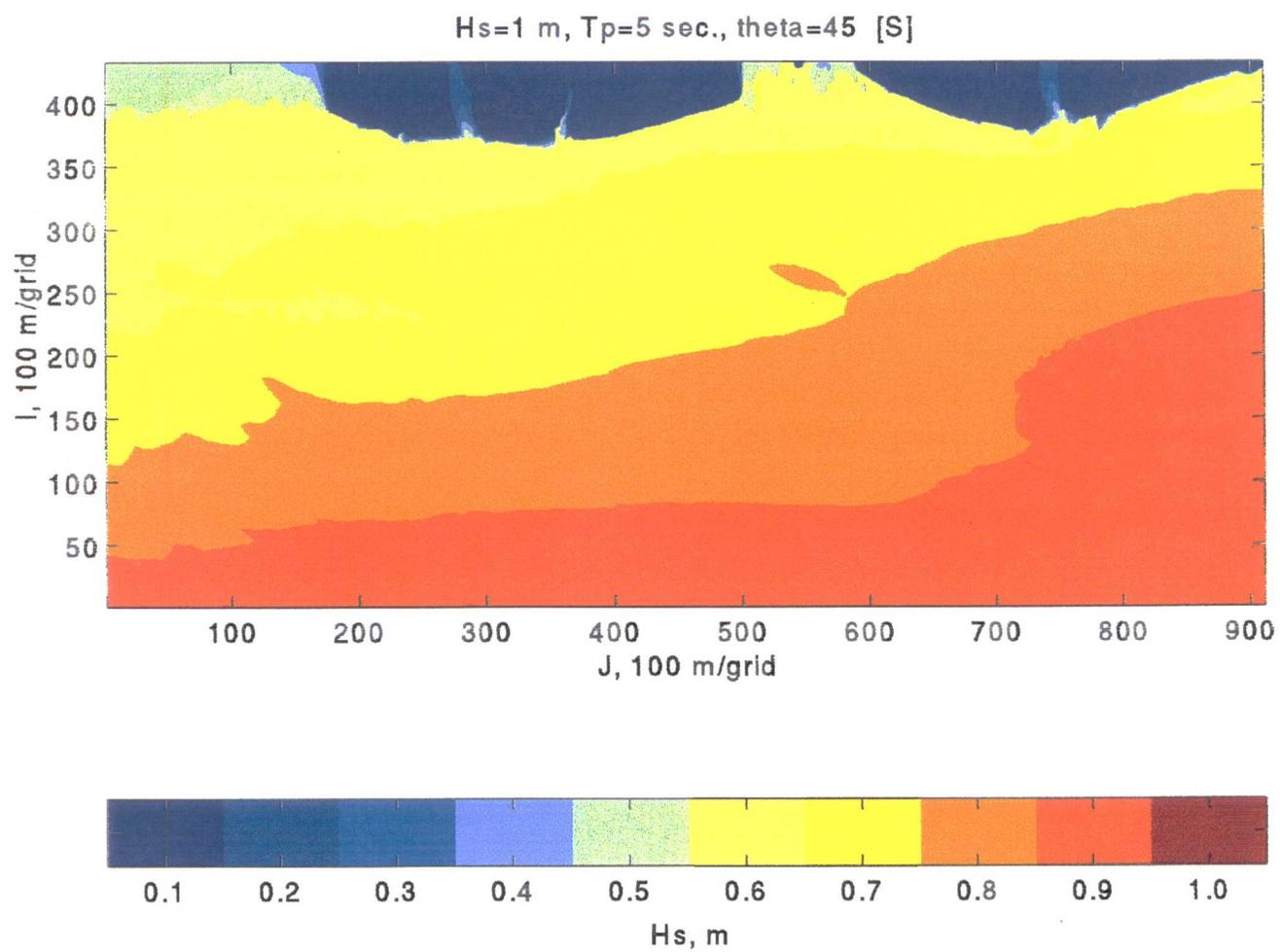Figure A-4 Image of modeled significant wave height, Case 2, θ=45°, without Ship Shoal.
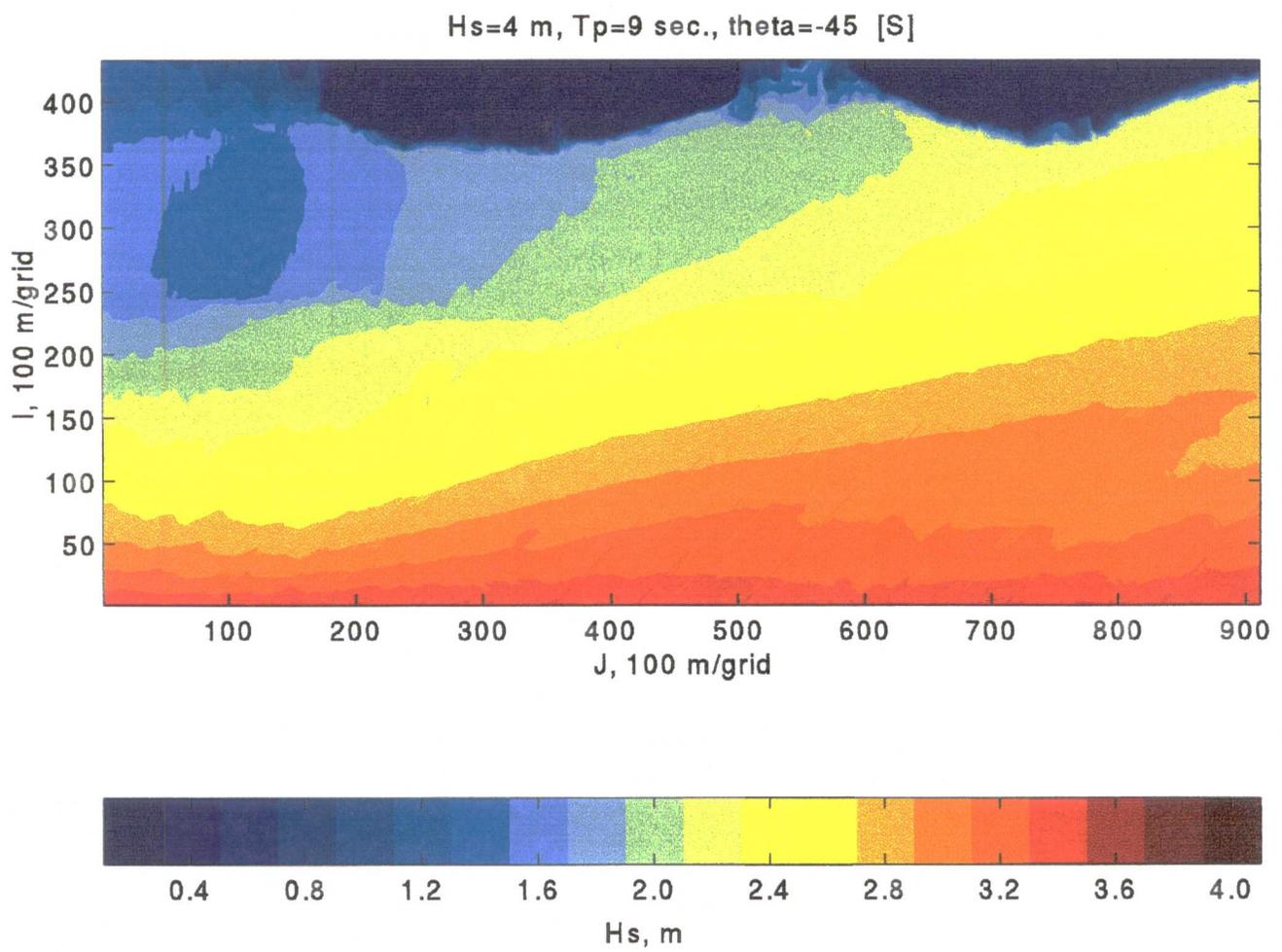
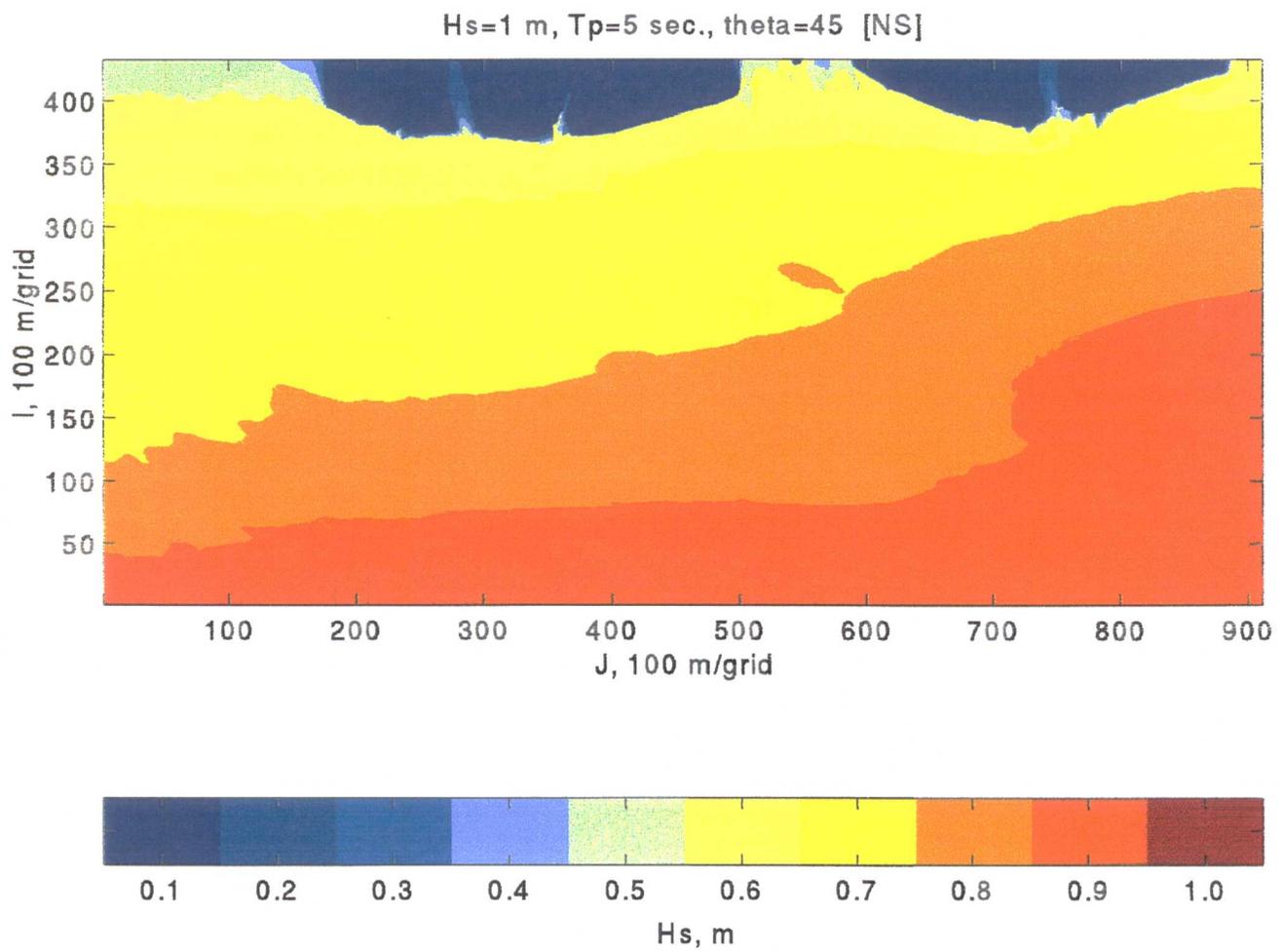Figure A-5 Image of modeled significant wave height, Case 2, $\theta = -45°$, with Ship Shoal.
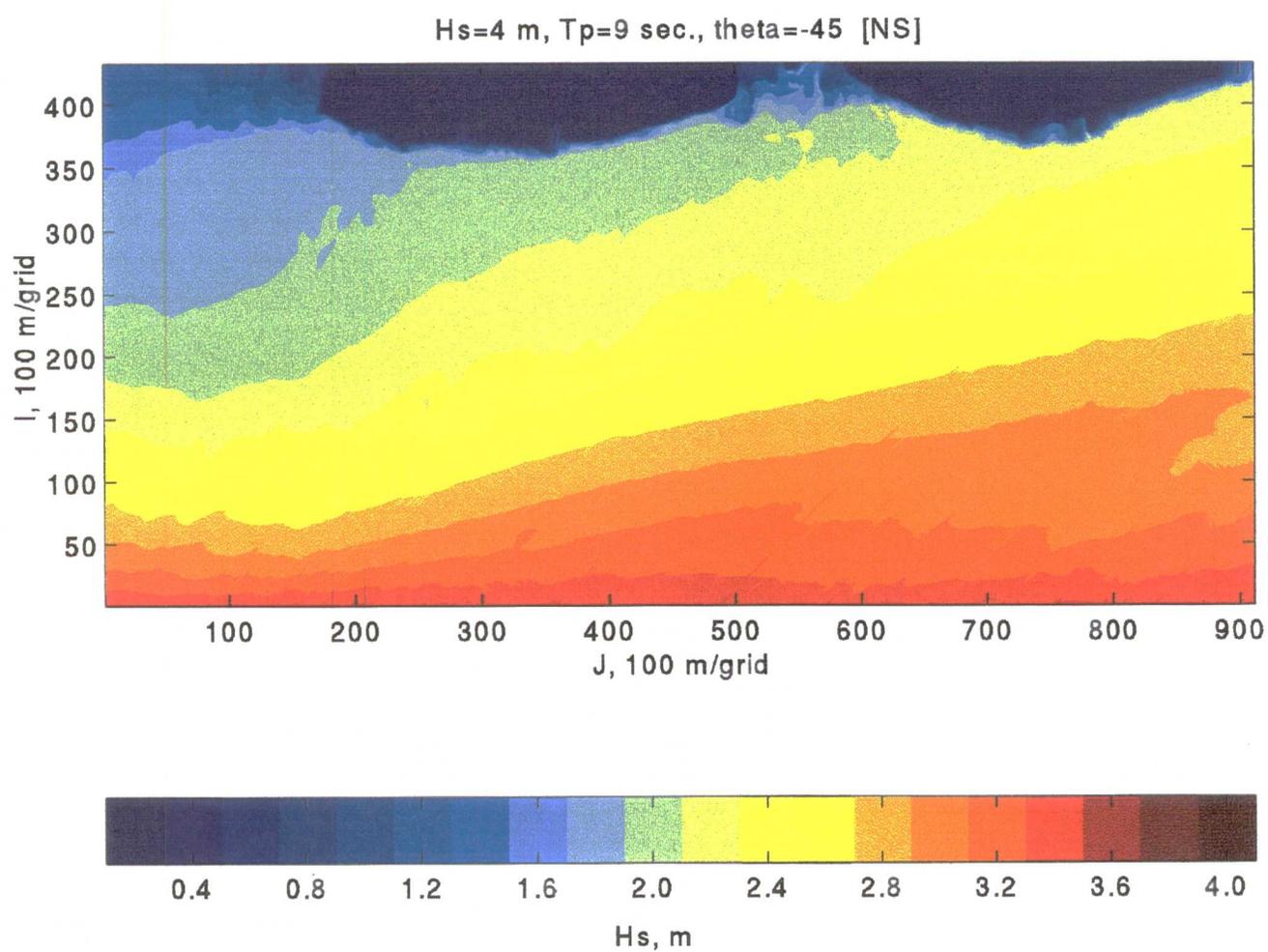
Figure A-6 Image of modeled significant wave height, Case 2, θ = -45°, without Ship Shoal.
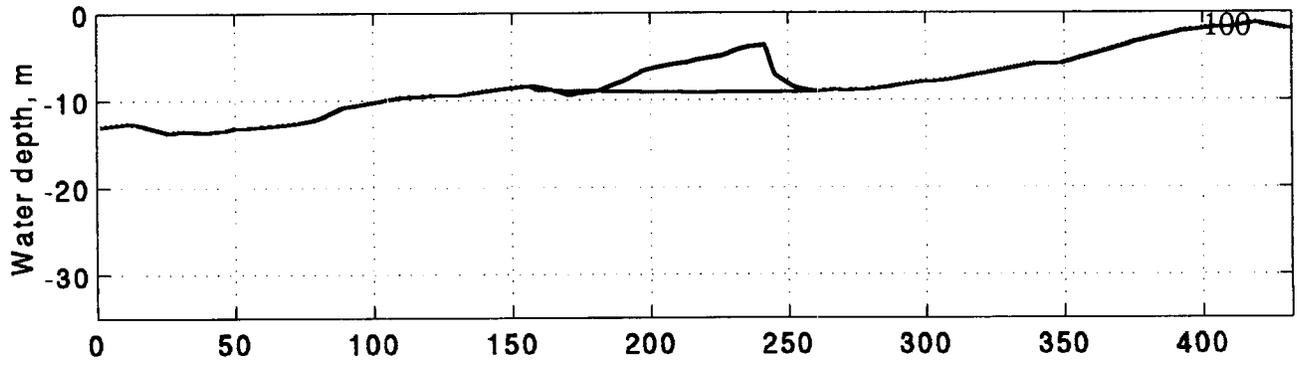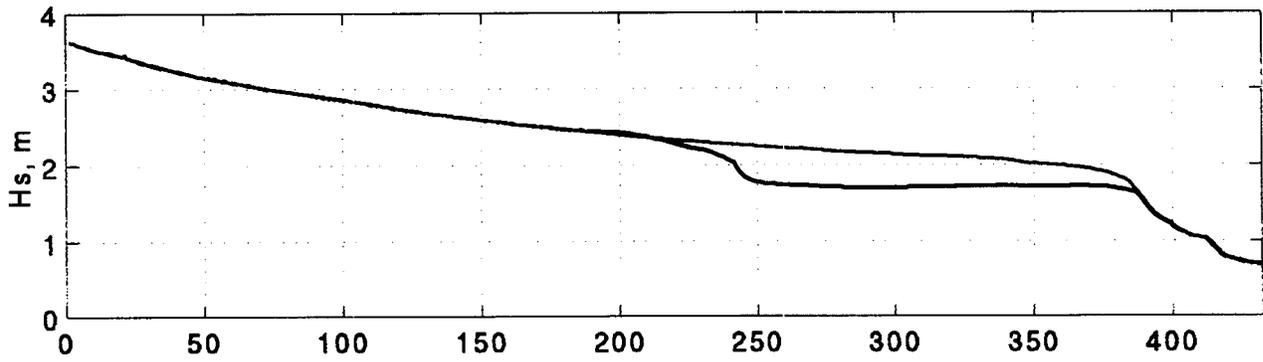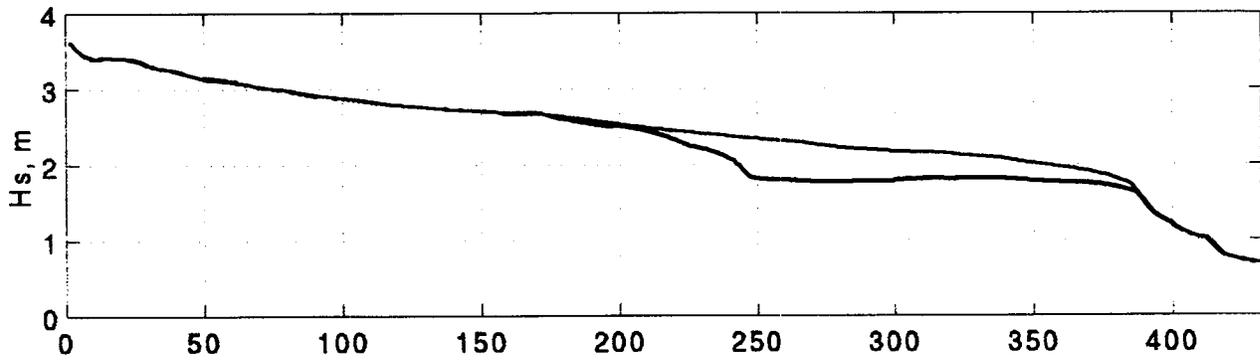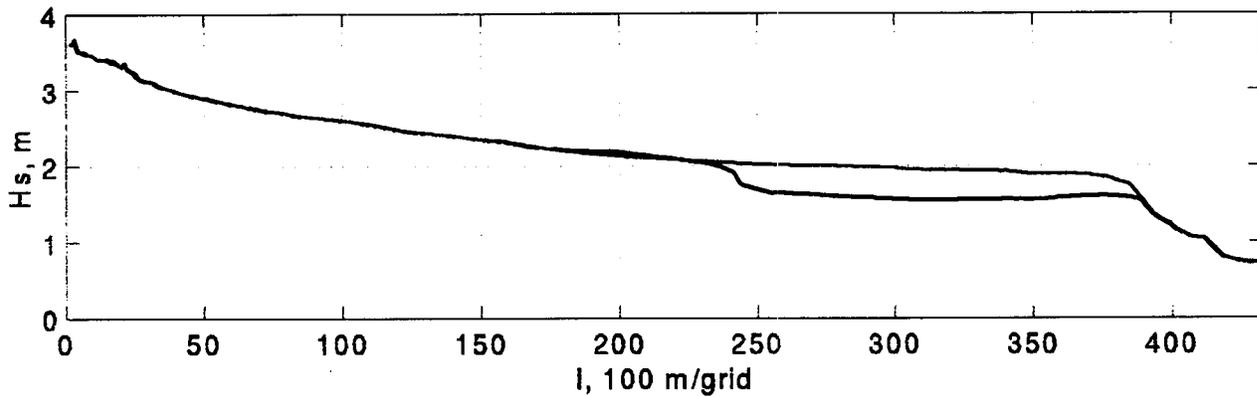
Figure A-7 Cross-sectional profiles of significant wave height, H_s, along $J = 150$ in Case 2.
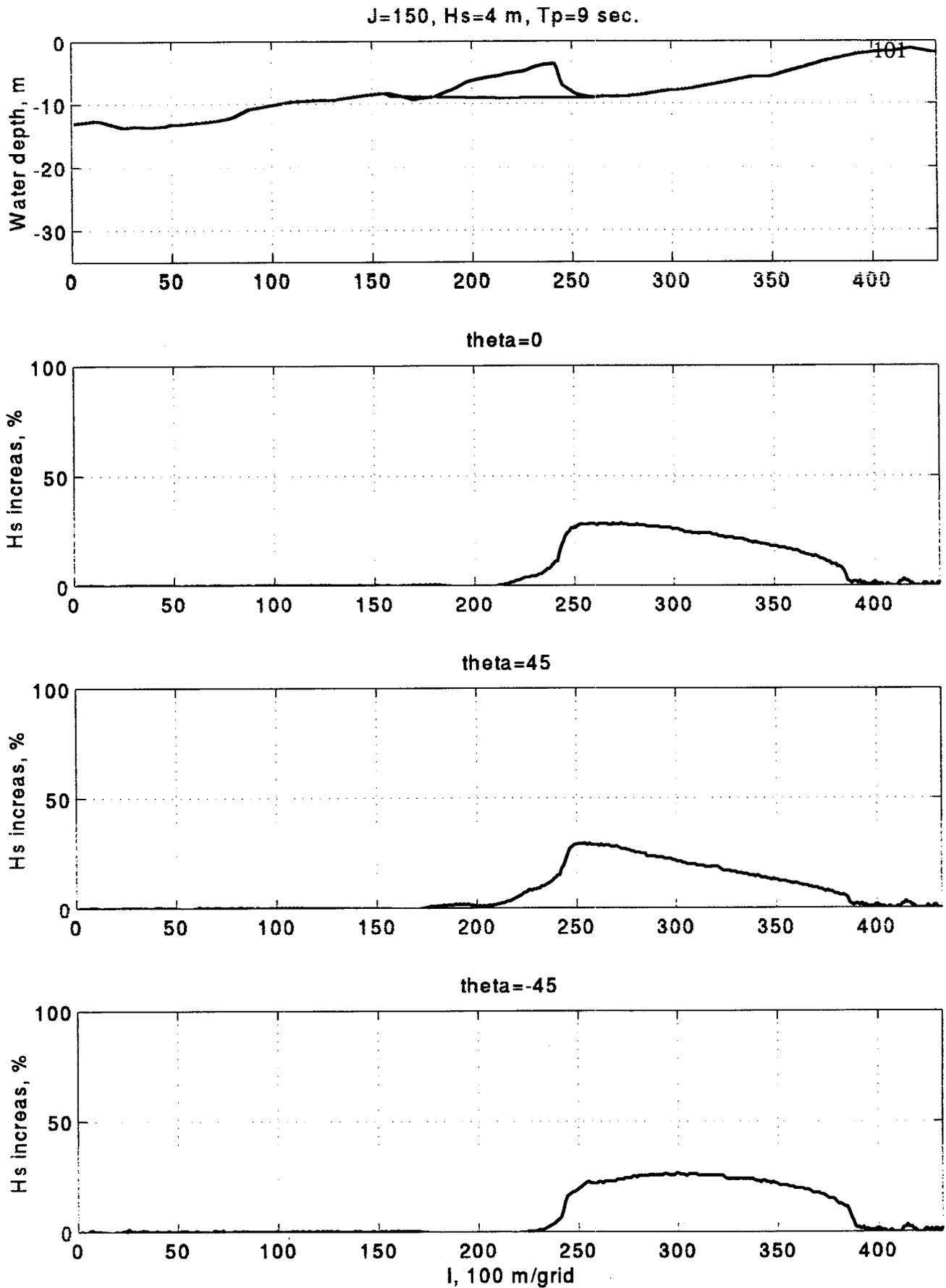
Figure A-8 Cross-sectional profiles of percentage of Hs increase due to shoal removal along J=150 in Case 2.
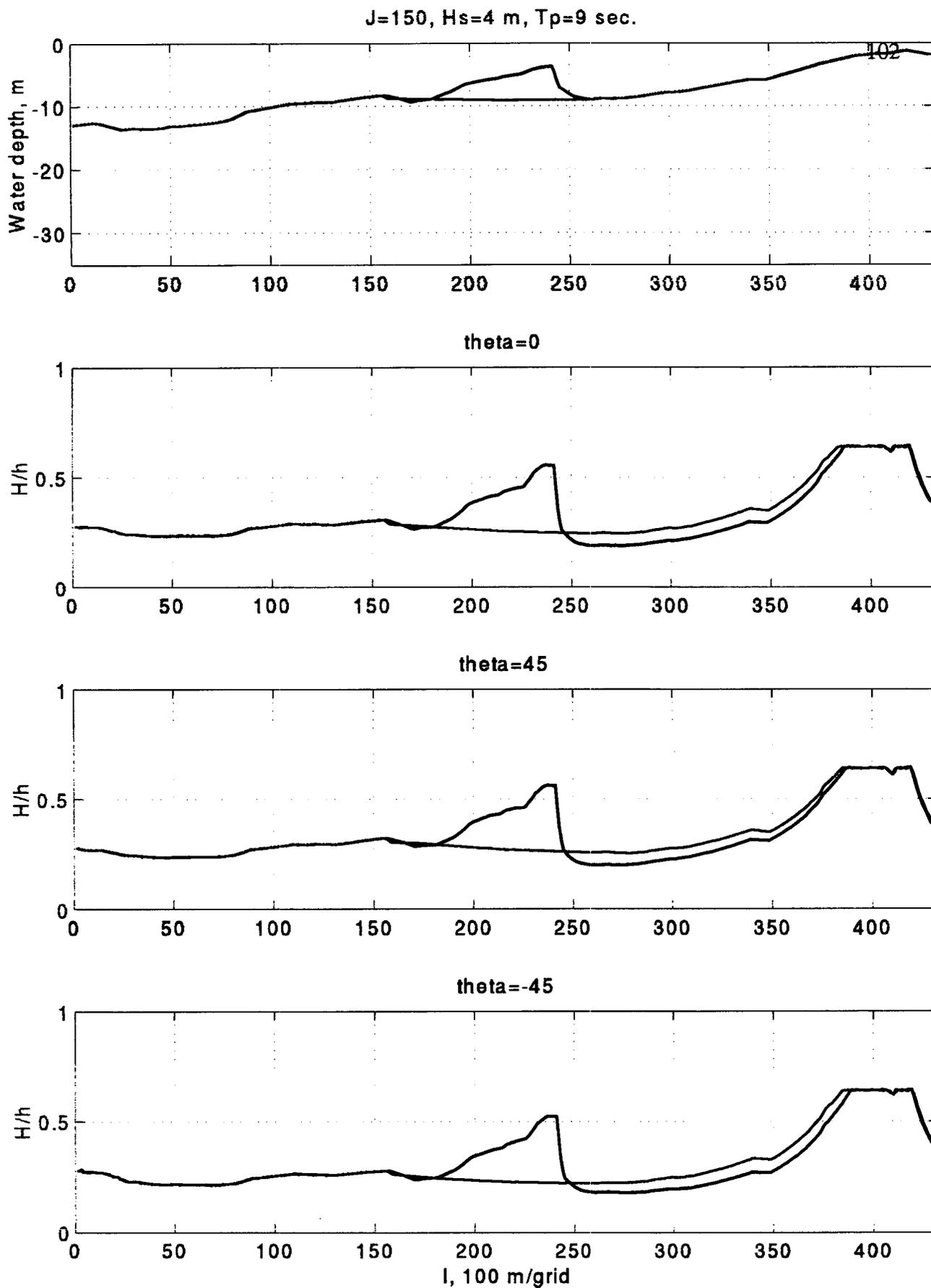
Figure A-9 Cross-sectional profiles of depth-limited wave breaking index, H/h, along J=150 in Case 2.
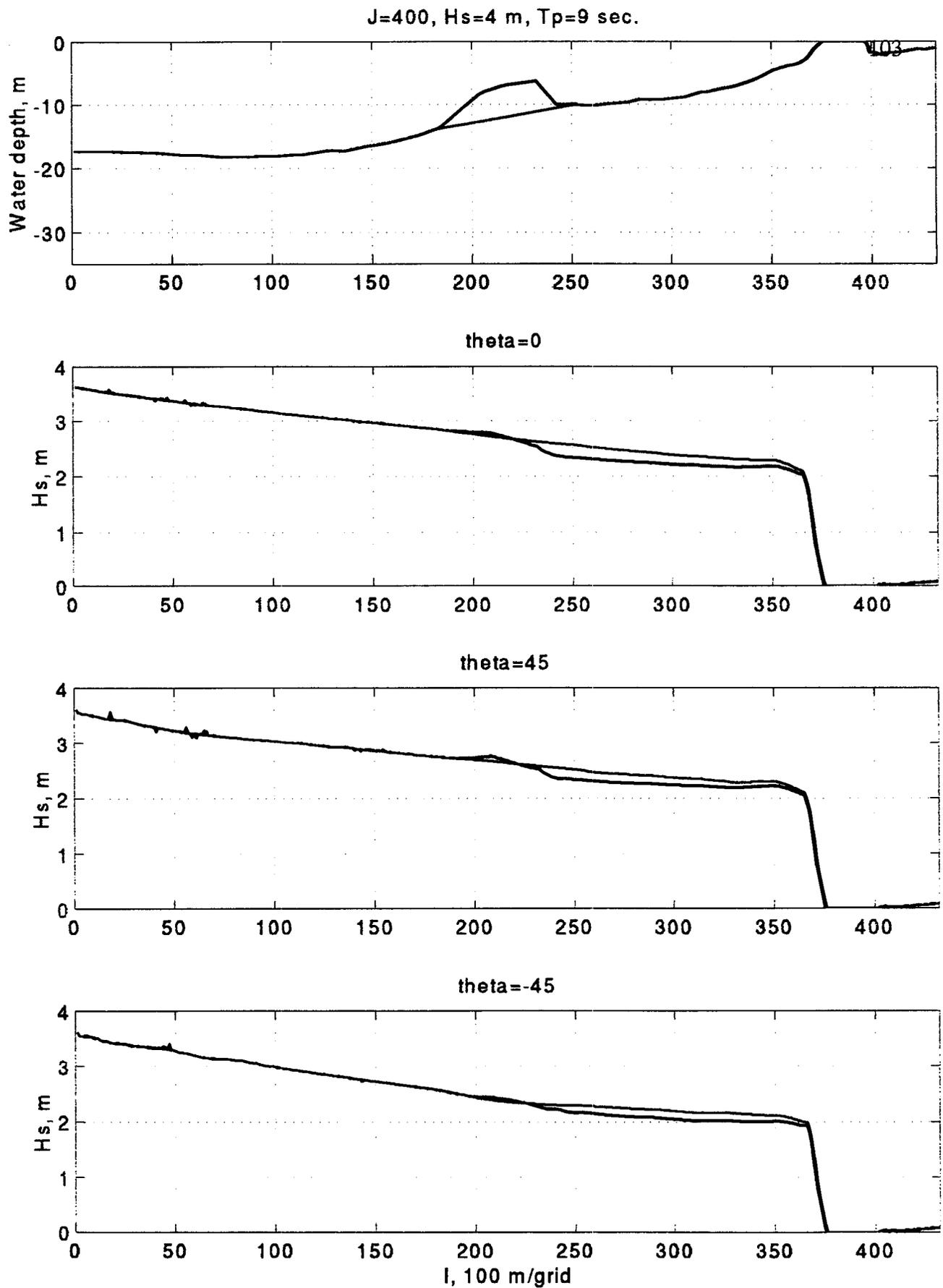
Figure A-10 Cross-sectional profiles of significant wave height, H_s, along J=400 in Case 2.
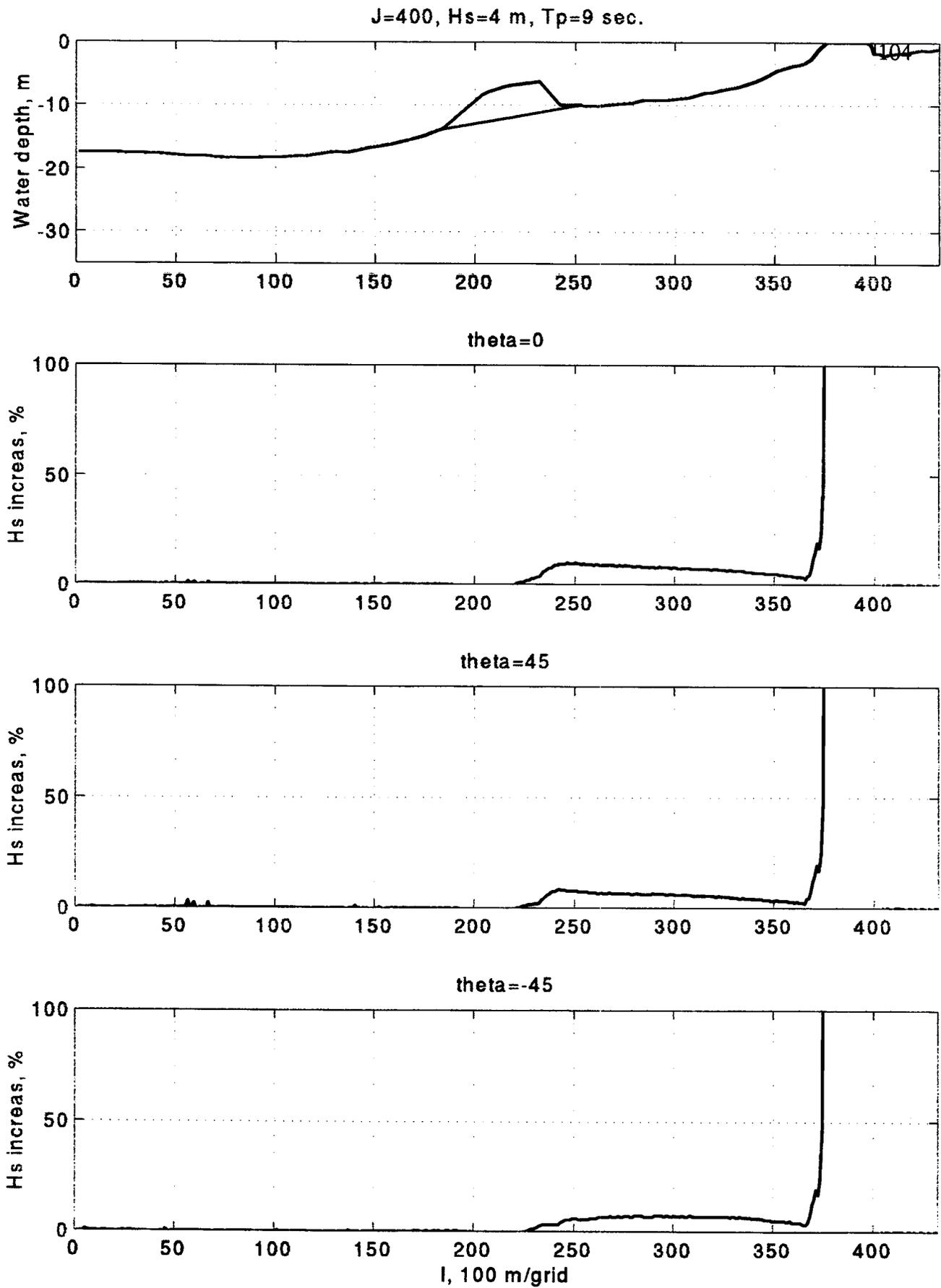
Figure A-11 Cross-sectional profiles of percentage of Hs increase due to shoal removal along J=400 in Case 2.
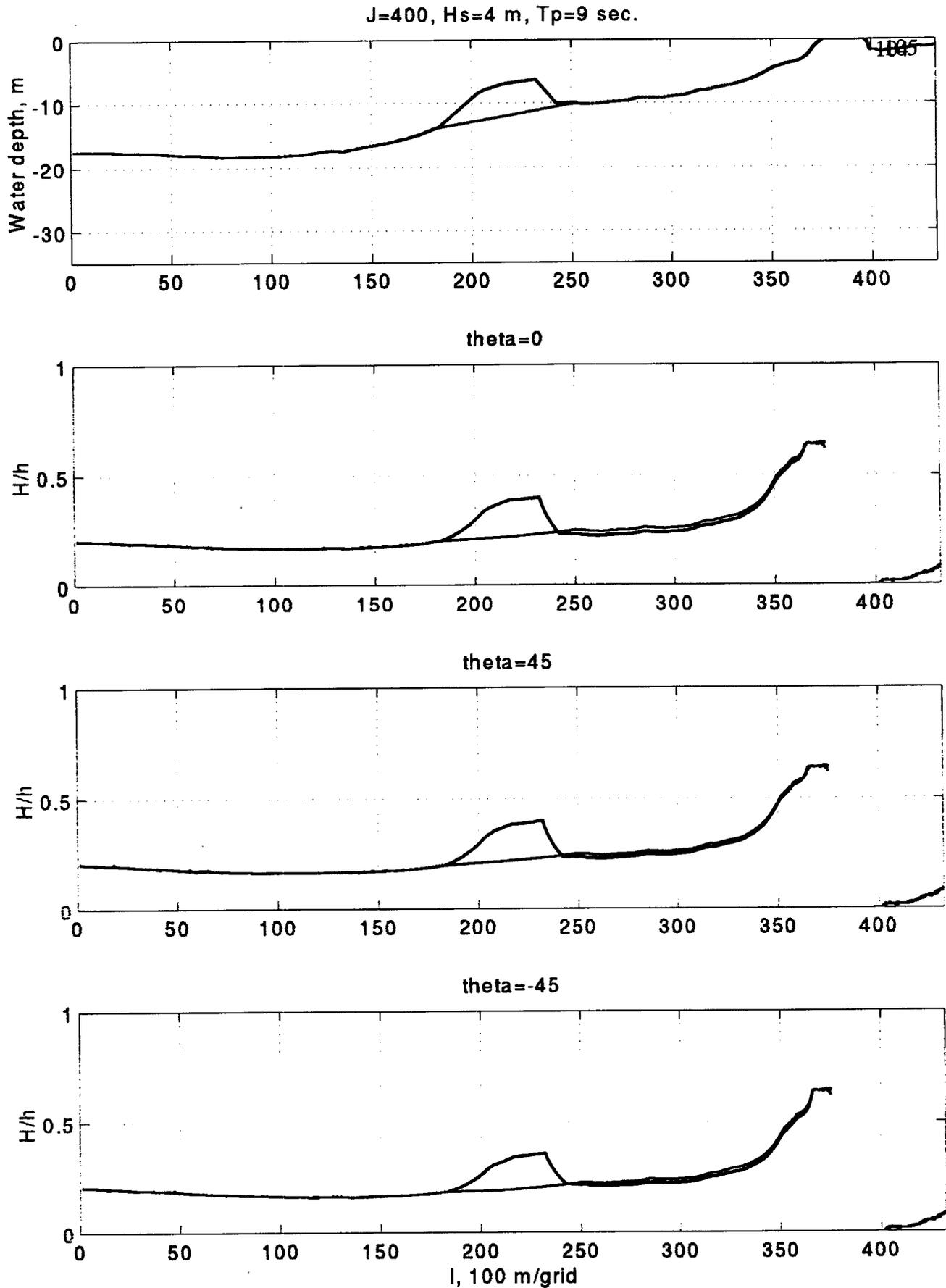
Figure A-12 Cross-sectional profiles of depth-limited wave breaking index, H/h, along J=400 in Case 2.

Hs=4 m, Tp=9 sec., theta=0 [S]
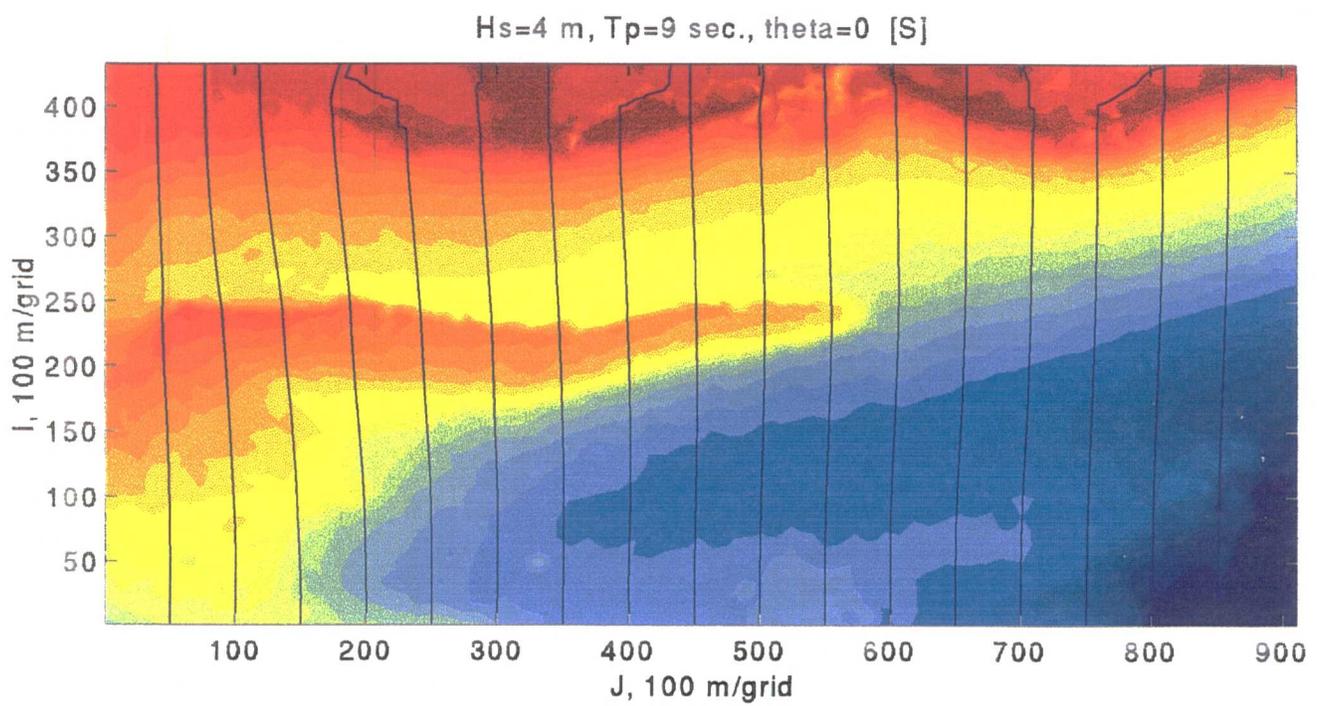
Figure A-13 Modeled wave rays, Case 2, θ=0°, with Ship Shoal.
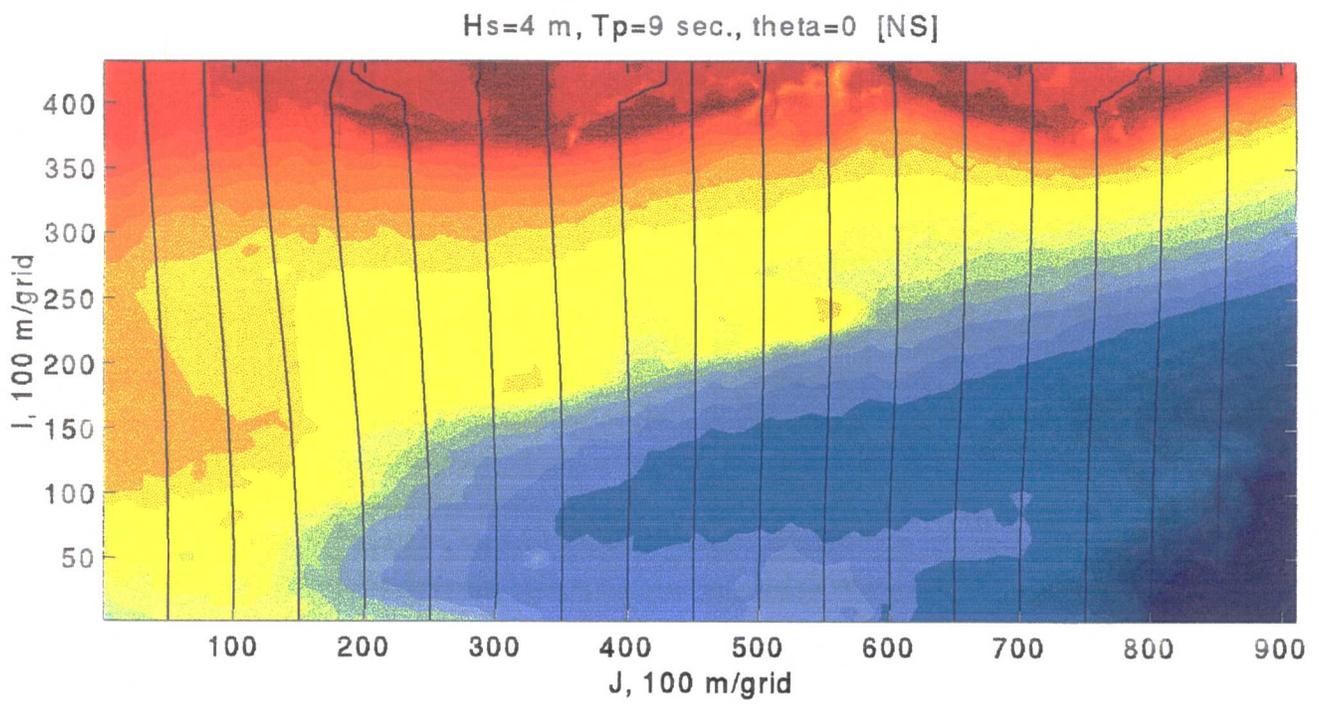
Figure A-14 Modeled wave rays, Case 2, $\theta = 0°$, without Ship Shoal.
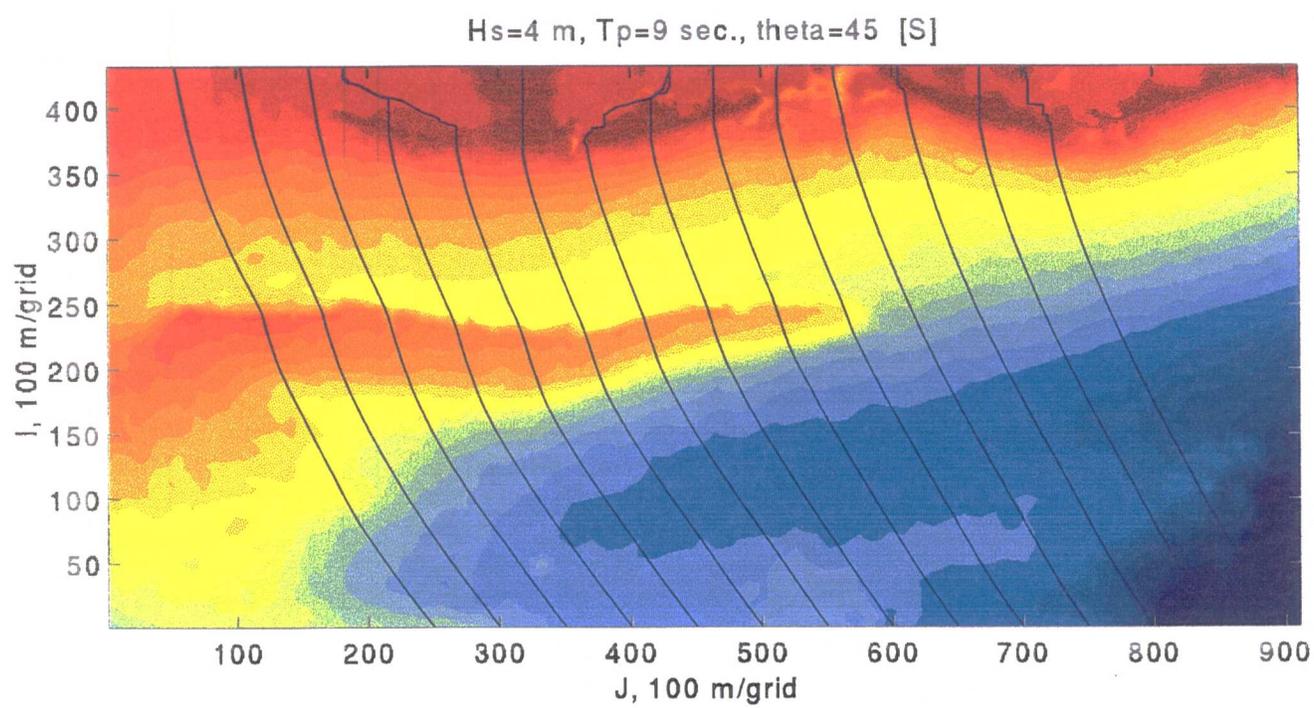
Figure A-15 Modeled wave rays, Case 2, θ=45°, with Ship Shoal.

Figure A-16 Modeled wave rays, Case 2, θ=45°, without Ship Shoal.

Figure A-17 Modeled wave rays, Case 2, θ=-45°, with Ship Shoal.

Figure A-18 Modeled wave rays, Case 2, $\theta = -45°$, without Ship Shoal.

APPENDIX B.   Case 3: $H_s = 2$ m, $T_p = 6$ seconds
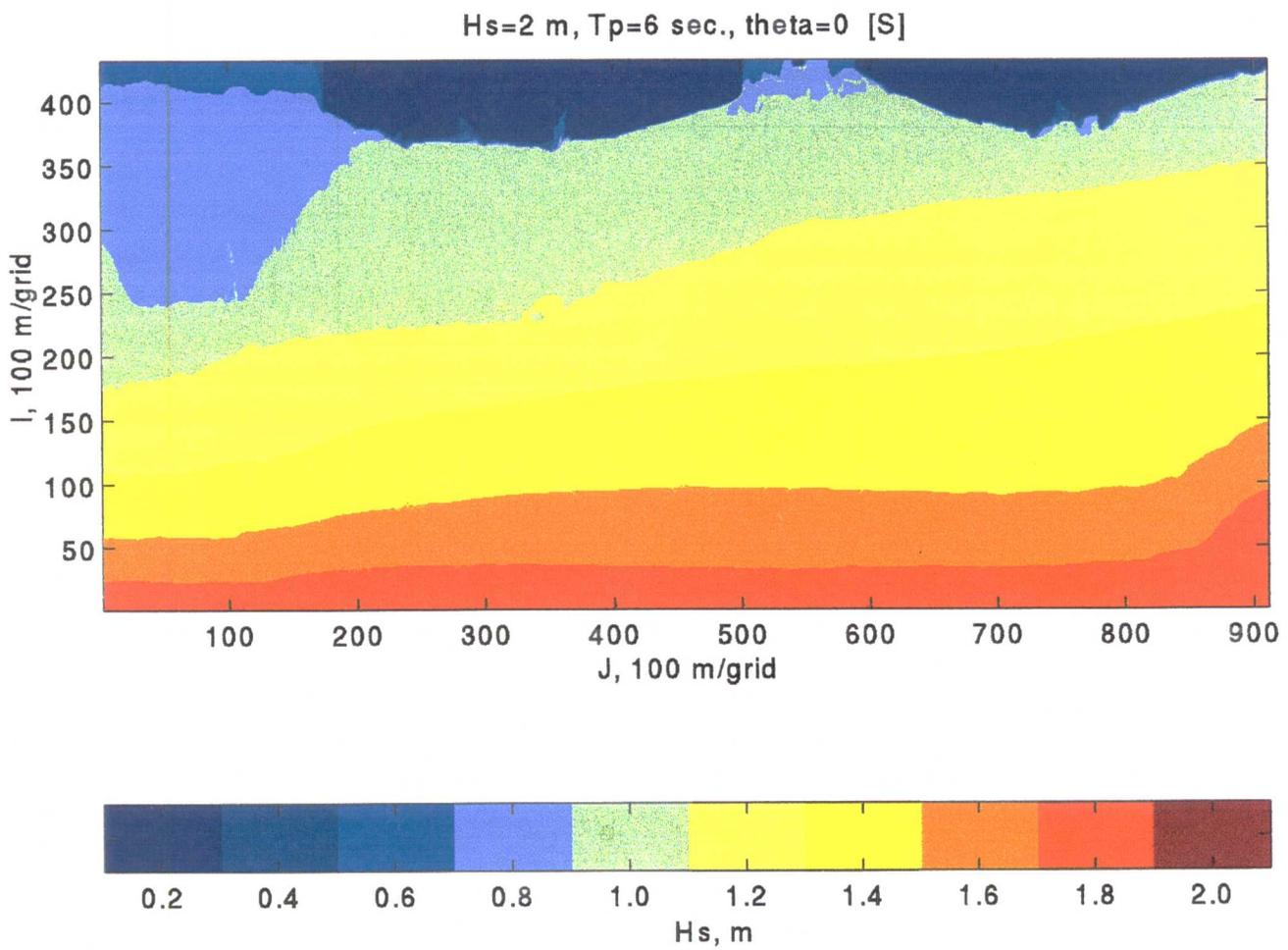
Figure B-1 Image of modeled significant wave height, Case 3, $\theta=0°$, with Ship Shoal.
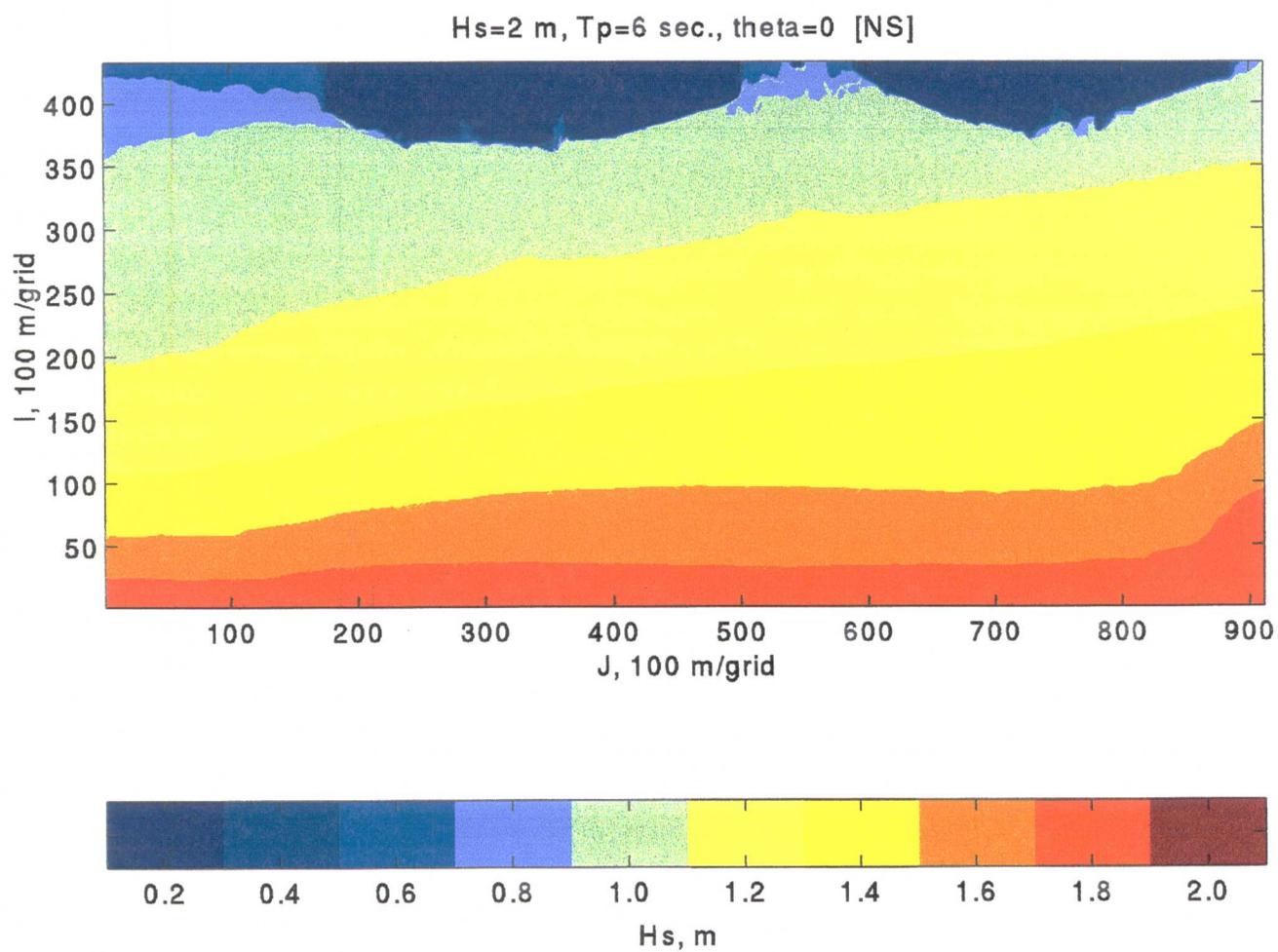
Figure B-2 Image of modeled significant wave height; Case 3, θ=0°, without Ship Shoal.

Hs=2 m, Tp=6 sec., theta=45 [S]
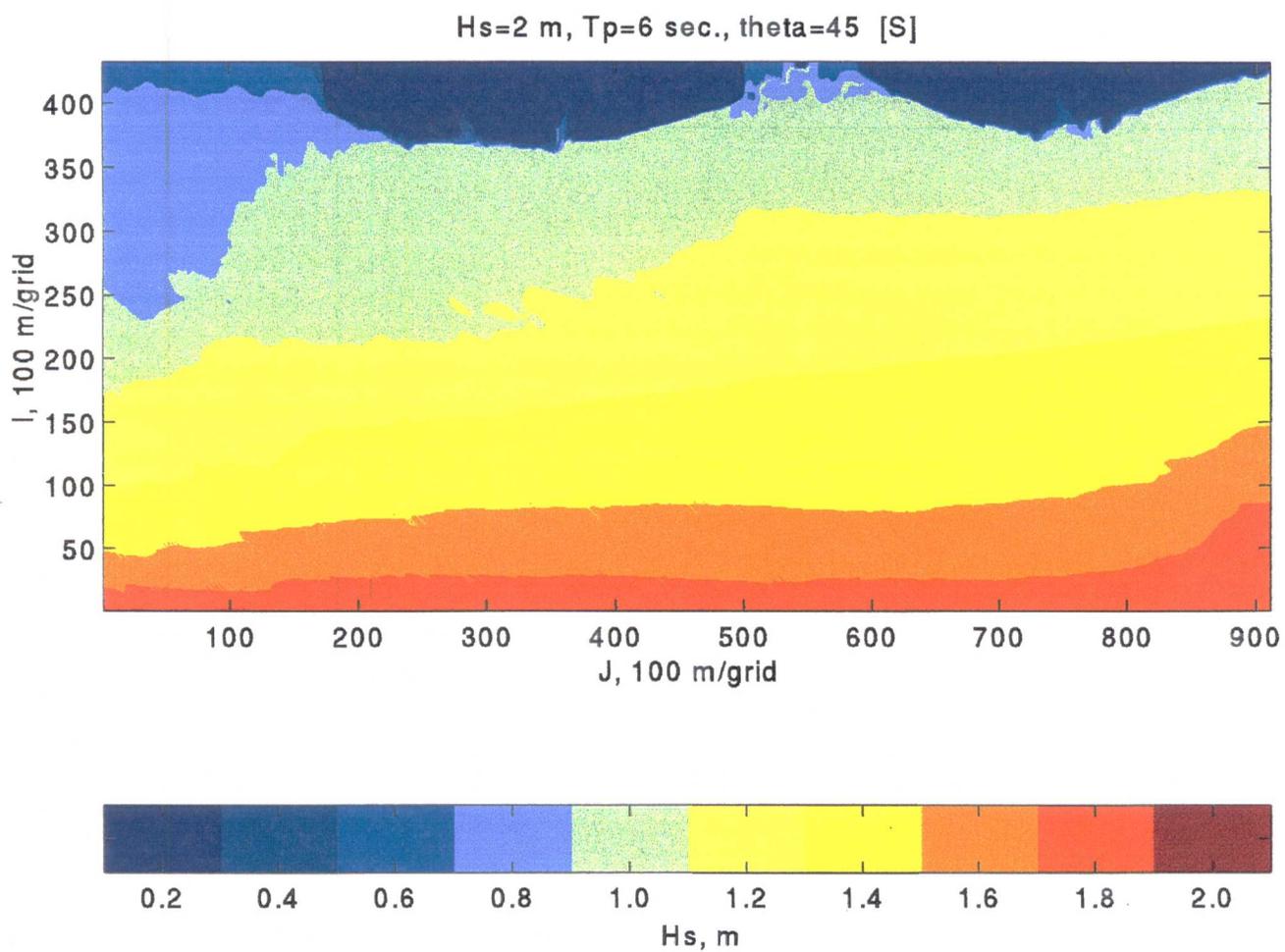
Figure B-3 Image of modeled significant wave height, Case 3, θ=45°, with Ship Shoal.

Hs=2 m, Tp=6 sec., theta=45 [NS]

Figure B-4 Image of modeled significant wave height, Case 3, $\theta=45°$, without Ship Shoal.

Hs=2 m, Tp=6 sec., theta=-45 [S]
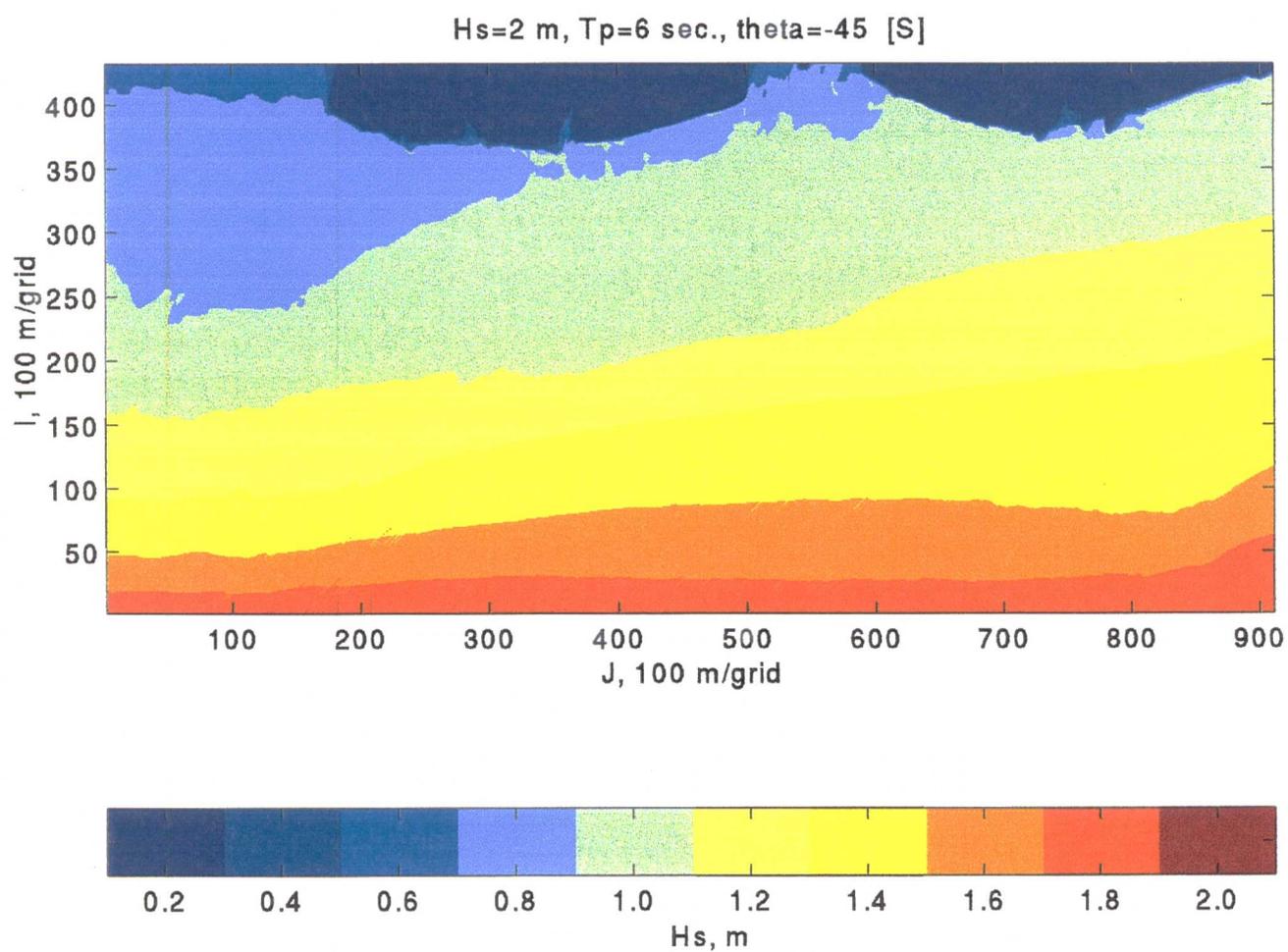
Figure B-5 Image of modeled significant wave height, Case 3, θ=-45°, with Ship Shoal.
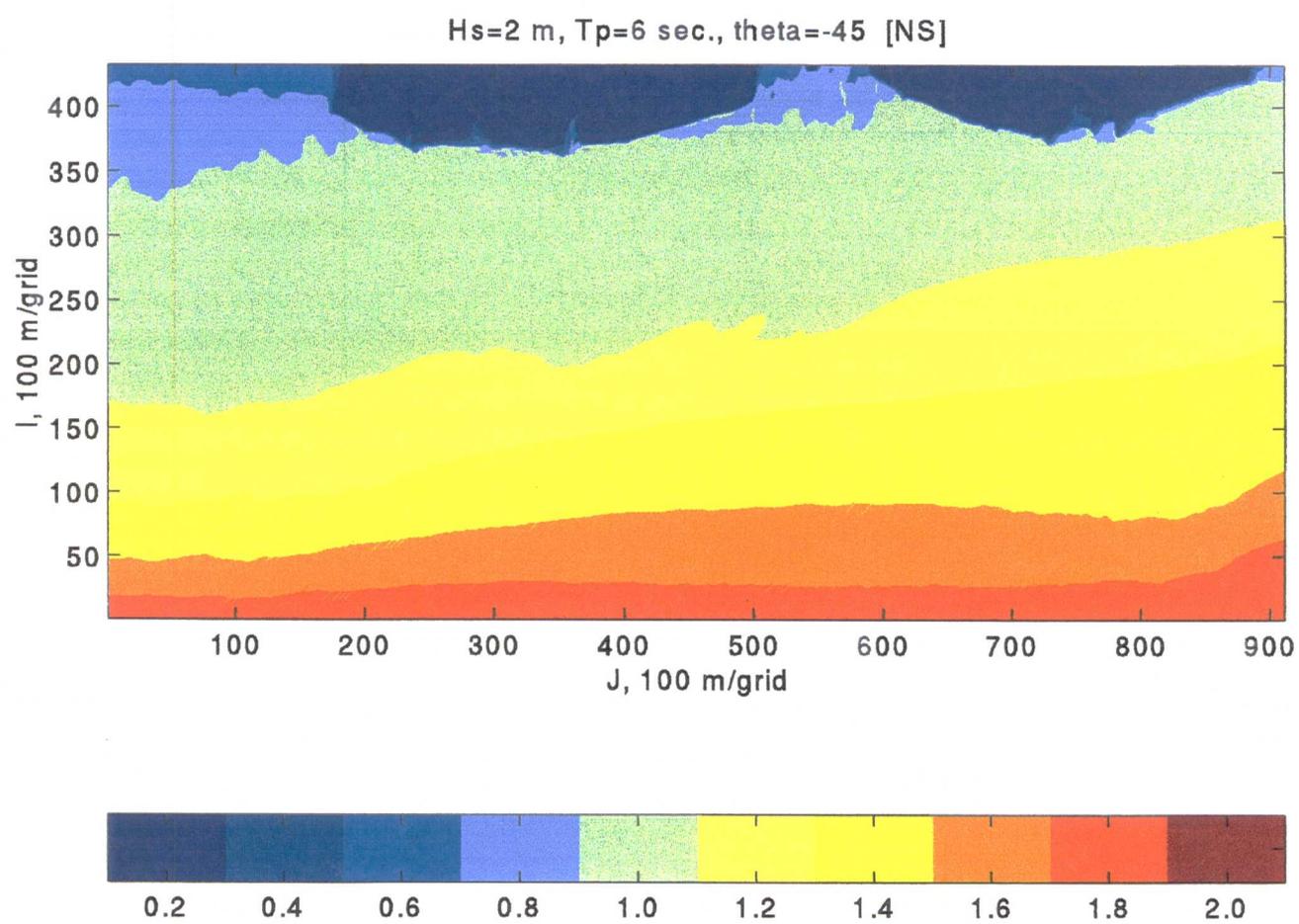
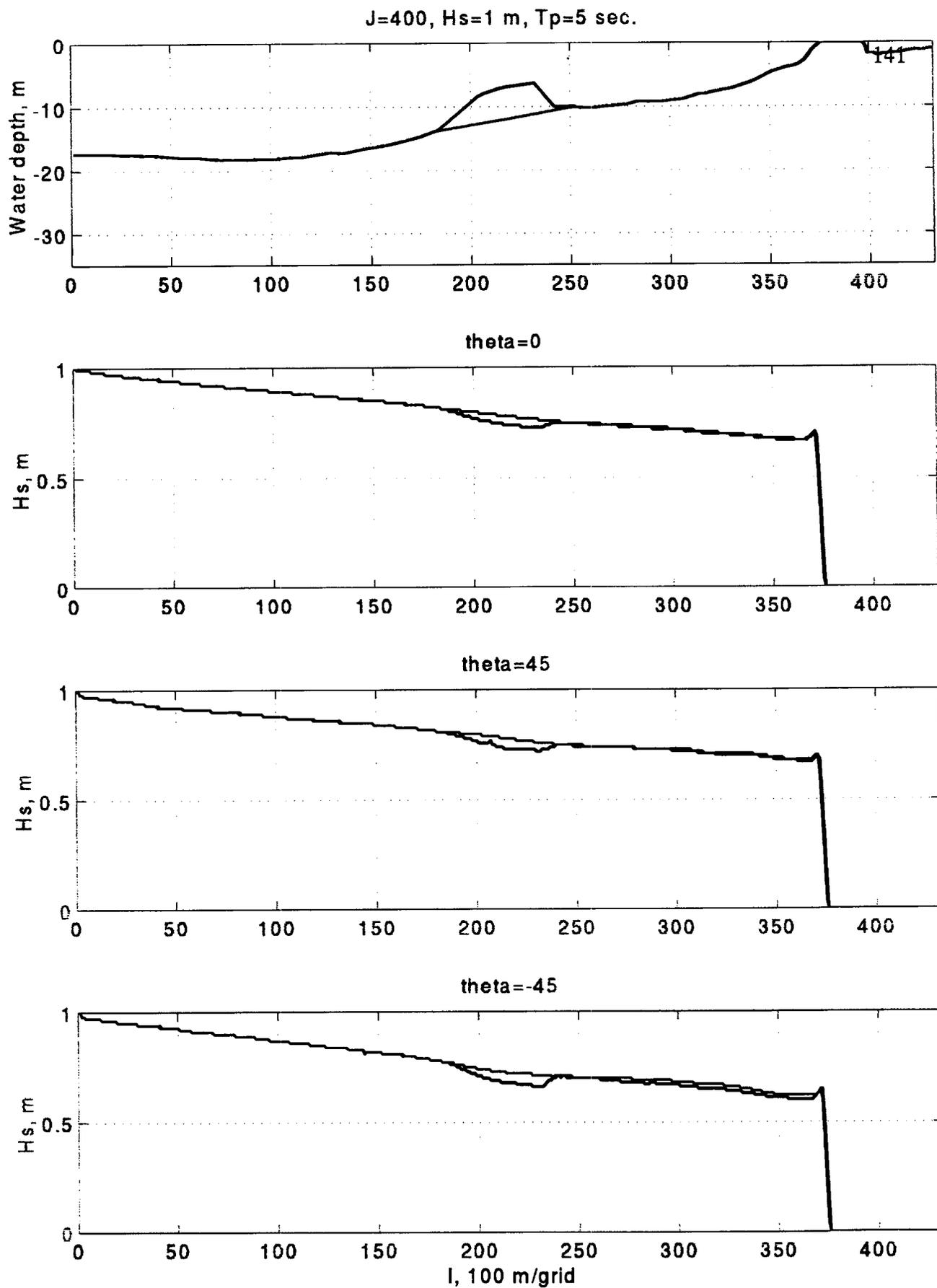Figure B-6 Image of modeled significant wave height, Case 3, θ=-45°, without Ship Shoal.
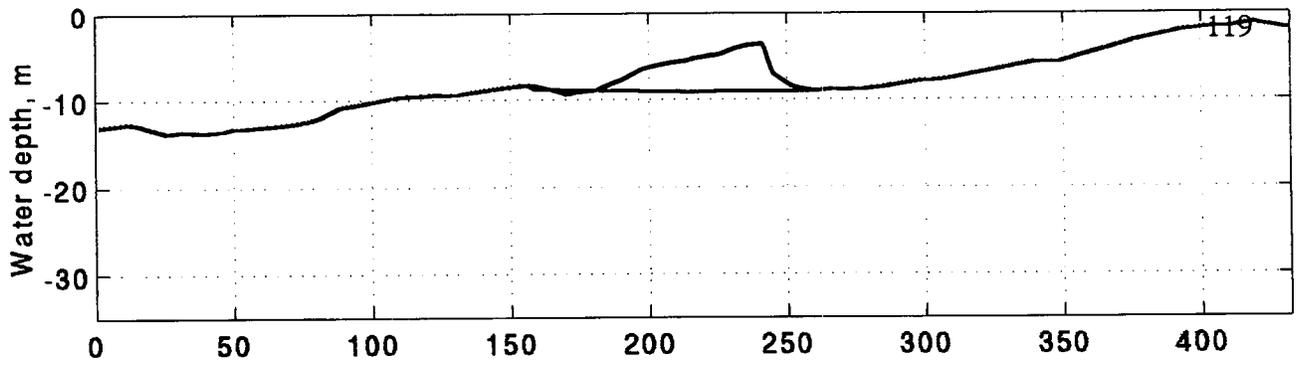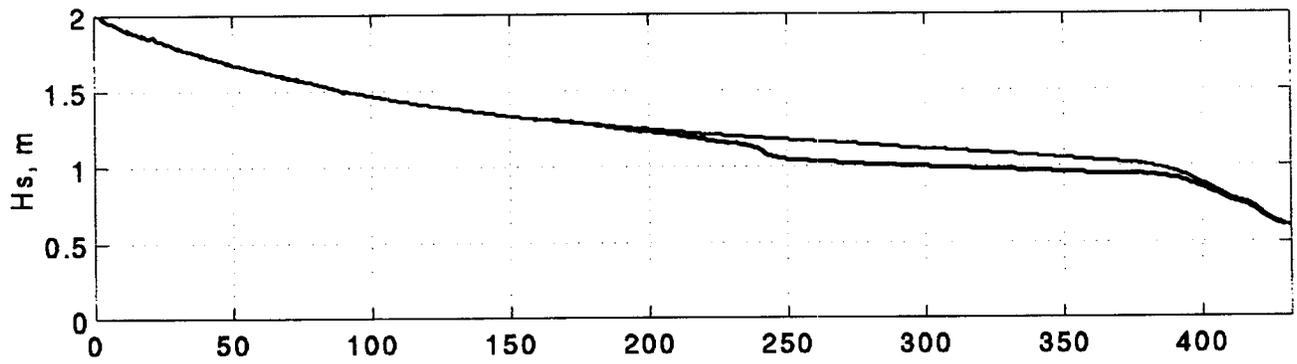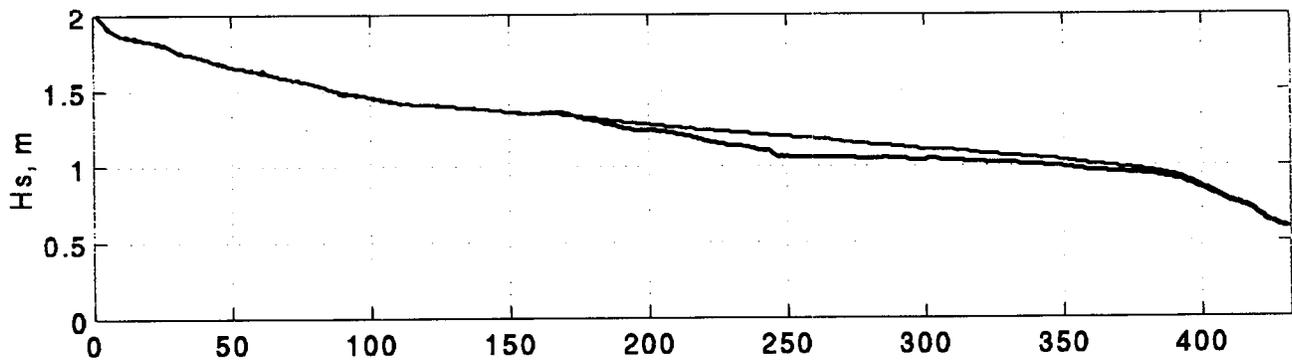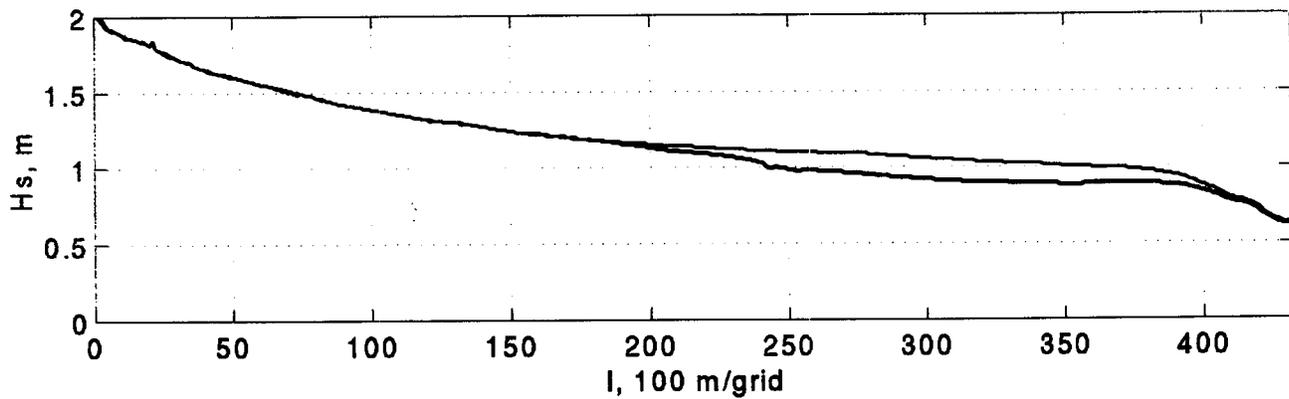
Figure B-7 Cross-sectional profiles of significant wave height, H_s, along J=150 in Case 3.

119
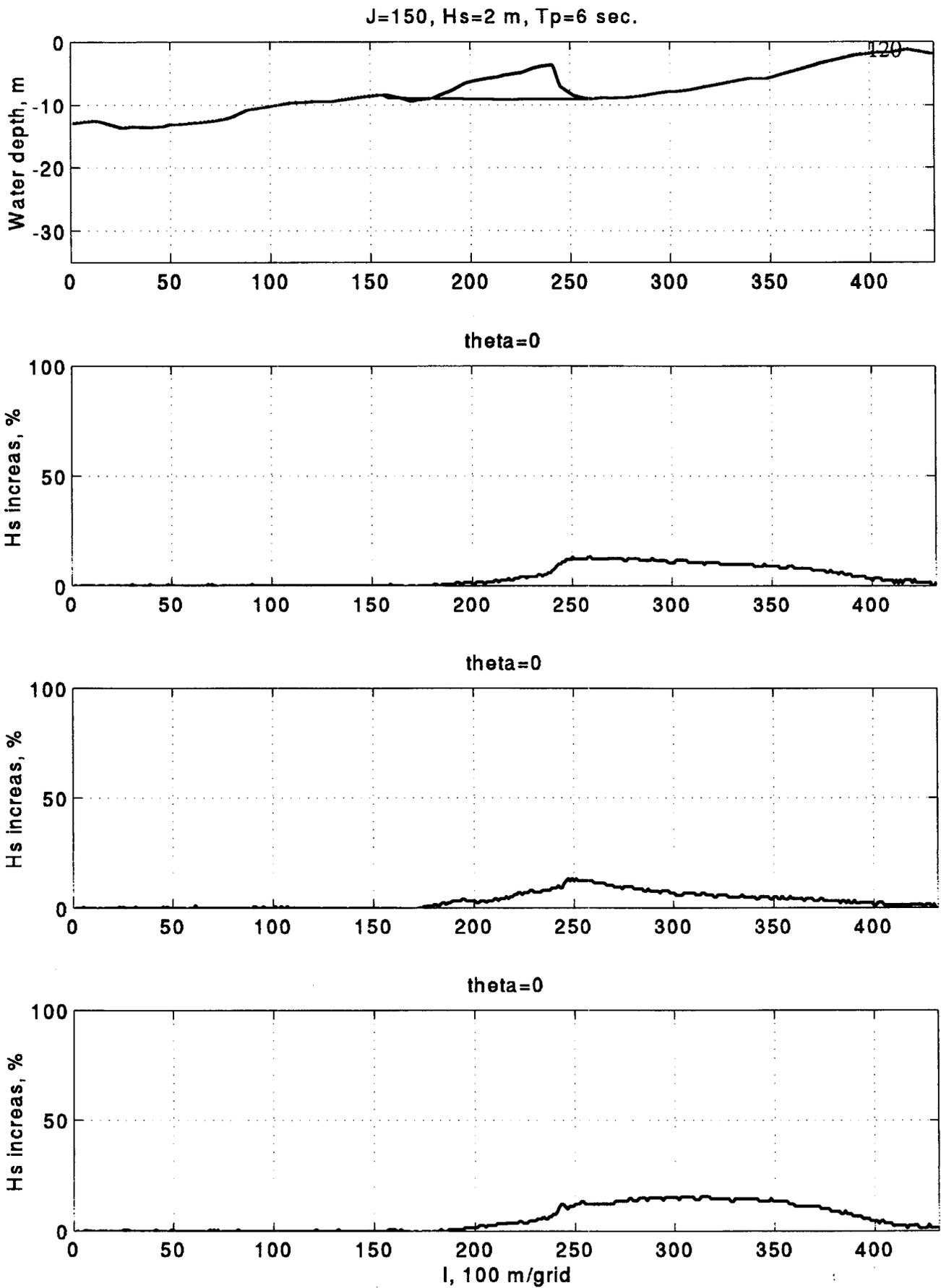
Figure B-8 Cross-sectional profiles of percentage of Hs increase due to shoal removal along J=150 in Case 3.
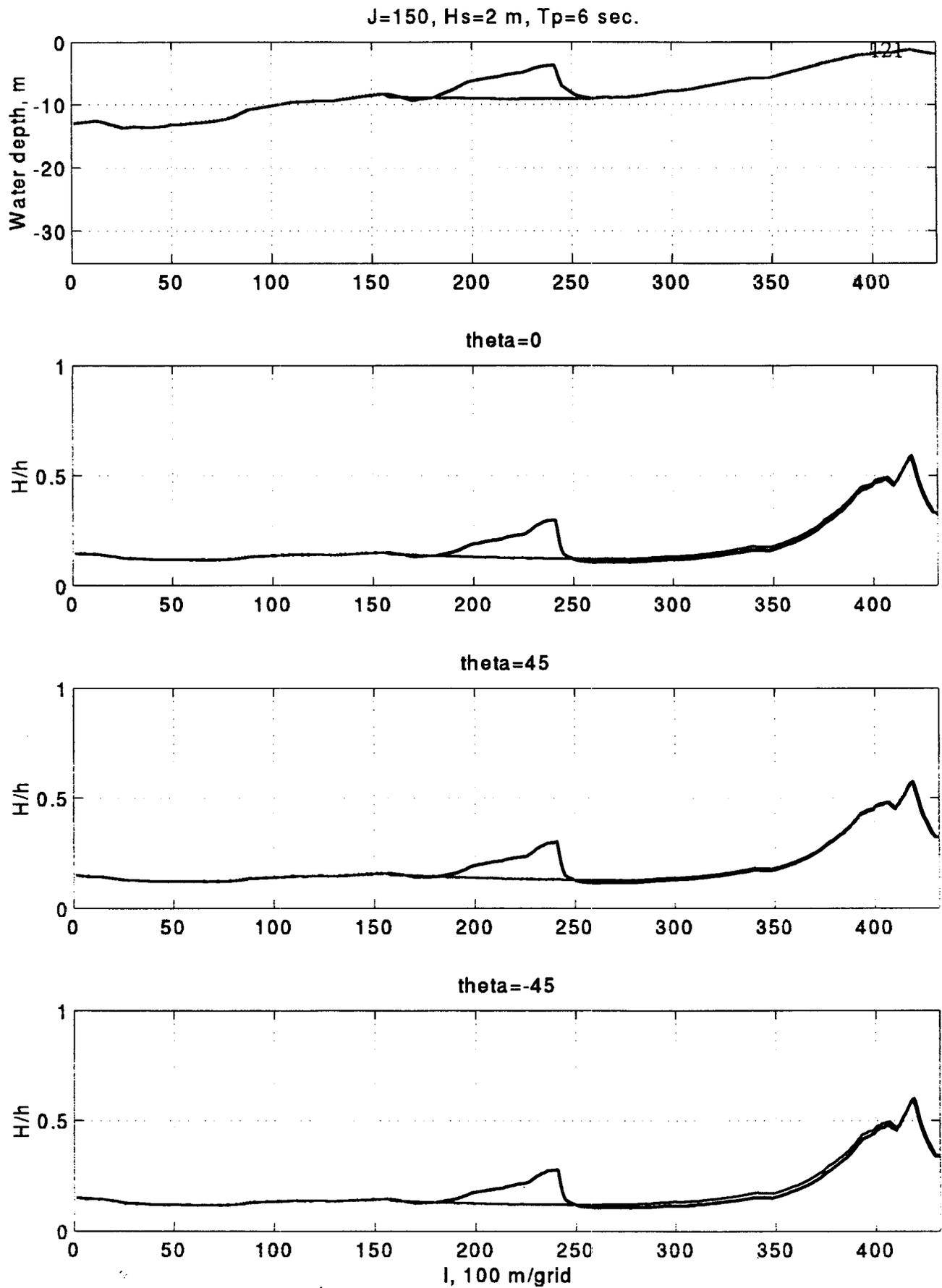
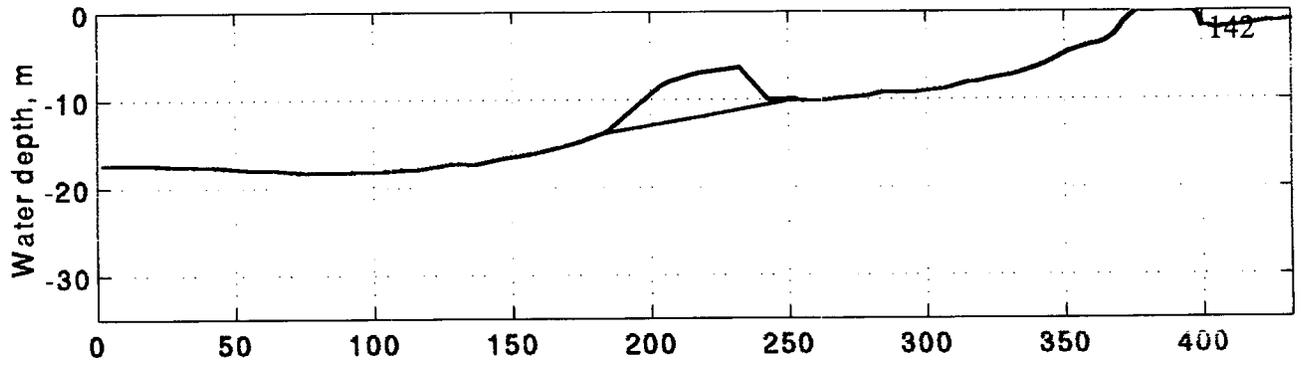Figure B-9 Cross-sectional profiles of depth-limited wave breaking index, H/h, along J = 150 in Case 3.
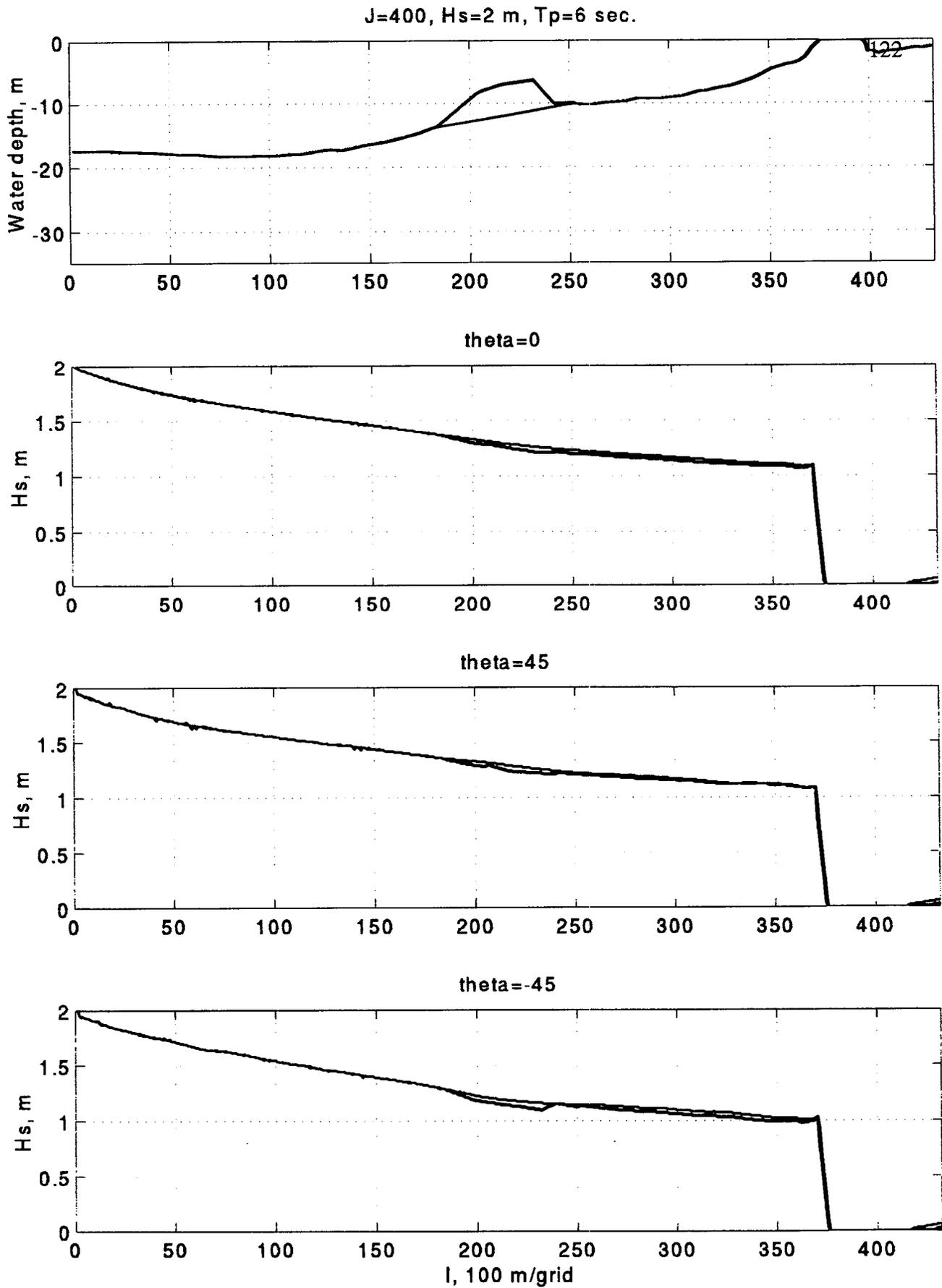
Figure B-10 Cross-sectional profiles of significant wave height, H_s, along J=400 in Case 2.
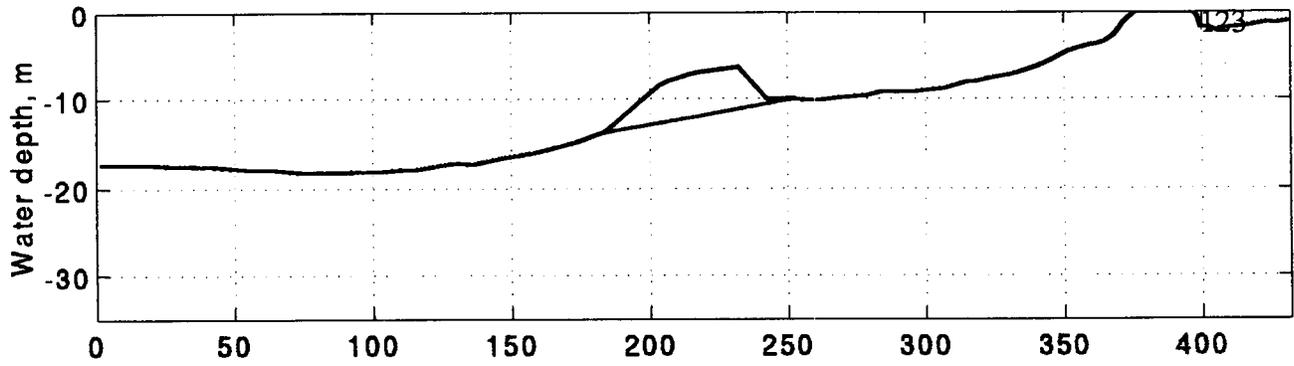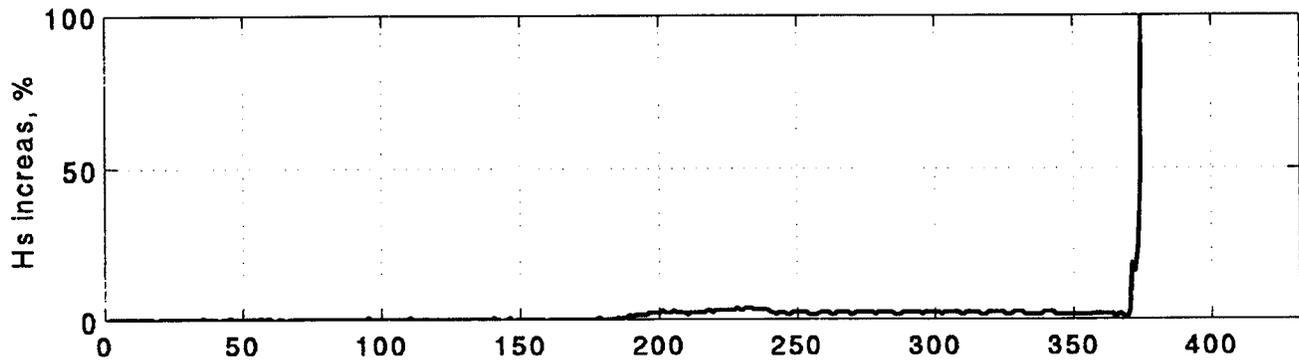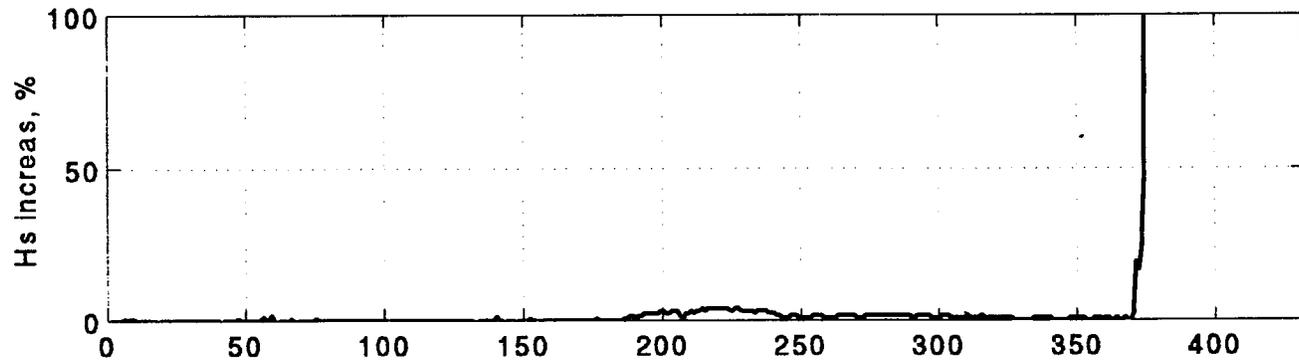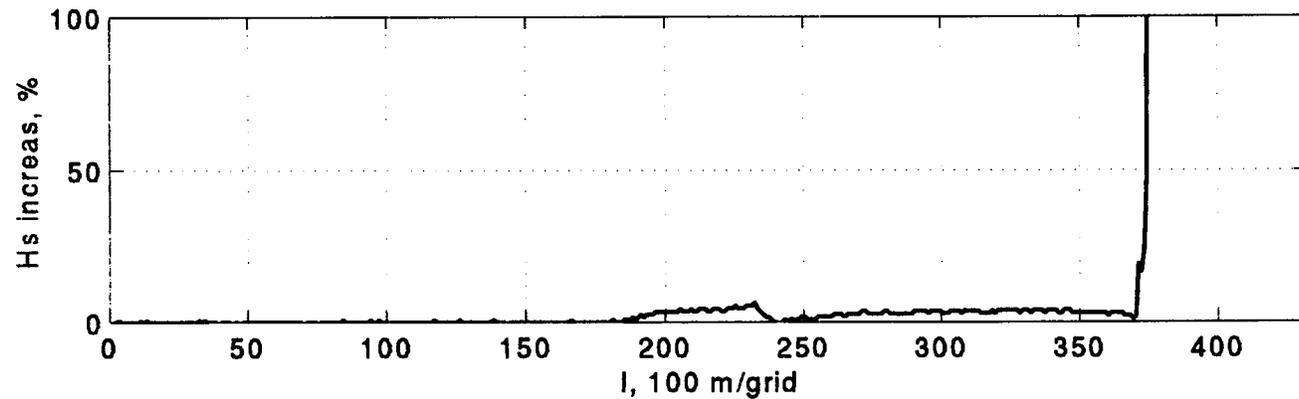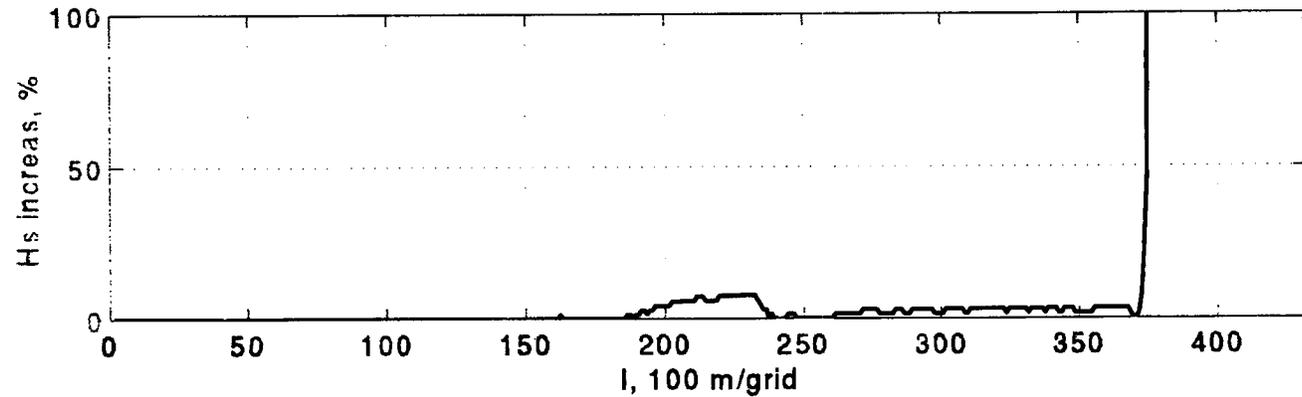
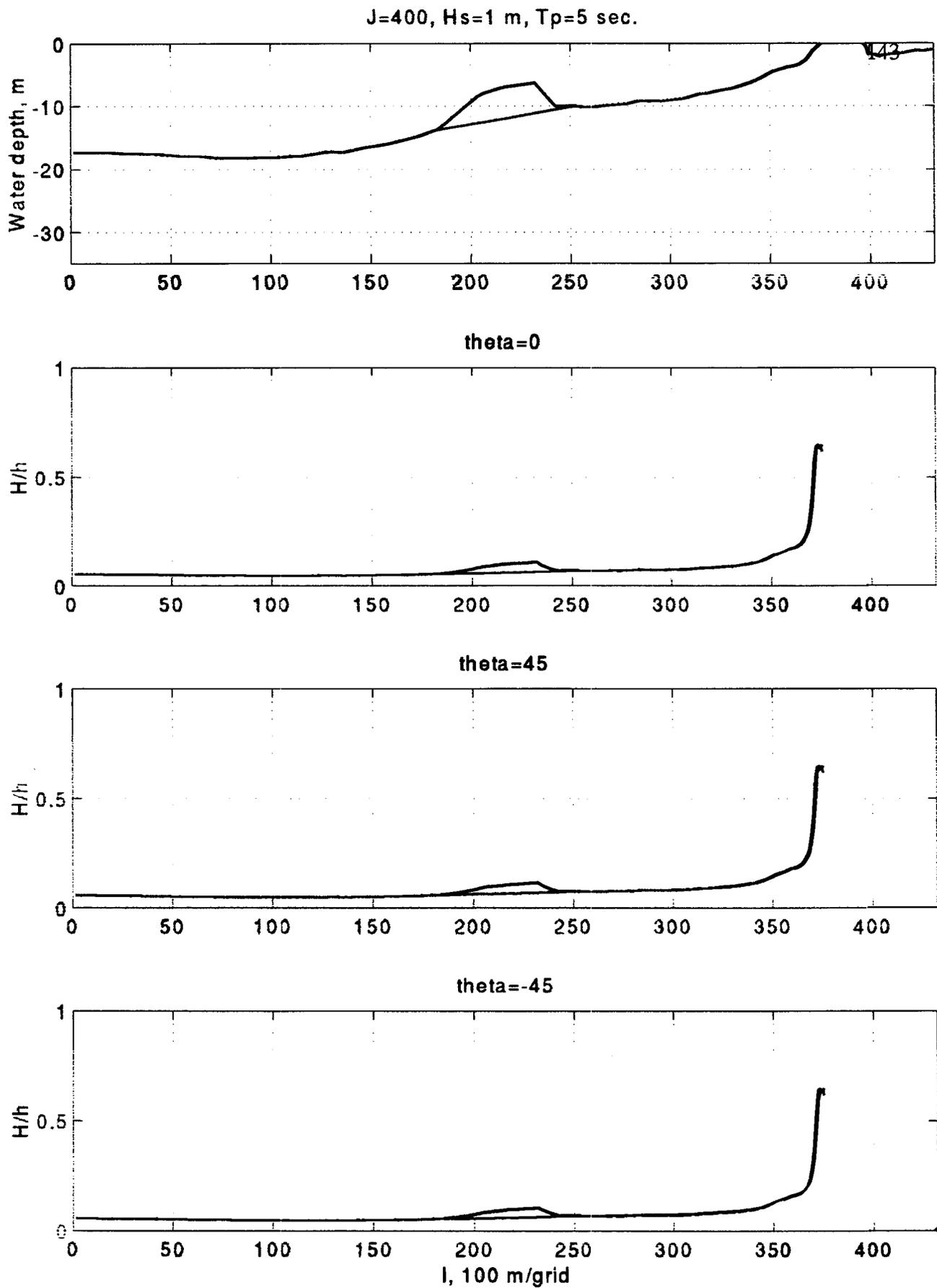Figure B-11 Cross-sectional profiles of percentage of Hs increase due to shoal removal along J=400 in Case 3.
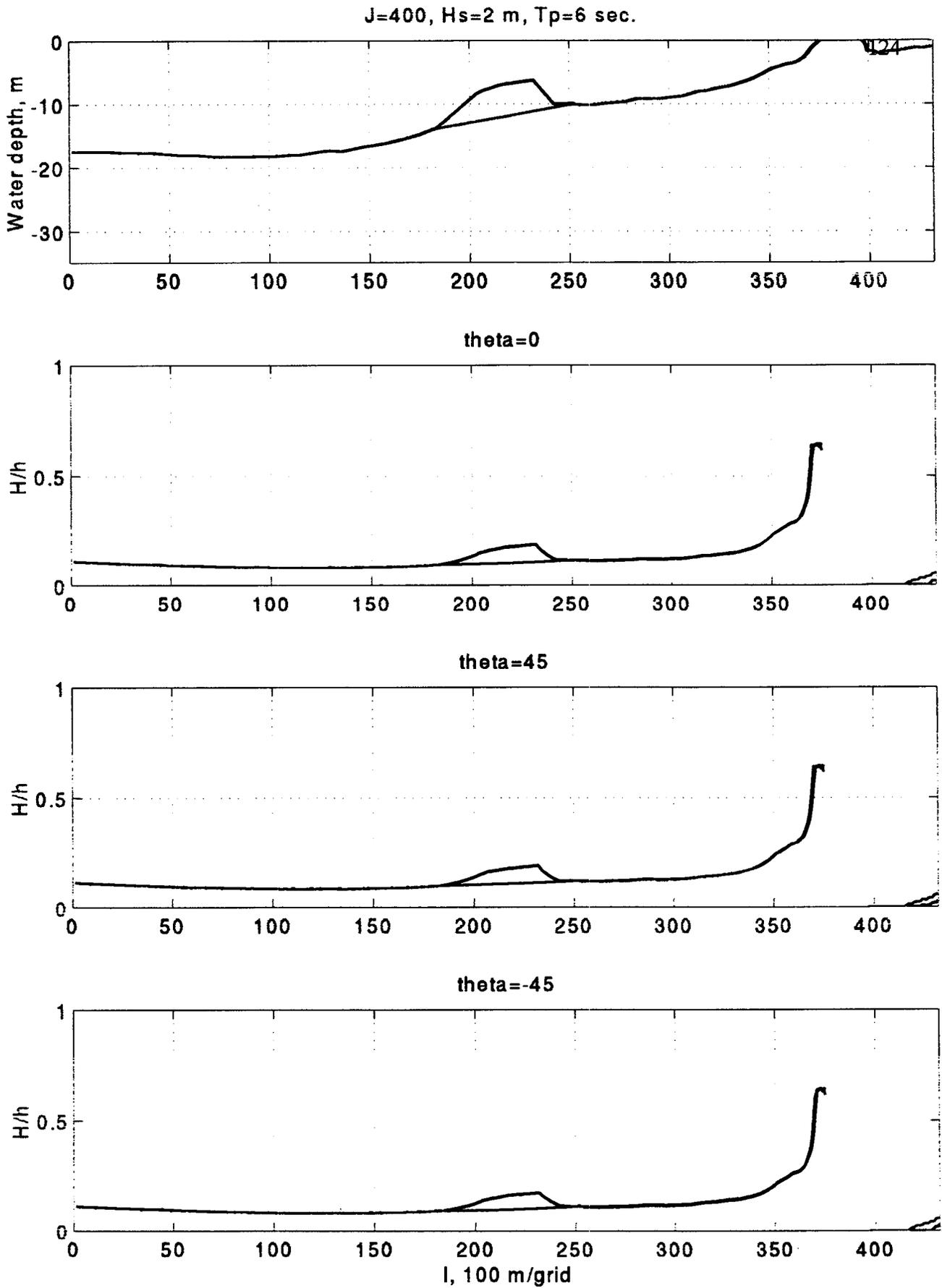
Figure B-12 Cross-sectional profiles of depth-limited wave breaking index, H/h, along J=400 in Case 3.
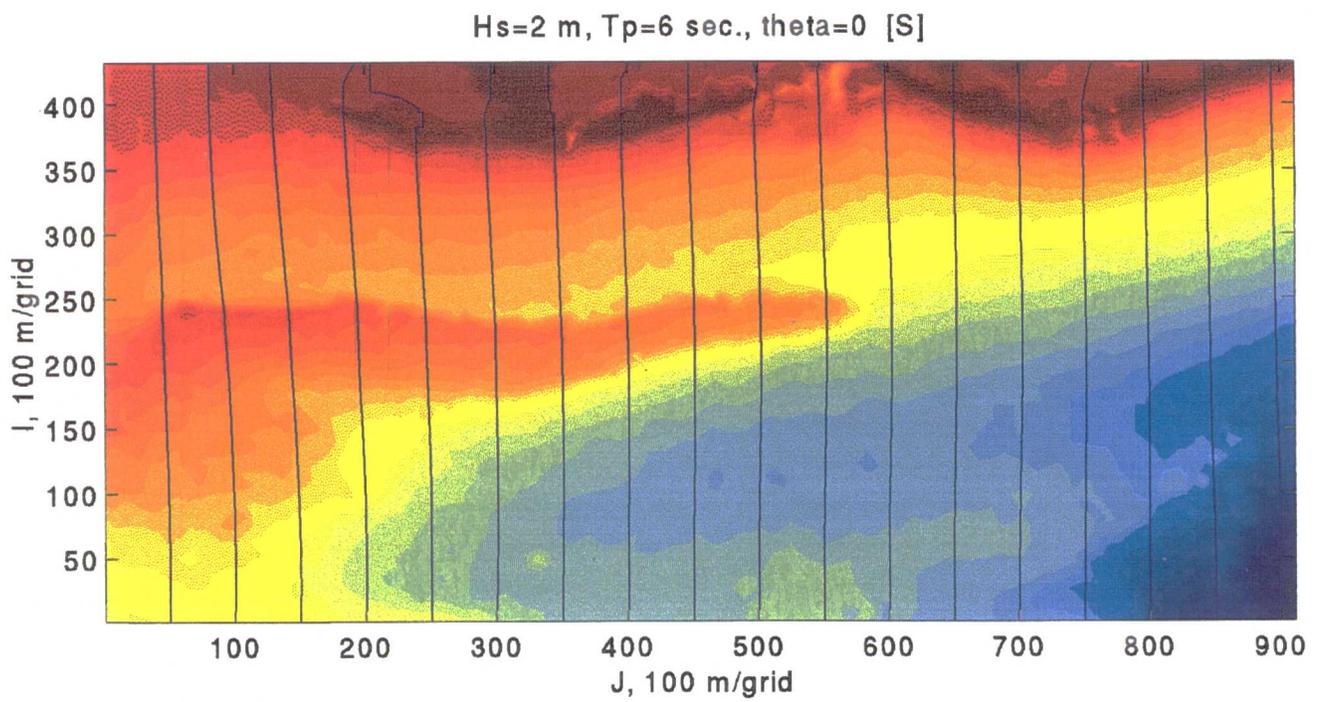
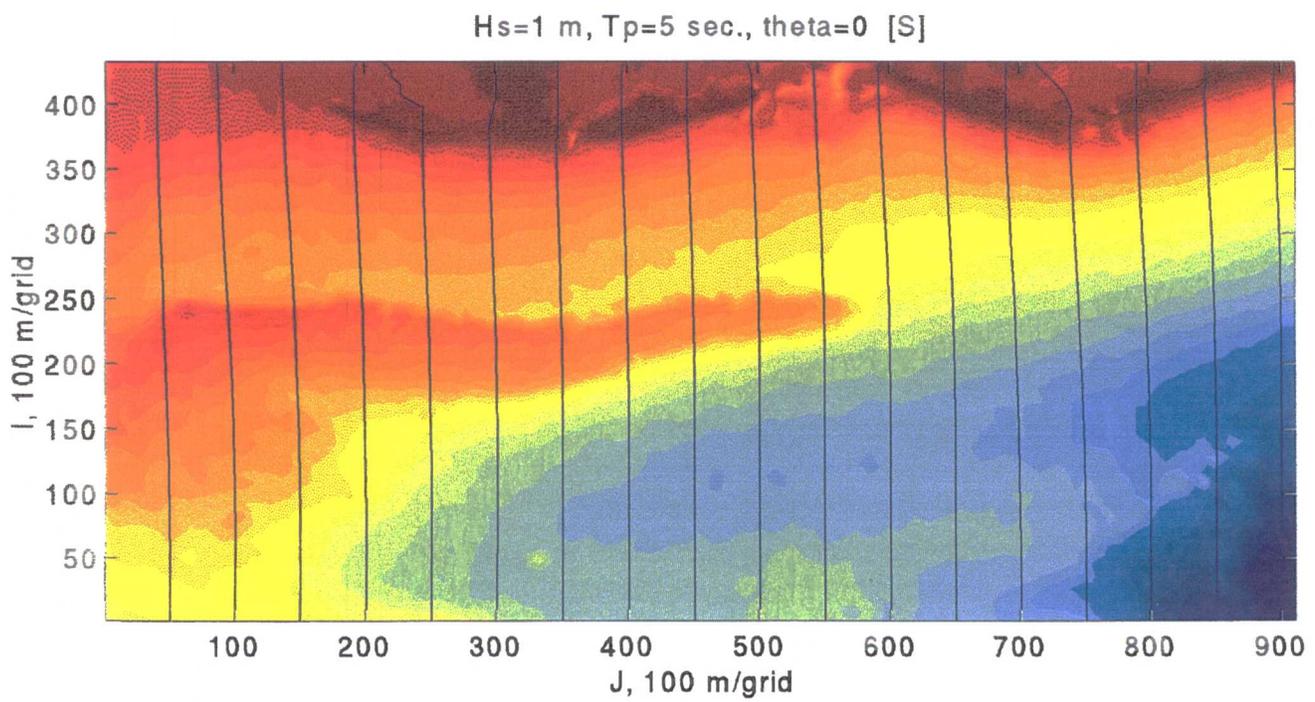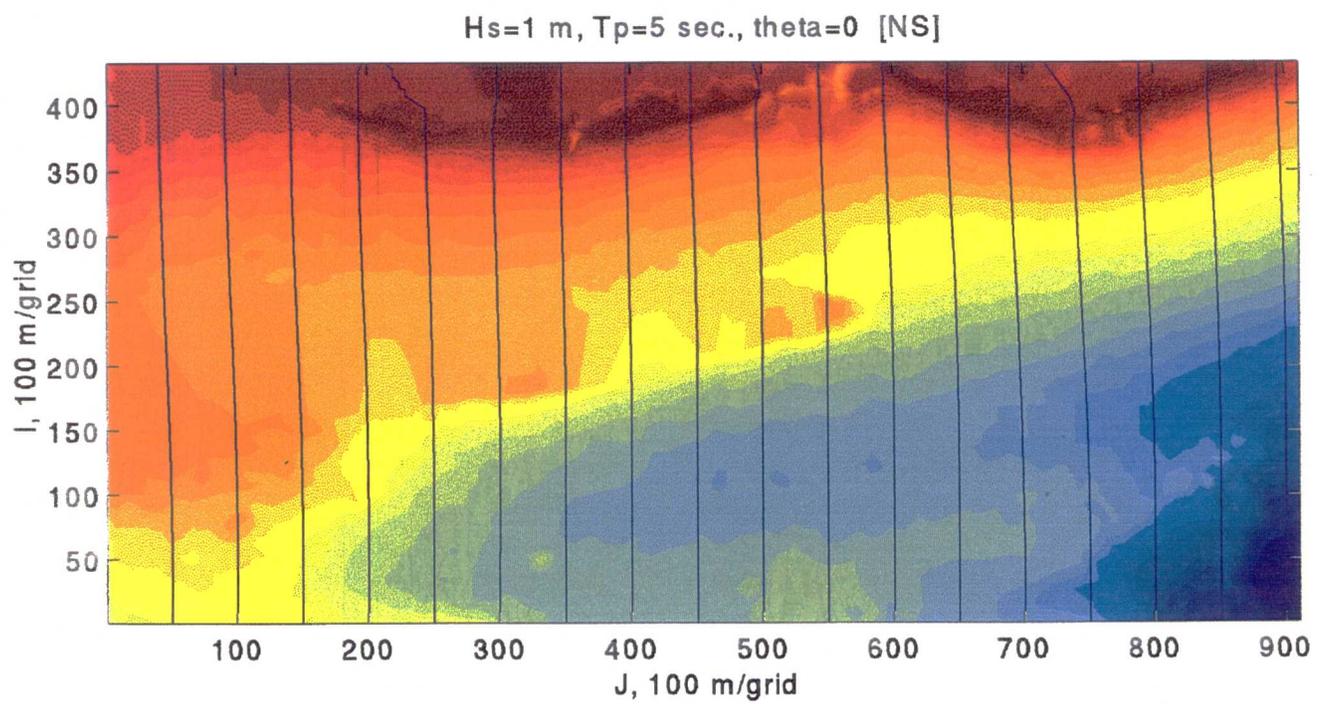Figure B-13 Modeled wave rays, Case 3, $\theta = 0°$, with Ship Shoal.
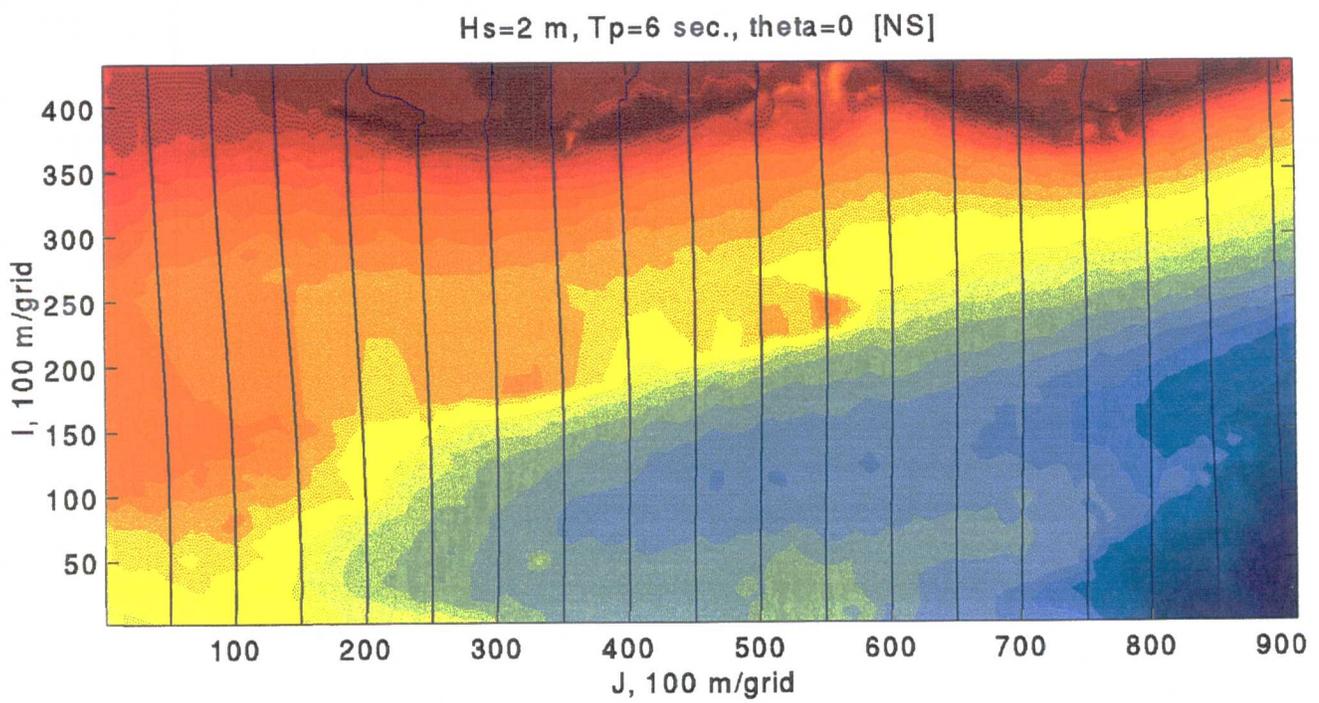
Figure B-14 Modeled wave rays, Case 3, $\theta = 0°$, without Ship Shoal.

127
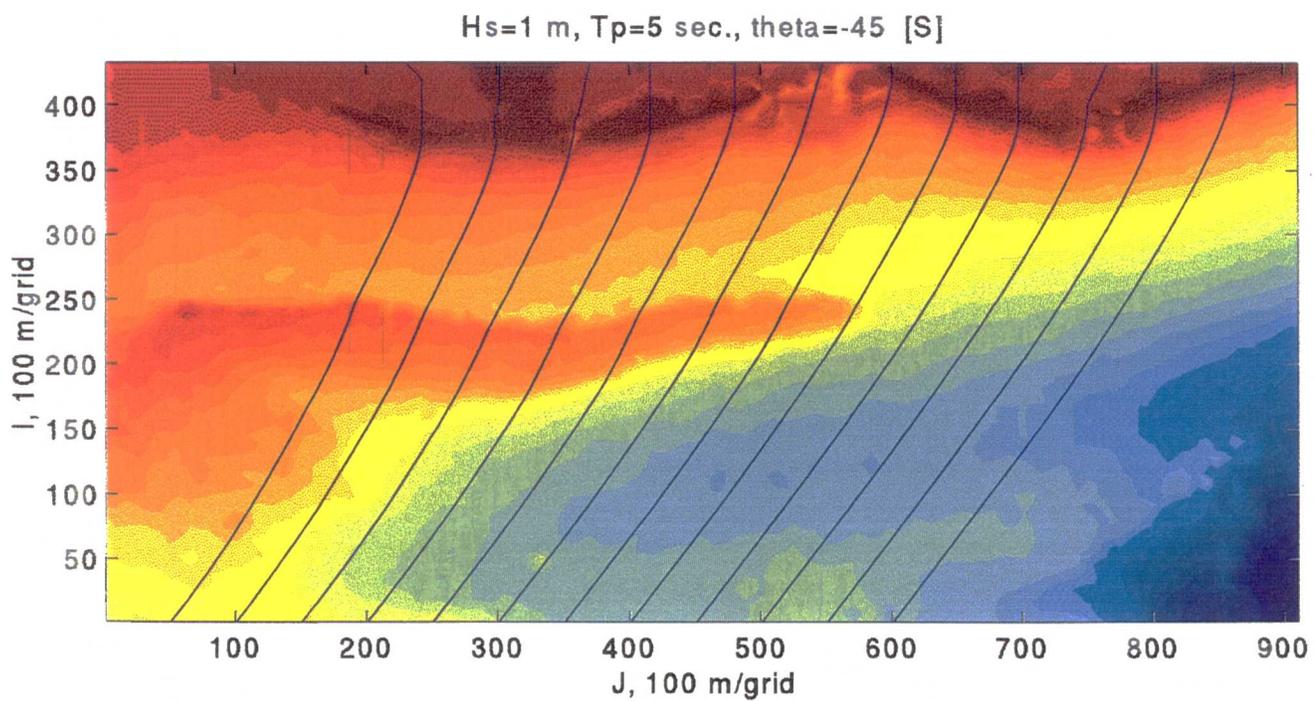

Hs=2 m, Tp=6 sec., theta=45 [S]
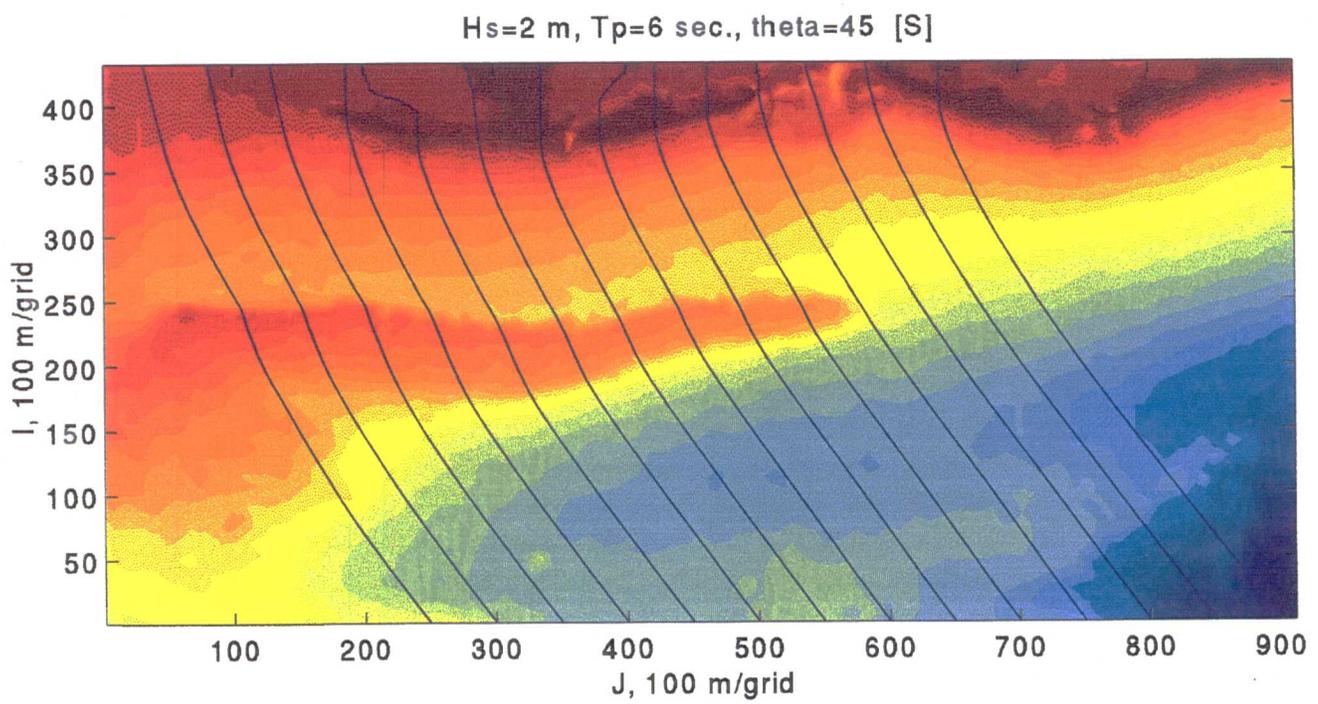
Figure B-15 Modeled wave rays, Case 3, θ=45°, with Ship Shoal.
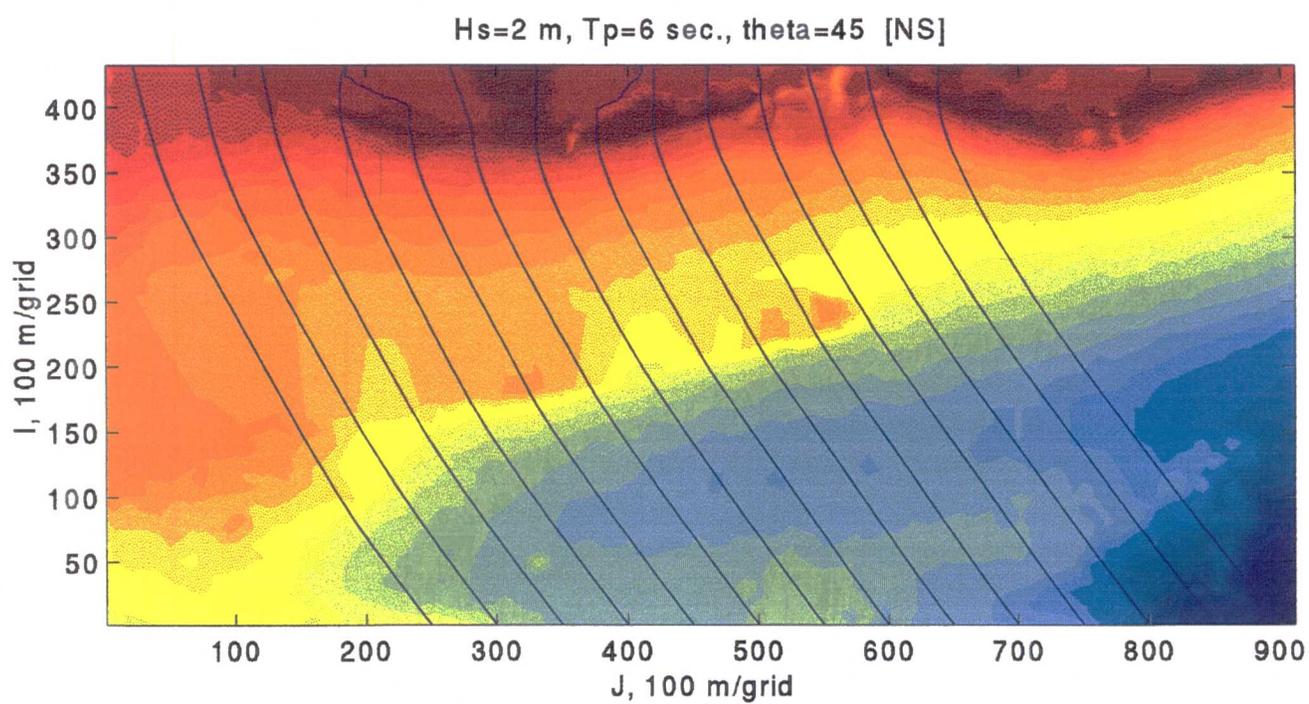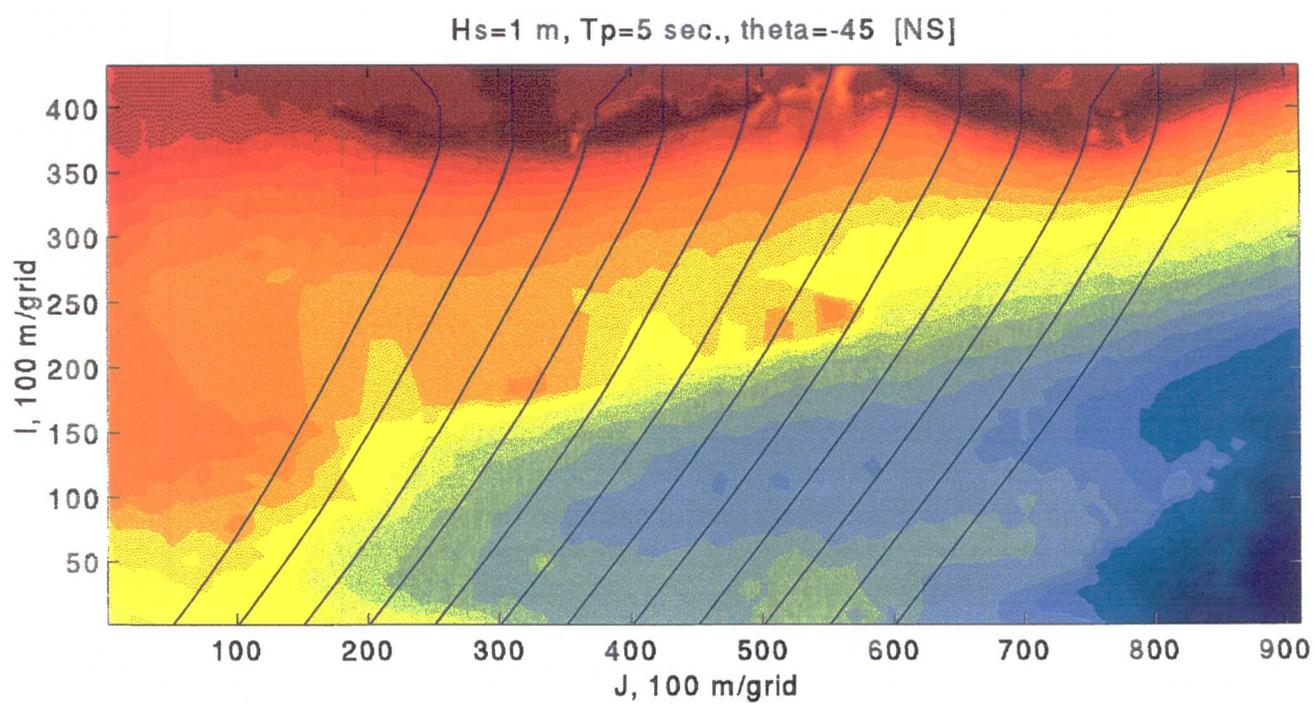
Figure B-16 Modeled wave rays, Case 3, $\theta = 45°$, without Ship Shoal.
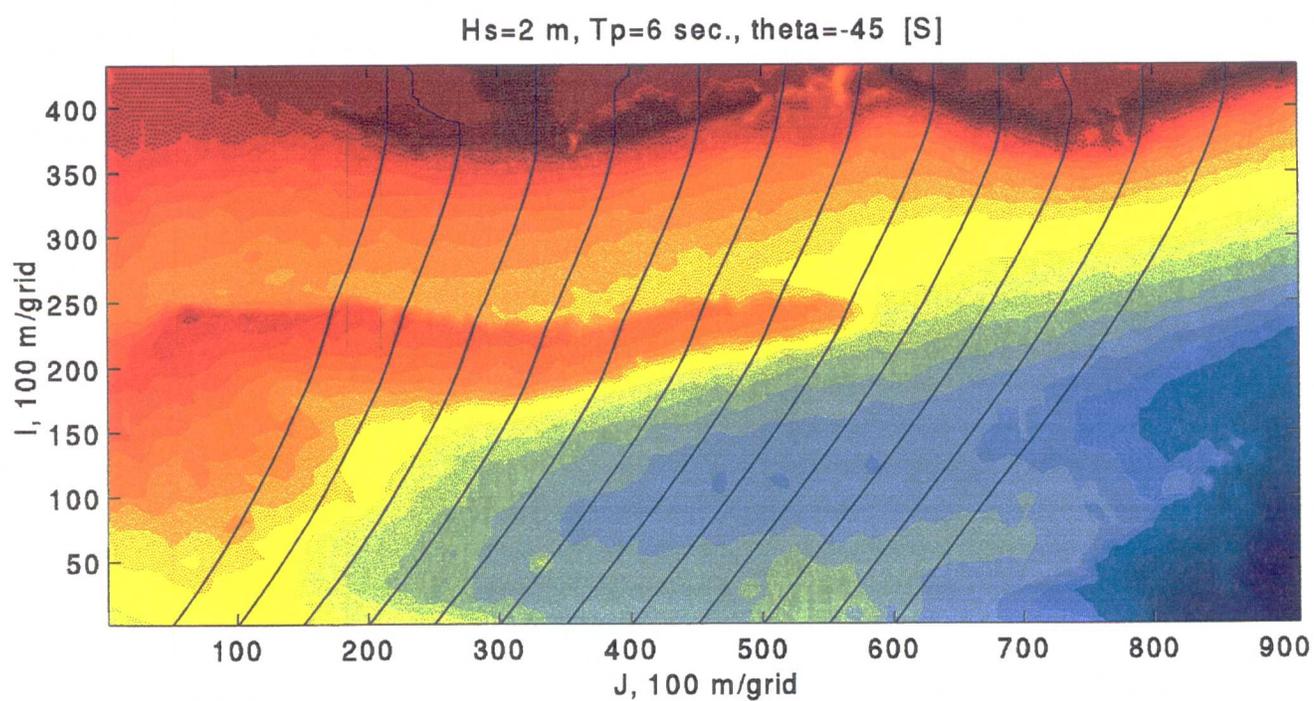
Figure B-17 Modeled wave rays, Case 3, θ=-45°, with Ship Shoal.

Hs=2 m, Tp=6 sec., theta=-45 [NS]
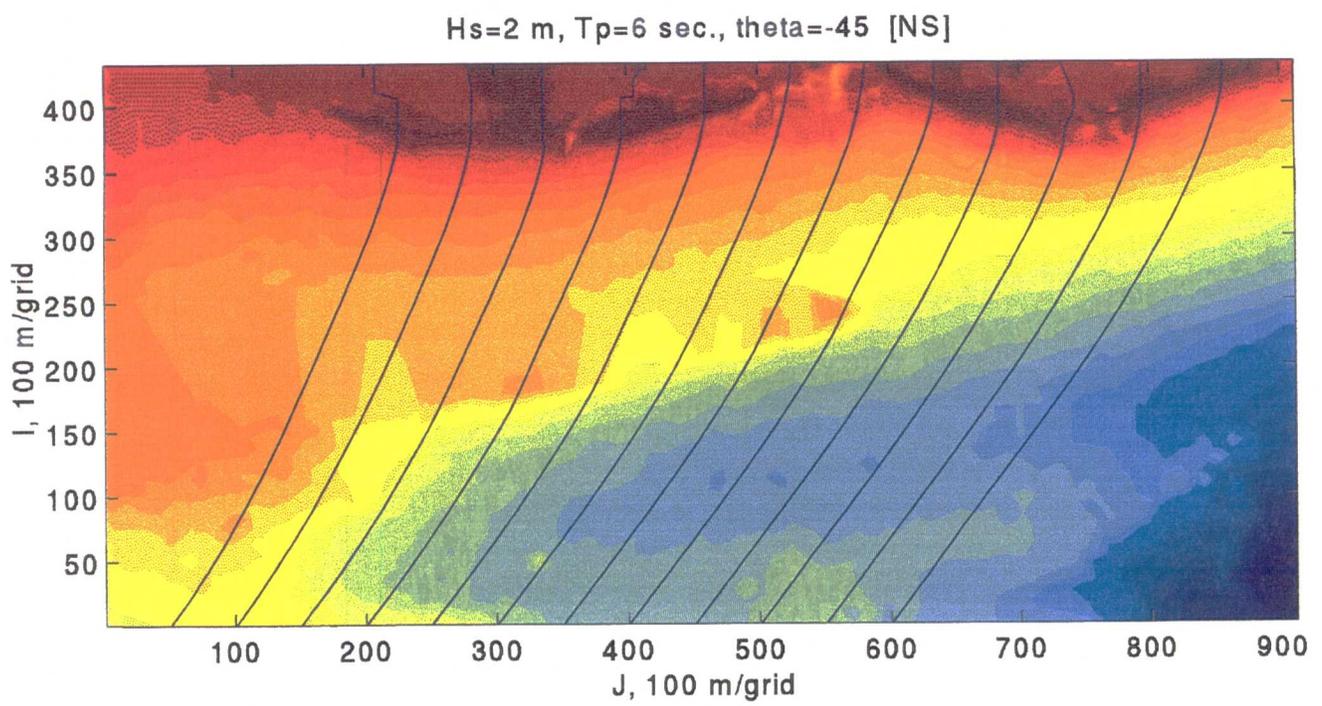
Figure B-18 Modeled wave rays, Case 3, $\theta = -45°$, without Ship Shoal.

APPENDIX C. Case 4: $H_s = 1$ m, $T_p = 5$ seconds

Figure C-1 Image of modeled significant wave height, Case 4, θ=0°, with Ship Shoal.

Figure C-2 Image of modeled significant wave height, Case 4, $\theta = 0°$, without Ship Shoal.

Figure C-3 Image of modeled significant wave height, Case 4, $\theta=45°$, with Ship Shoal.

Figure C-4 Image of modeled significant wave height, Case 4, $\theta = 45°$, without Ship Shoal.
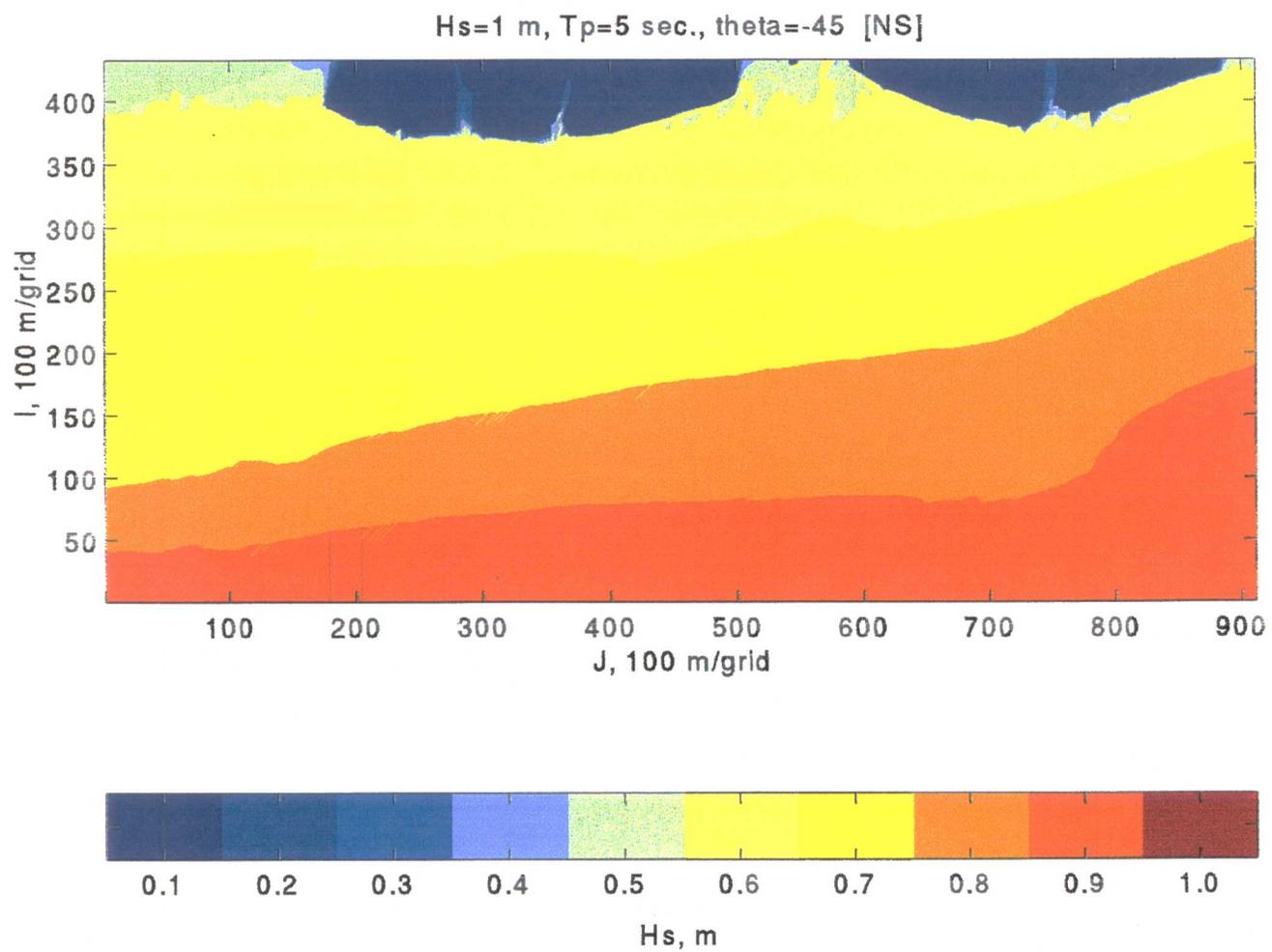
Figure C-5 Image of modeled significant wave height, Case 4, $\theta = -45°$, with Ship Shoal.
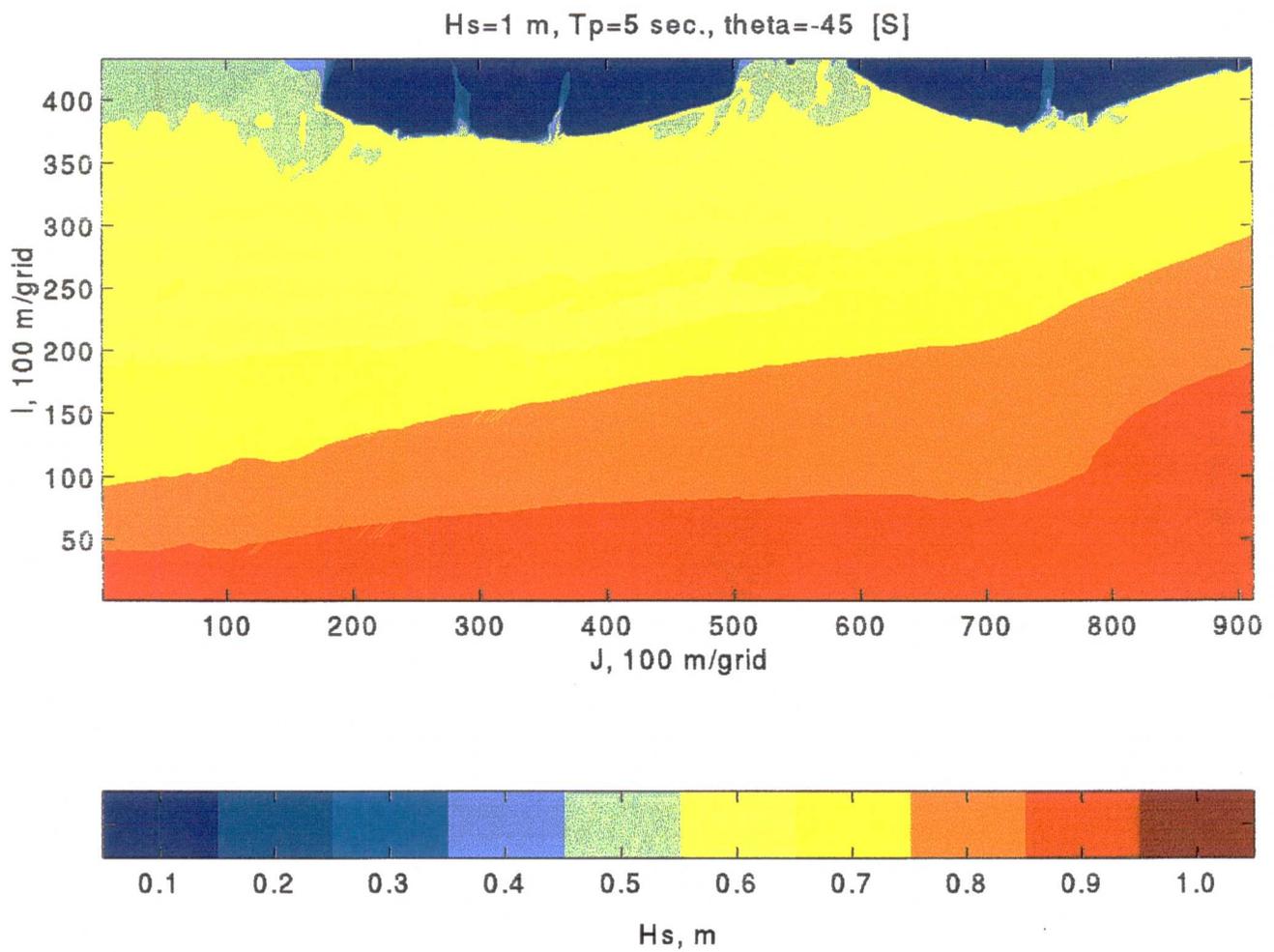
Figure C-6 Image of modeled significant wave height, Case 4, $\theta = -45°$, without Ship Shoal.
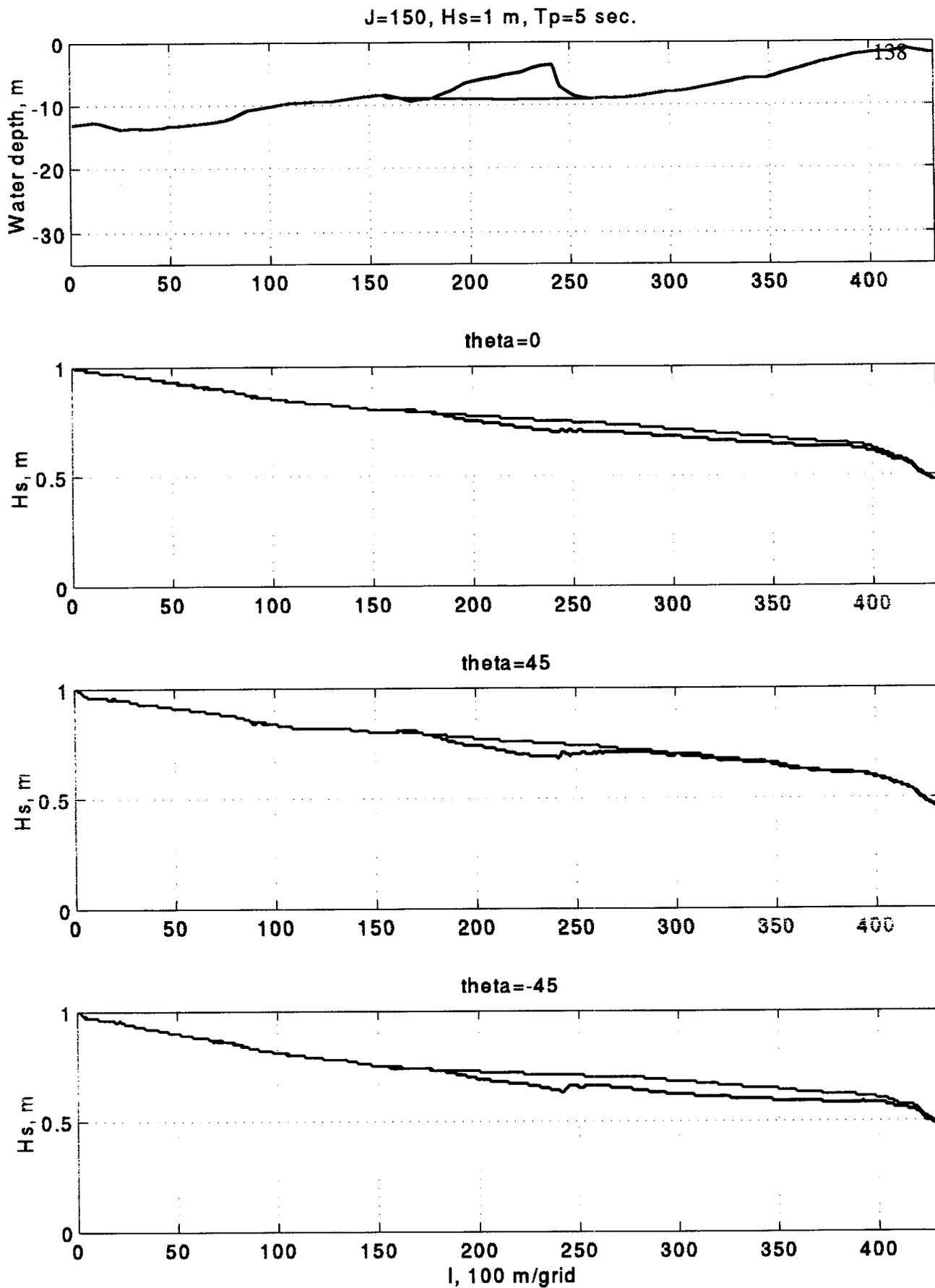
Figure C-7 Cross-sectional profiles of significant wave height, H_s, along J=150 in Case 4.
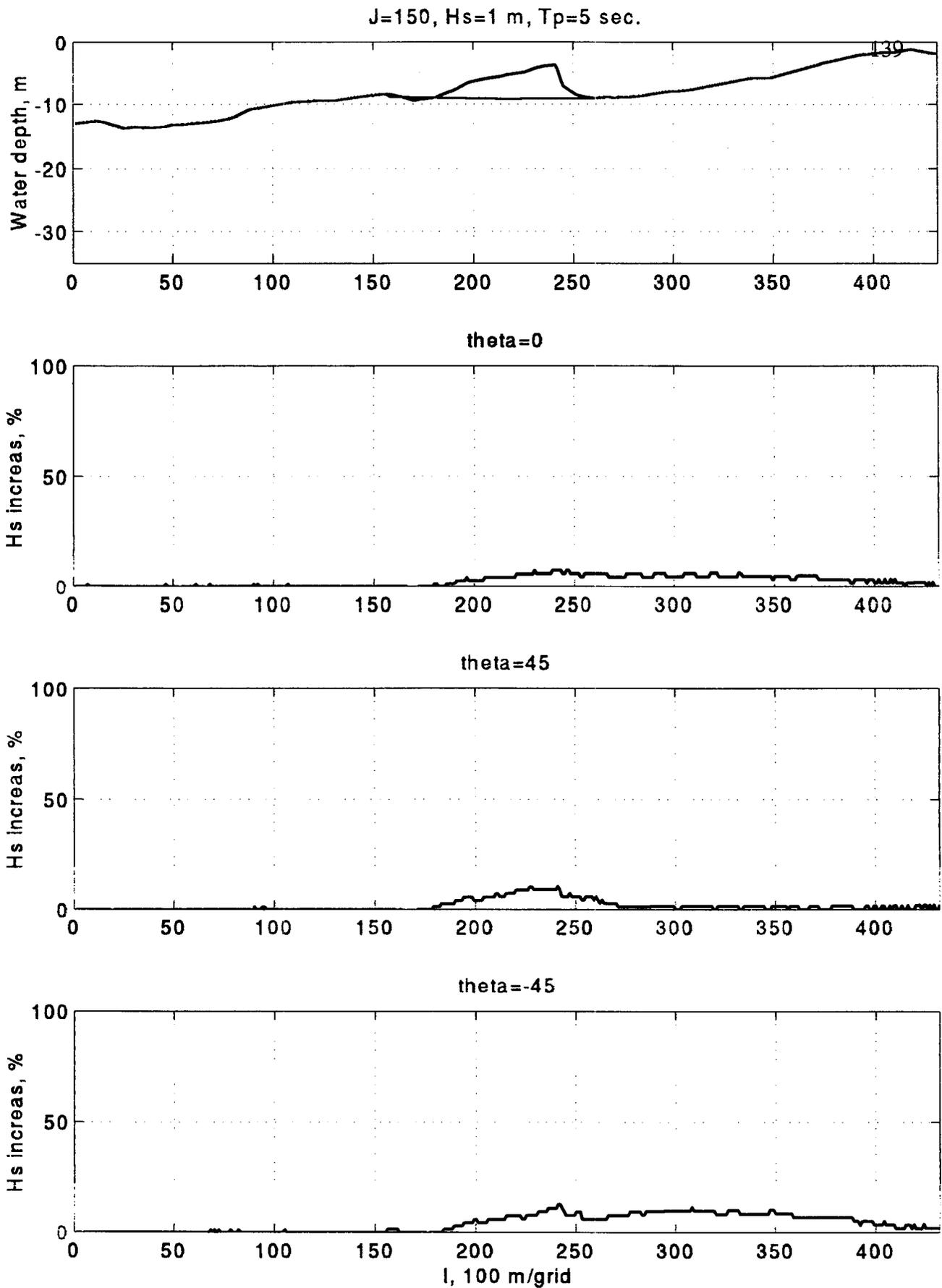
Figure C-8 Cross-sectional profiles of percentage of Hs increase due to shoal removal along J=150 in Case 4.
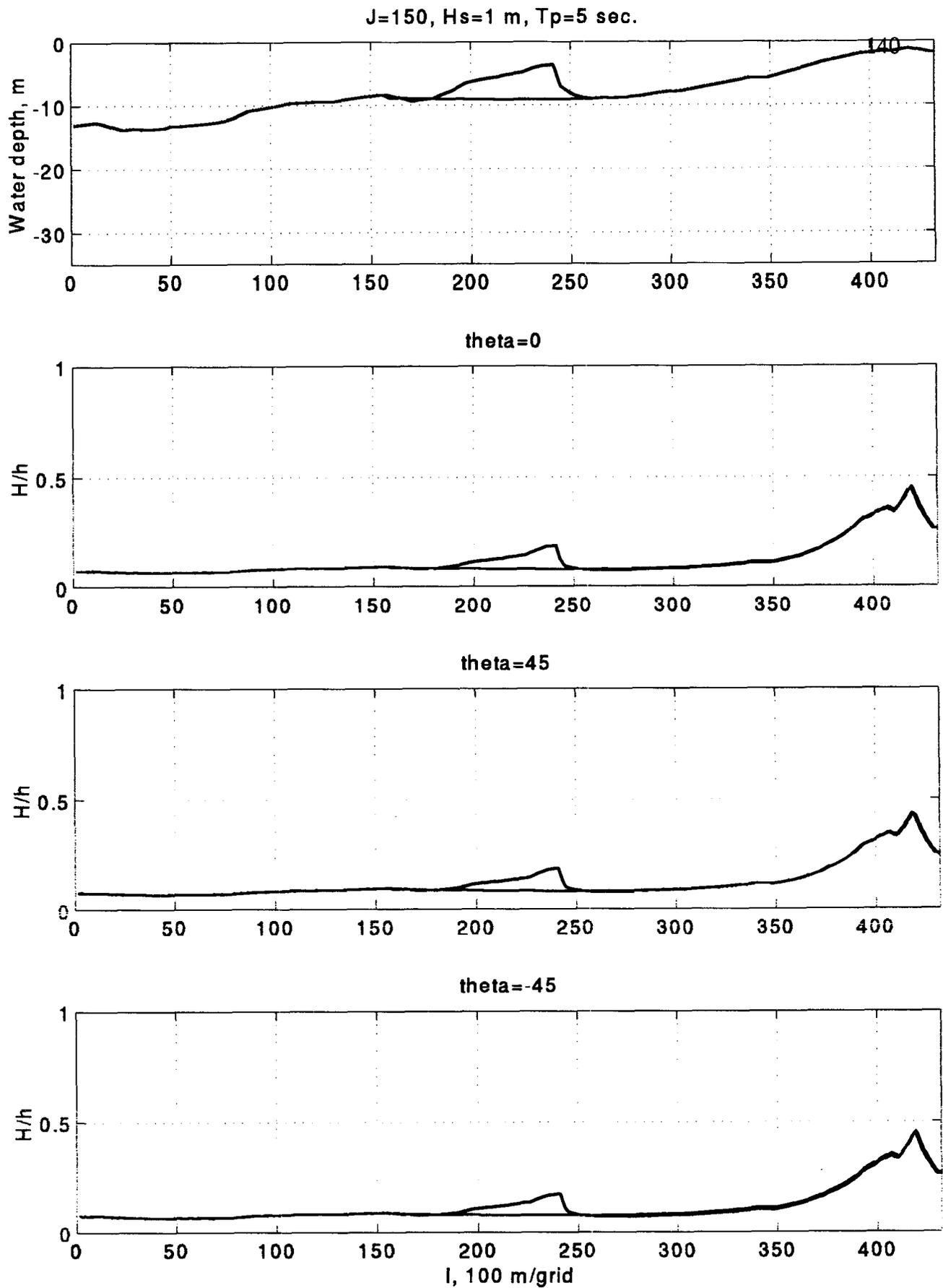
Figure C-9 Cross-sectional profiles of depth-limited wave breaking index, H/h, along J=150 in Case 4.

Figure C-10 Cross-sectional profiles of significant wave height, H_s, along J=400 in Case 2.
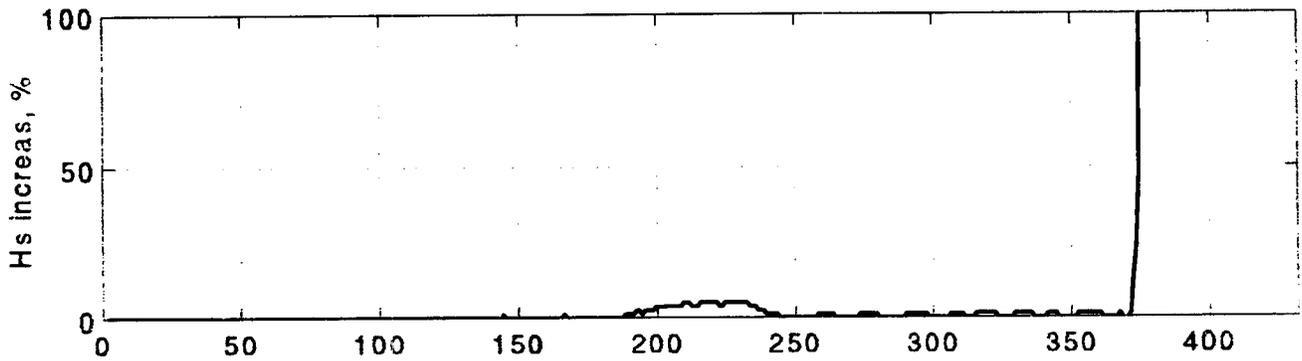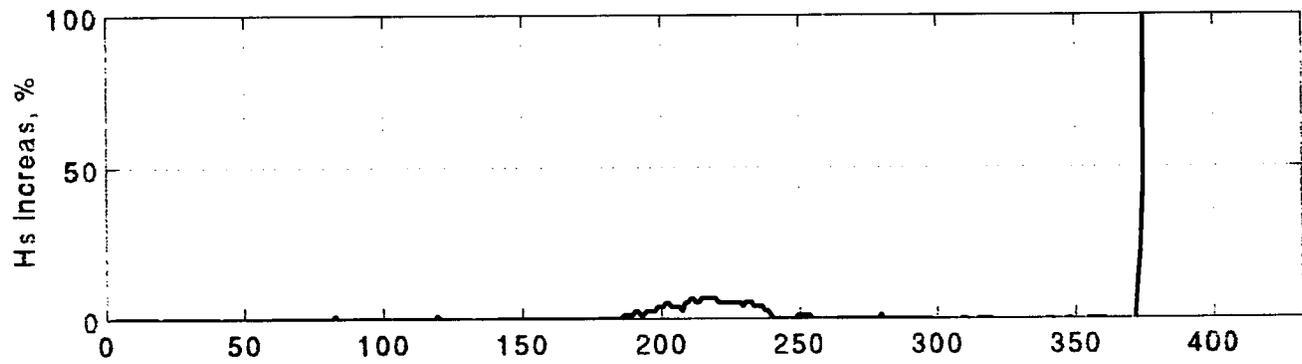
Figure C-11 Cross-sectional profiles of percentage of Hs increase due to shoal removal along J=400 in Case 4.

Figure C-12 Cross-sectional profiles of depth-limited wave breaking index, H/h, along J=400 in Case 4.

Figure C-13 Modeled wave rays, Case 4, $\theta = 0°$, with Ship Shoal.

Hs=1 m, Tp=5 sec., theta=0 [NS]

Figure C-14 Modeled wave rays, Case 4, $\theta = 0°$, without Ship Shoal.

Figure C-15 Modeled wave rays, Case 4, $\theta = 45°$, with Ship Shoal.

Figure C-16 Modeled wave rays, Case 4, $\theta = 45°$, without Ship Shoal.

Hs=1 m, Tp=5 sec., theta=45 [S]
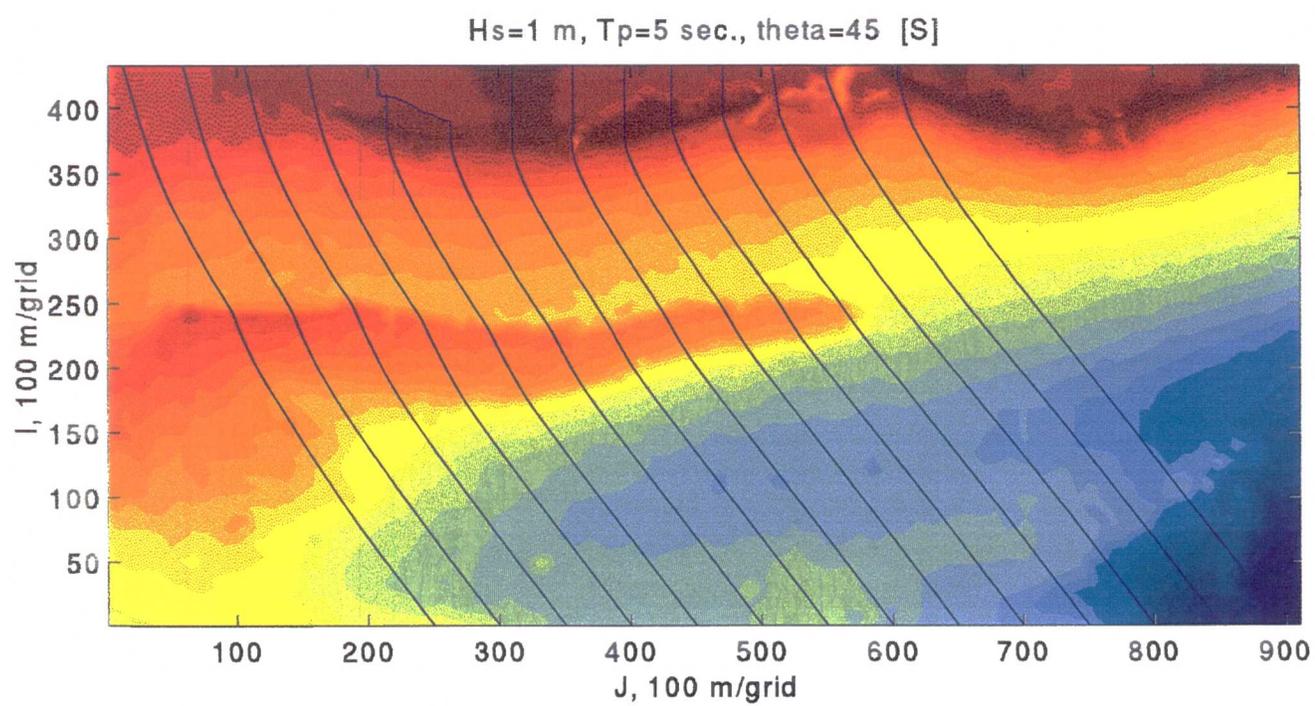
Figure C-17 Modeled wave rays, Case 4, $\theta = -45°$, with Ship Shoal.
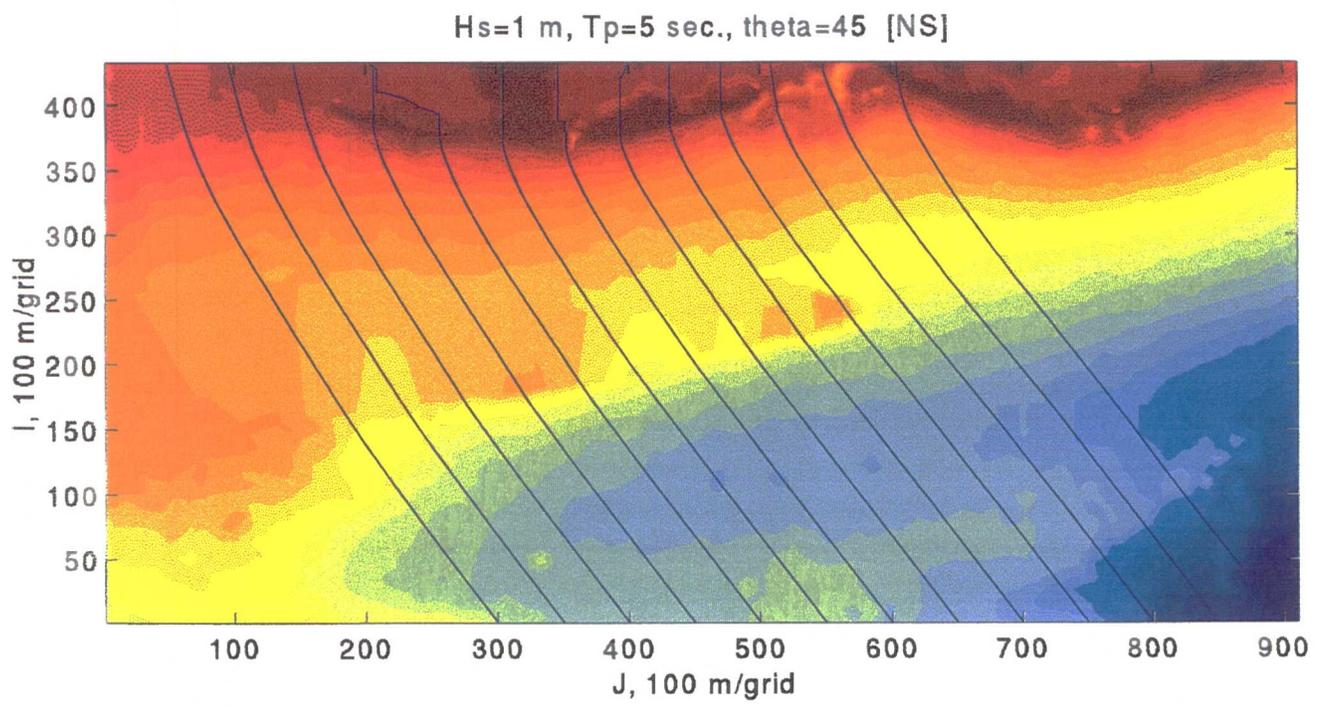
Figure C-18 Modeled wave rays, Case 4, $\theta = -45°$, without Ship Shoal.

APPENDIX D. Wave height distribution with wind forcing function included for cases 1 through 4.
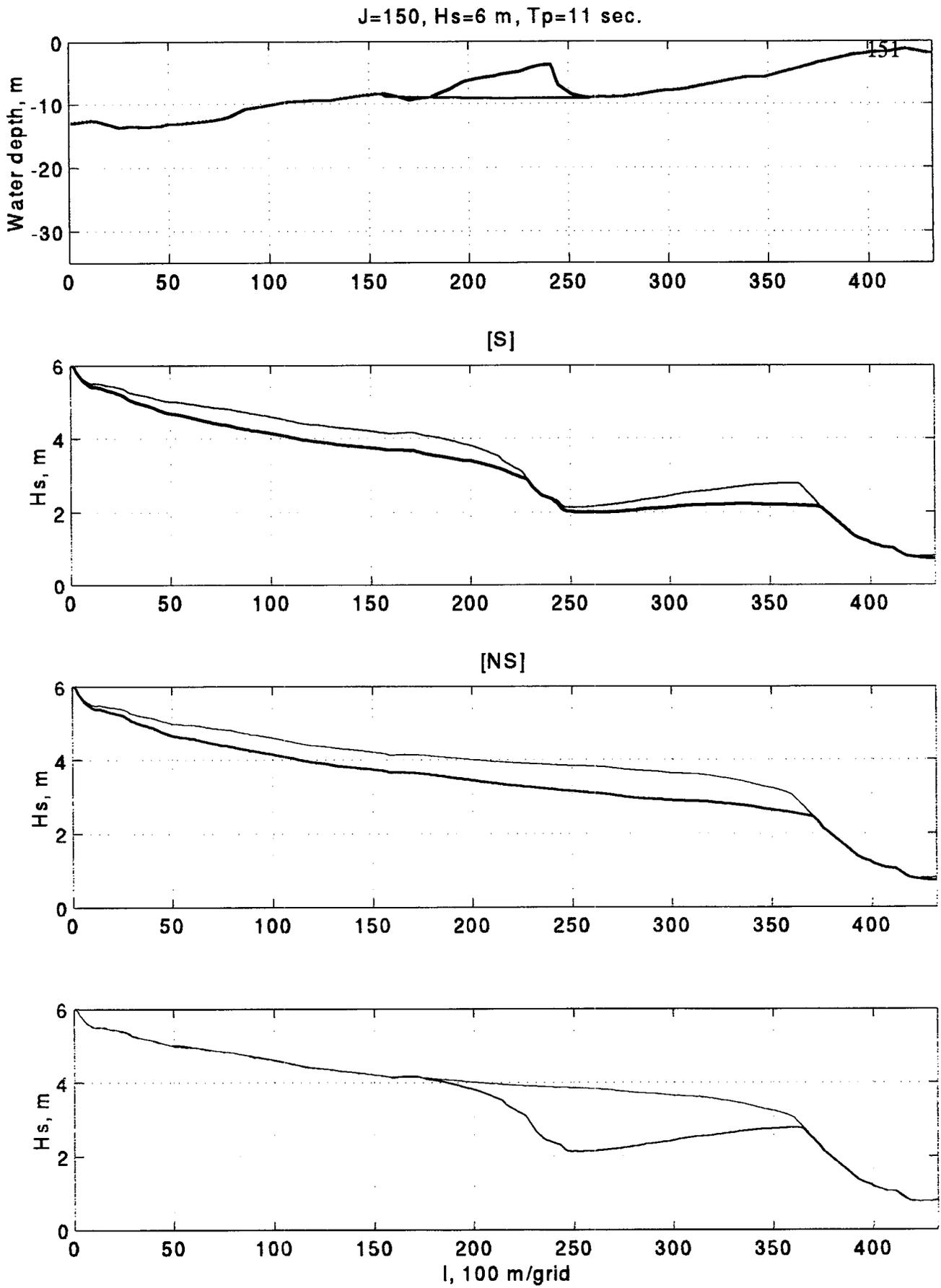
Figure D-1 Wind effect on the wave height distribution in Case 1, sectional profiles at J=150.
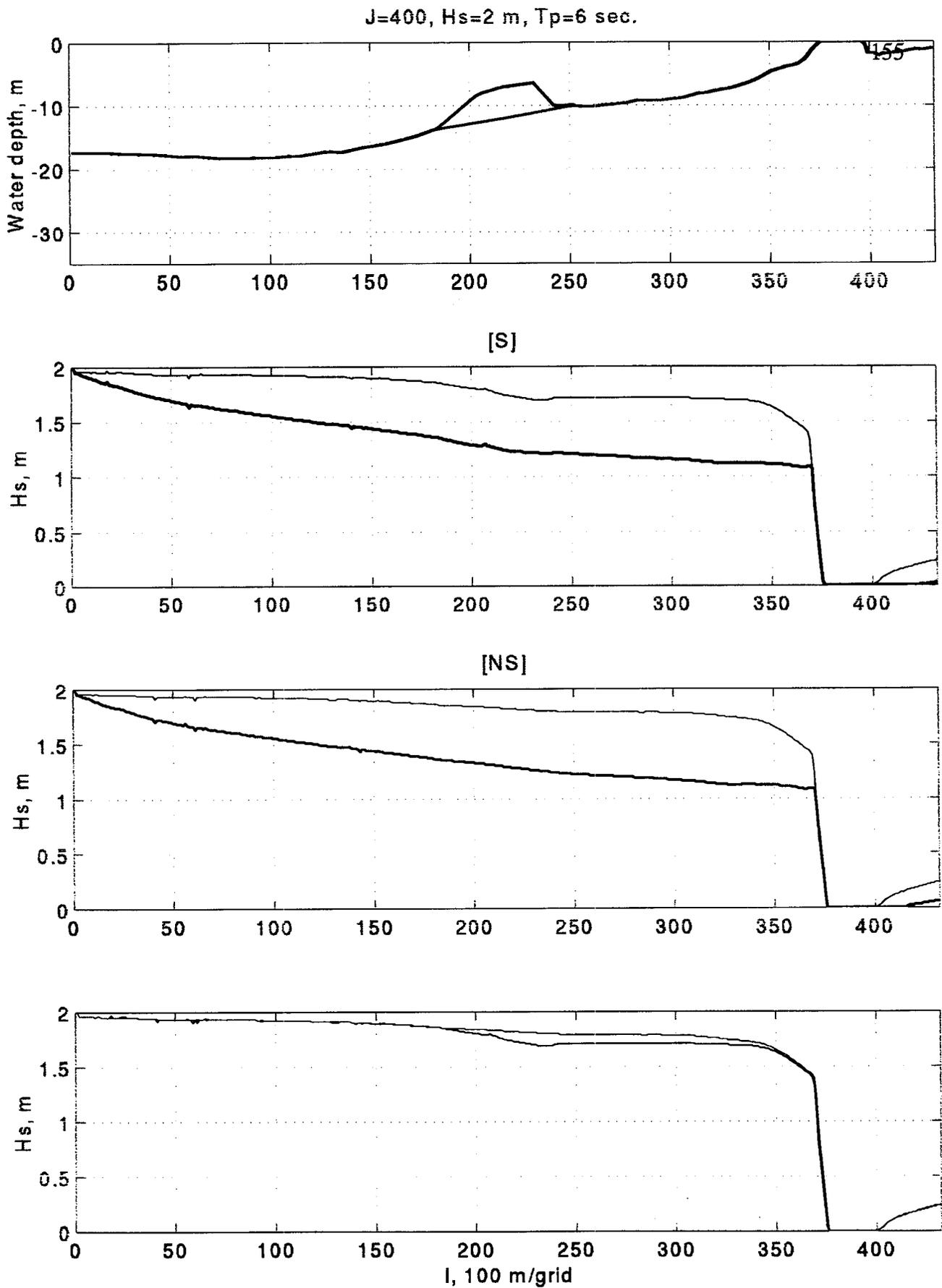
J=400, Hs=6 m, Tp=11 sec.

[S]

[NS]
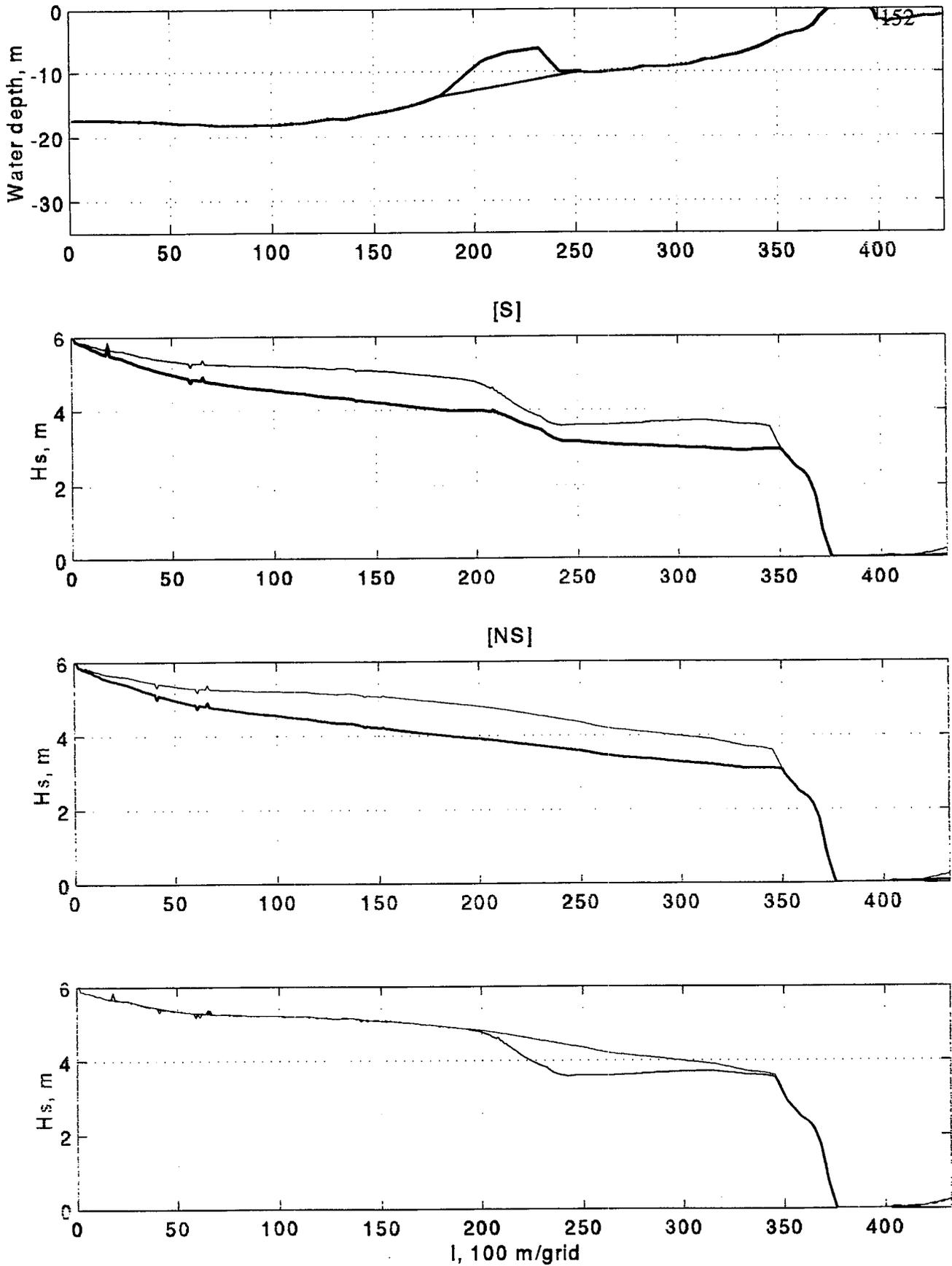
Figure D-2   Wind effect on the wave height distribution in Case 1, sectional profiles at J=400.
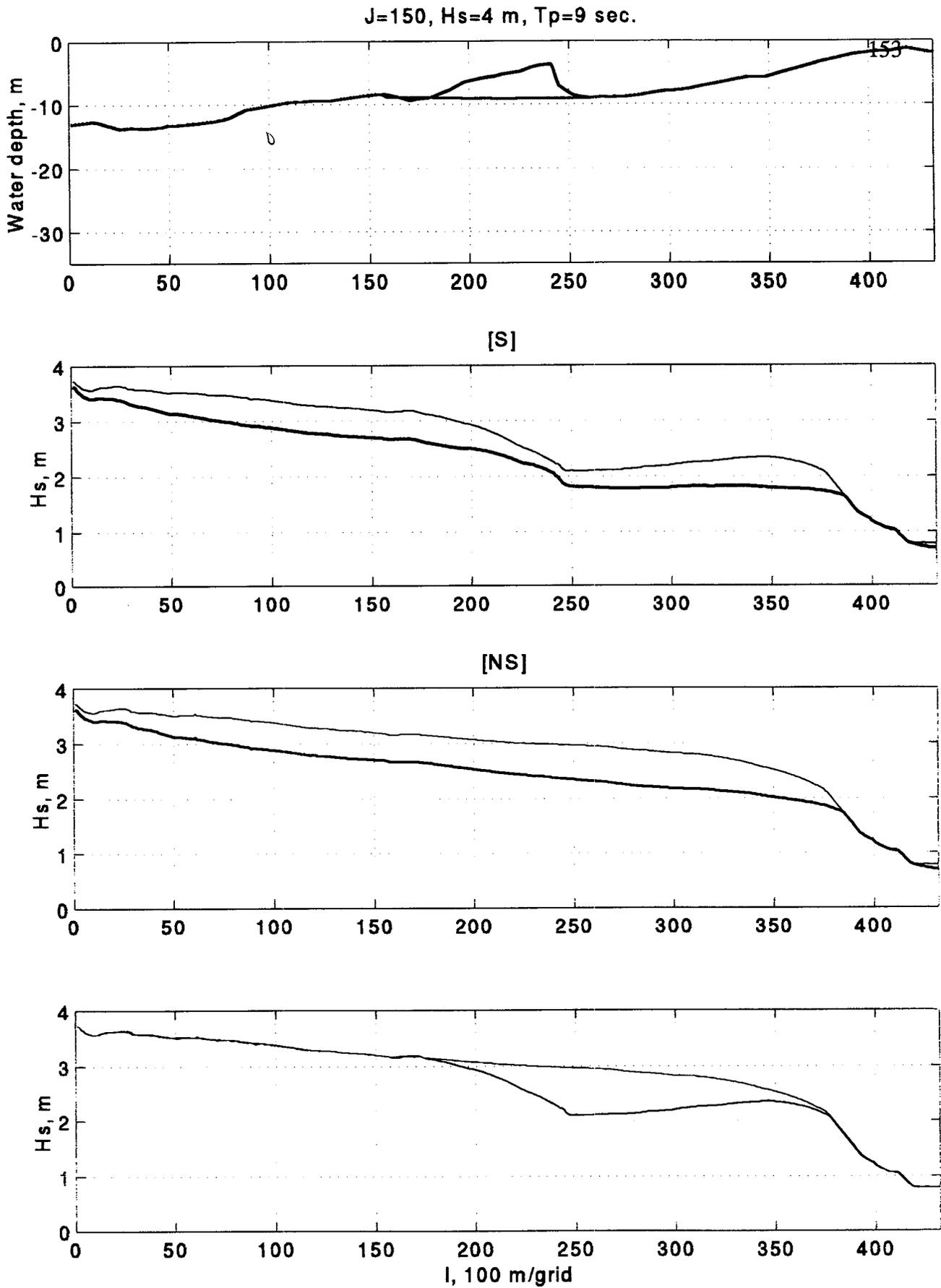
Figure D-3   Wind effect on the wave height distribution in Case 2, sectional profiles at J=150.
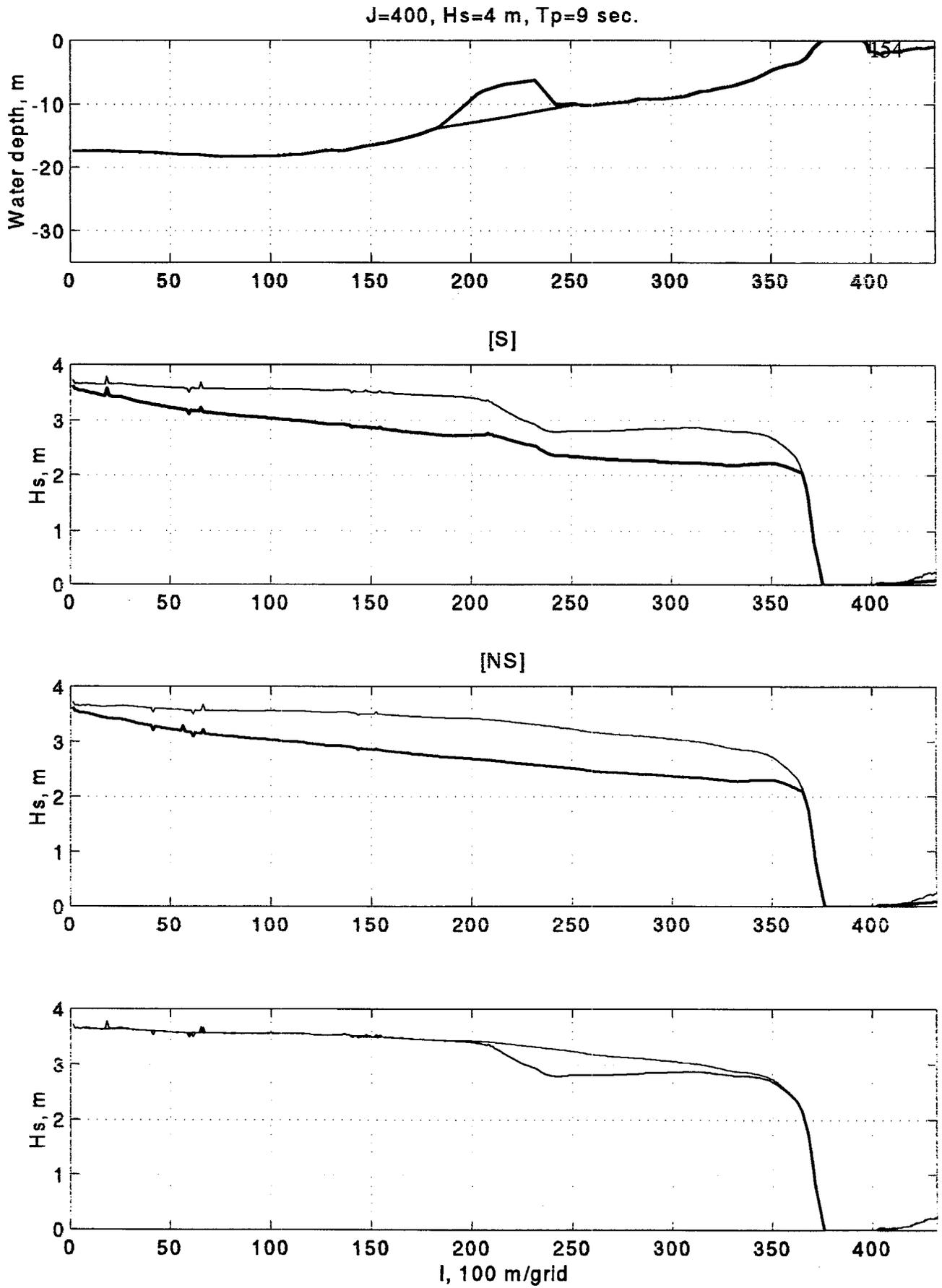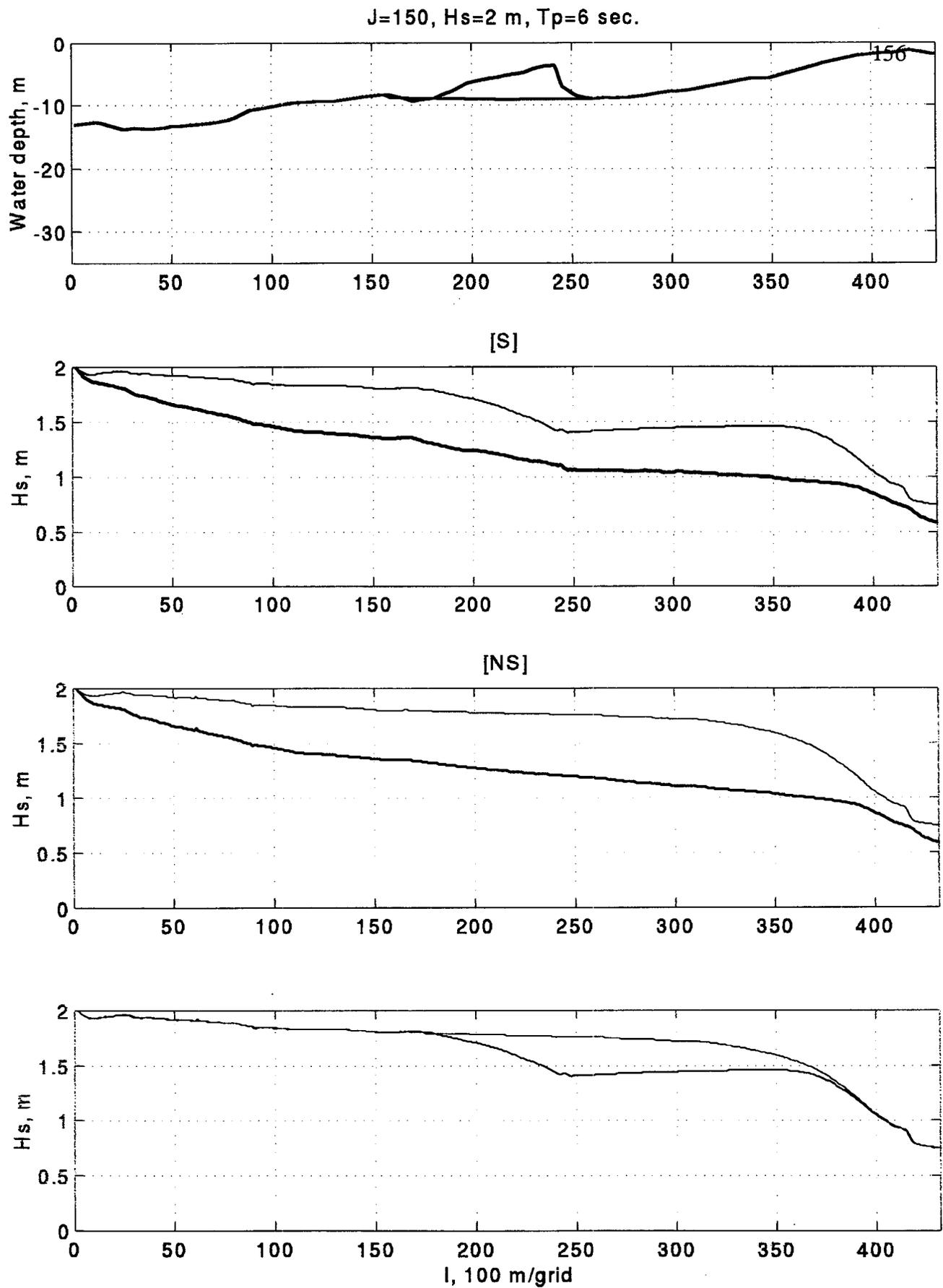
Figure D-4 Wind effect on the wave height distribution in Case 2, sectional profiles at J=400.

Figure D-5 Wind effect on the wave height distribution in Case 3, sectional profiles at J=150.

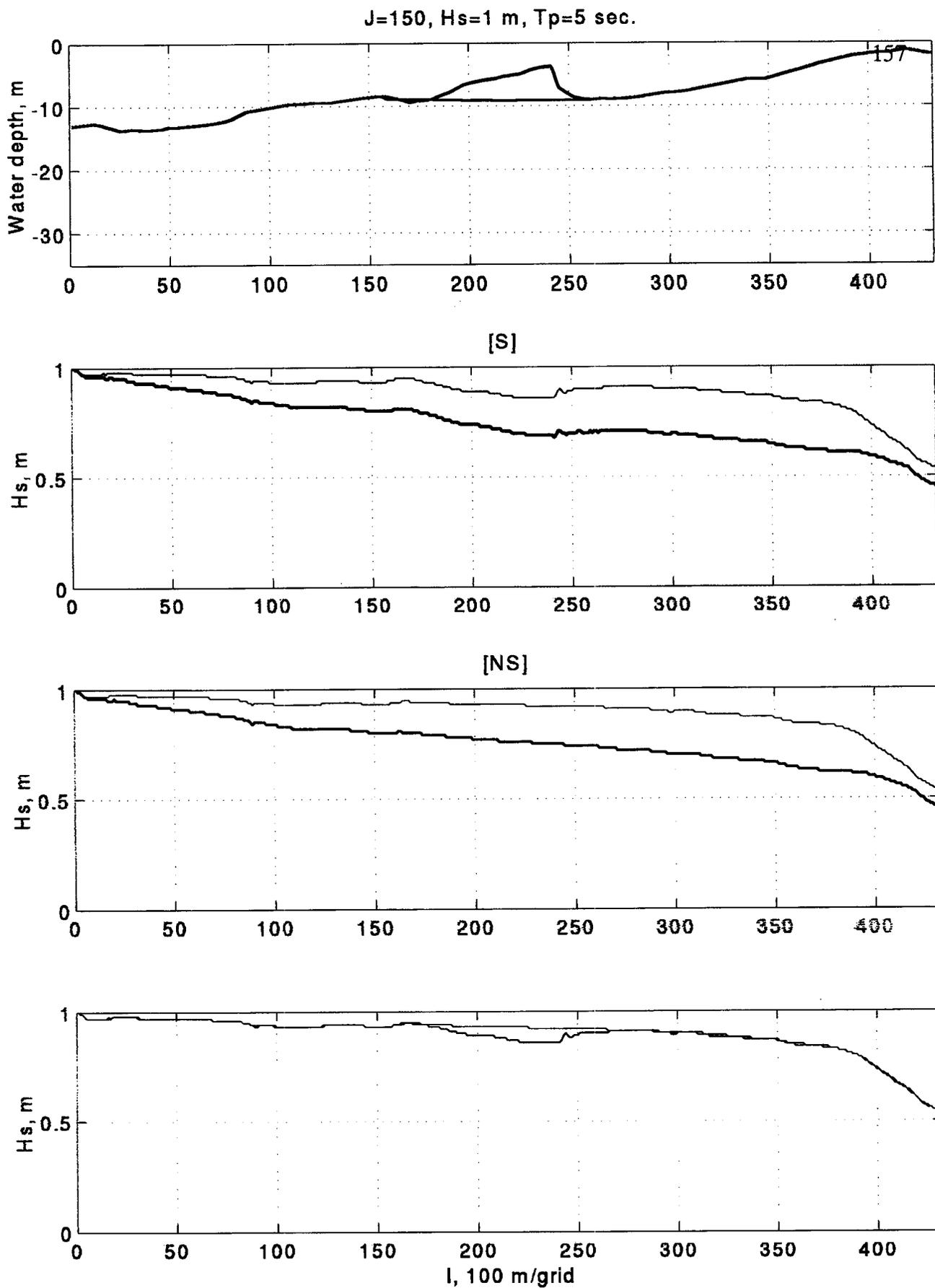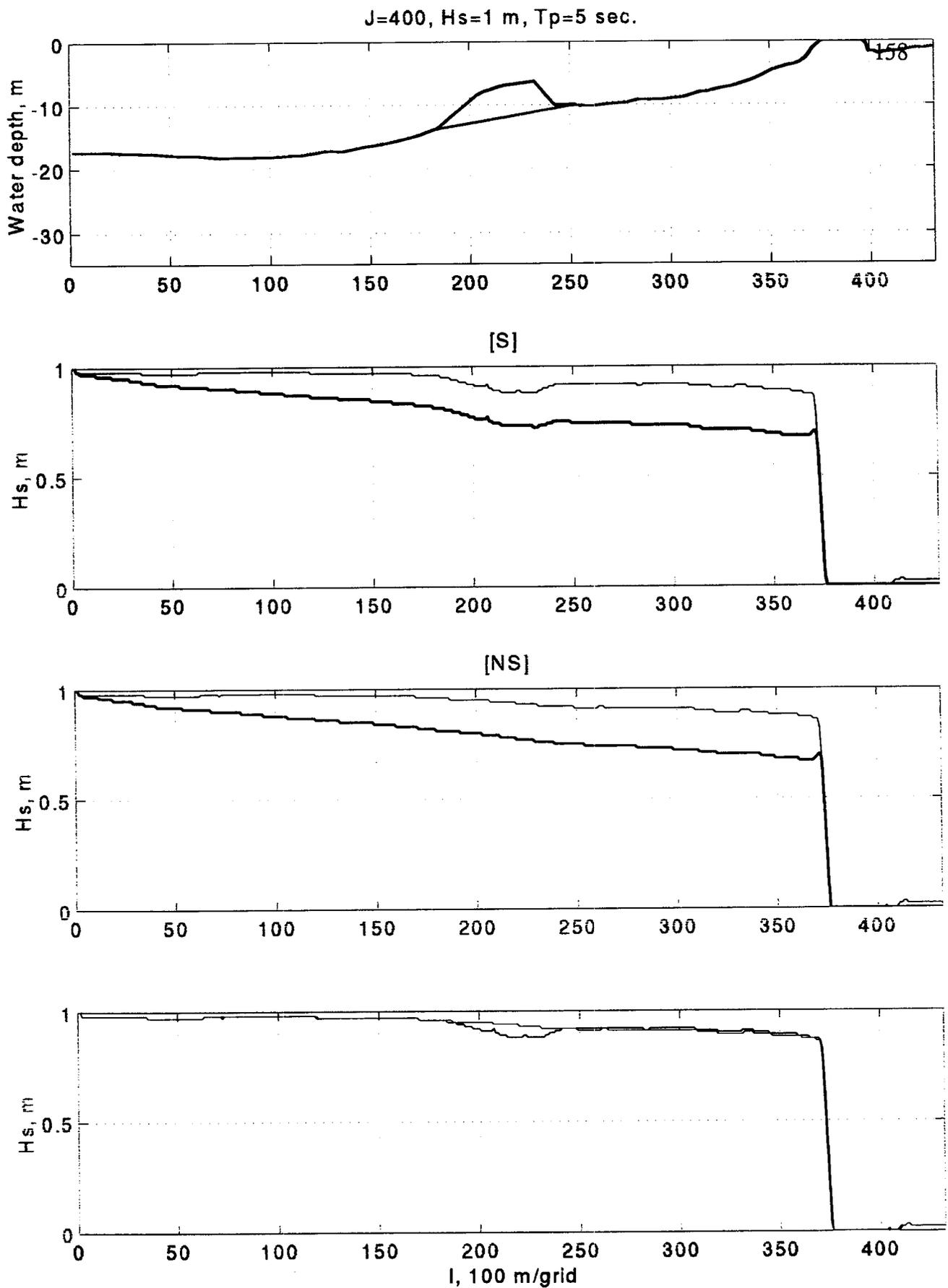Figure D-6 Wind effect on the wave height distribution in Case 3, sectional profiles at J=400.
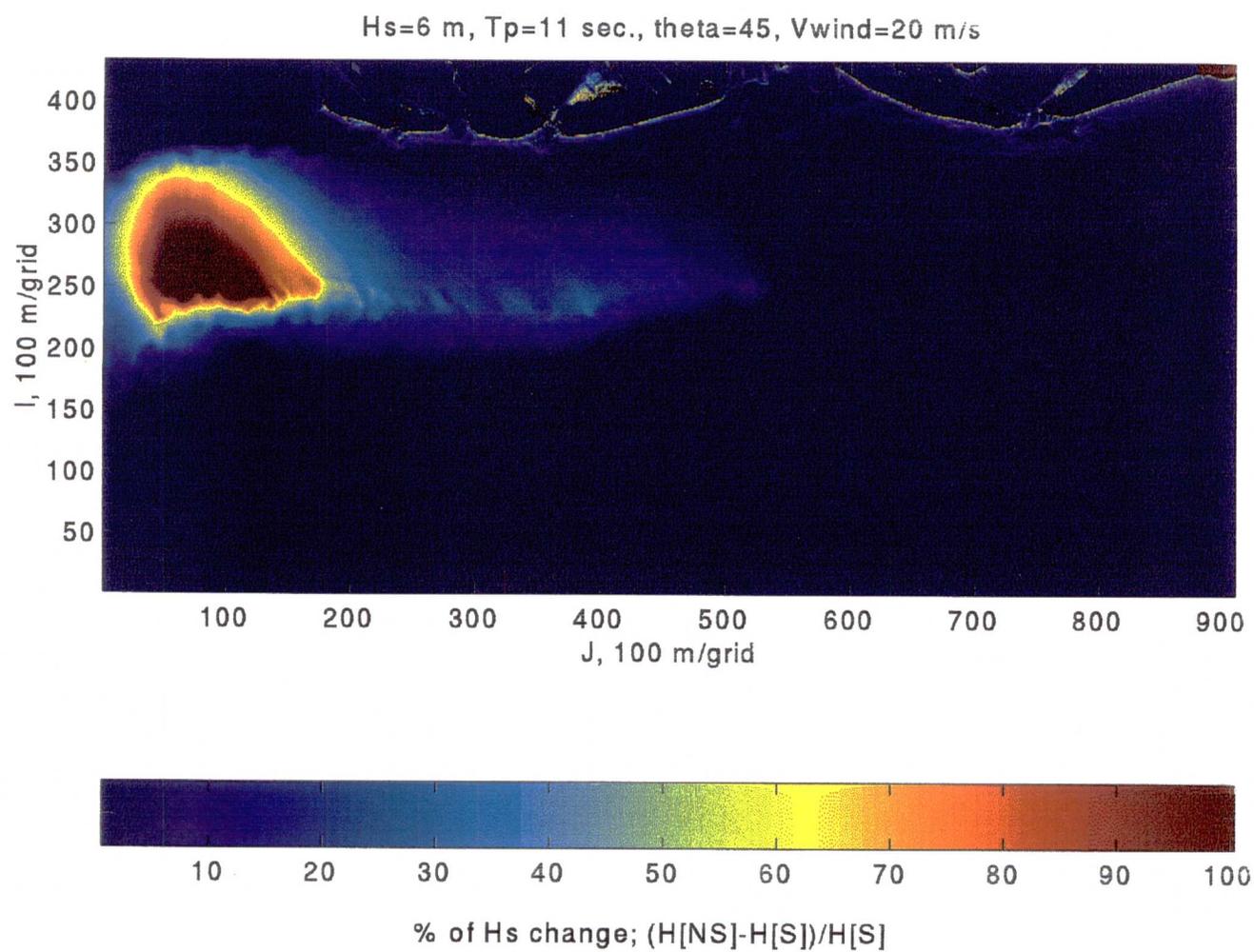
Figure D-7 Wind effect on the wave height distribution in Case 4, sectional profiles at J=150.

J=400, Hs=1 m, Tp=5 sec.

[S]

[NS]

Figure D-8 Wind effect on the wave height distribution in Case 4, sectional profiles at J=400.

Hs=6 m, Tp=11 sec., theta=45, Vwind=20 m/s

% of Hs change; (H[NS]-H[S])/H[S]

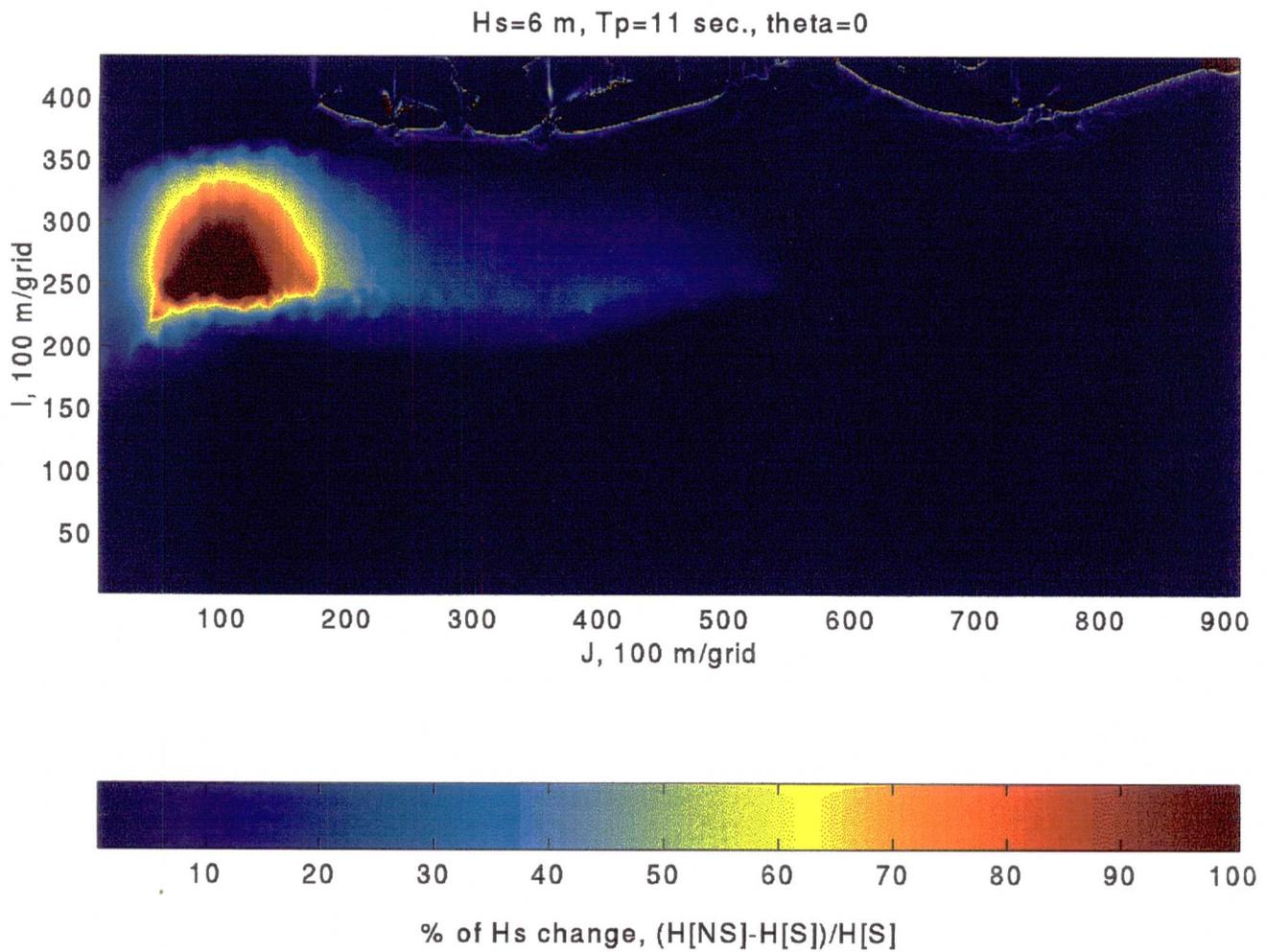Figure D-9 Modeled percentage of H_s increase under effect of wind forcing. Case 1, V_{wind}=20 m/s, θ=0°.

Figure D-10 Modeled percentage of H_s increase under effect of wind forcing. Case 1, V_{wind}=20 m/s, θ=45°
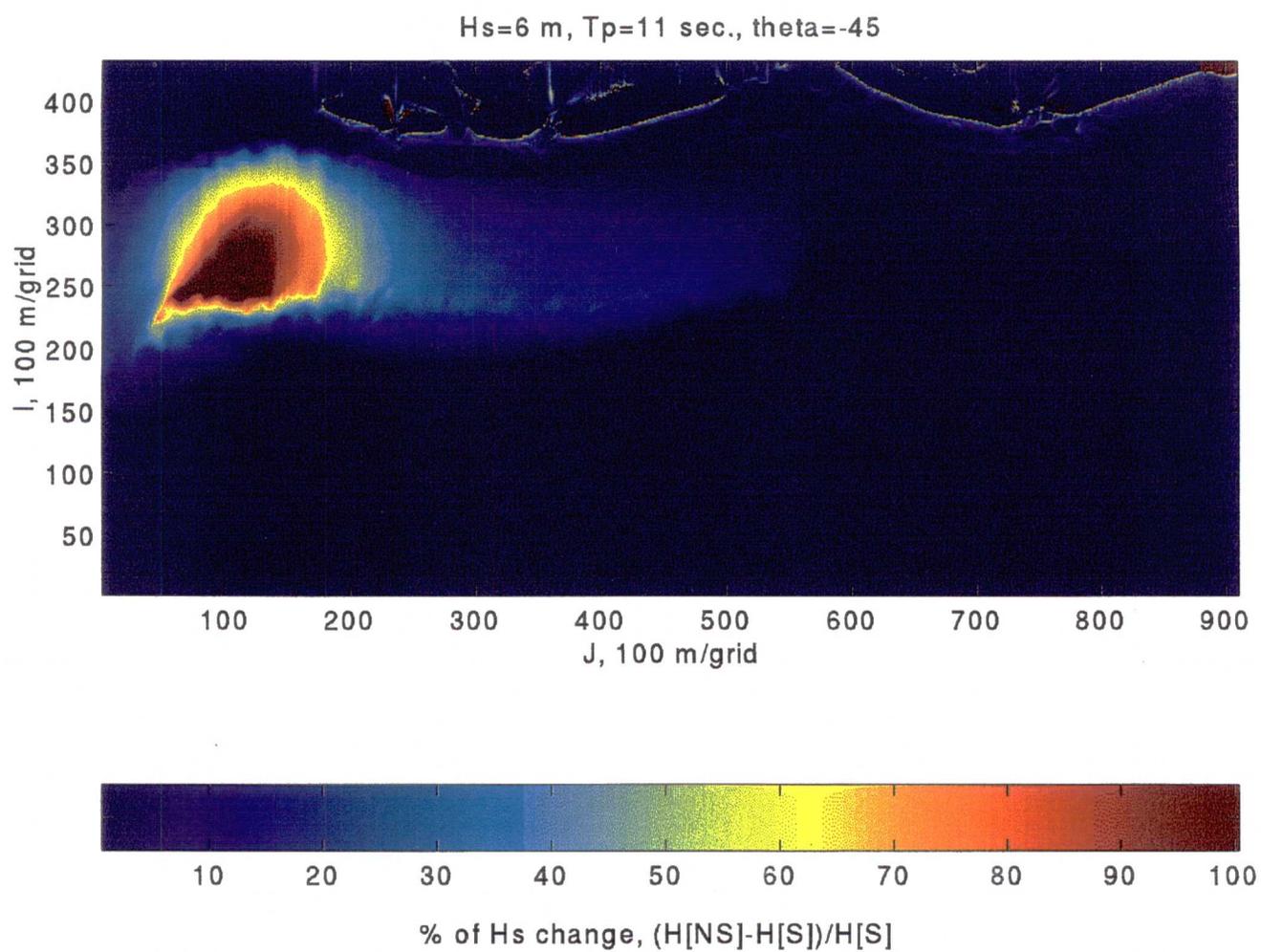
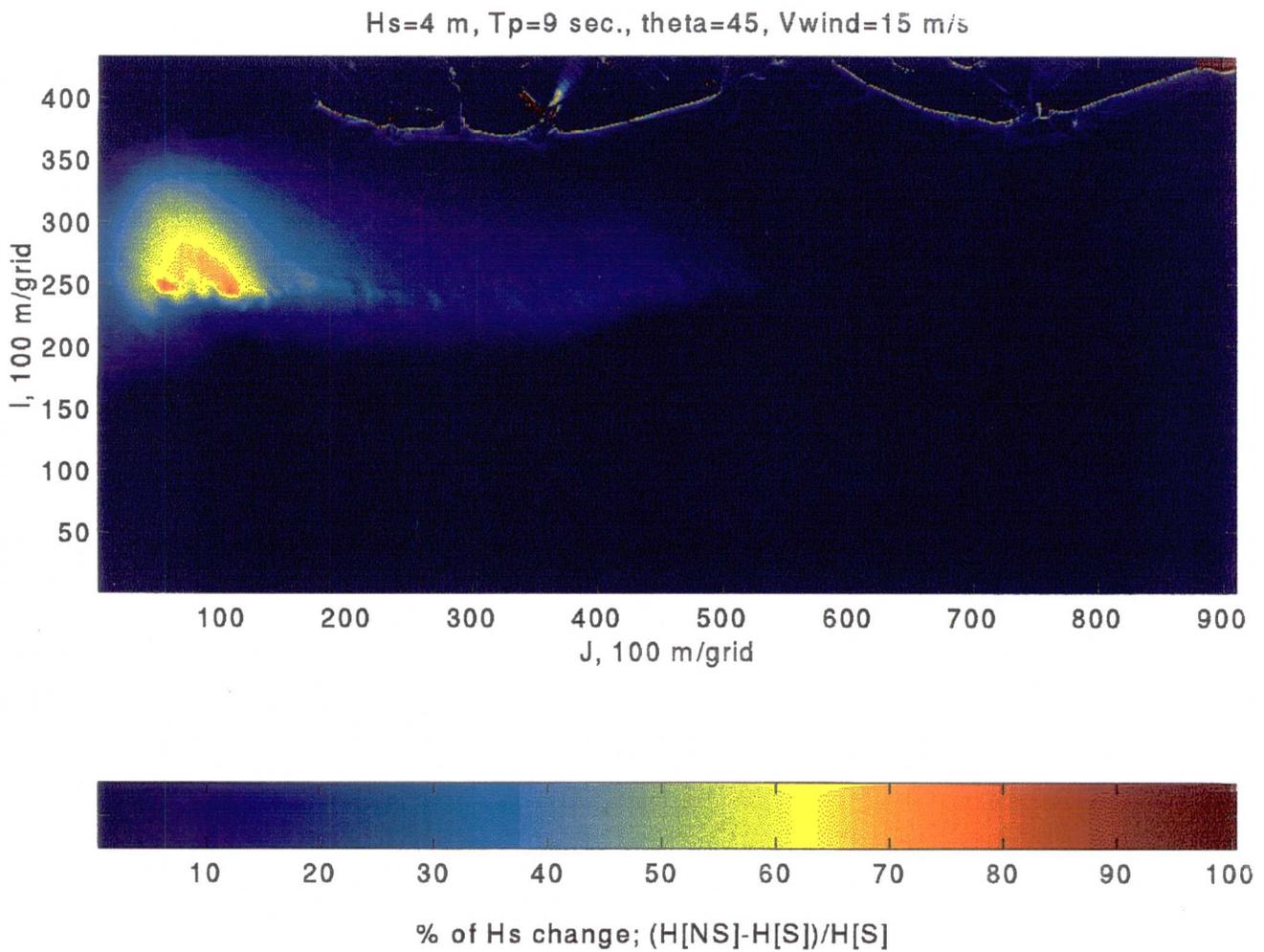Figure D-11 Modeled percentage of H_s increase under effect of wind forcing. Case 1, V_{wind}=20 m/s, θ=-45°

Figure D-12 Modeled percentage of H_s increase under effect of wind forcing. Case 2, V_{wind}=20 m/s, θ=0°

Hs=4 m, Tp=9 sec., theta=0

% of Hs change; (H[NS]-H[S])/H[S]

Figure D-13 Modeled percentage of H_s increase under effect of wind forcing. Case 2, V_{wind}=20 m/s, θ=45°

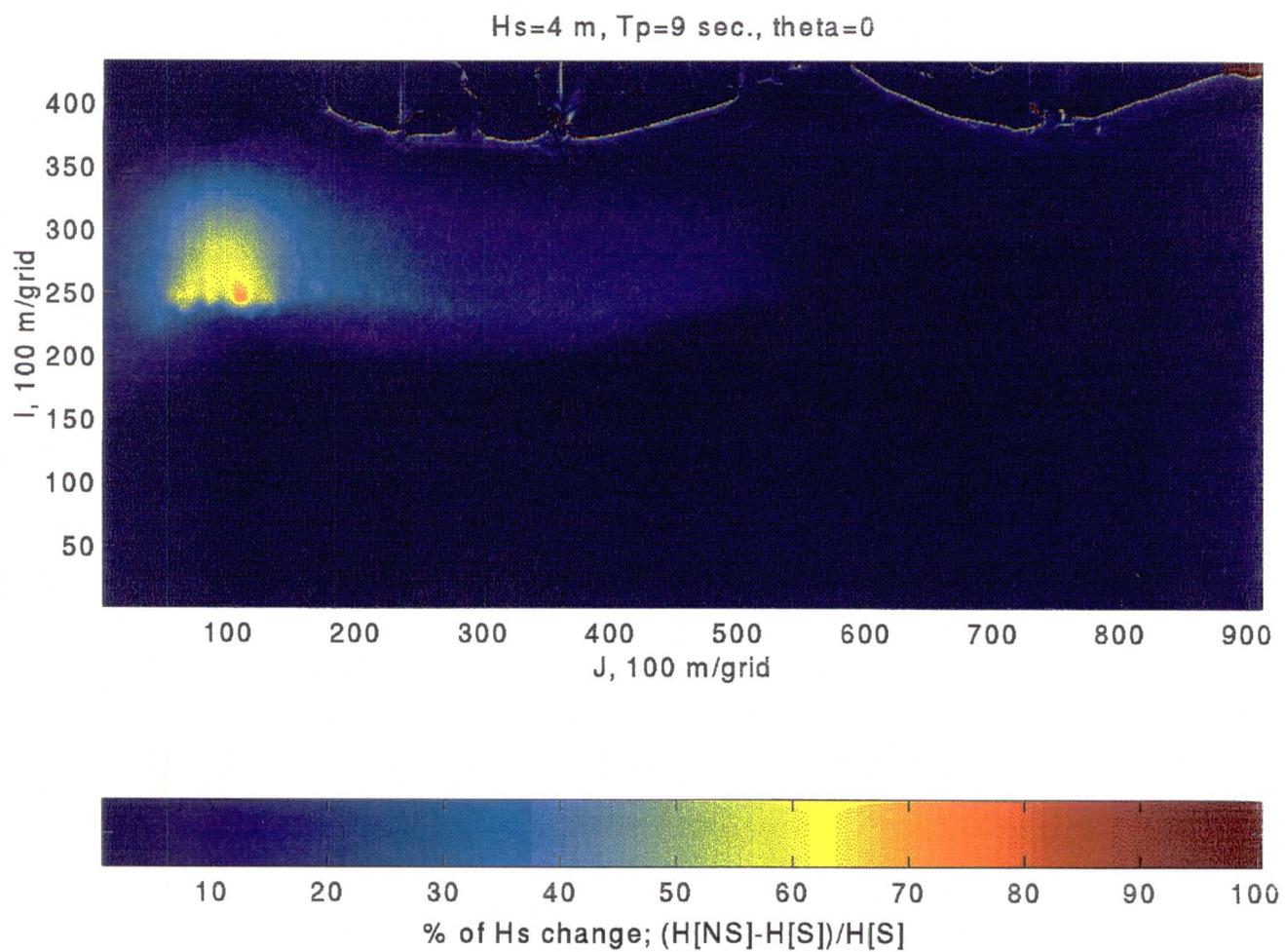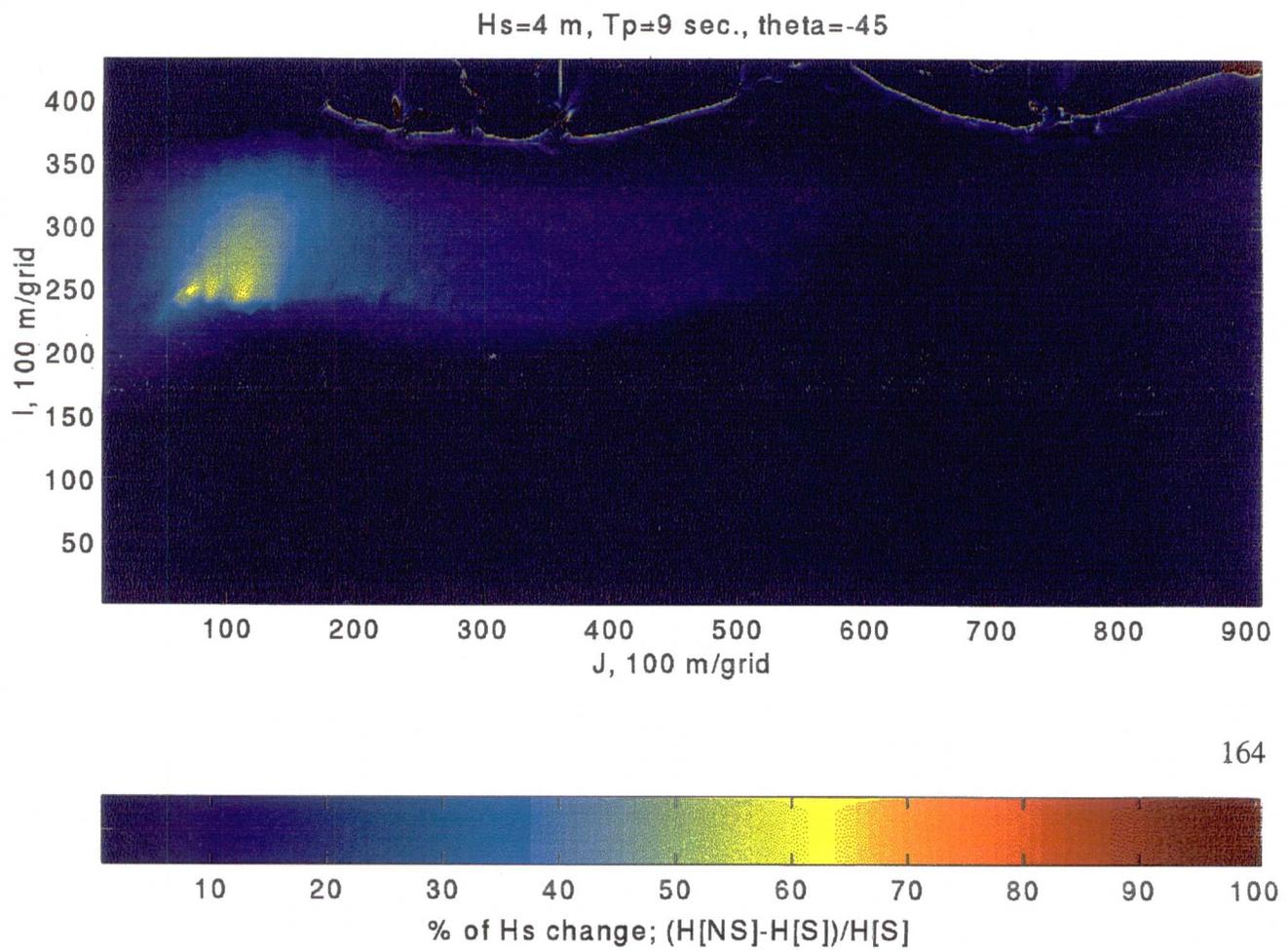Hs=4 m, Tp≂9 sec., theta=-45

% of Hs change; (H[NS]-H[S])/H[S]

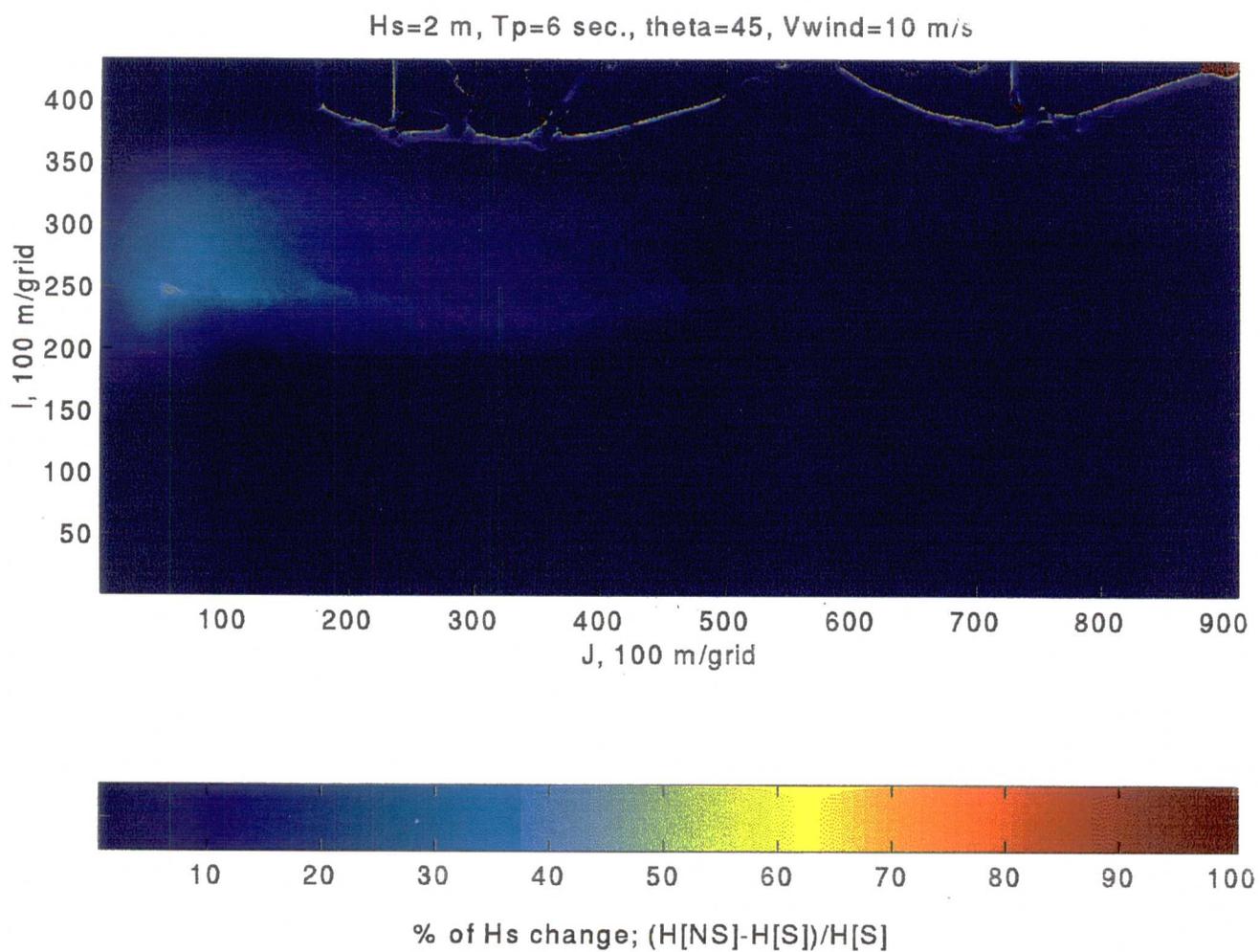Figure D-14 Modeled percentage of H_s increase under effect of wind forcing. Case 2, V_{wind}=20 m/s, θ=-45°

Figure D-15 Modeled percentage of H_s increase under effect of wind forcing. Case 3, V_{wind}=20 m/s, θ=0°

Figure D-16 Modeled percentage of H_s increase under effect of wind forcing. Case 3, V_{wind} =20 m/s, θ =45°

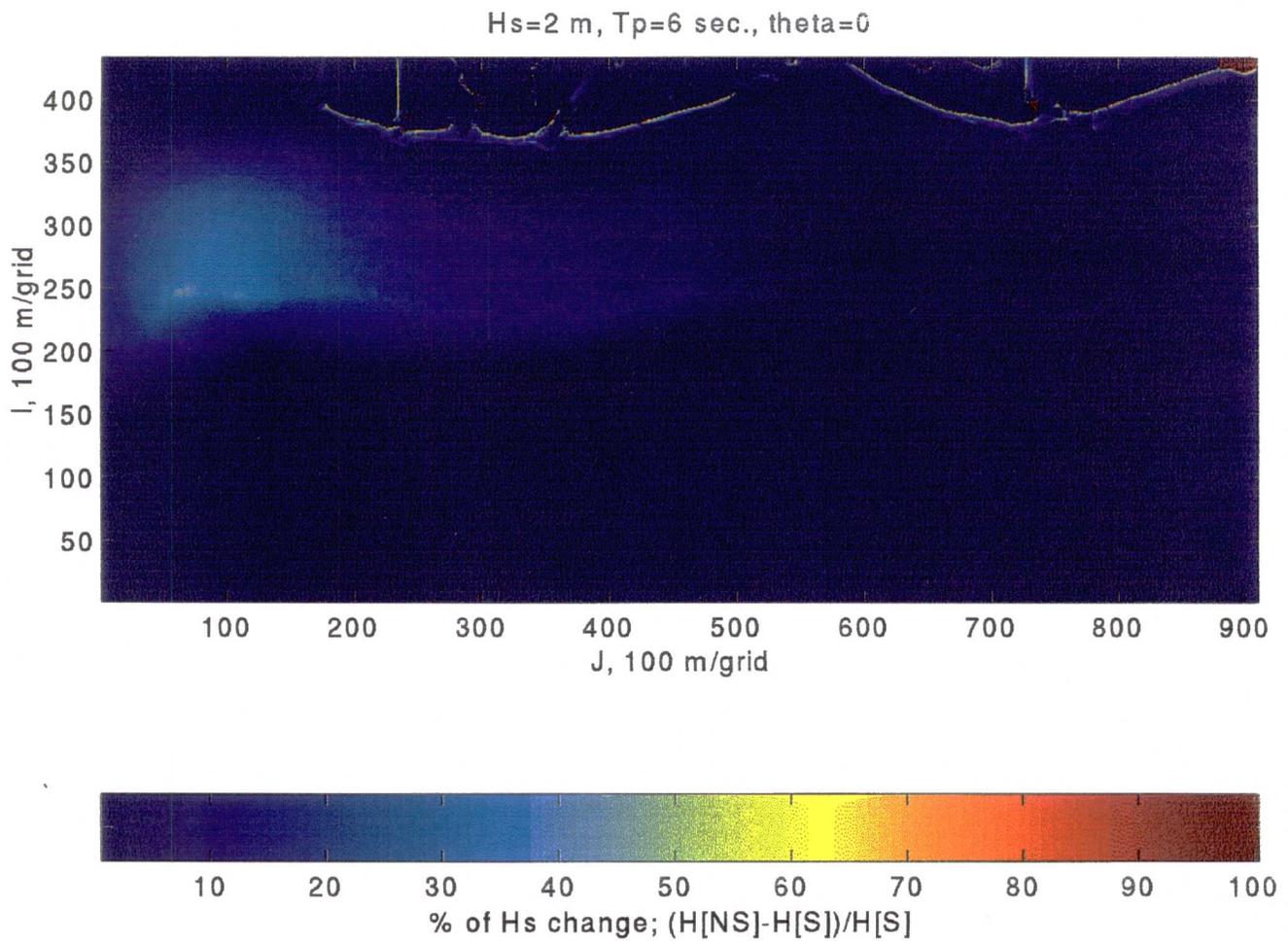Hs=2 m, Tp=6 sec., theta=-45

% of Hs change; (H[NS]-H[S])/H[S]

Figure D-17 Modeled percentage of H_s increase under effect of wind forcing. Case 3, V_{wind}=20 m/s, θ=-45°

Figure D-18 Modeled percentage of H_s increase under effect of wind forcing. Case 4, V_{wind}=20 m/s, θ=0°
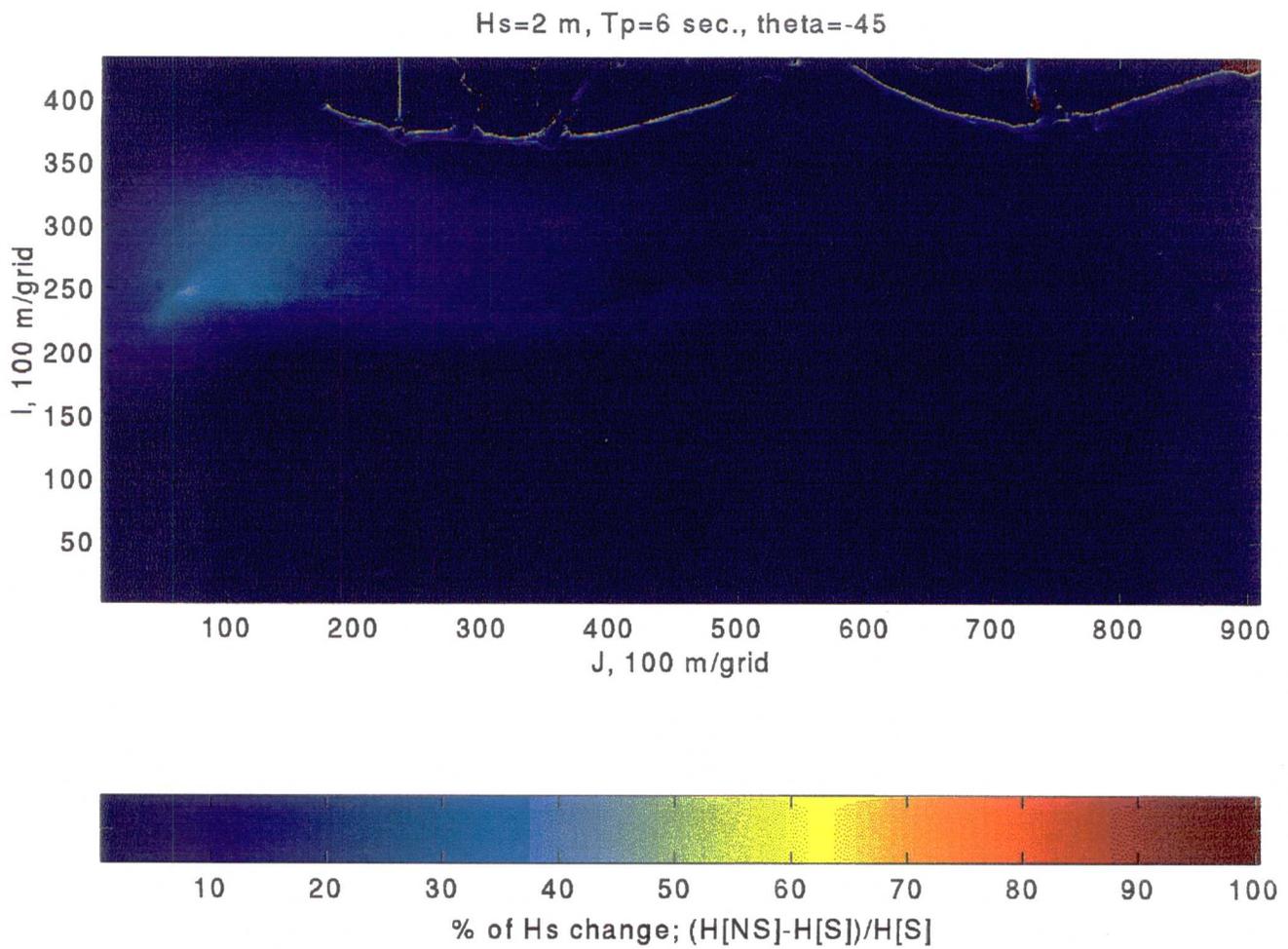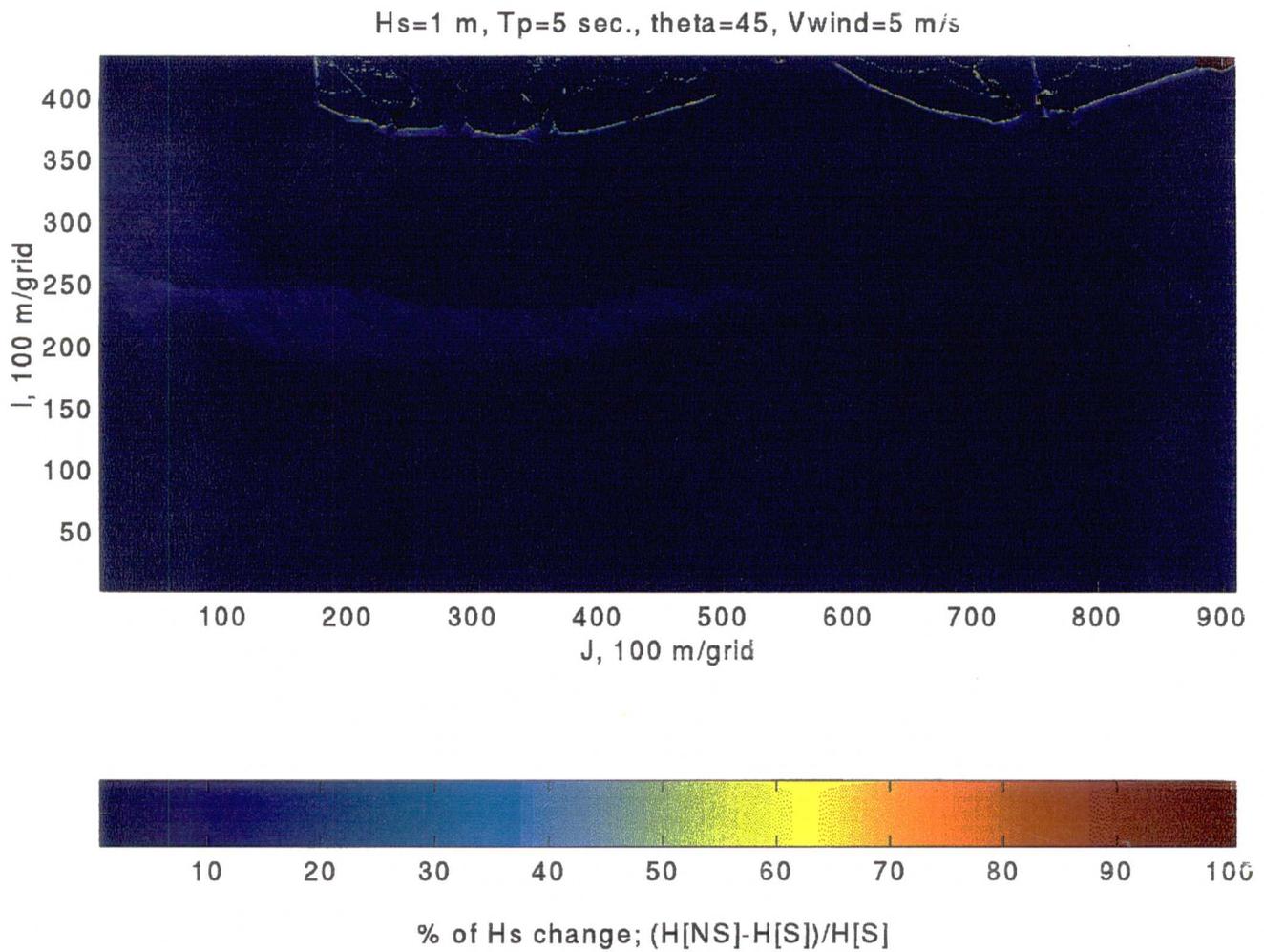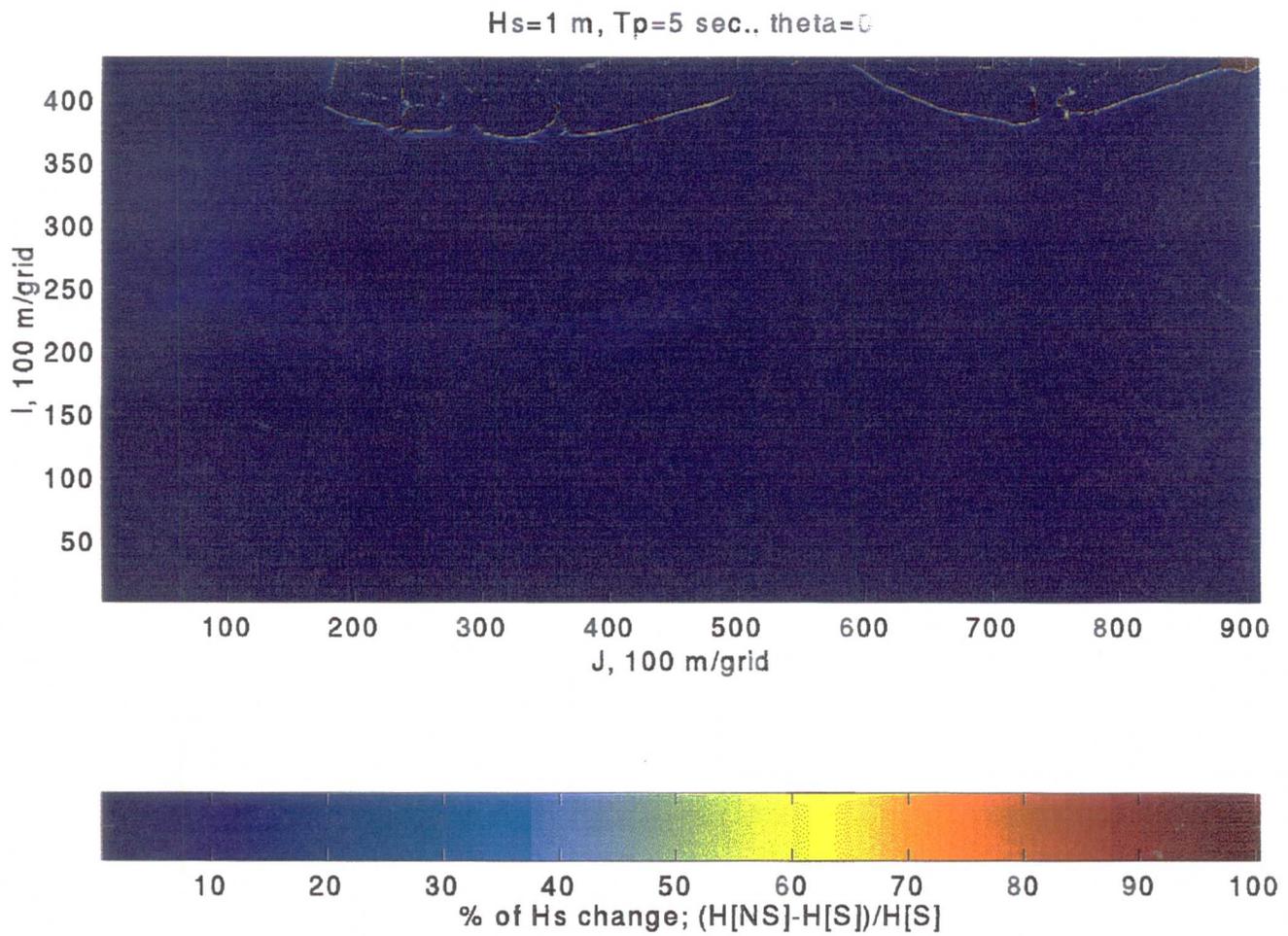
Figure D-19 Modeled percentage of H_s increase under effect of wind forcing. Case 4, $V_{wind} = 20$ m/s, $\theta = 45°$
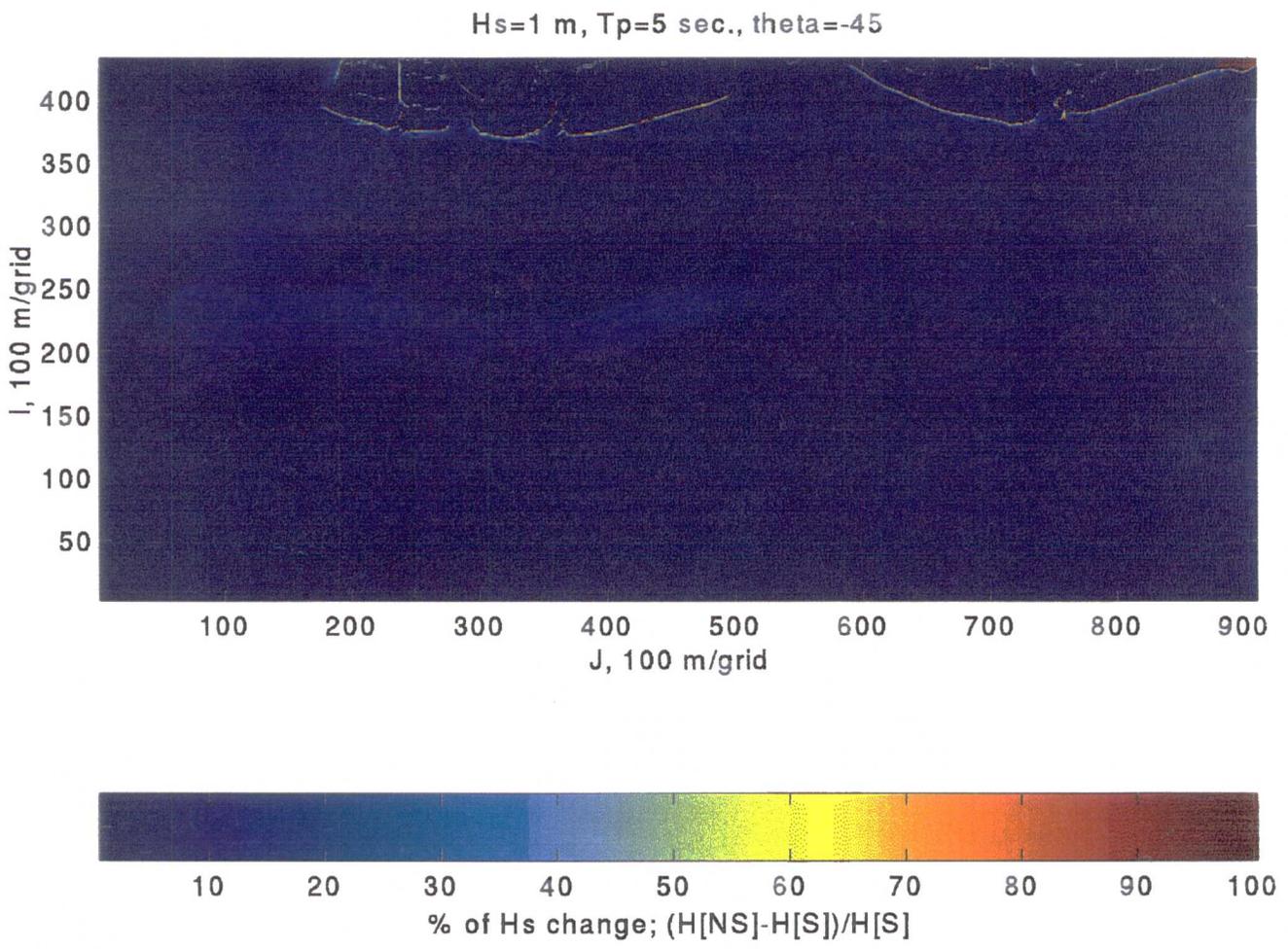
Figure D-20 Modeled percentage of H_s increase under effect of wind forcing. Case 4, $V_{wind} = 20$ m/s, $\theta = -45°$

The Department of the Interior Mission

As the Nation's principal conservation agency, the Department of the Interior has responsibility for most of our nationally owned public lands and natural resources. This includes fostering sound use of our land and water resources; protecting our fish, wildlife, and biological diversity; preserving the environmental and cultural values of our national parks and historical places; and providing for the enjoyment of life through outdoor recreation. The Department assesses our energy and mineral resources and works to ensure that their development is in the best interests of all our people by encouraging stewardship and citizen participation in their care. The Department also has a major responsibility for American Indian reservation communities and for people who live in island territories under U.S. administration.

The Minerals Management Service Mission

As a bureau of the Department of the Interior, the Minerals Management Service's (MMS) primary responsibilities are to manage the mineral resources located on the Nation's Outer Continental Shelf (OCS), collect revenue from the Federal OCS and onshore Federal and Indian lands, and distribute those revenues.

Moreover, in working to meet its responsibilities, the **Offshore Minerals Management Program** administers the OCS competitive leasing program and oversees the safe and environmentally sound exploration and production of our Nation's offshore natural gas, oil and other mineral resources. The MMS **Minerals Revenue Management** meets its responsibilities by ensuring the efficient, timely and accurate collection and disbursement of revenue from mineral leasing and production due to Indian tribes and allottees, States and the U.S. Treasury.

The MMS strives to fulfill its responsibilities through the general guiding principles of: (1) being responsive to the public's concerns and interests by maintaining a dialogue with all potentially affected parties and (2) carrying out its programs with an emphasis on working to enhance the quality of life for all Americans by lending MMS assistance and expertise to economic development and environmental protection.